

Clustering Kinetics in Al-Mg-Si Alloys Investigated by Positron Annihilation Techniques

vorgelegt von

Dipl.-Phys.

Meng Liu

aus Xuzhou, V.R. China

**von der Fakultät III – Prozesswissenschaften
der Technischen Universität Berlin
zur Erlangung des akademischen Grades**

Doktor der Naturwissenschaften

– Dr. rer. nat. –

genehmigte Dissertation

angefertigt am Helmholtz-Zentrum Berlin für Materialien und Energie
Institut für Angewandte Materialforschung

Promotionsausschuss:

Vorsitzender: Prof. Dr. Walter Reimers

Gutachter: Prof. Dr. John Banhart

Gutachter: Prof. Dr. Reinhard Krause-Rehberg

Tag der wissenschaftlichen Aussprache: 02. Juli 2014

Berlin 2014

D83

*Dedicated to
my parents and sister
for their love and encouragements*

Eidesstattliche Erklärung

Ich erkläre an Eides Statt, dass ich die vorliegende Dissertation in allen Teilen selbstständig verfasst und keine anderen als die angegebenen Quellen und Hilfsmittel benutzt habe. Alle Ausführungen, die anderen veröffentlichten oder nicht veröffentlichten Schriften wörtlich oder sinngemäß entnommen wurden, habe ich kenntlich gemacht.

Ort, Datum

Unterschrift

Kurzfassung

Die Clusterbildungsprozesse in abgeschrecktem reinem Al, Al-Mg und Al-Si, sowie in reinen oder Cu/Ge-haltigen Al-Mg-Si-Legierungen wurden während der Kaltauslagerung mittels Positronen-Lebensdauer-Spektroskopie, Dopplerverbreiterungs-Spektroskopie sowie Thermoanalyse (DSC) untersucht.

In reinem Al, Al-Mg- und Al-Si-Legierungen werden Positronen entweder in der Matrix oder in einzelnen-Leerstellen (Al) bzw. in Aggregaten aus Leerstellen und gelösten Atomen (Al-Mg- und Al-Si-Legierungen) vernichtet. Während der Kaltauslagerung werden Leerstellencluster in verschiedenen Größen und Dichten gebildet. Der Prozess ist abhängig von der Sprungfrequenz der Leerstelle, die an entweder Mg oder an Si Atome gebunden ist.

Direkt oder kurz nach dem Abschrecken konnten zwei konkurrierende Positronenfallen in reinen Al-Mg-Si-Legierungen identifiziert werden. Die erste Falle enthält Leerstellen ist tief (~ 1 bis 2 eV) und fängt die meisten Positronen irreversibel ein. Die zweite Falle wird von leerstellenfreien Atomclustern gebildet und ist flach ($0,031$ eV). Aus dieser können Positronen wieder entweichen. Während der ersten 80 min der Kaltauslagerung fangen Cluster aus gelösten Atomen aufgrund der Zunahme Ihrer Größe und Dichte zunehmend Positronen ein, und der Beitrag der Leerstellen nimmt kontinuierlich ab. Die Bildung und das Wachstum von Clustern aus gelösten Atomen ist in Al-0,6%Mg-0,8%Si wesentlich schneller als in Al-0,4%Mg-0,4%Si Legierungen, wahrscheinlich aufgrund der höheren Konzentration von gelösten Atomen. Bei fortschreitender Kaltauslagerung wird das weitere Wachstum der zuvor gebildeten Si-reichen Cluster durch Mg dominiert. Nach 1 Woche Kaltauslagerung werden die meisten Positronen vor allem von Clustern eingefangen, die ein Mg/Si-Verhältnis nahe 1 aufweisen.

In Al-Mg-Si-Legierungen mit Cu verlangsamt Cu zunächst die Bildung von Clustern aus gelösten Atomen, fördert aber das anschließende Wachstum. In Al-Mg-Si-Legierungen mit Ge, wird die Kinetik der Raumtemperaturalterung durch Ge mehr verzögert als durch Si. All diese Effekte werden durch die Wechselwirkung zwischen Leerstellen und gelösten Atomen oder Clustern erklärt.

Abstract

The clustering kinetics in quenched pure Al, Al-Mg and Al-Si, as well as in pure or Cu/Ge-containing Al-Mg-Si alloys during natural ageing have been studied by applying positron annihilation lifetime spectroscopy, Doppler broadening spectroscopy and differential scanning calorimetry.

In Al, Al-Mg and Al-Si alloys, positrons annihilate either in the bulk material, or in vacancy-type defects such as mono-vacancies (Al) and vacancy-solute complexes (Al-Mg and Al-Si alloys). Upon natural ageing, vacancy clusters of various sizes and number densities are formed. Such process depends on the jump frequency of the vacancy attached either to Mg or to Si atoms.

Directly or shortly after quenching, two competing positron trapping sites could be identified in pure Al-Mg-Si alloys. The first trap related to vacancy-type defects is deep (~1 to 2 eV), i.e. traps most of the positrons irreversibly. The second trap associated with vacancy-free solute clusters is shallow (0.031 eV) and positrons can escape. During the first 80 min of natural ageing, solute clusters increasingly trap positrons due to their increase in size and number density and the contribution from vacancy-type defects continuously decreases. The formation and growth of solute clusters is much more efficient in Al-0.6%Mg-0.8%Si than in Al-0.4%Mg-0.4%Si alloys, probably due to a higher concentration of solute atoms. As ageing proceeds, the further growth of the previously formed Si-rich solute clusters is increasingly dominated by Mg. After 1 week of natural ageing, most positrons are trapped by solute clusters that have a Mg/Si ratio close to 1.

In Cu-containing Al-Mg-Si alloys, Cu first slows down the formation of solute clusters but later promotes their subsequent growth. In Ge-containing Al-Mg-Si alloys, the natural ageing kinetics are notably retarded by Ge compared to Si. All these effects are explained by the interactions between vacancies and solute atoms or clusters.

List of Abbreviations

AA	artificial ageing
ACS	angular correlation spectroscopy
ADC	analog-to-digital converter
Amp	amplifier
APLT	average positron lifetime
AQ	as-quenched
CDBS	coincidence Doppler broadening spectroscopy
CFD	constant fraction discriminator
CuQ	Cu block quenching
DBAR	Doppler broadening annihilation radiation
DFT	density functional theory
DSC	differential scanning calorimetry
dt	deep trap
fcc	face-centered cubic
FDA	fast data acquisition
FWHM	full width at half maximum
GP	Guinier-Preston
hcp	hexagonal close-packed
HMA	high-momentum analysis
HV	high voltage
IA	isochronal annealing
it	intermediate trap
IWQ	ice water quenching
KMC	kinetic Monte Carlo
LN ₂	liquid nitrogen
LqQ	liquid quenching
LT	low temperature
MCA	multi-channel analyzer
NA	natural ageing
NDA	normal data acquisition
NN	nearest neighbor
NPA	natural pre-ageing
PALS	positron annihilation lifetime spectroscopy
PLT	positron lifetime
PMT	photomultiplier tube
RCL	rapid cooling
RT	room temperature
SCA	single-channel analyzer
SHT	solution heat treatment
SSSS	super-saturated solid solution
st	shallow trap
STM	simple trapping model
TAC	time-to-amplitude converter
TP	temperature profile

Contents

1	Introduction	1
2	Basics of Positron Annihilation Spectroscopy.....	5
2.1	Positron Sources.....	5
2.1.1	^{22}Na Source.....	5
2.1.2	^{68}Ge Source.....	6
2.2	Positron Annihilation Spectroscopy.....	7
2.2.1	Positron Annihilation Lifetime Spectroscopy.....	7
2.2.2	Doppler Broadening Annihilation Radiation.....	9
3	Experimental Techniques	11
3.1	Samples	11
3.1.1	Chemical Compositions.....	11
3.1.2	Sample Preparation.....	11
3.1.2.1	Solution Heat Treatment and Quenching.....	13
3.1.2.2	Mg Losses during Solution Heat Treatment.....	18
3.2	Source Production.....	20
3.2.1	^{22}Na Source.....	20
3.2.2	^{68}Ge and ^7Be Sources.....	21
3.3	Instruments and Data Analysis.....	22
3.3.1	Positron Annihilation Lifetime Spectroscopy.....	22
3.3.1.1	Sample Environment.....	22
3.3.1.2	Detection System.....	24
3.3.1.3	NIM-standard Electronics.....	25
3.3.1.4	Determination of the Channel Width.....	26
3.3.1.5	Data Acquisition and Evaluation.....	26
3.3.1.6	Detector Alignment.....	28
3.3.2	Doppler Broadening Annihilation Radiation.....	34
3.3.2.1	Sample Environment.....	35
3.3.2.2	High-purity Ge Detector.....	35
3.3.2.3	Stabilizer.....	36
3.3.2.4	Energy Resolution.....	36
3.3.2.5	Data Analysis.....	37
3.3.3	Differential Scanning Calorimetry.....	38
3.4	Temperature Profiles.....	39
3.5	Overview of the PAS Experiments.....	40

4	Results and Discussion	41
4.1	Pure Al.....	41
4.1.1	Positron Annihilation Lifetime Spectroscopy.....	41
4.1.1.1	Results and Discussion Based on Experiments.....	41
4.1.1.2	Results and Discussion Based on Modelling	43
4.1.2	Doppler Broadening Annihilation Radiation	47
4.2	Binary Al-Mg and Al-Si Alloys.....	51
4.2.1	Positron Annihilation Lifetime Spectroscopy.....	51
4.2.1.1	Validation of the 2-component Fitting.....	51
4.2.1.2	Evolution of τ_i & I_i during NA	52
4.2.1.3	Evolution of τ_i & I_i during IA.....	61
4.2.2	Doppler Broadening Annihilation Radiation	62
4.3	From Binary Al-Mg and Al-Si to Ternary Al-Mg-Si Alloys.....	66
4.3.1	Positron Annihilation Lifetime Spectroscopy.....	66
4.3.1.1	Adding 0.05% Si (Mg) to Al-0.5%Mg (Si) Alloy.....	66
4.3.1.2	Adding 0.1% or 0.5% Si (Mg) to Al-0.5%Mg (Si) Alloy.....	69
4.3.2	Differential Scanning Calorimetry.....	72
4.3.2.1	Adding 0.05% Si (Mg) to Al-0.5%Mg (Si) Alloy.....	72
4.3.2.2	Adding 0.1% or 0.5% Si (Mg) to Al-0.5%Mg (Si) Alloy	72
4.3.3	Electrical Resistivity	73
4.4	Ternary Al-Mg-Si Alloys.....	74
4.4.1	Positron Annihilation Lifetime Spectroscopy.....	75
4.4.1.1	τ_{1C} Evolution in Al-Mg-Si Alloys at Room Temperature (FDA)	75
4.4.1.2	τ_{1C} Evolution in Alloys F and H at Low Temperatures (FDA).....	76
4.4.1.3	Temperature and Time Dependence of τ_{1C} in Alloy H (NDA + FDA).....	81
4.4.1.4	Temperature and Time Dependence of τ_{f+s} & I_{f+s} in Alloy H (NDA).....	85
4.4.1.5	Time Dependence of τ_i & I_i in Alloy H (NDA, Prague)	88
4.4.1.6	Time Dependence of τ_i & I_i in Alloys F and H (FDA)	92
4.4.1.7	τ_{1C} Evolution in Artificially Aged Alloys F and H during NA (FDA)	95
4.4.1.8	Modelling of the Temperature Dependence of τ_i & I_i in Alloy H (NDA)	97
4.4.1.9	Modelling of the Time Dependence of τ_{f+s} & I_{f+s} in Alloy H (FDA).....	104
4.4.2	Doppler Broadening Annihilation Radiation	108
4.4.2.1	Low-momentum Region of Alloys F and H during NA (HMA)	109
4.4.2.2	Intermediate-momentum Region of Alloys F and H during NA (HMA)	114
4.4.2.3	High-momentum Region of Alloys F and H during NA (HMA).....	115
4.4.2.4	Ratio Curve Analysis of Alloy H during NA (CDBS, Prague).....	116
4.4.3	Comparison with Differential Scanning Calorimetry Measurements.....	119
4.4.4	Comparison with Electrical Resistivity Measurements	121
4.4.5	Comparison with Hardness Measurements.....	123

4.4.6	Comparison with Kinetic Monte Carlo Simulations.....	124
4.4.7	Overview of the Stages Observed with Different Experimental Methods	125
4.5	Cu/Ge-containing Al-Mg-Si Alloys.....	126
4.5.1	Positron Annihilation Lifetime Spectroscopy.....	126
4.5.1.1	Cu-containing Al-Mg-Si Alloys.....	126
4.5.1.2	Ge-containing Al-Mg-Si Alloys.....	132
4.5.2	Differential Scanning Calorimetry.....	134
4.5.2.1	Cu-containing Al-Mg-Si Alloys.....	134
4.5.2.2	Ge-containing Al-Mg-Si Alloys.....	135
4.5.3	Hardness.....	136
4.5.3.1	Cu-containing Al-Mg-Si Alloys.....	136
4.5.3.2	Ge-containing Al-Mg-Si Alloys.....	137
5	Conclusions.....	139
	Appendix.....	143
A.1	Positron Affinities and Bulk Lifetimes	143
A.2	Comparison between LT PALS and Resistivity Experiments	144
A.3	Modified High Voltage Divider for XP2020Q PMT	145
A.4	Three-view Drawing of the Sample Environment	146
A.5	Cooling Baths.....	147
	References.....	149
	Acknowledgements	165

Chapter 1

Introduction

6000 series Al-Mg-Si alloys are extensively used in the automotive industry due to their excellent mechanical properties, namely medium to high strength, low specific weight combined with good formability, which fulfills the requirement of use as car body panel. These alloys can be strengthened through precipitation hardening during artificial aging (AA), by which the movement of dislocations is effectively hindered.

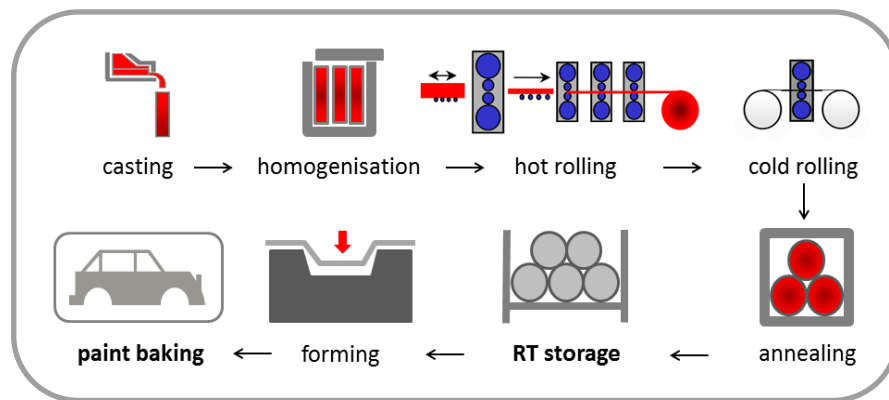


Figure 1.1. Schematic illustration of industrial car panel production chain [Fur11]. After casting, the ingot is homogenized, hot rolled, cold rolled and annealed to achieve the essential microstructural features for further processing.

Due to the practically unavoidable storage at room temperature (RT) for a certain time (equivalent to natural ageing, NA), as shown in Fig 1.1, industrial Al-Mg-Si alloys with various Mg and Si contents exhibit either a “positive” [Cha09, Zol65] or “negative” [Pas66] strength response during the subsequent paint baking process (equivalent to AA at ~ 180 °C for ~ 30 min). As an example, a considerable decrease in hardness response can be clearly observed in an Al-Mg-Si alloy during AA, if the alloy was naturally pre-aged (NPA) for 10080 min (1 week), see Fig. 1.2.

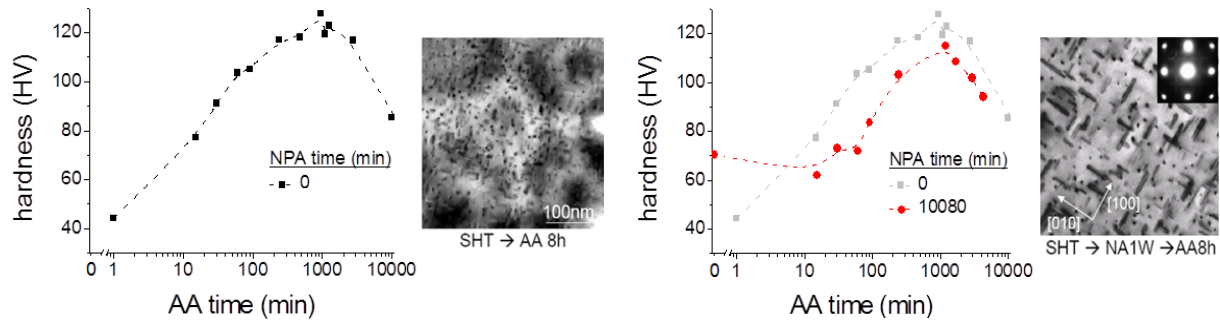


Figure 1.2. Negative strength response in an Al-Mg-Si alloy. (L) After solution heat treatment (SHT) and quenching, the Al-Mg-Si alloy was directly artificially aged, the corresponding hardness evolution during AA and the TEM image of the small but dense β'' precipitates formed after 8 h of AA are shown; (R) Between quenching and AA, the Al-Mg-Si alloy was stored at RT (naturally pre-aged, NPA) for 10080 min. Due to such a storage, larger but coarser β'' precipitates were formed after 8 h of AA, and a decrease in hardness response was observed. Figures were made by C.S.T. Chang.

Such effects are known to be caused by solute clusters formed during NA. These are difficult to observe, one hand due to the low Mg or Si content of the investigated alloys (giving rise to a low signal to noise ratio), on the other hand due to the similar electronic configuration of Mg, Al and Si atoms (leading to low elemental contrast for microscopy methods) [Ban10]. Even so, previous studies focused on cluster formation in Al-Mg-Si alloys by using different kinds of integral methods such as differential scanning calorimetry (DSC) and electrical resistivity showed that the entire cluster evolution is rather complex. In particular, by using positron annihilation lifetime spectroscopy (PALS) it was found that at least 4 clustering stages exist [Ban11]. However, the exact interpretation of the underlying microscopic processes is still under dispute.

The major goal of this thesis work is to improve the understanding of the fundamental clustering kinetics of Al-Mg-Si alloys during NA by carrying out in-situ or ex-situ positron annihilation experiments. In order to clarify the interactions between Mg, Si and vacancies during clustering, the NA behaviour of pure Al, binary Al-Mg or Al-Si and ternary Al-Mg-Si alloys were investigated.

The strength response during AA can be improved through pre-ageing, pre-straining (leads to the formation of dislocations which consequently promote heterogeneous nucleation) or by adding Cu. Particularly, Cu addition has been found to reduce the deleterious effect of NA

through producing finer structures [Li12, Mor06, Wen12]. In which way the Cu atoms influence the clustering kinetics of Al-Mg-Si alloys was clarified.

In addition, the alloying element Si was replaced by the electrochemically similar element Ge. Although Ge is considerably larger in terms of atomic radius compared to Si, previous studies have shown that the precipitation processes in Al-Mg-Si and Al-Mg-Ge alloys are alike [Mat10]. Therefore, it is of great interest to carry out investigations on Al-Mg-Ge alloys. This will not only generate fundamental knowledge about its clustering behavior during NA, but could also help in designing new alloys with improved properties.

The questions mentioned above were mainly addressed using PALS combined with Doppler broadening annihilation radiation (DBAR) method. The experimental results were validated by introducing various theoretical positron trapping models. Other techniques such as DSC, electrical resistivity and hardness were also employed in order to obtain complementary information about the solute clustering processes during NA.

Chapter 2

Basics of Positron Annihilation Spectroscopy

2.1 Positron Sources

Positron can be produced via e.g.:

- (e^+ , e^-) pair production utilizing bremsstrahlung:



- decay of anti-muon μ^+ :



- decay of isotopes such as ^{22}Na or ^{68}Ge , details of both isotopes will be given in the following sections.

2.1.1 ^{22}Na Source

^{22}Na is the most widely used positron source in laboratories. The decay equation of ^{22}Na is shown in Eq. (2.1.3):



The positron and electron neutrino are produced by β^+ decays (90.4%) to an excited state of ^{22}Ne , after which a 1.275 MeV γ quantum is “simultaneously” emitted within 3.7 ps due to further decays to the ground state of ^{22}Ne , see Fig. 2.1.1. Such a feature makes ^{22}Na an ideal source for positron lifetime measurements. However, the 1.275 MeV γ quanta cause a significant Compton background in energy spectra. Therefore the nearly background-free positron source ^{68}Ge is more suitable for energy resolving methods such as Doppler broadening annihilation radiation spectroscopy, see section 2.1.2.

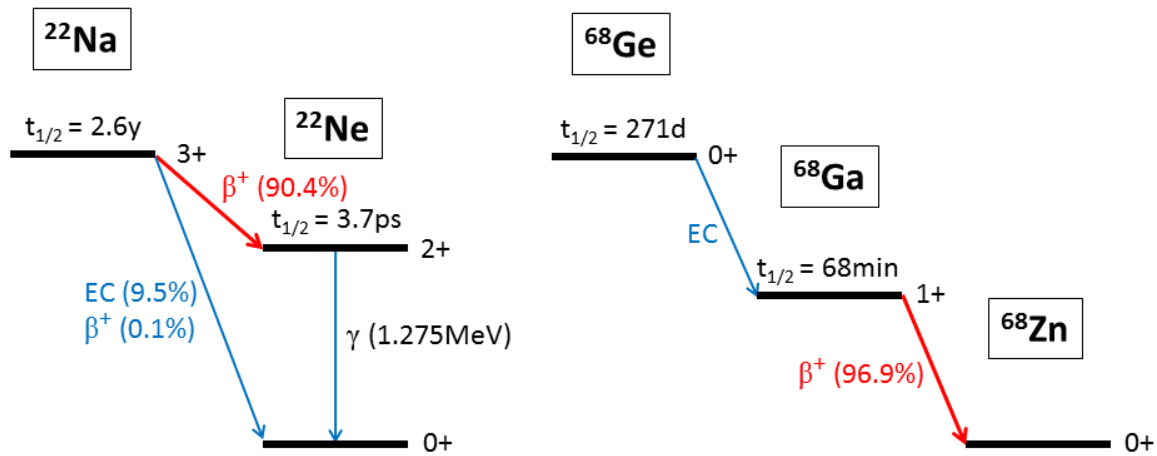


Figure 2.1.1. Decay diagrams of (L) ^{22}Na , beside the main decay channel (β^+ , red arrow) which produces positrons, process such as electron capture (EC) and direction transition to the ground state of ^{22}Ne are also shown; (R) ^{68}Ge , most positrons are produced through the β^+ decay as indicated by the red arrow. “y” and “d” refer to year and day, respectively.

2.1.2 ^{68}Ge Source

^{68}Ge was used as the positron emitter for the DBAR experiments due to its significant lower background than ^{22}Na , thus enabling the analysis of the high-momentum part of the annihilation radiation even with a single Ge detector. As shown in Fig. 2.1.1, ^{68}Ge decays into ^{68}Ga by electron capture (EC), followed by further β^+ decay to ^{68}Zn . This can be described by the following decay equation:



In addition, the other 3.1% of ^{68}Ga produce a γ line of 1.077 MeV, which will be neglected in this study.

[Ber67] characterized the cold-worked Al samples with both ^{22}Na and ^{68}Ge sources by angular correlation spectroscopy (ACS). It was found that although a positron from a ^{68}Ge source penetrates the sample much deeper than the one from ^{22}Na due to the much higher end point energy of ~ 1.9 MeV (^{68}Ge) compared to ~ 0.6 MeV (^{22}Na) [BNLxx], identical results were obtained with these two sources. Therefore, the effects observed in the present study should be volume rather than surface effects using any of the two sources.

2.2 Positron Annihilation Spectroscopy

Positron annihilation spectroscopy (PAS) is a nuclear technique which is used in solid state physics, materials science, chemistry etc. After a positron has entered a solid, it will annihilate with electrons after certain time and 0.511 MeV γ quanta will be released as a consequence. These quanta can be detected and provide the signal for different methods such as PALS, DBAR and ACS accordingly. The spectroscopic signals, which depend on defects and phase compositions, give useful information about the microstructure of solids. Compared to other experimental techniques, PAS has some great advantages: it is non-destructive, there are almost no limits about the sample geometry, measurement in a broad temperature range is possible and it is uniquely sensitive to open volume defects such as vacancies, as one of the most important ingredients in all quenched Al-Mg-Si alloys.

2.2.1 Positron Annihilation Lifetime Spectroscopy

By bremsstrahlung, inelastic scattering with electrons and excitation of plasmons or phonons, positrons are rapidly thermalized within a few ps [Haa09, Klo10], i.e. the kinetic energy of a positron from a ^{22}Na source will be reduced from hundreds of keV to about 40 meV (at RT) within 1 to 3 ps. After the thermal energy has been reached, positrons begin to diffuse in the periodic lattice and occupy a delocalized state in the Al matrix. Due to its positive charge a positron is repelled by the nuclei. Thus, the maximum probability density of the position wave function is localized in interstitial regions. By the presence of open volume defects such as vacancies, positrons are trapped, as shown in Fig. 2.2.1 [Kra03]:

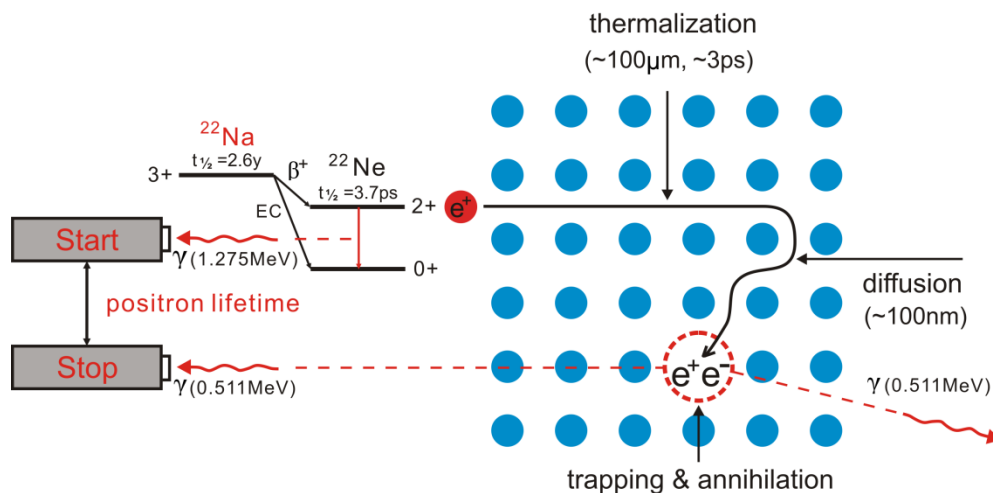


Figure 2.2.1. Schematic illustration of PALS method.

Besides vacancies, precipitates (solute clusters) and their corresponding interfaces are also potential positron traps. Fig. 2.2.2 shows the positron wave functions Ψ_+ of various kinds of positron traps with the corresponding potentials $V_+(x)$ [Kra03]:

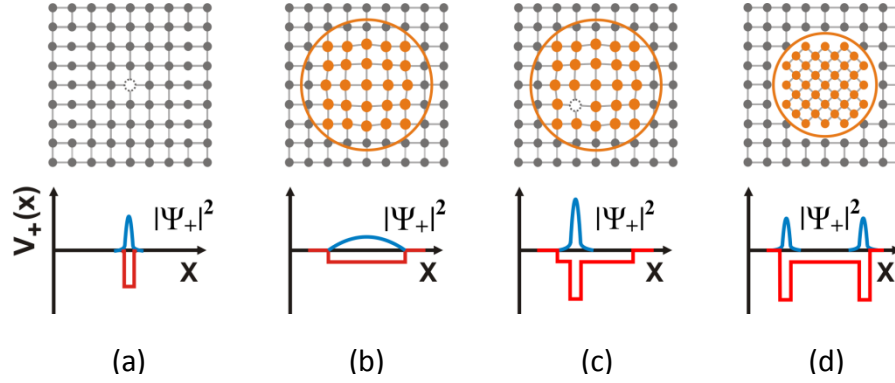


Figure 2.2.2. Positron wave functions ψ_+ and potentials $V_+(x)$ of different types of positron traps. (a) Mono-vacancy; (b) Fully coherent precipitate (yellow dots); (c) Fully coherent precipitate containing a vacancy; (d) Semi-coherent and incoherent precipitates.

The positron wave functions Ψ_+ are spread over the entire coherent precipitates. However, in the presence of open volume defects inside the matrix of coherent precipitates the wave function is strongly localized. For the semi-coherent and incoherent precipitates, the probability of positron trapping at the interface containing a misfit is also high [Kra03].

Positrons trapped by crystal defects annihilate with electrons into 2 γ quanta of 0.511 MeV energy by mass-energy transformation (1 γ and 3 γ processes are also possible but will be neglected due to the low probabilities of such events). The positron lifetime (PLT) is then measured as the time difference between the start signal (1.275 MeV γ quantum, almost simultaneously emitted with the positron) and one of the stop signals (0.511 MeV annihilation γ quanta), see Fig. 2.2.1. The PLT τ is the reciprocal of the annihilation rate λ , which is a function of the positron and electron density $n_{\pm}(r)$ at the annihilation site:

$$\tau = 1/\lambda, \quad (2.2.1)$$

$$\lambda \propto \int n_+(r)n_-(r)\Gamma dr, \quad (2.2.2)$$

where r is the real space vector and Γ is a function accounting for the (e^+ , e^-) Coulomb interaction [Kra03]. The PLT is about 0.165 ns in bulk Al, while by the presence of mono-vacancy, it increases to 0.250 ns due to the locally reduced electron density there.

2.2.2 Doppler Broadening Annihilation Radiation

The non-zero momentum of the annihilation (e^+ , e^-) pair is transferred to the annihilation γ quanta according to the law of momentum conservation. The momentum component p_L in the propagation direction is a variable randomly distributed around zero which leads to an energy shift ($\pm p_L c / 2$) of the 0.511 MeV annihilation peak and a deviation θ from collinearity of the annihilation γ quanta [Kra03], see Fig. 2.2.3. After collecting sufficient events, a symmetrical broadening of the annihilation peak is observed.

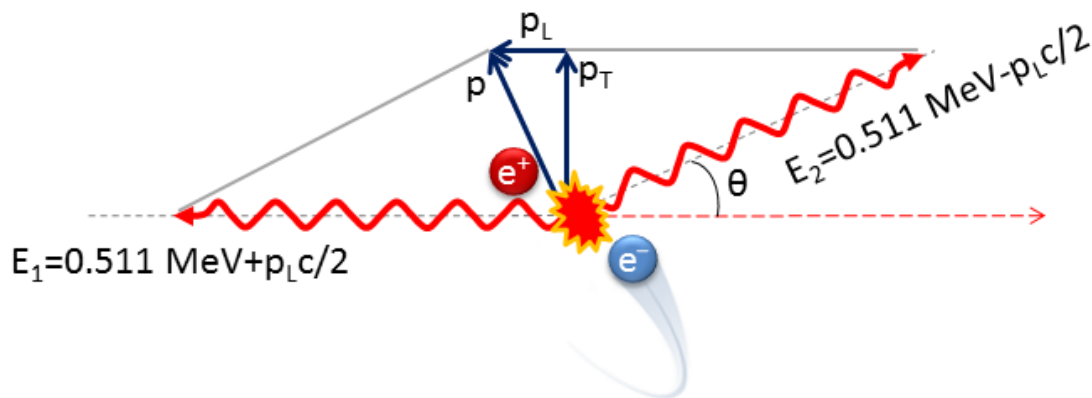


Figure 2.2.3. Schematic illustration of DBAR method.

The chemical surroundings of the annihilation sites can be probed by measuring the high-momentum distribution of the core electrons, which are element specific. However, to extract information from this region is not straightforward due to the high background (some orders of magnitude higher than the signal) caused by e.g. Compton scattering of the 1.275 MeV γ quanta if a ^{22}Na source is applied. In order to access the chemical information, the high-momentum region is usually resolved using the coincidence method of DBAR employing two high-purity germanium detectors (CDBS). Herewith not only the background can be markedly reduced by at least two orders of magnitude, but also the energy resolution improved by a factor of ~ 1.4 [Kra03].

An alternative approach to access the high-momentum region using only a single Ge detector is high-momentum analysis (HMA). HMA entails a sophisticated way of background reduction which considers, for example, Compton scattering, pile-up effects at the detector and incomplete charge collection and requires a nearly background-free positron source like ^{68}Ge . Detailed information can be found from [Haa06, Haa09] and Section 3.3.2.5.

Chapter 3

Experimental Techniques

3.1 Samples

3.1.1 Chemical Compositions

Pure Al, binary Al-Mg and Al-Si and Cu/Ge-free ternary Al-Mg-Si alloys were cast by Hydro Aluminium Bonn, based on pure elements (Al 5N, Mg 4N, Si 5N). Chemical analyses showed that all samples had impurity contents less than 20 ppm, i.e. $< 2/5$ of the smallest solute content. Cu/Ge-containing Al-Mg-Si alloys were prepared by SINTEF Norway. The chemical compositions determined by X-ray microprobe show that the impurity level is less than 100 ppm. The measured compositions of all samples investigated are summarized in Table 3.1.1.

3.1.2 Sample Preparation

The samples used for PALS measurement had a size of $10 \times 10 \times 1 \text{ mm}^3$, while for DBAR experiments samples of equal surface area but 3 mm thickness are required. Such thicknesses ensure that most positrons annihilate in the sample material rather than in the surroundings. All samples were cut from homogenized (24 h at 530 °C) and extruded or cold rolled bars (1.2 or 3.0 mm thick) to the required geometry, followed by mechanical grinding and ultrasonic cleaning in alcohol to reduce surface effects. Besides the chemical analysis as mentioned above, the quality of the samples was also controlled by light microscope, shown in figures 3.1.1 as an example. On the left hand side, agglomerations of Si particles (inside the gray box) were found on the edge of the Al-0.1%Si alloy prepared by our own laboratory, which therefore could not be used. The fine distribution of Si particles by the Hydro Al-1%Si alloy on the right hand side is very satisfactory. Such alloys were used for the experiments. The heat treatments of the samples will be presented in detail in the next section.

Table 3.1.1. Measured chemical compositions of all samples investigated (all in at.%).

sample (nominal composition)	designation	Mg	Si	Cu	Ge
pure Al (5N)	–	–	–	–	–
binary Al-Mg alloys					
Al-0.005%Mg	–	0.006	–	–	–
Al-0.01%Mg	–	0.012	–	–	–
Al-0.05%Mg	–	0.061	–	–	–
Al-0.1%Mg	–	0.115	–	–	–
Al-0.5%Mg	–	0.566	–	–	–
Al-1%Mg	–	1.131	–	–	–
binary Al-Si alloys					
Al-0.005%Si	–	–	0.006	–	–
Al-0.01%Si	–	–	0.016	–	–
Al-0.05%Si	–	–	0.052	–	–
Al-0.1%Si	–	–	0.101	–	–
Al-0.5%Si	–	–	0.500	–	–
Al-1%Si	–	–	1.047	–	–
ternary Al-Mg-Si alloys (I)					
Al-0.05%Mg-0.05%Si	(21)	0.049	0.060	–	–
Al-0.05%Mg-0.1%Si	(22)	0.049	0.096	–	–
Al-0.05%Mg-0.5%Si	(23)	0.049	0.509	–	–
Al-0.1%Mg-0.05%Si	(31)	0.099	0.043	–	–
Al-0.1%Mg-0.1%Si	(32)	0.099	0.092	–	–
Al-0.1%Mg-0.5%Si	(33)	0.099	0.519	–	–
Al-0.5%Mg-0.05%Si	(41)	0.488	0.055	–	–
Al-0.5%Mg-0.1%Si	(42)	0.477	0.091	–	–
Al-0.5%Mg-0.5%Si	(43)	0.510	0.519	–	–
ternary Al-Mg-Si alloys (II)					
Al-0.4%Mg-1%Si	(E)	0.444	0.970	–	–
Al-0.6%Mg-0.8%Si	(F)	0.655	0.758	–	–
Al-0.8%Mg-0.6%Si	(G)	0.887	0.585	–	–
Al-0.4%Mg-0.4%Si	(H)	0.433	0.384	–	–
Al-1%Mg-0.4%Si	(I)	1.131	0.393	–	–
Cu/Ge-containing Al-Mg-Si alloys (I)					
Al-0.40%Mg-0.85%Si	(A2)	0.408	0.829	–	–
Al-0.40%Mg-0.85%Si-0.13%Cu	(A2Cu)	0.494	0.872	0.121	–
Al-0.58%Mg-0.72%Si	(A3)	0.568	0.658	–	–
Al-0.58%Mg-0.72%Si-0.13%Cu	(A3Cu)	0.648	0.701	0.069	–
Al-0.87%Mg-0.43%Si	(A11)	0.840	0.397	–	–
Al-0.87%Mg-0.43%Si-0.13%Cu	(A11Cu)	0.861	0.451	0.113	–
Al-0.58%Mg-0.71%Ge	(G3)	0.222	–	–	0.590
Al-0.58%Mg-0.36%Ge-0.36%Si	(GS3)	0.243	0.310	–	0.195
Al-0.87%Mg-0.43%Ge	(G11)	0.249	–	–	0.137
Al-0.86%Mg-0.22%Ge-0.22%Si	(GS11)	0.440	0.175	–	0.041
Al-0.87%Mg-0.43%Ge-0.13%Cu	(G11Cu)	0.243	–	0.109	0.129
Al-0.86%Mg-0.22%Ge-0.22%Si-0.13%Cu	(GS11Cu)	0.447	0.176	0.129	0.047
Cu-containing Al-Mg-Si alloys (II)					
Al-1.2%Mg-0.5%Si	(A6)	1.178	0.481	–	–
Al-1.1%Mg-0.5%Si-0.1%Cu	(A6Cu)	1.069	0.462	0.123	–
Al-0.5%Mg-1.2%Si	(A9)	0.456	1.213	–	–
Al-0.4%Mg-1.2%Si-0.1%Cu	(A9Cu)	0.390	1.176	0.115	–

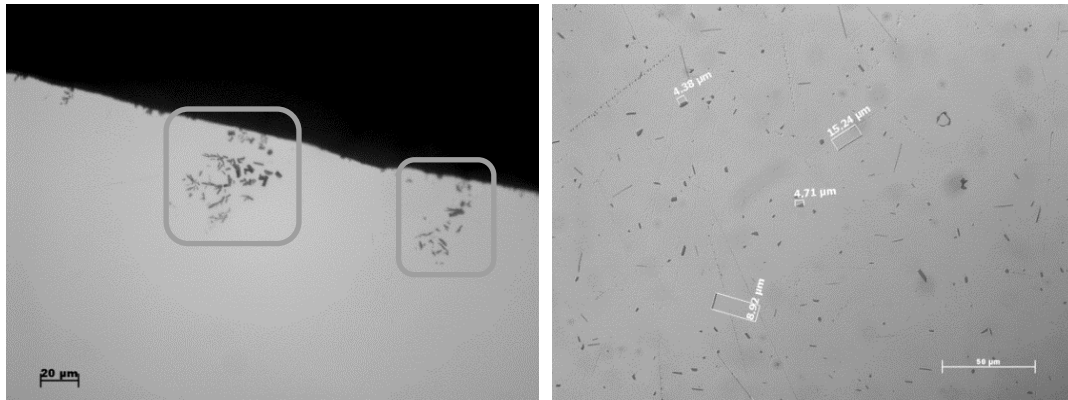


Figure 3.1.1. Light microscopic images of (L) Al-0.1%Si alloy cast at HZB and (R) Al-1%Si alloy made by Hydro Aluminium Bonn.

3.1.2.1 Solution Heat Treatment (SHT) and Quenching

The heat treatments of the samples included solutionizing at 540 °C (600 °C for Ge-containing alloys) for 1 h and quenching into different types of pre-cooled quenching media.

Fig. 3.1.2 shows the schematic illustration of the apparatus used for most samples:

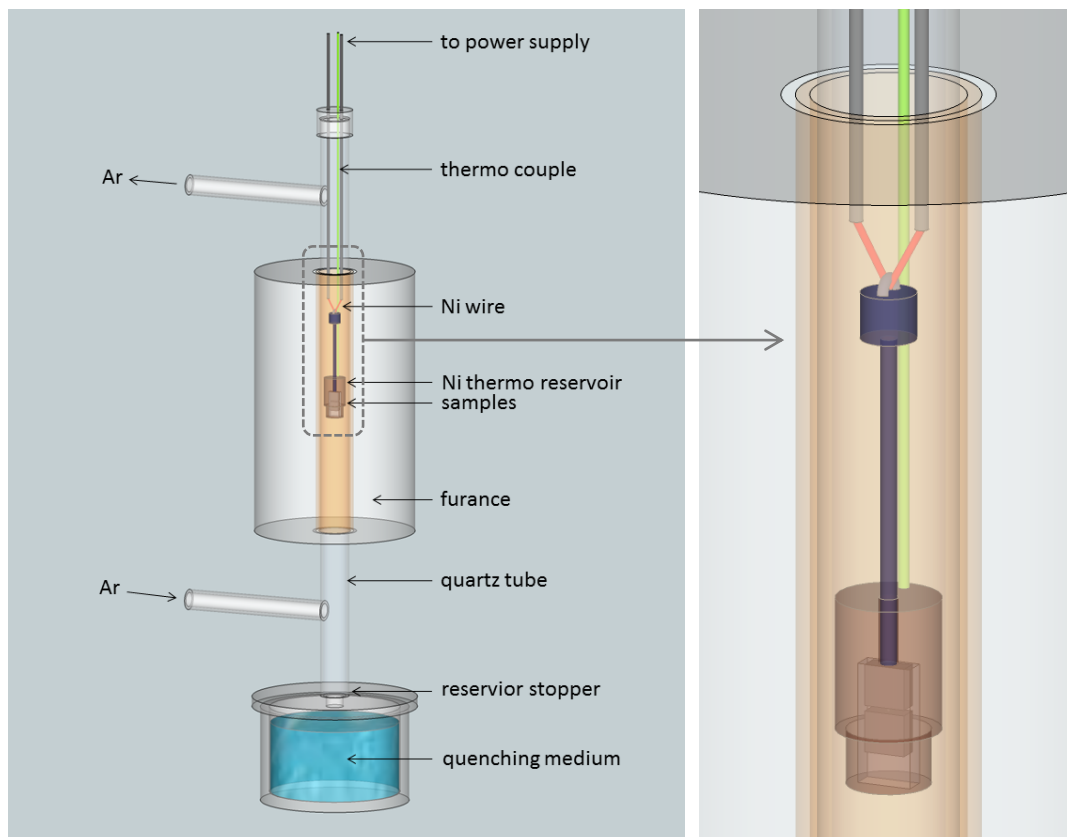


Figure 3.1.2. Schematic illustration of the (L) quenching furnace and (R) thermo reservoir.

In the furnace, the samples are held in a block of Ni metal acting as a thermo reservoir in an argon atmosphere. During quenching, the samples and the reservoir drop together. Before reaching the surface of the quenching medium, the reservoir is blocked by a stopper, while the samples are pulled out of the reservoir and fall into the quenching medium. Thus, premature cooling during dropping is prevented by the reservoir due to its large heat capacity and a high quenching rate is ensured [Len76].

Delayed quenching corresponds to an extended time at intermediate temperatures. This leads to a reduced level of super saturation of Mg and Si and probably to the formation of some stable or metastable phases during quenching [Ema03]. Hence, the achievable mechanical properties such as strength and hardness could be lower. Due to its importance, the effect of quenching rate on clustering behavior during RT ageing of alloys F and H was studied using PALS. In order to vary the quenching rate, various kinds of media were used, including water (0 and 20 °C), ethanol (0 °C) and CaCl₂ solution (-50 and -30 °C), see Fig. 3.1.3. Some commonly used cooling baths are listed in appendix A.5.

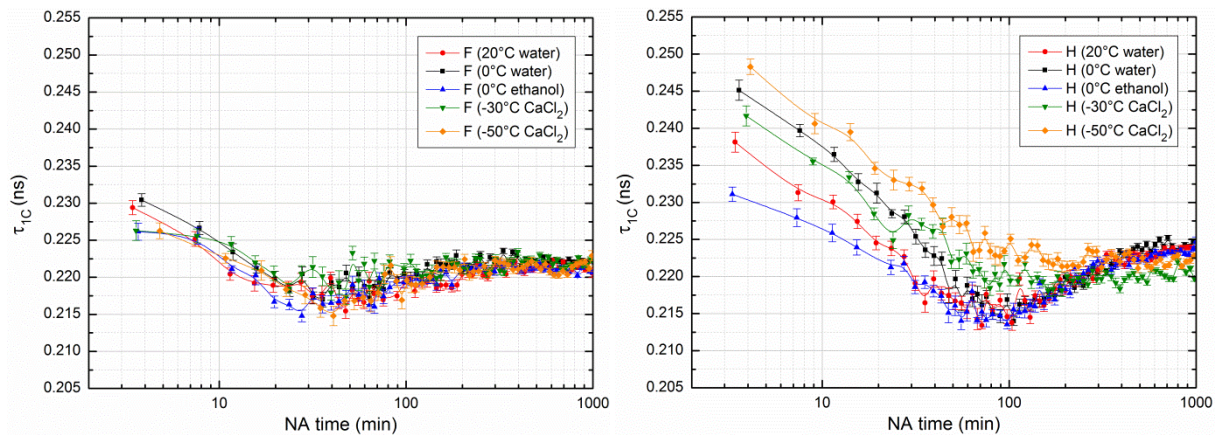


Figure 3.1.3. Quenching sensitivity of (L) alloy F and (R) alloy H.

- Alloy H: the initial PLT (τ_{1C} from 1-component fit of the positron lifetime spectra) in alloy H exhibits a strong dependence on quenching conditions. A very high value of 0.248 ns is found through effective quenching (-50 °C CaCl₂ solution). Clusters formed during slower quenching result in a shorter initial PLT. The reduction of τ_{1C} during the first 100 min of NA is caused by the increasing influence of positron traps with a shorter PLT (e.g. vacancy-free solute clusters). Due to its sensitive response to quenching rate, alloy H can thus be used as an indicator for quenching rate.

- Alloy F: no obvious quenching dependence of the course of PLT during NA is observed. Coherent clusters are already formed during and shortly after quenching since: (1) higher vacancy concentration than in alloy H, see Section 4.4.1.5; (2) much higher Si and Mg contents than in alloy H, in other words, much smaller distances between solutes, which are favorable for solute cluster formation. The interpretation of the PLT evolution can be found in [Ban11] and will be discussed in Chapter 4 in detail.

It is sometimes not appropriate to use liquid quenching (LqQ) media such as ice water for low temperature (LT) experiments, since the samples should be kept at temperatures lower than $-60\text{ }^{\circ}\text{C}$ after quenching to avoid any ageing effect before the experiment starts, namely, no warming up is allowed after quenching. This is, however, a problem because the water used for quenching will freeze and remains on the sample surface (difficult to remove). Results obtained could be misleading due to annihilation of positrons in these ice layers [Eld71, Sau11]. In order to solve this problem, we tested gaseous and solid quenching media, namely a spray of liquid nitrogen (LN_2), and a pre-cooled Cu block (CuQ) due to its high thermal conductivity [Pow66] and heat capacity, respectively, shown as follows:

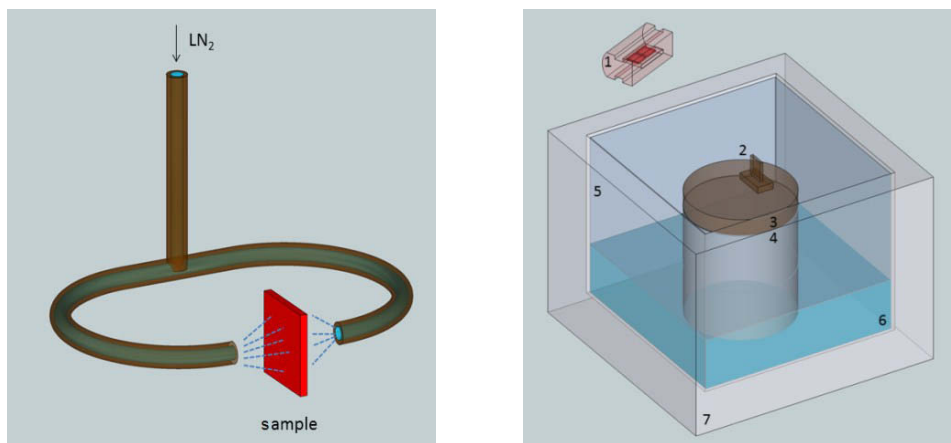


Figure 3.1.4. (L) Quenching with LN_2 ; (R) Quenching by a cold Cu block. 1-Ni reservoir and samples (red), 2-Cu stamp, 3-Cu block, 4-Al holder, 5-cold N_2 gas, 6- LN_2 , 7- styrofoam box.

To directly quench samples solutionized in a simple air furnace with LN_2 , a single specimen was placed into the LN_2 jets rapidly, as shown in Fig. 3.1.4 (L). For the test with a solid Cu block, samples are heat-treated in the air furnace inside a Ni thermo reservoir in order to avoid pre-cooling before quenching. The Cu block is cooled down to a temperature lower than $-100\text{ }^{\circ}\text{C}$ by LN_2 before quenching. The cooling time of the block to LN_2 temperature is markedly reduced to less than 1 min by not using a single large Cu block, but an Al block on

which the Cu block was put. The Cu block is sufficiently large to allow for safe quenching and high enough above the level of LN₂ to allow for handling. To quench the samples, the reservoir is taken out of the furnace using pliers and transferred to a position slightly higher than the Cu block. By tilting the reservoir, both samples slide on to the quenching block. The pre-cooled Cu stamp is then placed onto the two samples in order to cool from both sides. The LN₂ bath on the one hand cools the Cu block, on the other hand, it produces cold and dry N₂ in the box, thus preventing icing. No visible ice was observed on the sample surface for a time up to 15 min, which is long enough for packaging the samples and source into the required “sandwich” geometry.

If even longer handling time is required, the entire procedure is carried out inside a glove box, see Fig. 3.1.5:

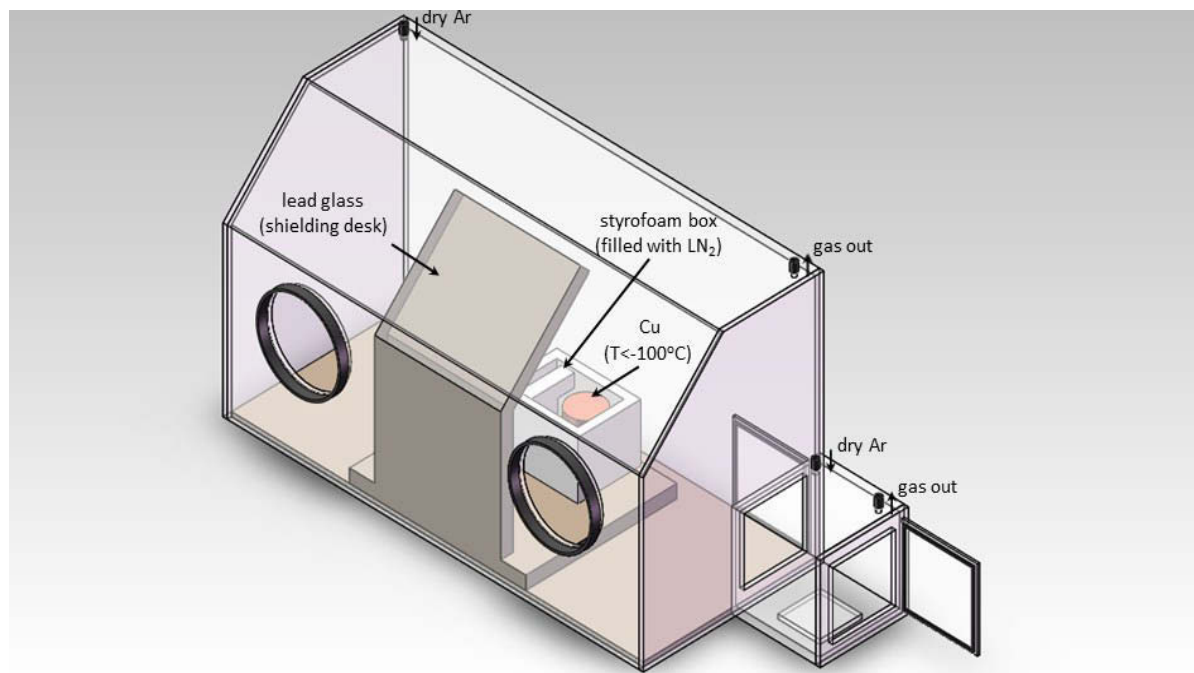


Figure 3.1.5. *Glove box used for sample preparation (gloves are not shown).*

The air humidity problem is solved by continuously charging the glove box with dry Ar gas as shown in Fig. 3.1.5. The lock space on the right is used for temporary storage of the quenching box (the same box as shown in Fig. 3.1.4 (R)), and avoids the humidity incoming through the door.

The efficiency of quenching in both approaches (gas and solid) follows from Fig. 3.1.6.

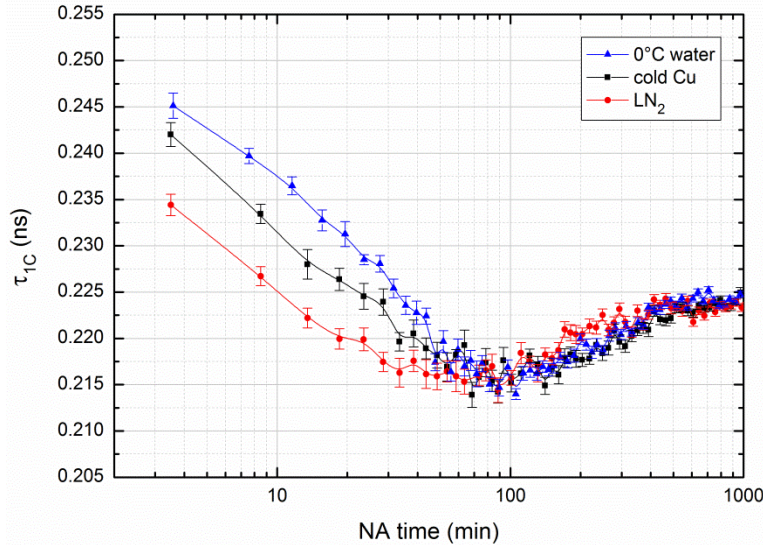


Figure 3.1.6. Quenching experiments on alloy H using LN₂ and cold Cu block.

It can be clearly seen that the quenching efficiency using Cu block is very close to the case of ice water. However, the advantage is that the samples remain at LT after quenching. In contrast, LN₂ is not a suitable quenching medium as shown by a low initial PLT of 0.235 ns. Such a low efficiency is probably caused by the vapor layer produced when LN₂ evaporated on the hot sample surface, the so-called Leidenfrost effect. This happens even if LN₂ is pressurized as in our trial.

Manual operation could also affect quenching efficiency, e.g. proficiency. After several quenching experiments with a Cu block, it was found that the corresponding quenching rate is even comparable to the case of -50 °C CaCl₂ solution, see Section 4.4.1.2.

If conventional quenching into a fluid was applied, the samples were immediately cleaned with alcohol, dried, and assembled to the required geometry. This handling usually takes 1 to 2 min. In the LT experiments, the samples were directly processed after quenching on the Cu block, and the delay is no more important since the sample temperature was always kept below -60 °C throughout processing and transfer. All measurements were either carried out at “RT” (20 ± 2 °C) or at specified temperatures, depending on the experiments.

Before we further proceed to the next topic, it is of great importance to investigate possible Mg losses during SHT as claimed by [Cha73, Hid77, Kov75]. If this were true, the ageing kinetics of Al-Mg-Si alloys would be affected by the reduced solute content and Mg/Si ratio, which would have a key influence on the cluster formation processes during NA [Cha12].

3.1.2.2 Mg Losses during Solution Heat Treatment

The PLT evolution of alloy I (Al-1.0%Mg-0.4%Si) was measured during NA. Heat treatment includes solutionizing at 540 °C (without Ar and pre-cooling prevention) for different SHT times (10 min to 15 h), followed by an ice water quenching (IWQ) and ~1.5 min delay caused by sample preparation.

The sample surface was ground before heat treatment. An oxide layer was observed for samples which had been solutionized longer than 1 h in air. After 5 or 15 h of SHT, due to different orientations, crystallites (0.5 to 1 mm in diameter) became visible on the sample surface, as shown in Fig. 3.1.7. These crystallites are slightly larger than the ones found in alloy F (~0.5 mm in diameter) after 30 min of SHT at 535 °C [Ban11].

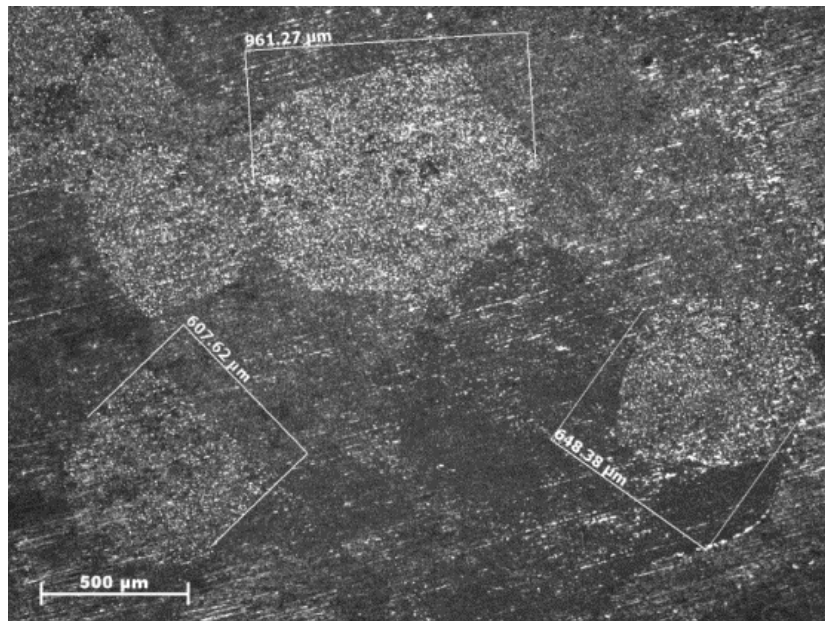


Figure 3.1.7. Light microscopic image of the grains observed on the sample (alloy I) surface after 5 h of solution heat treatment at 540 °C.

[Kov75] showed that after ~5 h of solution heat treatment, the change of resistivity during NA is just 50% of the change in the sample solutionized for 30 min. If this were true, a similar PLT evolution as in alloy H (Al-0.4%Mg-0.4%Si) should be observed in alloy I for prolonged solutionizing time due to the reduced Mg content. This is, however, obviously not the case. All PLT evolutions show very similar or identical tendencies, i.e. are independent of the thermal histories, as shown in Fig. 3.1.8.

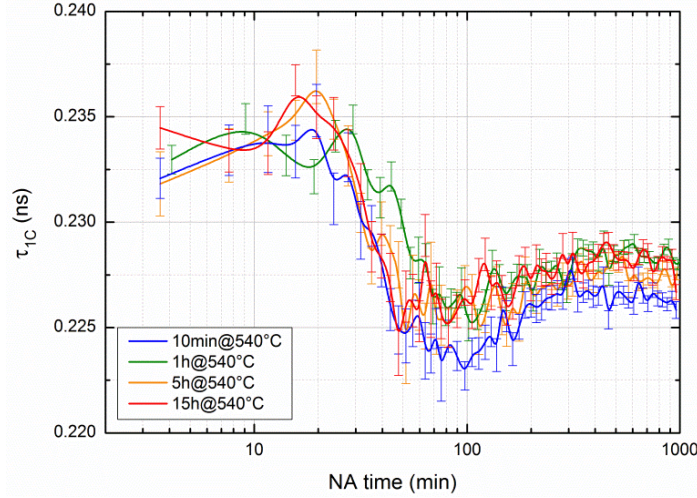


Figure 3.1.8. Evolution of PLT τ_{1C} during NA of alloy I solutionized for different times.

One can argue that during SHT, Mg atoms migrate to the surfaces and lead to a localization of Mg in the oxidized layer (the thickness of an oxidation layer ranges from nm to several μm depending on the material, heat treatment and atmosphere) of the Al-Mg-Si alloys and further “loss” of Mg will thus be hindered. However, the Mg atoms still remain in the sample or on the sample surface, and are not finally lost. This could be a reason why all PLT evolve in a similar way. In addition, the penetration depth of the positrons emitted from ^{22}Na can be calculated by the empirical equation proposed by [Bra77]:

$$\frac{1}{R_+} = \frac{2.8 \cdot \rho \cdot Z^{0.15}}{\bar{E}^{1.19}}, \quad (3.1.1)$$

where R_+ is the penetration depth, ρ the density of the material, Z the corresponding atomic number and \bar{E} the average kinetic energy of positrons (0.15 MeV for positrons emitted by ^{22}Na). The penetration depth of positrons (in Al) emitted from ^{22}Na equals $\sim 100 \mu\text{m}$ using Eq. (3.1.1). This depth is much higher than the thickness of the oxidation layer, thus, the annihilation behavior in the entire volume of a sample rather than on the surface is measured. Enrichment in Mg in the oxidation layer should not be a dominant factor affecting the PLT evolution. The similar or identical PLT evolution on variously solution heat treated Al-Mg-Si alloys suggests an independency of Mg distribution in the Al matrix on SHT time.

In short, Mg has a strong influence on the PLT evolution of Al-Mg-Si alloys during NA, see Chapter 4. However, such influence was not observed in Fig. 3.1.8. Thus, an effect of Mg losses could not be verified from the view point of positron annihilation.

3.2 Source Production

3.2.1 ^{22}Na Source

The ^{22}Na source was produced at University of Halle. It was delivered in the form of a Na_2CO_3 mother solution. Depending on the desired activity, a few droplets of the concentrated solution were extracted by a micropipette and were deposited on the center of a 7- μm thick Kapton foil (Du Pont). After drying the solution for several minutes by an infrared lamp, the foil was covered with another piece of foil of the same type. Both foils were glued together and sealed by using a ring cut from a 20- μm thick Kapton tape. The ^{22}Na source used for this study had an activity of 28 μCi in April 2011 and its diameter is about 8 mm. The schematic drawings of the source as well as the “sandwich” (samples + source) geometry are shown in Fig. 3.2.1:

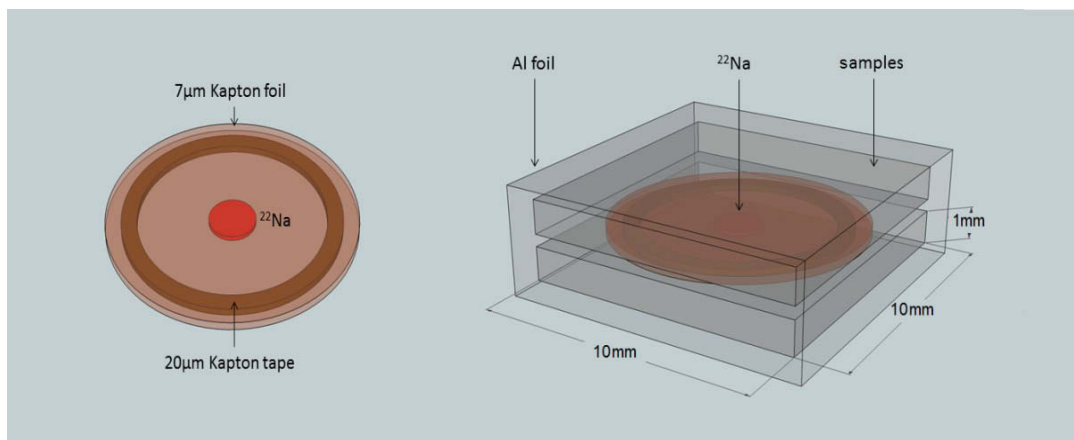


Figure 3.2.1. (L) ^{22}Na source; (R) “Sandwich” geometry used in PALS experiments.

Using supporting foils can protect the source from being damaged, but a part of the positrons will annihilate in these foils. Thus, a source correction has to be carried out. Positrons have a lifetime close to 0.380 ns in Kapton and it was reported that this PLT does not depend on temperature [Mac80, Mon94, Wei67]. This feature will be used for the PALS experiments performed at LTs. Various studies showed that the PLTs in the ^{22}Na salt itself and in Kapton foil are very similar. The former PLT ranges from 0.382 to 0.400 ns [Djo95, Has94, Kan96, Mac80, Mon94, Vri87] and can hardly be separated from that in Kapton. Thus, we treat both components as one. In addition, a very long PLT around 3 ns was identified, corresponding to the formation of positronium [Sta96]. The corresponding intensities are $\sim 10\%$ for (salt + Kapton) and less than 1% for positronium [Ban12, Has94].

3.2.2 ^{68}Ge and ^7Be Sources

The ^{68}Ge source was produced via a (d, 3n) nuclear reaction. Deuterons are accelerated to 27 MeV with the cyclotron at the Helmholtz-Institut für Strahlen- und Kernphysik (HISKP, University of Bonn) and directed on a commercially available semiconductor wafer GaP with a thickness of $\sim 100\ \mu\text{m}$ (metallic Ga could not be used as a target material due to its low melting point). The excitation function is shown in Fig. 3.2.2 [Kar69]:

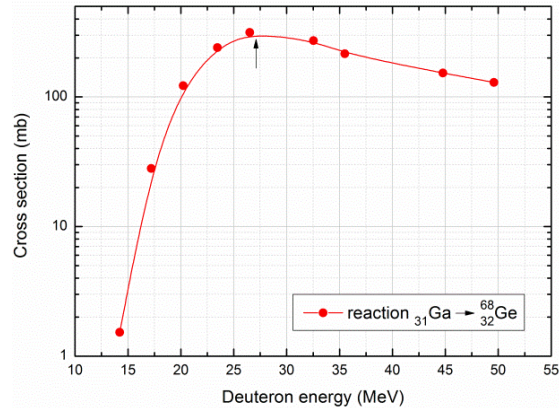


Figure 3.2.2. Excitation function for the production of ^{68}Ge in the deuteron irradiation of Ga.

After irradiation for 10 h with a current of $0.5\ \mu\text{A}$, a “clean” ^{68}Ge source with an activity of $\sim 13.5\ \mu\text{Ci}$ was produced. “Clean” means that ^{68}Ge is fully enclosed inside the wafer. Other undesired isotopes like ^{69}Ge were also produced through the (d, 2n) reaction but will decay in some weeks due to their short half-lives. If its activity is sufficiently high, a ^{68}Ge source is placed directly on the sample surface. Otherwise it is put into the slot of one sample and covered by another sample in order to increase the count rate, see Fig. 3.2.3:

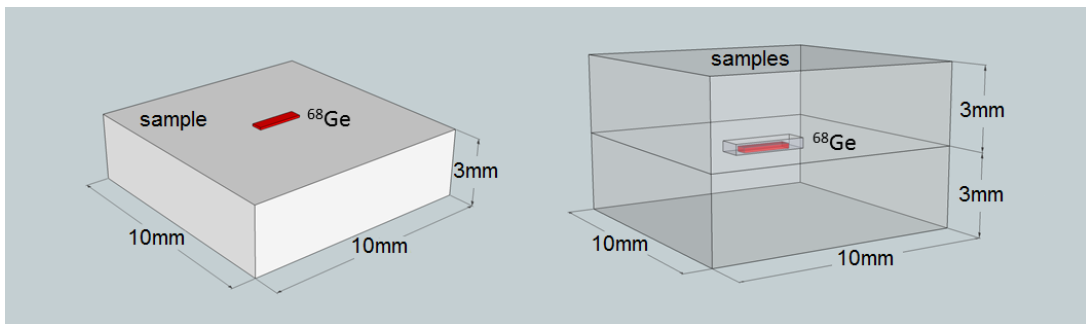


Figure 3.2.3. Samples and ^{68}Ge source for DBAR experiments.

In addition, ^7Be was also used in DBAR experiments, see Section 3.3.2.3. This isotope was also produced at HISKP, by directing 40 MeV He-3 onto a graphite wafer.

3.3 Instruments and Data Analysis

3.3.1 Positron Annihilation Lifetime Spectroscopy

The overview of the “fast – fast” PALS system is shown in Fig. 3.3.1. It consists of 3 main parts, the sample environment, the detection system and the NIM-standard (nuclear instrument module) electronics. A detailed description will be given in the following sections.

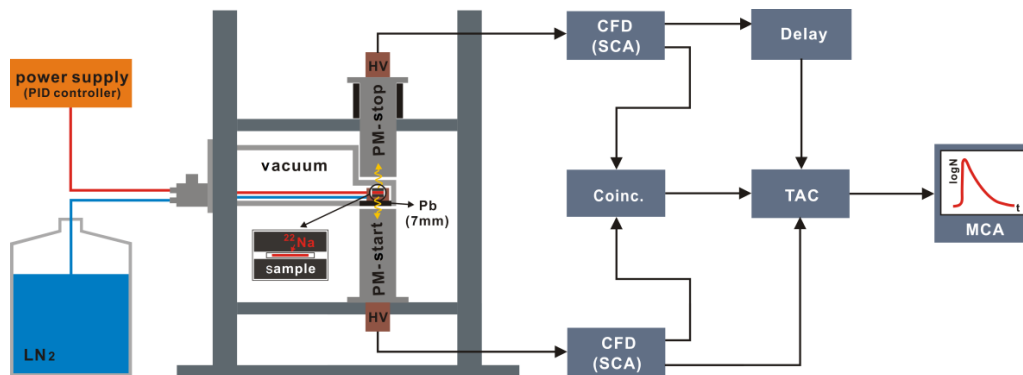


Figure 3.3.1. Schematic illustration of the PALS system.

3.3.1.1 Sample Environment

For certain experiments, the samples should be kept at LTs in vacuum. Thus, a sample environment as shown schematically in Fig. 3.3.2 is used (for details see appendix A.4):

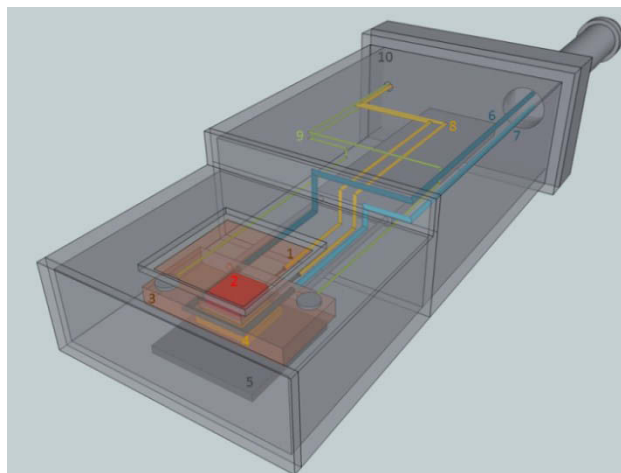


Figure 3.3.2. Sample environment. 1-Kapton window (brown), 2-sample (red), 3-sample holder (brown), 4-heating element (yellow), 5-Pb shielding (dark gray), 6&7-LN₂ channel (blue), 8-cable (yellow), 9-K type thermo elements (green), 10-Al housing (gray).

The sample environment initially designed by [Klo07] was further modified for this work. A sample (module 2 in Fig. 3.3.2) was placed into the Cu sample holder (module 3) having a

high thermal conductivity. By connecting the LN₂ channel (partly inside the sample holder) to a membrane pump, LN₂ can pass through the channel due to the suction and thus cool the holder. The flow rate was controlled externally by a dosis valve. The silicone pipe (light blue pipe in Fig. 3.3.3) which is connected to the membrane pump is sufficiently long, in order to ensure that the outgoing LN₂ is gasified before reaching the pump, thus preventing damage:

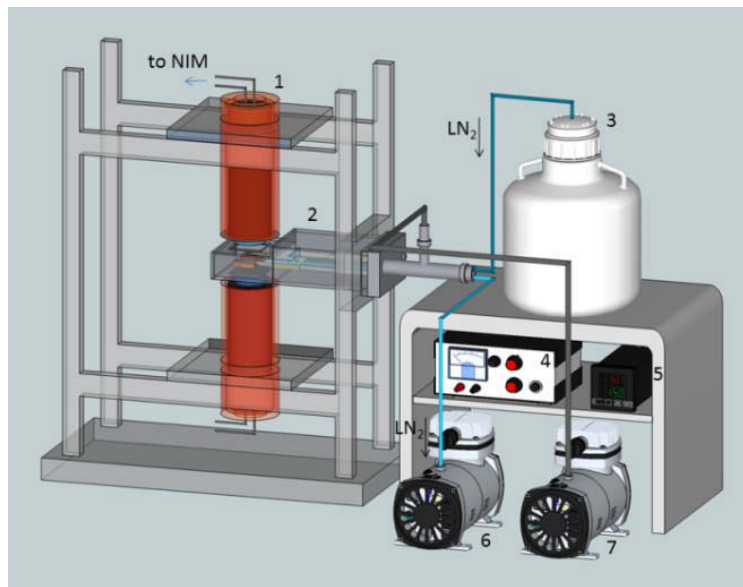


Figure 3.3.3. Sample handling system. 1-detector, 2-sample environment, 3-LN₂ container, 4-power supply, 5-PID controller, 6-pump for LN₂, 7-pump for vacuum.

For electrical heating, a wire (55% Cu, 44% Ni, 1% Mn, all in wt.%) was shaped to a meander and mounted below the Cu holder (a mica flake was used to isolate the wire from the holder, module 4 in Fig. 3.3.2). The current is controlled to obtain the required heating. During simultaneous cooling and heating, the temperature is measured through two individual thermo couples, while control of the desired temperature is realized by a PID (proportional integral differential) controller. The achievable temperature ranges from -100 to 200 °C, and a maximum cooling or heating rate of ~1 K/s can be applied [Klo07].

As shown in Fig. 3.3.2, a 75- μm thick Kapton window was used (module 1), which minimizes the absorption of the 0.511 MeV stop signal in Al housing, whereas a 7-mm thick Pb plate (in a groove cut into the Al housing, module 5) was placed in front of the start detector to avoid backscattering of the 1.275 MeV photons, see Section 3.3.1.6. The vacuum inside the chamber is $\sim 10^{-3}$ mbar. The distance between both detectors is ~ 20 mm. This sample environment is portable and can be used for both PALS and DBAR experiments.

3.3.1.2 Detection System

The detection system consists of BaF₂ scintillators (Ø 40 mm × 12 mm, will be discussed in Section 3.3.1.6) coupled to Hamamatsu H3378-50 photomultiplier tubes (PMT, operated at -2.7 kV), see Fig. 3.3.4:

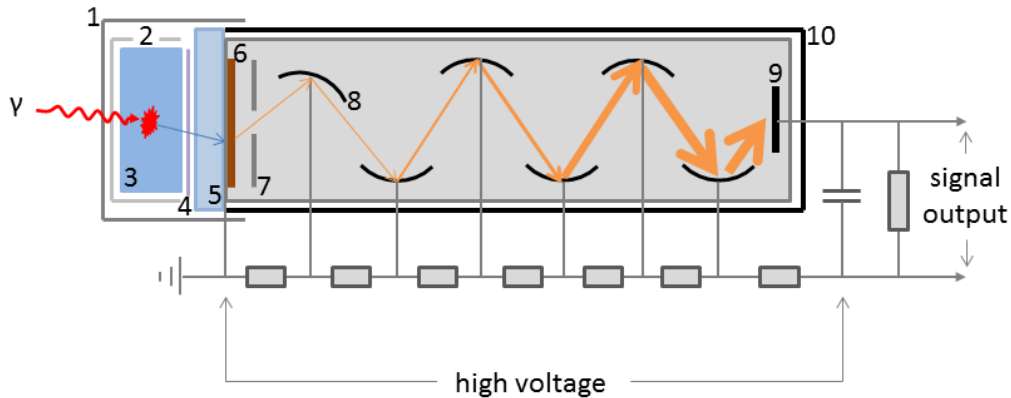


Figure 3.3.4. Schematic illustration of the detection system. 1-black tape and Al foil, 2-Teflon tape, 3-scintillator, 4-silicone grease, 5-quartz window, 6-photocathode, 7-gitter (focusing electrode), 8-first dynode, 9-anode, 10-Mu-metal shielding.

- Inorganic BaF₂ scintillator (good time resolution)

Incident γ rays are absorbed by the BaF₂ crystal. Electrons are excited from the valence band to the conduction band. The de-excitation, i.e. the transition of electrons from the excited state back to the ground state leads to the emission of photons. In order to improve the light collection efficiency, the scintillator was wrapped into Teflon tape and Al foil. In this way, the escaping light is partially back reflected into the crystal and eventually reaches the PMT. Furthermore, black tape was also used to minimize the effect of external sources of visible light [Leo94].

Silicone grease was used to couple the scintillator and the PMT. This agent has a refraction index close to the scintillator and the quartz window of the PMT, so that the light transmission from the scintillator to the PMT is high. Few droplets of this agent were homogeneously distributed taking care that no air is entrapped between the scintillator and the PMT window. Otherwise, the transmission of portions of the light in the scintillator would be affected [Leo94].

The light signals were collected, converted and amplified by the PMT into appropriate electrical pulses for the subsequent analysis (details are given in the following).

- Photomultiplier

An electron is emitted via the photoelectric effect whenever an incident photon strikes the photocathode. Under the applied electrical field, this electron is directed by the focusing electrode and accelerated towards the dynode. Upon striking the first dynode, some low energy secondary electrons are emitted. These electrons will be accelerated and directed again to the next dynode and consequently release more electrons, see yellow arrows in Fig. 3.3.4. Finally, a current signal can be detected at the anode output.

Besides Hamamatsu H3378-50 PMTs, older Philips XP2020Q PMTs were also used for the experiments shown in Section 4.5.1. The self-made high voltage (HV) divider of these tubes was modified according to [Vri87]. It was reported that a well-distributed electrical field between the cathode and the first dynodes can minimize the time difference for electrons coming from different parts of the cathode (“transition time spread” [Leo94]). Thus, the time resolution of the PMT could be improved. In practice, this was realized by tuning both potentiometers of “gitter” and “D2” (the set-up of the HV divider can be found in appendix A.3) until the maximum output pulse height was finally observed with the oscilloscope. In this way, charge collection was also maximized.

3.3.1.3 NIM-standard Electronics

- Constant fraction discriminator (CFD)

Output pulses from the PMT vary in amplitude or rise time (“time walk” effect [Leo94]), and these fluctuations could affect the time resolution of the system. Particularly for the signals with equal rise times but different amplitudes, the CF timing technique can be applied to generate walk-free timing signals at a constant fraction of the peak height. Thus, trigger time will be no more depend on the amplitude of the signal. The applied FAST ComTec 7029A CFD model provides in addition fast signal level discrimination (single-channel analyzer, SCA). The amplitude of the annihilation signal is proportional to the energy that is deposited in the detector by the photons. Pulses will be accepted only if their amplitudes fall into the selected energy window and just the desired nuclear events will be counted. Using either an oscilloscope or the ^{22}Na energy spectrum, both the start signals from the 1.275 MeV γ quanta and the stop signals from 0.511 MeV photons can be easily identified. The windows were set individually according to these signals for the start and stop channels.

- Time-to-amplitude converter (TAC) and coincidence unit

An Ortec 567 TAC is triggered by the start pulse and stopped by the stop signal from the CFDs. The time interval between both signals is converted to a pulse with an amplitude proportional to its duration. A delay line is added into the circuit in order to allow the TAC to work in the linear regime.

For the applied 28 μCi ^{22}Na source, about 10^6 positrons per second are emitted which corresponds to one positron every 1000 ns. This time is much longer than the time range of the TAC (~ 50 to 100 ns). In this case, the TAC also acts as a coincidence unit. In addition, a positron typically annihilates within 0.1 to 0.5 ns (annihilation rate $\sim 10^{10} \text{ s}^{-1}$). Therefore, most of the time, there is either no positron or just one positron in the sample, and false coincidences from two unrelated annihilation events can thus be excluded.

The output pulse can then be analyzed by the multi-channel analyzer (MCA).

- Multi-channel analyzer (MCA)

Counts registered from different amplitudes (energies, also called channels) are accumulated to build up the energy spectrum, this is done using a FAST ComTec MCA-3A module which scans the whole energy range and records the number of pulses counted in each channel.

3.3.1.4 Determination of the Channel Width

The time corresponding to each channel can be calculated applying the “delay line” method. A set of peaks of the prompt curve can be measured with different delay lines and a plot of delay time versus the corresponding channel number then provides the channel width. In this study, it was calculated to be 0.0253 ns/channel.

3.3.1.5 Data Acquisition and Evaluation

In order to obtain a reliable analysis of positron lifetime, a PALS decay spectrum should contain at least 2×10^6 annihilation events (even more events are essentially required if the spectrum is to be decomposed into various components) [Bec00, Gow92, Seg84]. This would take approximately 30 min at a count rate of 1000 s^{-1} . However, the observation of the early ageing kinetics of quenched Al-Mg, Al-Si and Al-Mg-Si alloys during NA requires a much faster data acquisition. This problem can be solved by the following methods.

(1) applying a very strong source in order to increase the count rate. However this is normally not applicable due to the intrinsic dead time of the detection system during processing the signals [Leo94]; (2) interrupting the NA process of an alloy and measure the PLT at a temperature lower than $-40\text{ }^{\circ}\text{C}$ to avoid any undesired microstructural changes [Klo10, Liu11, Røy06]; (3) alternatively, shorter accumulation times should be applied. [Ban11, Ban12] showed that the PLT in 6000 alloys after quenching and during NA can be approximately described by 1-component analysis, and a reliable estimation of this PLT can be obtained using the data collected in the fast data acquisition (FDA) mode. However, after quenching pure Al, dilute binary Al-Mg or Al-Si alloys, the decay spectra usually consist of two PLT components (bulk and vacancy cluster components [Dlu80, Kan85, Kra03]). Sufficient statistics are required in the normal data acquisition (NDA) mode to reduce the uncertainties caused by spectra decomposition. It is interesting to know whether the FDA mode is applicable to these alloy systems. As an example, a quenched Al-0.005%Si alloy was measured and data sets were sequentially acquired every 60 s during NA. Four data sets were then binned into one new data set to improve statistics ($\sim 3 \times 10^5$ counts). After initial pronounced changes, no notable PLT change was observed any more after 3000 min of NA. Therefore, data was collected in the NDA mode with adequate statistics ($\sim 2 \times 10^6$ counts). After evaluating the spectra with LT9 [Dry96, Kan96], the following figure was obtained (for detained information concerning data processing, see [Ban11]):

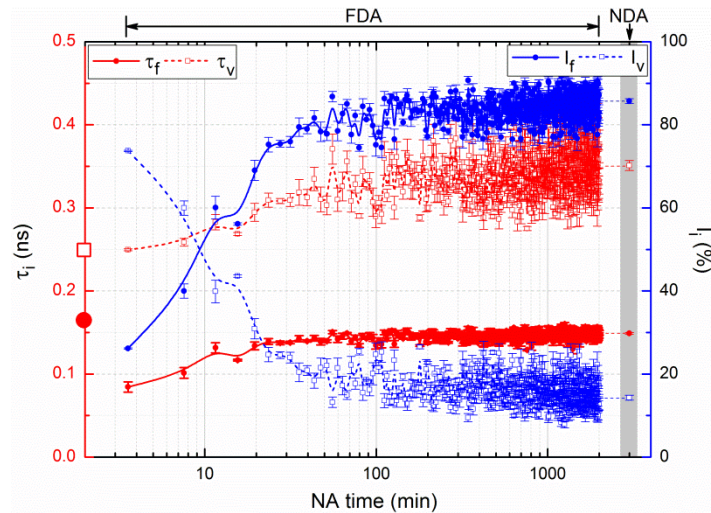


Figure 3.3.5. Evolution of decomposed PLT components of Al-0.005%Si alloy during NA. Data were collected in the FDA mode for the first 2000 min, after which the NDA mode was applied. The PLT in bulk Al (~ 0.165 ns) and in mono-vacancies in Al (~ 0.250 ns) are also given, indicated by the solid sphere and the open square symbols, respectively.

Two PLTs τ_f , τ_v (“f” for free and “v” for vacancy) and their corresponding intensities I_f , I_v can be clearly distinguished after decomposing the PLT spectra of Al-0.005%Si alloy in the FDA mode. All the fitted components change notably during the first 100 min of NA but then level off and fluctuate within an acceptable range. The PLTs and intensities obtained from the data collected after 3000 min of NA in the NDA mode lie within the scattered range of the data from FDA mode. [Dry96] investigated how the determination of PLT components could be affected by statistics, and it was found that apart from the larger scatter of the data points, results evaluated by LT9 and Positronfit did not differ much for the decay spectra which contain 1.4×10^6 and 6.5×10^5 events. Furthermore, the scatter of the decomposed PLTs and intensities can be compensated by using an averaging procedure used by [Ban11]. In order to check the validity of the 2-component fits, the PLT τ_f was also calculated according to the simple trapping model (STM) and it was found that the calculated and experimental values coincide with each other (this will be shown in Section 4.2.1.1). Therefore, we conclude that apart from the fluctuations of data caused by low statistics, a reliable estimation of the individual PLTs and the relevant intensities can be obtained by using a much faster data acquisition [Liu12]. This method was applied for most experiments of this study, see Chapter 4.

3.3.1.6 Detector Alignment

In conventional PALS detection systems, “face-to-face” arranged detectors are placed closely together with the “sandwich” in between to ensure a high count rate. However, it is known 1.275 MeV γ quanta backscattered from the scintillators cause considerable problems in such an alignment [Dan81, Van80]. The backscattering effect depends on many factors, among which the most important are the scintillator and detector geometry. Work was carried out aiming at the improvement of the performance of the PALS system by selecting the appropriate scintillators and testing different detector alignments.

- Selection of scintillators

The detection system consists of two quartz window PMTs (H3378-50 and XP2020Q) coupled with high-density BaF₂ scintillators with some main properties listed in Table 3.3.1. Other types of scintillators such as plastics which are also commonly used for PALS experiments are also given for comparison.

Table 3.3.1. Comparison between some primary properties of various scintillators.

scintillator	density (g/cm ³)	Z _{eff}	decay time (ns)	light yield (photons/keV)
BaF ₂	4.88 ^[Lav83, Sah13]	54 ^[Sah13]	0.6(fast) ^[Lav83, Sah13]	2(fast) ^[Lav83, Sah13]
plastics	1.03 – 1.20 ^[Den09]	4.5 ^[Jus12]	1.4 – 285 ^[Den09]	~10 ^[Zhu05]
LSO	7.49 ^[Haa07, Kon10, Sah13]	65.8 ^[Haa07, Kon10, Sah13]	~40 ^[Mel92, Sah13]	27 ^[Haa07, Sah13]

- BaF₂: BaF₂ scintillators were chosen for this study, benefiting from their fast scintillation component which ensures the precision of the fast timing applications. It is known that γ photons are absorbed due to the photoelectric effect, the Compton effect and pair production. The cross sections for the Compton effect are related to the atomic number Z of the material linearly, while for photoelectric and pair production, the Z dependency becomes much stronger, i.e. Z^5 [Gre00] and Z^2 [Leo94], respectively. Therefore, high Z materials are favored in γ photon detection due to high efficiency. For example, a 10 mm BaF₂ scintillator can detect about 35% of the incoming 0.511 MeV photons, while a plastic scintillator of the same thickness exhibits only 9% detection efficiency [Raj87]. In addition, the energy spectrum of ²²Na acquired by BaF₂ scintillators exhibits pronounced photoelectric peaks owing to its high atomic number. This can be used for the energy window selection. However, using BaF₂ gives rise to more backscattering events compared to plastics as a side effect of its high atomic number.
- Plastics: the timing behavior of plastics is slightly inferior to that of BaF₂ (decay time > 1.4 ns). More importantly, as a consequence of the low effective atomic number, applications of plastics in γ ray detection are limited. The spectrum of ²²Na using plastics is dominated by Compton scattering while photoelectric peaks can hardly be observed, thereby making the energy window determination based on photoelectric peaks difficult. On the other hand, there are fewer “pile-up” events in plastic scintillators [Raj87], as explained in the following.
- LSO (Lu₂SiO₅): apart from the widely used BaF₂ and plastic scintillators, LSO becomes a very promising candidate for timing applications. The relatively inferior timing behavior will be compensated by its high light yield up to 27 photons/keV, which is 13.5 times higher than that of the fast component of BaF₂ [Haa07, Val05]. This excellent property combined with the high stopping power for γ photons suggests to apply LSO in future PALS experiments, in which the data accumulation time could be markedly reduced, thus allowing to acquire spectra in much shorter time intervals.

- Problems caused by the “face-to-face” alignment of detectors based on BaF₂ scintillators. Aligning detectors and the sandwich (samples + source) in 180° geometry will distort the spectrum due to the following effects (due to the large solid angle by such an alignment):

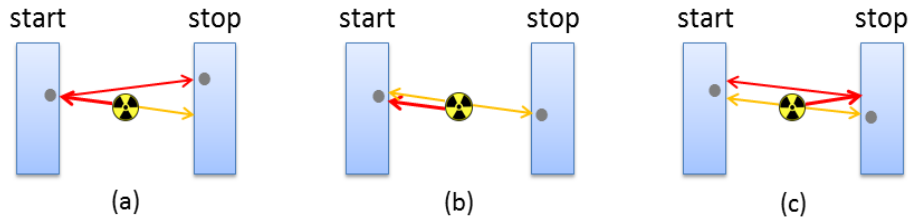


Figure 3.3.6. Problems of the 180° alignment. Blue rectangles are scintillators, red arrow represents 1.275 MeV γ photon, while yellow arrows denote the 0.511 MeV γ quanta, and gray dots refer to the accepted signals at the start and stop detectors.

- Backscattering effect: a high count rate can be achieved by widening the energy window. However, [Dan81] found that one often encounters problems arising from inelastically backscattered (large-angle Compton scattering) 1.275 MeV γ photons at the start detector, which sequentially trigger the stop detector if their energy lies within the window of this channel. Thus, a wrong coincidence event will be registered, see Fig. 3.3.6 (a). The PLT spectrum will be seriously distorted due to these “false” coincidences, which behave like a prompt curve in time distribution but shift towards later times due to the flight time of the backscattered quanta. As a result, not only the time resolution will be influenced [Van81] but also the fitted PLT will be shortened. Scattering effects can be inhibited by introducing precise energy selection, i.e. using a narrow window, which is however not common practice because of the very low counting efficiency of such a setting.
- Pile-up effect: the second deleterious effect is pile-up (summation). The rise times (time between 10% and 90% of the maximum anode signal) of the PMT output pulse are 0.7 ns for H3378-50 [Kra09] and 1.6 ns for XP2020Q [Pho07] PMTs, respectively, much longer than the time between the start and stop signal which is typically less than 0.3 ns [Gow92]. Thus, the pulse from the 0.511 MeV γ quanta could directly sum up with the one generated by the 1.275 MeV γ and, consequently be accepted by the start channel as a “start” signal, if the energy of this sum signal fit into the start energy window, as shown in Fig. 3.3.6 (b). These “start” – stop coincidences will lead to similar artefacts as backscattering [Raj87, Vri87]. In addition, the combination of backscattering and pile-up effects is also possible, see Fig. 3.3.6 (c).

- Solutions

The following methods can be used to suppress these artefacts: (1) move the sandwich out of the common axis so that only one annihilation γ will be detected [Bec00]; (2) rotate one of the detectors by a certain angle to avoid “face-to-face” geometry [Raj87, Van80]; (3) increase the distance between two detectors [Van80]; (4) shield the start detector with lead to attenuate the undesired events at the cost of count rate [Li11, Van80].

Obviously, applying one of the first three methods will lead to a pronounced decrease in count rate, which is not acceptable for the study of the fast ageing kinetics of the investigated alloys, for which fast data acquisition is mandatory. Therefore, the emphasis was put on the latter possibility, i.e. shielding. Lead was used to suppress the backscattering effect. According to Beer’s law: $I(d) = I_0 \cdot \exp(-\mu d)$, where the total absorption coefficients μ in lead is 1.78 cm^{-1} [Kon10] and 0.66 cm^{-1} [Cor44] for 0.511 and 1.275 MeV photons, respectively, see Fig. 3.3.7. This implies that 1 cm of lead absorbs 83.1% of all 0.511 MeV and 48.3% of all 1.275 MeV γ rays. 6 and 8 mm lead plates were used by [Gow92, Van81] which could also reduce the pile-up effect by a factor of 5 to 6. As a compromise, 7 mm lead plate was placed in front of the start detector for this study.

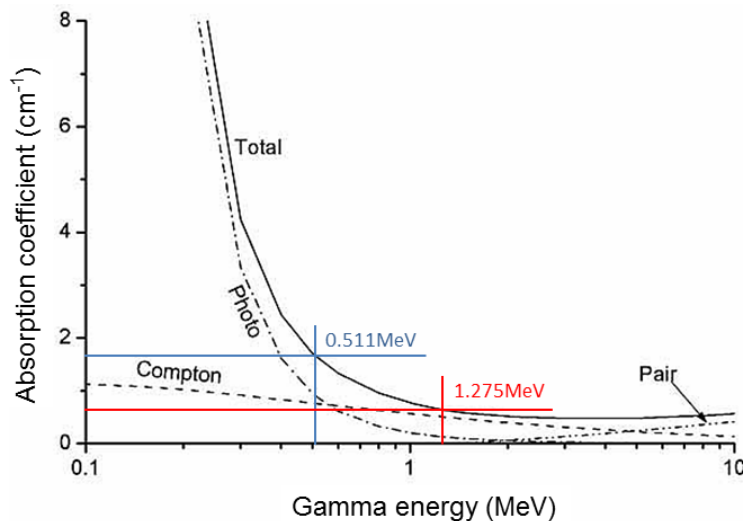


Figure 3.3.7. Gamma absorption coefficient of lead as a function of gamma energy [Wikxx].

However, in order to investigate the influence caused by these scattering phenomena, we placed the energy window slightly above the 0.511 MeV photoelectric peak for the start signal and around the peak for the stop signal. Different combinations of the methods listed above were tested using a Si reference sample, as shown in Fig. 3.3.8.

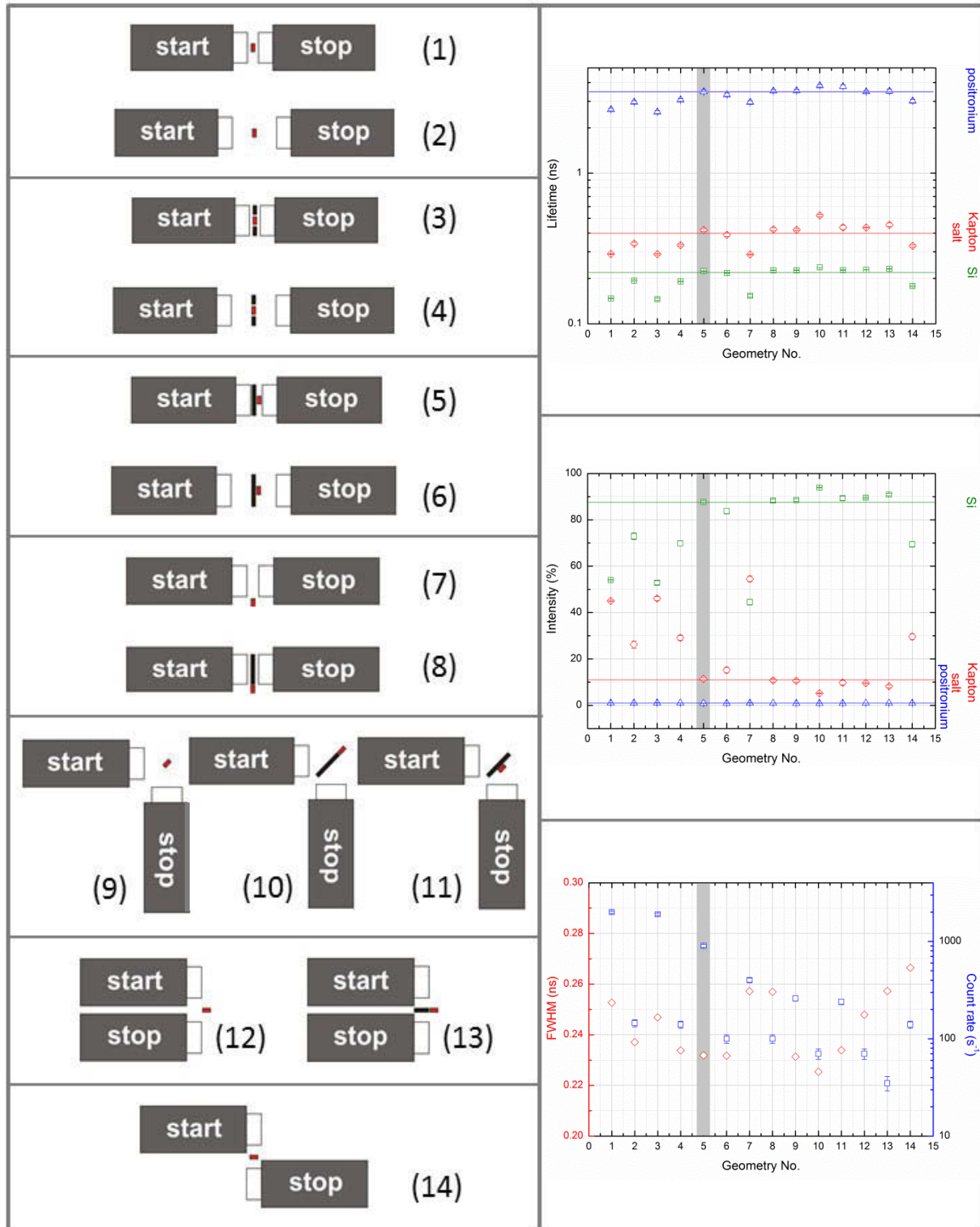


Figure 3.3.8. (L) Different detector alignments, red dots represent the sandwich and black lines indicate the lead shielding; (R) Measured PLTs and intensities of the sample and source itself. The time resolution (FWHM, full width at half maximum) and count rate in each alignment are also given. Gray bar in the right figures represents the geometry actually selected for all further measurements.

Four annihilation parameters were used as criteria, The reference material Si exhibits a PLT of 0.218 ns from experiments [Kor07, Kra03, Kri08] and 0.215 to 0.221 ns from theoretical calculations [Pus94, Sai96]. The PLTs and intensities of the sources have been given in Section 3.2.1, and are compared to the results in Fig. 3.3.8. The FWHM of the spectrometer is ~ 0.220 ns and the count rate should be as high as possible. As shown in Fig. 3.3.8, a clear geometry dependence of these parameters could be seen:

- 1–4: much shorter PLTs in Si were obtained. Backscattering could be partly suppressed by increasing the distance between two detectors from 1 to 5 cm (solid angle decreases), while placing the sandwich in the hole of the lead shield as in geometry 3 and 4 could not notably improve the situation, since large-angle Compton scattering along the detector axis still exists.
- 5–6: placing the lead plate between the sandwich and the start detector (geometry 5) shows the best results, i.e. expected PLTs and intensities, optimum FWHM, and more importantly, a high count rate (~ 900 s⁻¹). This geometry was chosen for all PALS experiments. Combining a larger distance and shielding as in geometry 6 is not reasonable due to the low count rate.
- 7–8: just moving the sandwich out of the detector axis is inadequate, but inserting an additional lead plate between both detectors yields similar results (except for the degraded FWHM and the very low count rate) as geometry 5. These geometries have been applied by some authors [Gow92, Li11, Vri87]. [Van80] mentioned that positioning the sandwich as for geometry 7 and 8 causes the broadening of the FWHM, which agrees with the present results. 1.4 cm was found to be the optimum separation distance by [Bec00].
- 9–11: triangular geometries with or without a lead plate can solve the problems caused by backscattering and pile-up. Compared to geometry 1, the FWHM is improved by rotating one detector by 90°, which agrees with [Vri87] who found that the detector arrangement hardly affects the PLT in tungsten but the FWHM of the spectrometer.
- 12–13: apart from the lowest count rate and poor FWHM, PLTs and corresponding intensities obtained from these geometries are acceptable.
- 14: besides the wrong PLTs, intensities, the worst FWHM was obtained in this configuration. This can be ascribed to the changes in the diameter to height ratio of the

scintillators when light propagates through them [Van80]. [Ryt82] demonstrated that for scintillators of different shape but equal volume, thin scintillators with a large diameter give the best FWHM (large diameter to height ratio), due to the high light collection efficiency. [Wei04] obtained a FWHM of 0.108 ns for ^{60}Co using an $\text{Ø } 30 \text{ mm} \times 10 \text{ mm}$ BaF_2 scintillator. A larger and thicker scintillator (e.g. $\text{Ø } 40 \text{ mm} \times 30 \text{ mm}$) leads to a degradation of the FWHM to 0.145 ns but an increase in the count rate.

3.3.2 Doppler Broadening Annihilation Radiation

The schematic drawing of the DBAR system is shown in Fig. 3.3.9:

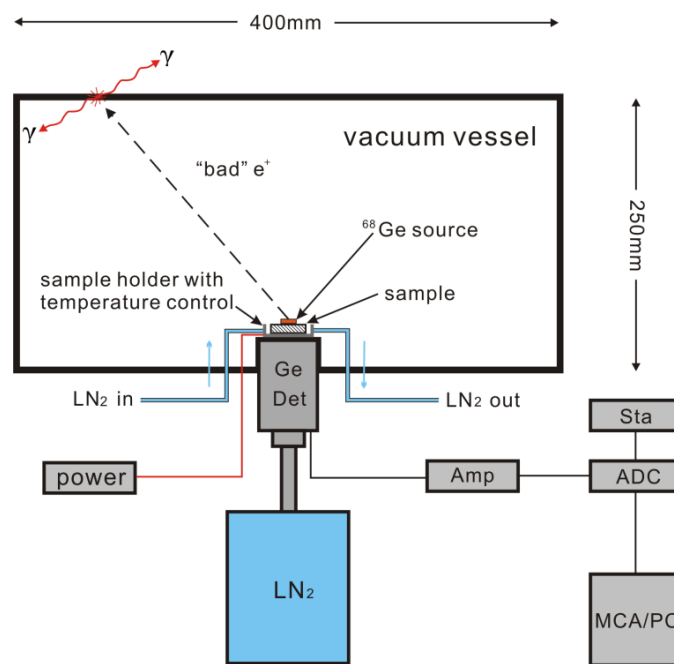


Figure 3.3.9. Schematic drawing of the DBAR setup.

The ^{68}Ge source and sample were directly placed above the Ge-detector for RT measurements. Alternatively, the sample environment introduced in Section 3.3.1.1 was used for LT experiments. The vacuum vessel is 400 mm in diameter and 250 mm high. Using such a design, signals produced by “bad” positrons annihilating in the vessel walls are avoided since they annihilate at a sufficiently large distance from the detector. The “good” signals were collected and pre-amplified by the detector. These signals were further processed by the main amplifier (Amp) followed by analog-to-digital conversion (ADC). Using a stabilizer (Sta) and a ^{7}Be source placed beside the ^{68}Ge source, the energy spectrum could be stabilized. Finally, the digitized signals were stored in the MCA [Haa06].

3.3.2.1 Sample Environment

Except for the Al housing, the entire sample environment used for PALS was mounted to the Doppler recipient from the side for LT DBAR experiments, as shown in Fig. 3.3.10. The sample could be cooled down and heated up in the same manner as for PALS measurements. The recipient could be evacuated and ventilated taking care that the loosely situated ^{68}Ge source was not blown away from streaming air.



Figure 3.3.10. Sample environment and detection system of the DBAR setup. 1-vessel, 2-vacuum gauge, 3-sample environment, 4-Ge detector, 5-LN₂ container, 6-styrofoam plate, 7-LN₂ container, 8-power supply, 9-PID controller, 10-pump for LN₂, 11-pump for vacuum, 12-crane.

3.3.2.2 High-purity Ge Detector (good energy resolution)

As a detector for 0.511 MeV γ photons, a CANBERRA high-purity (HP) Ge detector (operated at 4 kV) was used. The energy of the incident γ radiation is absorbed by the scintillator, which leads to the production of electrons and holes in the p-n junction region. Under the applied electrical field these electrons and holes drift to the electrodes and produce signals in the outer circuit. With increasing temperature, the thermally excited valence electrons are able to cross the band gap to the conduction band and produce electrical noise. Therefore, such a detector has to be kept at LN₂ temperature, see Fig. 3.3.10.

3.3.2.3 Stabilizer

A SILENA 8915 spectrum stabilizer was used to detect, measure, and correct any drift from preceding system components such as the detector, pre-amplifier, main amplifier and HV unit in order to maintain the stability of the γ spectrometer. For this purpose, 2 digital windows are symmetrically selected at the lower and higher energy sides of the 0.478 MeV ^7Be peak (± 5 and ± 10 channels, as shown in Fig. 3.3.11 by white dots). The change of counts in the (-10 to -5) and (+5 to +10) channels of the ^7Be peak due to electrical drift would lead to a voltage signal, which will be used as a feedback to stabilize the system.

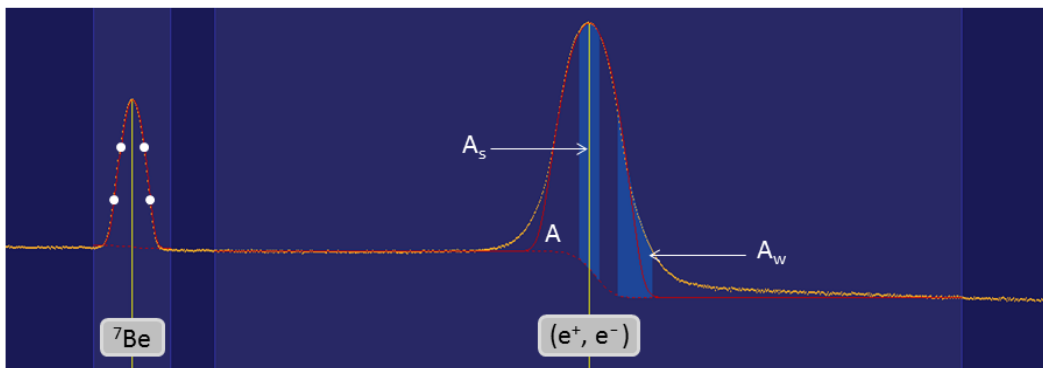


Figure 3.3.11. 0.478 MeV peak from ^7Be decay and 0.511 MeV peak from e^+ annihilation.

3.3.2.4 Energy Resolution

Applying the method mentioned above, the spectrometer resolution and peak position was stabilized against short-term drifts of the electronics. The energy resolution of the device is given by the FWHM of the ^7Be peak, which is ~ 1.275 keV throughout the measurements:

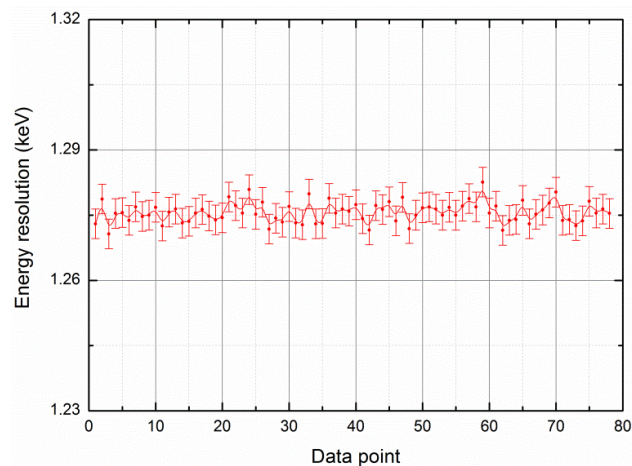


Figure 3.3.12. Energy resolution of the DBAR spectrometer during a measurement of the ^7Be line, each data point represents accumulation for 15 min.

3.3.2.5 Data Analysis

- Peak shift correction

Instability of the electronics during long-term experiments due to e.g. temperature variations in the laboratory could lead to a deteriorated energy resolution and random peak shifts. Such influences were corrected by using the program M_Spec (developed by M. Haaks) for each of the separately recorded spectra (data were saved every 15 min), which were added up to one spectrum for further analysis.

- Line shape parameters analysis

For a quantitative evaluation of the Doppler spectra, line shape parameters S and W are defined. The S parameter is calculated by dividing the central low-momentum area A_s by the total area A below the curve. The W parameter is defined as the ratio between the high-momentum area A_w to A as indicated in Fig. 3.3.11 [Kra99].

For the evaluation of S and W parameters, the energy interval was set to 511 to 511.75 keV (0 to $2.77 \times 10^{-3} m_0c$, S/2) around the annihilation line so that S roughly equals 0.5 as suggested by [Kra03]. The range of 513.1 to 515.6 keV (8.32 to $18.04 \times 10^{-3} m_0c$) was chosen for the W parameter. Such settings were used for all investigated spectra, see Fig. 3.3.11.

- High-momentum Analysis (HMA)

The high-momentum analysis can be used for the determination of the chemical surroundings of the annihilation site. The term “HMA” itself entails a sophisticated way of background reduction which considers, e.g. Compton scattering, incomplete charge collection and pile-up effects, and requires a nearly background-free positron source such as ^{68}Ge .

To subtract these backgrounds, two energy windows around the 0.511 MeV line are selected empirically, in which the asymmetry of the annihilation peak is minimized. This process is illustrated in Fig. 3.3.13. By mirroring the low energy side of the spectrum to the high energy side, the sum of both can be plotted. Taking the ratio of a Doppler broadening curve to a reference Doppler curve (e.g. pure Al annealed at 500 °C for 3 h), one obtains so-called fingerprint curves or ratio plots. Ultimately, by using HMA, the high-momentum region can be probed up to $30 \times 10^{-3} m_0c$ in a reliable way.

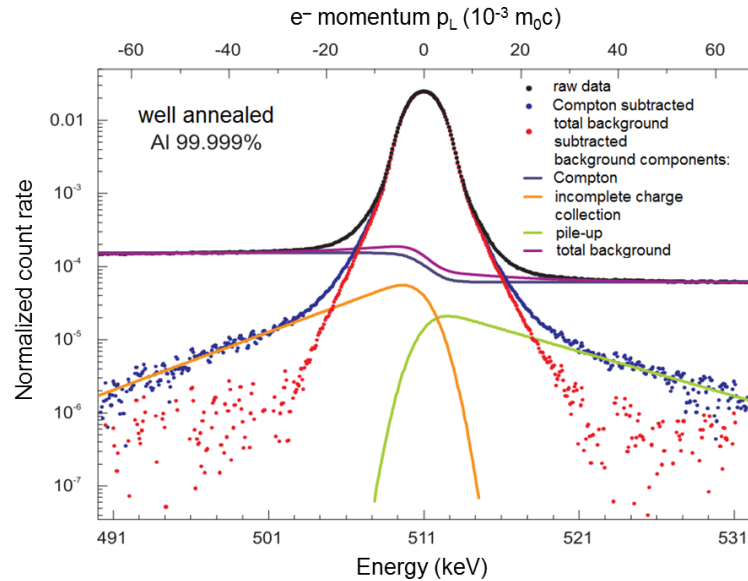


Figure 3.3.13. Subtraction of the annihilation spectrum consisting 3 background components, arise from Compton scattering (dark blue), incomplete charge (yellow) and pile-up effects (green) [Haa06, Haa09].

3.3.3 Differential Scanning Calorimetry

Some alloys were characterised by thermoanalysis using a Netzsch 204 F1 differential scanning calorimeter. After IWQ, DSC samples (~64 mg) were rapidly placed into the DSC chamber (pre-cooled to 0 °C), after which they were constantly heated from 0 to 600 °C at a rate of 10 K/min. The delay between quenching and measurement equals to ~1.5 min of NA. Data for pure Al (5N) was subtracted from the measured curve of the sample material to show the real heat effects due to phase transitions.

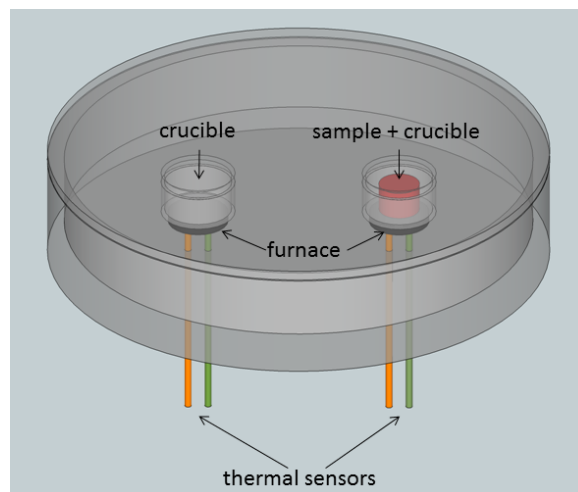


Figure 3.3.14. Schematic drawing of the DSC sample chamber.

3.4 Temperature Profiles (TP)

Fig. 3.4.1 schematically illustrates the thermal history of all investigated samples:

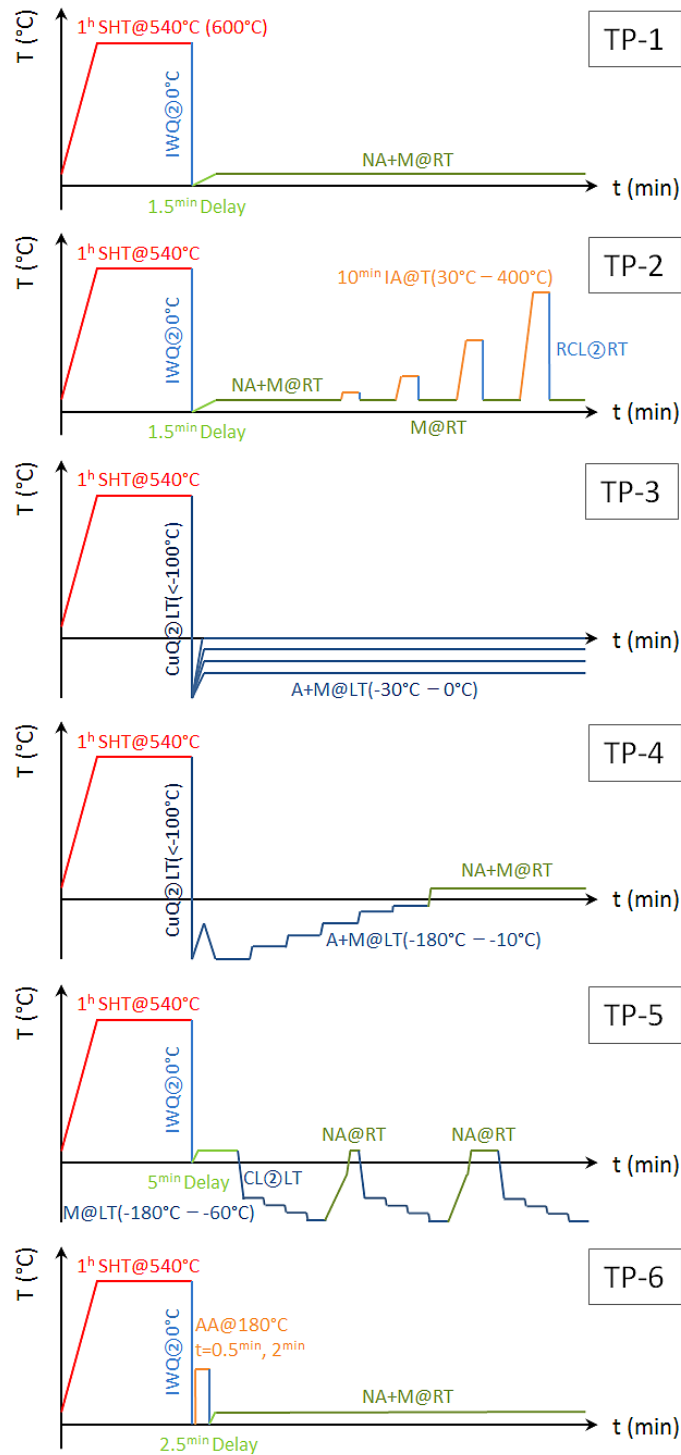


Figure 3.4.1. Temperature profiles. SHT-solution heat treatment, IWQ-ice water quenching, CuQ-(cold) Cu block quenching, NA-natural ageing, AA-artificial ageing, IA-isochronal annealing, M-measured, A-aged, RT-room temperature, LT-low temperature, RCL-rapid cooling, @-at, ②-to.

3.5 Overview of the PAS Experiments

The samples, methods, heat treatments, modes of data acquisition and data analysis applied for the PAS measurements, as shown in Chapter 4, are listed in Table 3.5.1:

Table 3.5.1. Overview of the PAS experiments. Figure numbers in the same color refer to the same or to the relevant experiments (figure number in black indicates an individual experiment). The notations 1C, 1.5C, 2C and 3C denote 1-component, 2-component (fixed τ_v), 2-component and 3-component analysis, respectively.

figure No.	measured samples	applied method	temperature profile	data acquisition	data analysis
4.1.1	pure Al	PALS	TP-1	FDA	2C
4.1.3	pure Al	PALS	TP-1	FDA	2C
4.1.4	pure Al	DBAR	–	NDA	HMA
4.2.1	Al-0.005%Si	PALS	TP-1	FDA	1C, 2C
4.2.2	Al-0.005%Mg, Al-0.05%Mg, Al-0.5%Mg	PALS	TP-1, TP-2	FDA, NDA	2C
4.2.3	Al-0.005%Si, Al-0.05%Si, Al-0.5%Si	PALS	TP-1, TP-2	FDA, NDA	2C
4.2.4	Al-0.005%Mg, Al-0.05%Mg, Al-0.5%Mg	PALS	TP-1	FDA	2C
	Al-0.005%Si, Al-0.05%Si, Al-0.5%Si	PALS	TP-1	FDA	2C
4.2.5	Al-0.005%Mg, Al-0.05%Mg, Al-0.5%Mg	PALS	TP-1, TP-2	FDA, NDA	2C
	Al-0.005%Si, Al-0.05%Si, Al-0.5%Si	PALS	TP-1, TP-2	FDA, NDA	2C
4.2.8	Al, Al-0.005%Mg (Si), Al-1%Mg (Si)	PALS	TP-1	FDA	2C
4.2.10	Mg, Si, Ge, Cu	DBAR	–	NDA	HMA
4.2.11	Al-1%Mg, Al-1%Si	DBAR	TP-1	NDA	HMA
4.3.1	Al-0.5%Mg (Si), 41, 23	PALS	TP-1	FDA	1C, 1.5C, 2C
4.3.2	Al-0.5%Mg (Si), 41, 23	PALS	TP-1	FDA	1C, 1.5C, 2C
4.3.3	Al-0.5%Mg (Si), 21, 22, 23, 31, 32, 33, 41, 42, 43	PALS	TP-1	FDA	2C
4.3.4	21, 22, 23, 31, 32, 33, 41, 42, 43	PALS	TP-1	FDA	1C
4.3.5	41, 42, 43	PALS	TP-1	FDA	1C
4.4.1	E, F, G, H, I	PALS	TP-1	FDA	1C
4.4.2	F, H	PALS	TP-3	FDA	1C
4.4.3	F, H	PALS	TP-3	FDA	1C
4.4.4	F, H	PALS	TP-3	FDA	1C
4.4.5	H	PALS	TP-5	FDA, NDA	1C
4.4.6	F, H	PALS	TP-4	FDA, NDA	1C
4.4.7	H	PALS	TP-5	FDA, NDA	1C
4.4.8	H	PALS	TP-5	NDA	1.5C
4.4.9	H	PALS	TP-3, TP-5	FDA, NDA	1.5C
4.4.10	H	PALS	TP-4, TP-5	NDA	1.5C, 3C
4.4.12	F, H	PALS	TP-3	FDA	1.5C
4.4.13	F, H	PALS	TP-3	FDA	1.5C
4.4.14	F, H	PALS	TP-3	FDA	1.5C
4.4.15	F, H	PALS	TP-1, TP-6	FDA	1C
4.4.22	binary alloys	PALS	TP-1	NDA	2C
4.4.25	F, H	DBAR	TP-1, TP-5	NDA	HMA
4.4.26	F, H	DBAR	TP-1, TP-5	NDA	HMA
4.4.27	F, H	DBAR	TP-1, TP-5	NDA	HMA
4.4.28	F, H	DBAR	TP-1, TP-5	NDA	HMA
4.4.29	H	CDBS	TP-5	NDA	–
4.4.30	F, H	PALS, DBAR	TP-5	NDA	1.5C, 3C, HMA
4.5.1	A2, A2Cu, A3, A3Cu, A11, A11Cu	PALS	TP-1	FDA	1C
4.5.4	G3, GS3, G11, GS11, G11Cu, GS11Cu	PALS	TP-1	FDA	1C
4.5.5	G3, GS3, G11, GS11	PALS	TP-1	FDA	1C

Chapter 4

Results and Discussion

4.1 Pure Al

The concentration of thermal vacancies increases with temperature. After quenching, a considerable fraction of thermal vacancies will be “frozen” inside the sample material. These vacancies are the simplest lattice defects and markedly affect the atomic diffusion and precipitation processes of age-hardenable Al based alloys. It is known that in pure Al, quenched-in vacancies diffuse quickly to sinks and disappear at RT [Pan58]. Therefore information related to the quenched-in vacancies is hard to access. Nevertheless, a “vacancy reference” in pure Al is desired for the interpretation of PALS and DBAR observations of binary Al-Mg, Al-Si and ternary Al-Mg-Si alloys. The results of the quenched Al (5N) measured by positron annihilation techniques will be presented in the following.

4.1.1 Positron Annihilation Lifetime Spectroscopy

4.1.1.1 Results and Discussion Based on Experiments

In pure Al, the vacancy concentration can be calculated by the following equation [Got98]:

$$c_v = \exp\left(\frac{S_f}{k_B}\right) \exp\left(-\frac{E_f}{k_B T}\right), \quad (4.1.1)$$

where $S_f = 0.7k_B$ is the vacancy formation entropy, $E_f = 0.67$ eV the formation energy of a vacancy in Al [Car03, Erh91], k_B is the Boltzmann constant and T equals 813 K (540 °C) in our case. A vacancy concentration of 1.39×10^{-4} /atom can thus be estimated theoretically. But due to vacancy loss during and after quenching, its effective concentration will be lower than the above mentioned theoretical value and the saturation positron trapping limit [Haa09, See73, Sta99]. Therefore, the 2-state trapping model was applied for the decomposition of the spectra collected in the FDA mode, see Fig. 4.1.1.

Two distinct PLT components can be evidently separated without fixing any fitting parameter. The vacancy-related component with a high PLT τ_v increases with time. It starts from 0.245 ns and approaches 0.300 ns within ~ 100 min at RT, meanwhile the corresponding intensity I_v drops markedly from 77% to 15%. Bulk annihilation has a much shorter PLT τ_f ranging from 0.085 to 0.140 ns and contributing only weakly at the beginning. As time proceeds, more and more positrons will annihilate in the bulk material and an intensity $I_f = 85\%$ was achieved after 1000 min, see Fig. 4.1.1:

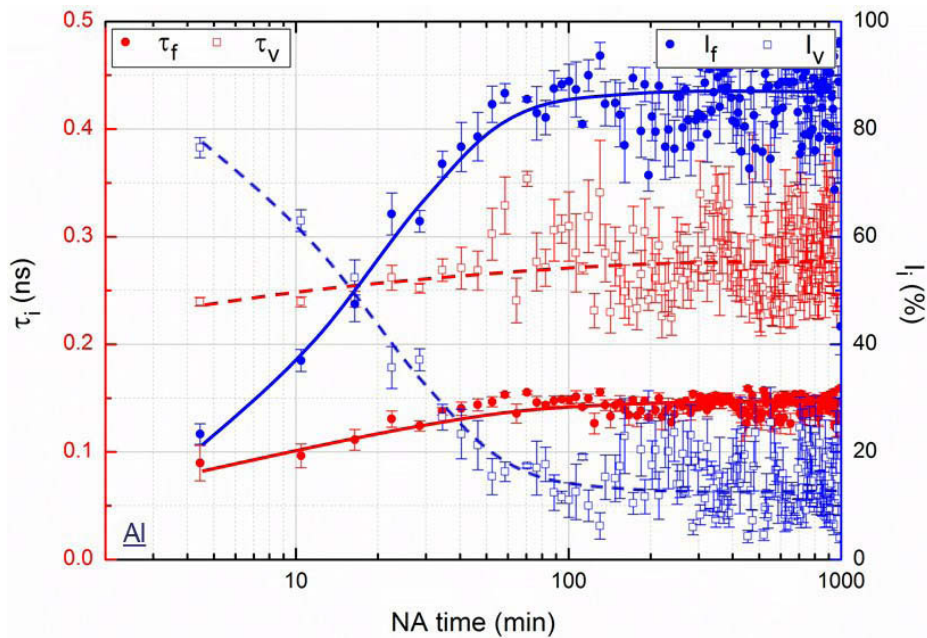


Figure 4.1.1. Evolution of decomposed PLT components of quenched Al during NA. The red solid or dashed lines correspond to lifetime of the free or localized positrons and blue ones represent the corresponding intensities. Data was collected in FDA mode.

The initial value of τ_v is the characteristic PLT in a mono-vacancy in an Al matrix which, according to various sources, ranges from 0.236 to 0.253 ns [Lun13, Pet98, Pus83, Sch86, Sch87]. For open volume larger in size, the corresponding PLT increases due to locally reduced electron density. The increase of τ_v strongly implies the growth of the related open volume, i.e. the migration of mono-vacancies and the agglomeration to small vacancy clusters. The orbital-free DFT calculations reported by [Gav07] agree with [Erh91] as well as with this work and confirmed from an electronic structure perspective that vacancy clustering is energetically favorable and vacancy clusters prefer to further condense rather than to split into mono or di-vacancies. Furthermore, it was claimed based on experimental observations employing electron transmission micrographs that vacancy clusters contain ~ 7 vacancies can

collapse to form stable vacancy loops [Hir58]. However, another DFT calculation found a negative binding energy for the nearest neighbor (NN) di-vacancy, which is unstable and therefore splits into two mono-vacancies [Car03]. This disagreement is possibly caused by the very limited number of atoms involved in the simulation, as pointed out by [Gav07].

During vacancy clustering, the number density of vacancy-related defects decreases due to the combined effects of mono-vacancy “consumption” for vacancy cluster formation and losses at sinks. Thus, these defects gradually trap fewer positrons, whereas bulk annihilation will become more and more dominant during NA.

Concerning the dependence of PLT on the number of vacancies, [Pus83] predicted the annihilation characteristics of positrons trapped in vacancy clusters of various sizes in Al. The results are listed in Table 4.1.1:

Table 4.1.1. Positron lifetimes in various vacancy clusters in Al [Pus83].

number of vacancies	1	2	4	6	13
positron lifetime (ns)	0.253	0.273	0.329	0.351	0.422

based on these values, the asymptotic PLT τ_v of ~ 0.300 ns at the end of the measurement corresponds to vacancy clusters containing on the average ~ 3 vacancies as a rough estimate. Compared to the larger vacancy clusters (~ 6 vacancies) found in Al-0.005%Si alloy, such a result suggests a lower jump frequency of vacancies in the absence of Si atoms, see Section 4.2.1.

4.1.1.2 Results and Discussion Based on Modelling

Besides free annihilations, positrons trapped in a single open-volume defect type can be described by the simple trapping model (STM) [Kra03]. There are two possibilities of positron annihilation after thermalization and diffusion:

- (1) directly in defect-free bulk with an annihilation rate λ_b ;
- (2) alternatively, they will be captured by a deep trap (dt) such as a vacancy with a trapping rate κ_v and annihilate afterwards with an annihilation rate λ_v (thermal de-trapping from vacancy is excluded).

Such processes are schematically shown in Fig. 4.1.2.

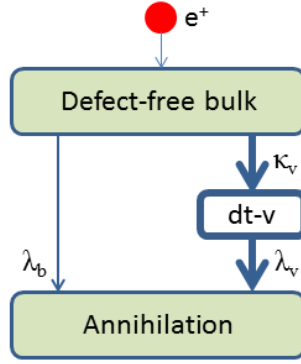


Figure 4.1.2. Schematic illustration of the STM. “dt-v” denotes deep trap-vacancy.

The rate equations are:

$$\begin{bmatrix} \dot{n}_b(t) \\ \dot{n}_v(t) \end{bmatrix} = \begin{bmatrix} -(\lambda_b + \kappa_v) & 0 \\ \kappa_v & -\lambda_v \end{bmatrix} \begin{bmatrix} n_b(t) \\ n_v(t) \end{bmatrix}, \quad (4.1.2)$$

where the number of positrons in the bulk and in the vacancies are denoted by n_b and n_v , and were initialized to N_0 and 0 for $t=0$, respectively. The solution of the equations above is the decay spectrum of positrons $D(t)$, i.e. number of remaining positrons at time t :

$$D(t) = I_f \exp\left(-\frac{t}{\tau_f}\right) + I_v \exp\left(-\frac{t}{\tau_v}\right). \quad (4.1.3)$$

τ_i and I_i (“i” equals f or v) can be obtained by non-linear fitting of an experimental spectrum (representing the time derivative of $D(t)$) after background subtraction and source correction.

The annihilation parameters involved in Eq. (4.1.3) can be expressed as:

$$\tau_f = \frac{1}{\lambda_b + \kappa_v}, \quad (4.1.4)$$

$$\tau_v = \frac{1}{\lambda_v}, \quad (4.1.5)$$

$$I_f = 1 - I_v, \quad (4.1.6)$$

$$I_v = \frac{\kappa_v}{\lambda_b - \lambda_v + \kappa_v}, \quad (4.1.7)$$

where τ_v equals the PLT in a vacancy, and the presence of such defects leads to a so-called “reduced bulk lifetime” τ_f (shorter than τ_b). κ_v is the trapping rate which is proportional to the defect concentration c and to the specific trapping rate μ , as shown in Eq. (4.1.8).

$$\kappa_v = \mu \cdot c = I_v \left(\frac{1}{\tau_f} - \frac{1}{\tau_v} \right) = \frac{I_v}{I_f} \left(\frac{1}{\tau_b} - \frac{1}{\tau_v} \right). \quad (4.1.8)$$

The average positron lifetime (APLT) can be calculated as the weighted sum of each individual component:

$$\tau_{APLT} = \tau_f \cdot I_f + \tau_v \cdot I_v. \quad (4.1.9)$$

The annihilation fraction η of positrons in the vacancies (fraction of trapped positrons) can be calculated by:

$$\eta = \int_0^{\infty} n_v(t) dt = \frac{\kappa_v}{\lambda_b + \kappa_v}, \quad (4.1.10)$$

where $n_v(t)$ is the number of positrons in the vacancies at time t , see Eq. (4.1.2).

Based on the data in Fig. 4.1.1 as well as Eq. (4.1.9) and Eq. (4.1.8), the evolution of APLT and the vacancy concentration were determined. The results are shown in Fig. 4.1.3:

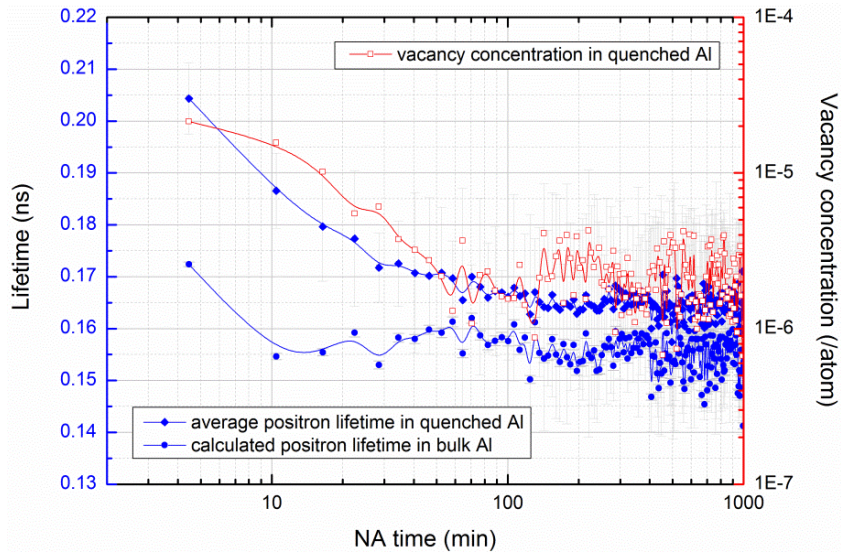


Figure 4.1.3. Evolution of average positron lifetime in quenched Al (blue solid diamonds), calculated positron lifetime in bulk Al (blue solid spheres) and vacancy concentration in quenched Al (red open squares) during NA.

Due to the dominance of positron annihilation in mono-vacancies shortly after quenching, the APLT starts from a relatively high value of 0.205 ns. Because of the formation of small vacancy clusters, contribution of vacancy annihilation decreases and the APLT levels off at 0.167 ns within ~100 min. The final APLT approaches the value of bulk Al since most positrons (> 85%) annihilate in the matrix rather in vacancies after a long NA time.

Using Eq. (4.1.8), a vacancy concentration of 0.21×10^{-4} /atom was calculated for the “as-quenched” Al (AQ, actually after ~ 2 min delay at RT), which is just $\sim 15\%$ of the theoretically value calculated with Eq. (4.1.1). This is probably due to the loss of vacancies during or after quenching. The further reduction in vacancy concentration should be ascribed to the formation of vacancy clusters during NA. The time evolution of the vacancy concentration has been derived in Eq. (4.1.8) assuming a constant specific trapping rate $\mu = 2.5 \times 10^{14} \text{ s}^{-1}$, as for a mono-vacancy in Al. However, μ increases with the size of a vacancy cluster [Nie79], as shown in Table 4.1.2. This implies that although the general decrease of the vacancy concentration is valid, the real concentration of vacancy clusters after certain NA time could be 2 to 3 times lower than the values given in Fig. 4.1.3.

Table 4.1.2. Specific trapping rates μ of positrons into vacancy clusters in Al [Nie79].

number of vacancies	1	2	3	4	5	10
specific trapping rate μ (10^{14} s^{-1})	2.5	5.9	7.7	9.7	12	16 – 19

In order to check the validity of the STM for the quenched Al, the PLT in bulk was calculated based on the experimental data using Eq. (4.1.11):

$$\tau_b^c = \left(\frac{I_f}{\tau_f} + \frac{I_v}{\tau_v} \right)^{-1}. \quad (4.1.11)$$

Taking the experimental inaccuracies into consideration, the calculated PLTs in bulk generally agree with the bulk PLT τ_b from literature, which ranges from 0.158 to 0.166 ns [Lun13, Pus83, Sch86, Sta00], as shown in Fig. 4.1.3. Thus the PLT components in the quenched Al sample can be reasonably described by the STM.

The PALS results of the as-quenched state of Al are compared to the previous study [Liu09] on an Al (5N) sample, quenched into $-70 \text{ }^\circ\text{C}$ HCl solution and measured at $-40 \text{ }^\circ\text{C}$ where undesirable microstructural changes can be largely avoided [Røy06]. At least 2×10^6 events were collected. The decomposed PLTs, corresponding intensities, and the calculated annihilation parameters are listed in Table 4.1.3.

Similar annihilation characteristics are found for both experiments and these results are in agreement with [Cal05], by whom a PLT of $\tau_v = 0.235 \pm 0.002 \text{ ns}$ and a corresponding intensity of $I_v = 58 \pm 1.5\%$ were obtained.

Table 4.1.3. Experimental and calculated annihilation parameters of the as-quenched Al.

parameter	$\tau_f(\text{ns})$	$\tau_v(\text{ns})$	$I_f(\%)$	$I_v(\%)$	$\tau_{\text{APLT}}(\text{ns})$	$\kappa(\text{ns}^{-1})$	$c_v(/\text{atom})$	$\eta(\%)$
<u>present (FDA)</u>								
value	0.090	0.240	23.3	76.7	0.204	5.4	0.21E-4	45.5
error	0.020	0.004	1.9	1.9	0.007	23.5	0.94E-4	2.8
<u>previous (NDA)</u>								
value	0.080	0.238	39.5	60.5	0.176	5.0	0.20E-4	43.9
error	0.003	0.001	0.6	0.6	0.002	4.2	0.16E-4	0.5

The annihilation fraction η from Table 4.1.3 is $\sim 44\%$, as calculated from Eq. (4.1.10). It will be used for the interpretation of DBAR ratio plots in Section 4.1.2.

4.1.2 Doppler Broadening Annihilation Radiation

To interpret a DBAR ratio curve of an Al-Mg-Si alloy, all possible reference curves from bulk Al, Mg, Si, mono-vacancy in Al, Mg, Si, and V-Mg, V-Si complexes (“V” for vacancy) in Al matrix are required. The plot of mono-vacancy in Al will be discussed in this section. After SHT, pure Al samples were rapidly quenched into RT water or -70°C HCl and were investigated employing HMA. Both measurements were performed at -40°C [Liu09], which is sufficiently low to suppress microstructural changes. The ratio plots with respect to annealed Al are indicated by the orange and blue symbols in Fig. 4.1.4:

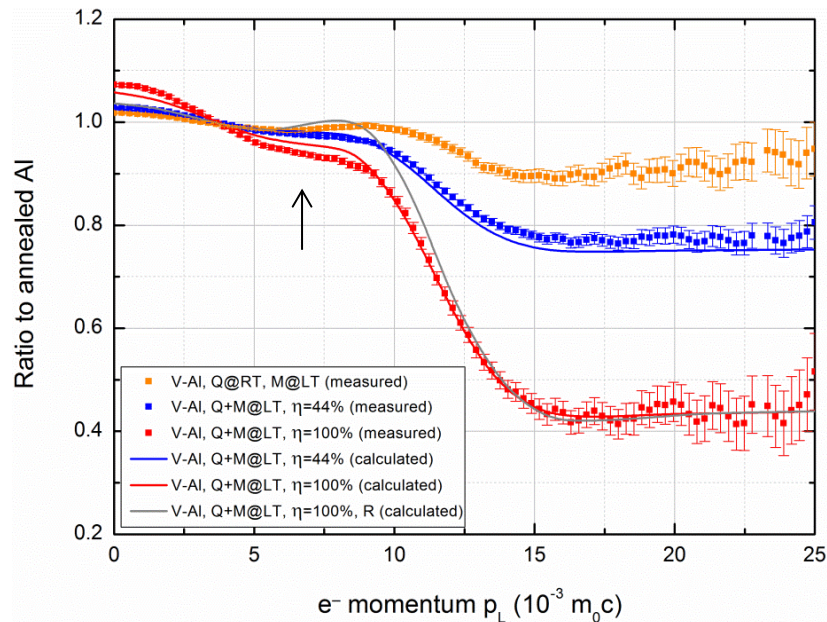


Figure 4.1.4. Ratio plots of pure Al quenched under different conditions. “V” for vacancy, “Q” for quenched, “M” for measured, “RT” for room temperature, “LT” for low temperature and “R” for relaxed atomic coordinate. Calculated results are also given for matters of comparison. The upward black arrow denotes the Fermi momentum p_F of Al.

Two different types of annihilation sites were verified by PALS experiments on the as-quenched Al samples, bulk and vacancies or vacancy clusters. Positron annihilation in the bulk is ascribed to a low concentration of defects which prevent saturated positron trapping. After quenching, the vacancy-related defects have a PLT around 0.240 ns corresponding to mono-vacancies. Annihilation at both sites should contribute to the DBAR signal. Compared to the samples quenched at -70 °C (blue squares) where the ratio is less than 0.8 for $p_L > 15 \times 10^{-3} m_0c$, the ratio of samples quenched at RT (orange squares) approaches 1, pointing at a reduced number density of vacancies (for Al containing no vacancy at all the ratio equals 1 over the entire momentum region) due to quenching and handling the sample at RT, although the whole procedure at RT took about 4.5 min only. Therefore, it is absolutely essential to quench and keep the samples sufficiently cold before or during the measurement in order to maximize the vacancy concentration in as-quenched Al.

As already mentioned, positron trapping at vacancies in the quenched Al samples is incomplete ($\eta = 44\%$), the “real” mono-vacancy ratio (R) and the corresponding momentum distribution has to be calculated from the experimental ratio (R_{exp}) containing both bulk (R_{Al}) and vacancy contributions using Eq. (4.1.12):

$$R = \frac{1}{\eta} [R_{exp} - (1 - \eta) \cdot R_{Al}] \text{ with } R_{Al} = 1 . \quad (4.1.12)$$

The calculated pure mono-vacancy ratio plot illustrated by the red squares in Fig. 4.1.4 has a value around 0.4 in the high-momentum region and is markedly reduced compared to the uncorrected one (blue squares). This low value is typically caused by the decrease in the core electron contribution due to positron localization at open volume defects.

The ratio plots can also be interpreted theoretically in terms of DBAR calculations for various annihilation sites, employing the program DOPPLER [Ala95, Ala96]. Prior to the computation, atomic coordinates with the presence of a mono-vacancy were relaxed by means of the numerical ab-initio code SIESTA [Koh10, SIExx, Sol02]. This code uses the density functional theory (DFT) approach [Hoh64, Koh65, Pus83, Tho27] which is widely applied for electronic structure calculations. Furthermore, due to the attractive interaction between the positron and the electron, the increment in local electron density surrounding a positron results in a higher annihilation rate. This will be considered by introducing an

enhancement factor [Bar95]. After combining this factor with the local density approximation (LDA) [Jen89] and the general gradient approximation (GGA) [Bar96], calculations of the DBAR ratio curves were carried out by [Kor07, Kor10]. The calculated results (solid lines) are shown together with the experimental data in Fig.4.1.4.

By assuming complete positron trapping in vacancy-type defects, the calculated result of mono-vacancy in Al by relaxed atomic coordinate (gray line) was convoluted by the energy resolution of the spectrometer (1.37 keV at the 0.478 MeV line of ^7Be) and compared to the sample quenched to a LT (red squares). Both ratio plots show enhanced free electron annihilation in the low-momentum region. It arises from localization of positrons by vacancies, and coincides with each other particularly in the high-momentum region. However in the intermediate-momentum region where the local peak is located ($p_L \approx 8 \times 10^{-3} m_0c$), an obvious deviation can be seen.

It was verified that the contribution from a positron spatially confined at a vacancy to the total momentum of the (e^+ , e^-) pair is different from a free positron moving at thermal energy in a crystal. The latter can actually be neglected [Shu76, Som02]. Such a confinement of a positron wave function leads to enhanced free and reduced core electron annihilation accordingly, and manifests itself as a smearing of the momentum distribution just above the Fermi momentum (indicated by the upward arrow in Fig. 4.1.4). As a result, a peak at $p_L \approx 8 \times 10^{-3} m_0c$ will be observed. It originates from additional counts collected for this momentum region where the reference momentum distribution is low [Cal05].

Based on preliminary LDA calculations, the relaxation of the Al atom positions around a vacancy in bulk Al is expected to be 1.7% inwards. However, if a positron is localized by a vacancy, due to the repulsive interaction between the positron and the surrounding positive nuclei, the relaxation will be 1.8% outwards instead [Makxx]. Nevertheless, how a confined positron affects the relaxation of its neighboring atoms had not been taken into account in the calculation [Kor10]. Therefore, by applying only inward relaxation for a vacancy, without considering that the positron will lead to a larger open volume and consequently will be weaker localized, the much higher ratio for the calculation (~ 1 at $p_L = 8 \times 10^{-3} m_0c$ in Fig. 4.1.4) than for the experiment can be explained. [Cal05] reproduced local relaxation by changing the nearest neighbor positions of the missing atoms from their normal lattice sites.

It was found that on the one hand the entire momentum distribution correlates strongly to the relaxation, while on the other hand, the energy resolution of the spectrometer also has a notable impact on the visibility of the local peak discussed above. The low resolution of 1.37 keV at the ^7Be line could be responsible for the barely visible peak as shown in Fig. 4.1.4, whereas by other authors, more pronounced peak structures have been observed probably attributed to better energy resolutions of the spectrometers employed [Ban12, Cal05, Dup07].

Finally, a comparison was made between the experiments (red squares) and the simulation without relaxation (red line), which reflects the relaxation of the atomic coordinates due to the presence of both a vacancy and a positron. As shown in Fig. 4.1.4, the inconsistency in the intermediate-momentum region was improved to a certain extent. The ratio plot related to incomplete trapping ($\eta = 44\%$) was also calculated (blue line) in a similar manner, and is consistent with the experimental one (blue square).

4.2 Binary Al-Mg and Al-Si Alloys

As an introductory study, positron lifetime experiments were carried out on pure Al-Mg and Al-Si binary alloys with solute concentrations ranging from 0.005% to 1% in order to clarify some of the influences of Mg and Si atoms on the clustering processes. The change of PLT during NA of binary alloys was characterized and compared to DSC and DBAR experiments to obtain a better understanding of the clustering stages in Al-Mg-Si alloys.

4.2.1 Positron Annihilation Lifetime Spectroscopy

4.2.1.1 Validation of the 2-component Fitting

Fitting the PLT spectra of all the binary alloys by one single component leads to unsatisfactory fit variances, but by introducing a second PLT component the situation can be greatly improved, see Fig. 4.2.1 as an example. We found that all investigated binary Al-Mg and Al-Si alloys exhibit annihilation characteristics similar to quenched Al, i.e. two distinct PLT components corresponding to annihilation in either bulk or vacancy-related defects.

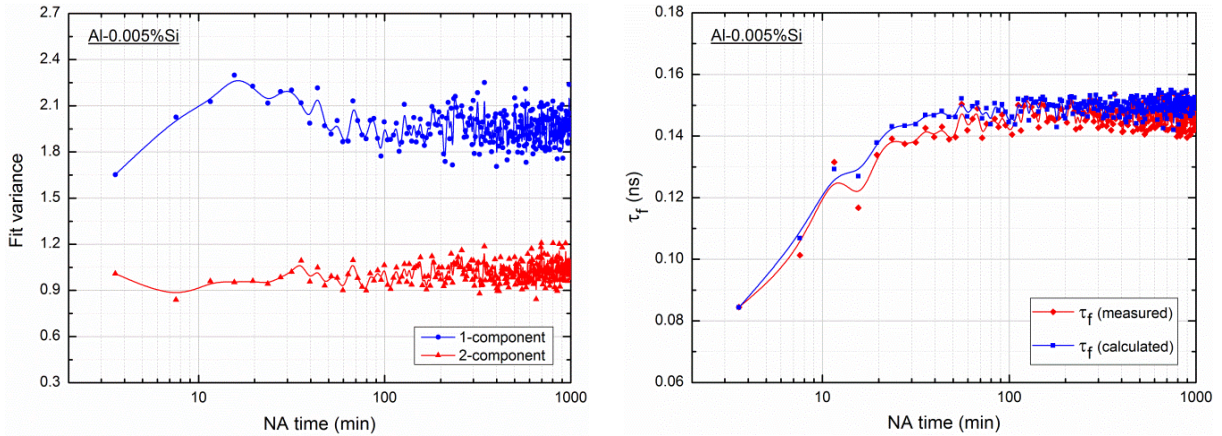


Figure 4.2.1. (L) Fit variances after applying 1 or 2-component fitting; (R) Comparison between τ_f obtained directly from experiments and theoretically determined by STM. An Al-0.005%Si alloy was investigated for both figures.

In order to check the validity of the 2-state trapping model (STM), the PLT τ_f was also calculated from the experimental parameters and the bulk PLT τ_b in Al using:

$$\tau_f^c = \frac{1}{\frac{1}{\tau_b} + I_v \left(\frac{1}{\tau_b} - \frac{1}{\tau_v} \right)}, \quad (4.2.1)$$

and compared to the measured PLT τ_f , see Fig. 4.2.1 (R). It was found that the calculated and experimental values coincide with each other. Thus, the STM can be employed to describe the ageing characteristics of binary alloys.

4.2.1.2 Evolution of τ_i & I_i during NA

The NA kinetics of decomposed PLT components for Al-Mg alloys are shown as below:

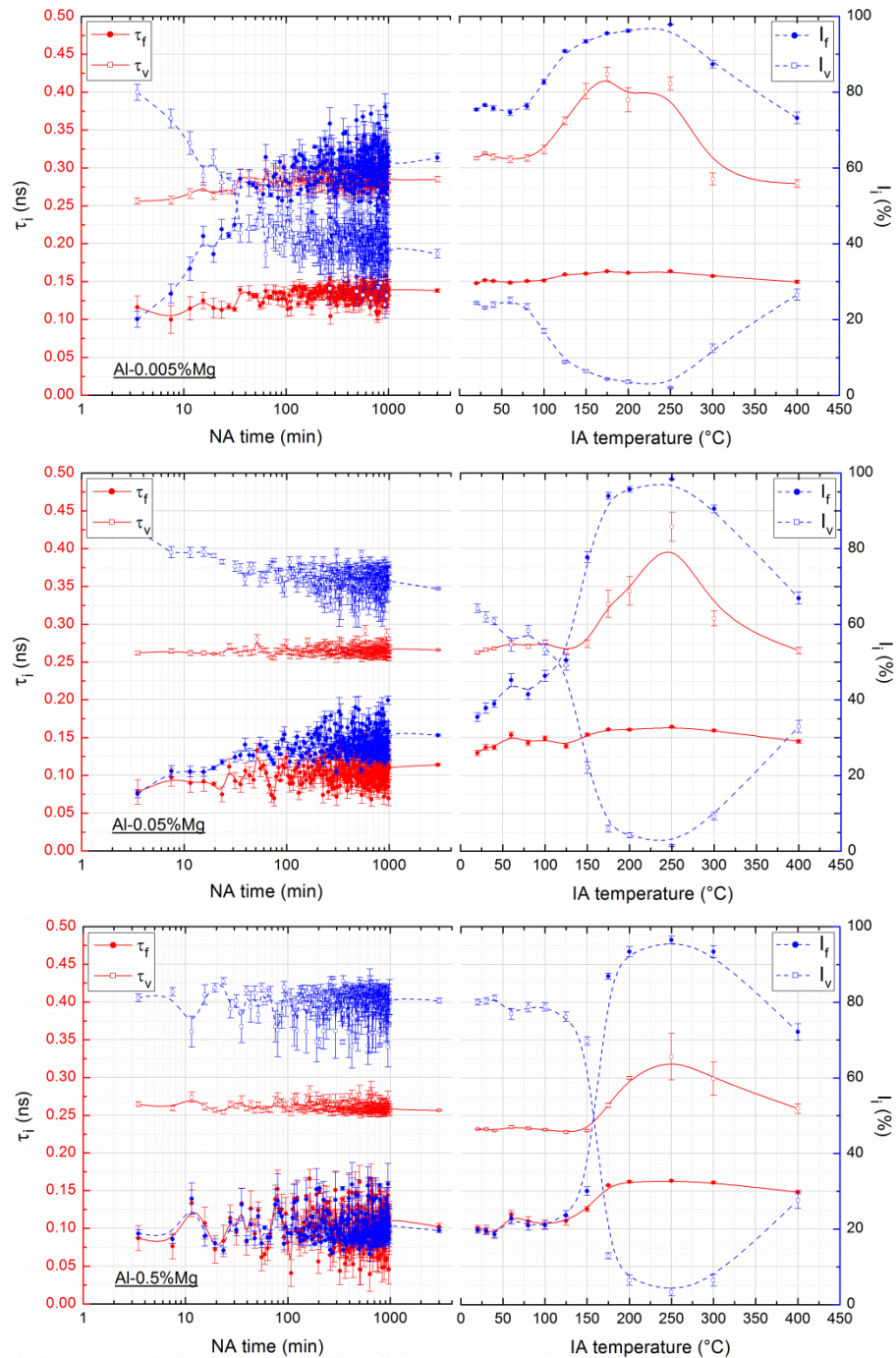


Figure 4.2.2. Evolution of decomposed PLT components of Al-Mg alloys during NA. Data was collected in FDA mode for the first 1000 min and the NDA mode at 3000 min of NA. After ~ 2 months of RT storage, these Al-Mg samples were isochronal annealed (IA) from 30 to 400 $^{\circ}\text{C}$. The temperature step was 10 or 20 K below 100 $^{\circ}\text{C}$ and increased to 100 K above 300 $^{\circ}\text{C}$. A 10 min annealing was applied for each step and data was collected in the NDA mode.

The NA kinetics of decomposed PLT components for Al-Si alloys are shown in the following figures:

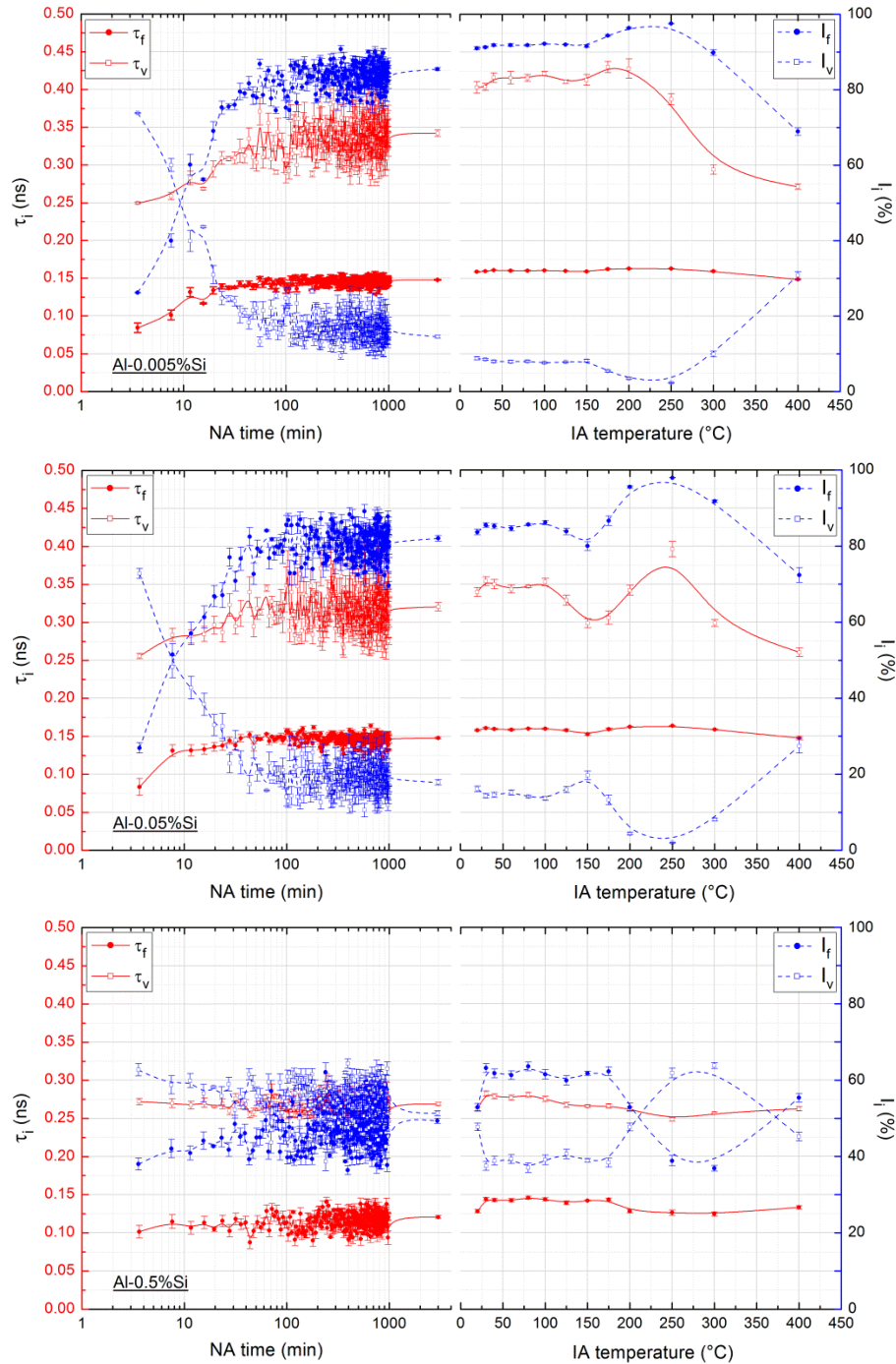


Figure 4.2.3. Evolution of decomposed PLT components of Al-Si alloys during NA. Data was collected in FDA mode for the first 1000 min and the NDA mode at 3000 min of NA. After ~2 months of RT storage, these Al-Si samples were isochronal annealed (IA) from 30 to 400 °C. The temperature step was 10 or 20 K below 100 °C and increased to 100 K above 300 °C. A 10 min annealing was applied for each step and data was collected in the NDA mode.

During the first 1000 min, two PLTs τ_f , τ_v and their intensities I_f , I_v can be distinguished after resolving the PLT spectra of Al-Mg and Al-Si alloys obtained in the FDA mode:

- Al-Mg alloys: (1) Al-0.005%Mg. τ_v increases from 0.255 to 0.285 ns and I_v reduces from $\sim 80\%$ to $\sim 40\%$, whereas τ_f and I_f both increase; (2) Al-0.05%Mg. Except the almost constant τ_v of ~ 0.260 ns, I_v decreases slightly while τ_f and I_f increase; (3) Al-0.5%Mg. τ_v roughly equals 0.260 ns and no obvious change takes place in τ_f , τ_v and I_f , I_v .
- Al-Si alloys: (1) Al-0.005%Si. τ_v increases from 0.250 to ~ 0.350 ns, I_v reduces from 74% to 15%, τ_f and I_f increase; (2) Al-0.05%Si. τ_v increases from 0.255 to 0.325 ns, I_v reduces from 73% to 19%, τ_f and I_f increase; (3) Al-0.5%Si. Only slight changes in τ_f , τ_v and I_f , I_v were observed, and shortly after quenching, τ_v has a value of 0.275 ns.

These results suggest that during NA, bulk annihilation becomes dominating and τ_f approaches 0.165 ns, while the increase of τ_v indicates clustering of vacancies, which is especially pronounced in dilute Al-Si alloys, consistent with [Seg84].

After 3000 min of NA, data in Fig. 4.2.2 and Fig. 4.2.3 were collected in the NDA mode. It can be seen that apart from the fluctuations of data caused by low statistics, a reliable estimation of the individual PLTs and the relevant intensities can be obtained by using a much faster acquisition in the FDA mode, and the “low statistics method” of 2-component fits is applicable to the binary alloys for investigating the fast kinetics during NA.

To discuss the NA kinetics of Al-Mg and Al-Si alloys in a clear manner, all PLT components in Fig. 4.2.2 and Fig. 4.2.3 are presented as a function of the intensities, see Fig. 4.2.4:

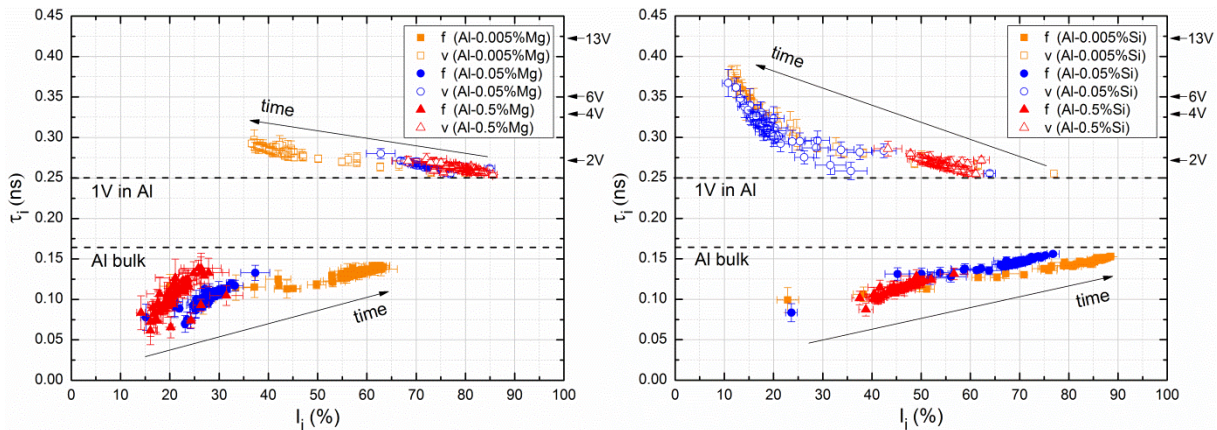


Figure 4.2.4. τ - I plots of (L) Al-Mg and (R) Al-Si alloys during the first 1000 min of NA. “f” stands for free annihilation in the bulk Al while “v” denotes annihilation in vacancy-type defects.

It has been shown that a single Mg or Si atom in Al cannot trap positrons [Dlu80, Dlu81, Sto75] although they have higher positron affinities [Pus89]. Therefore, the higher PLTs of τ_v observed in all results are vacancy-related. The notable difference in NA kinetics can be easily observed by comparing the binaries to pure Al, pointing at the interactions between vacancies and solutes. Table 4.2.1 shows the binding energies between vacancy, Mg and Si:

Table 4.2.1. Binding energies between vacancy and solute [Hir07], another set of values are also given in the parentheses [Lan13], and “+” sign refers to attractive binding.

2-body type	V-Mg	V-Si
binding energy (eV)	+0.015 (+0.026)	+0.025 (+0.033)

Such binding between vacancies and solutes can increase the concentration of thermal vacancies in binary Al-Mg and Al-Si alloys during solutionizing and after quenching as can be roughly estimated using the Lomer equation [Lom58]:

$$c_v = \exp\left(\frac{S_f}{k_B T}\right) \exp\left(-\frac{E_f}{k_B T}\right) \left[1 - 12c_{Mg(Si)} + 12c_s \exp\left(\frac{E_{V-Mg(Si)}}{k_B T}\right)\right], \quad (4.2.2)$$

where $c_{Mg(Si)}$ is the solute concentration, $E_{V-Mg(Si)}$ the binding energy between the vacancy and solute, S_f , E_f , k_B and T have been previously defined. Results are shown in Fig. 4.4.11.

During or after quenching, these vacancies will: (1) escape to the nearest sinks, but compared to quenched pure Al, this vacancy loss will be hindered by solute atoms owing to their attractive binding energies; (2) bind with solutes, as shown by the initial PLTs in Fig. 4.2.2 and Fig. 4.2.3. All initial PLTs in Al-Mg alloys equal a value of ~ 0.260 ns are probably related to V-Mg complexes, since binding with a Mg atom increases the PLT in a mono-vacancy from 0.250 to 0.260 [Cor81] and 0.269 ns [Dlu80]. In contrast, if the vacancy is decorated by a Si atom at one of the nearest neighbor (NN) positions, the corresponding PLT will be reduced to ~ 0.240 ns [Mel06]. Thus the $\tau_v \sim 0.250$ ns PLTs in as-quenched Al-0.005%Si and Al-0.05%Si alloys should correlate to positron annihilation in mono-vacancies or in di-vacancies attached to Si atoms, while the slightly higher τ_v of 0.275 ns in Al-0.5%Si alloy rather suggests the rapid formation of small vacancy clusters (probably also bound with certain amount of Si atoms) during or after quenching [Kra85]; (3) in most cases, they tend to form vacancy clusters, similar to the case of quenched pure Al. This process is reflected by the generally observed increase of τ_v , decrease of I_v and τ_{APLT} during NA, see Fig. 4.2.5.

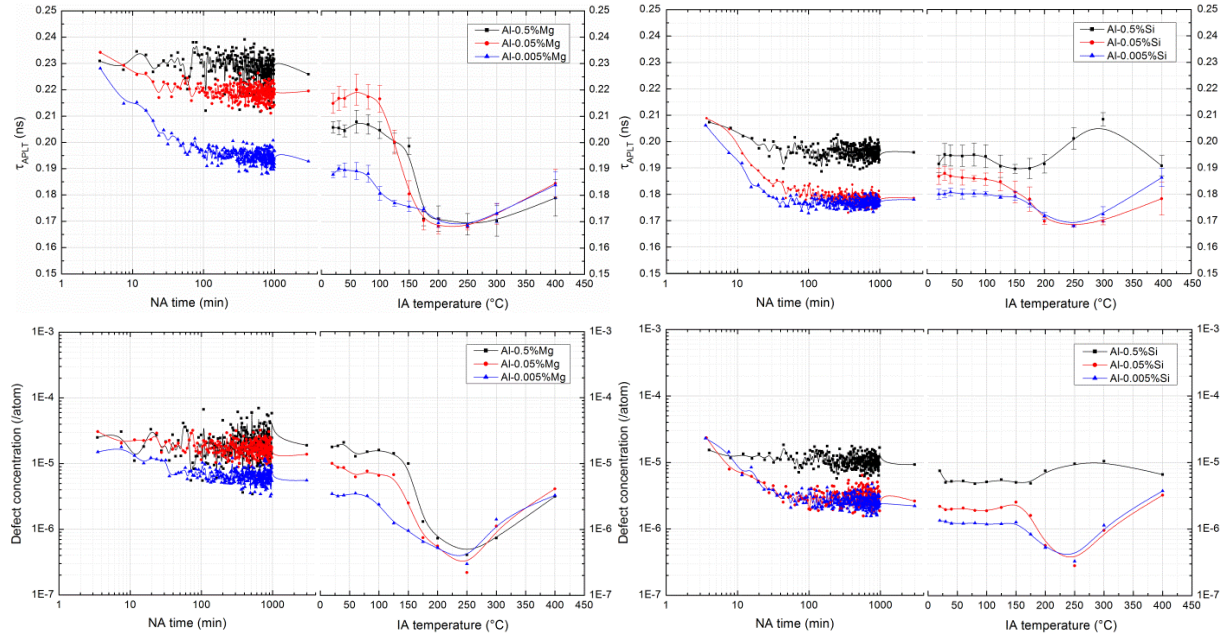


Figure 4.2.5. Evolution of APLT (above) and calculated vacancy-type defect concentration (below) during NA and IA, the same data as in Fig. 4.2.2 and Fig. 4.2.3 was used.

For the most dilute alloys, i.e. alloys containing 0.005% solutes, the changes in τ_{APLT} is different compared to pure Al, indicating that solutes markedly influence the formation of vacancy clusters. If the binding energy of a vacancy with Mg or Si is attractive, some of the vacancies will temporarily bind to a solute and form a V-Mg or V-Si complex. On the other hand, from atomistic calculations, binding between Mg-Mg and Si-Si appears unfavourable, with binding energies for Mg-Mg and Si-Si equal -0.04 and -0.03 eV, respectively [Hir07]. Also, no conspicuous solute clustering reaction can be observed in DSC runs, see Fig. 4.2.6:

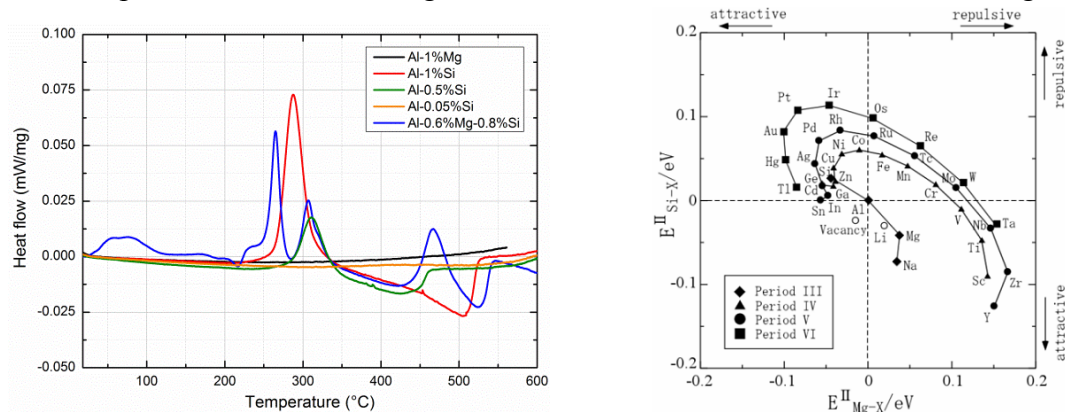


Figure 4.2.6. (L) 10 K/min DSC runs on ternary Al-0.6%Mg-0.8%Si and binary Al-Mg and Al-Si alloys, the overlapping clustering peaks located in the temperature range 20 to 120 °C as well as β'' , β' and β peaks of Al-Mg-Si alloys are clearly visible. However, in the case of binary alloys, except for the Si precipitation peaks at ~ 280 °C no signals from solute clustering can be observed; (R) Interaction energy map reported by [Hir07].

Clustering peaks are clearly visible in the ternary alloy, pointing at favourable binding between Mg and Si (+0.04 eV). The result agrees with DSC observations by [Cha11].

For the binary alloys, [Gup99] is inclined to exclude solute clustering in the binary alloys rather than assuming that the absence of clustering signal is caused by the very fast Si or Mg clustering or the very small heat effects related to that process. This view is supported by electrical resistivity measurements [Küh13], by which no observable change of resistivity was found in binary Al-0.5%Si alloy after quenching, see Fig. 4.3.8.

Whether a vacancy will detach from a pre-existing vacancy-solute complex as has been claimed by the vacancy-pump model [Gir65] cannot be clarified from the present result, as this will depend on a complete set of comparable binding energies between vacancy, solute and Al, plus the vacancy and solute concentration. However, the jump frequency of a vacancy will definitively be affected by the presence of solutes, as will be discussed in the following.

The vacancy-driven diffusion of solute atoms is achieved through the jump of the solute (vacancy) to one of the 12 nearest neighbor lattice positions. This process is thermally activated and enables solute cluster formation in Al-Mg-Si alloys. The jump frequency of a mono-vacancy from its initial lattice position j to the atom position i of its NN atom i can be approximated by the following equations [Lia12, Man09, Wer49]:

$$f_i = f'_i \cdot \exp\left[-\frac{E_i^a}{k_B T}\right] = f'_i \cdot \exp\left[-\frac{E_i^d - E_v^f - \Delta E_{i,j}^b}{k_B T}\right], \quad (4.2.3)$$

$$\Delta E_{i,j}^b = \sum_{k \in NN_i} (E_{k-s@i}^b - E_{k-v@i}^b) + \sum_{k \in NN_j} (E_{k-v@j}^b - E_{k-s@j}^b), \quad (4.2.4)$$

where $i, j = 1 \dots 12$ is the site number in the NN shell, f'_i is the effective jump frequency (or vibrational frequency of an atom [Vin57], based on the classical “five-frequency” model [Ada88]). E_i^a is the activation energy of a vacancy jump, E_i^d is the diffusion activation energy of a vacancy, E_v^f is the vacancy formation energy (0.63 eV, average value from [Man09]), $\Delta E_{i,j}^b$ is the differences of the binding energies of a vacancy (v) or solute atom (s) with their NN before and after the jump at sites i and j , k refers to any site in NN_i or NN_j . To simplify the calculation $\Delta E_{i,j}^b$ was neglected in this study.

The values used by [Lia12] were further adopted, based on [Hir07, Hos96, Man09], see Table 4.2.2:

Table 4.2.2. Kinetic parameters for the calculation of jump frequency [Man09].

kinetic parameter	Al	Mg	Si
effective jump frequency f' (s^{-1})	1.66×10^{13}	1.86×10^{13}	1.57×10^{13}
diffusion activation energy E^d (eV)	1.29	1.27	1.15

The jump frequencies of a vacancy associated with an Al, Mg or Si atom in Al matrix were calculated for temperatures ranging from -200 to 30 °C. At RT, the jump frequencies f_{V-Al} and f_{V-Mg} are equal to ~ 80 and $\sim 190 s^{-1}$, respectively, while for f_{V-Si} a much higher value of $\sim 18200 s^{-1}$ is obtained. All jump frequencies generally increase with temperature over the entire temperature range, see Fig. 4.2.7. The calculated jump frequencies related to Al and Mg are close to each other at every temperature, while the curve of Si always lies above both of them.

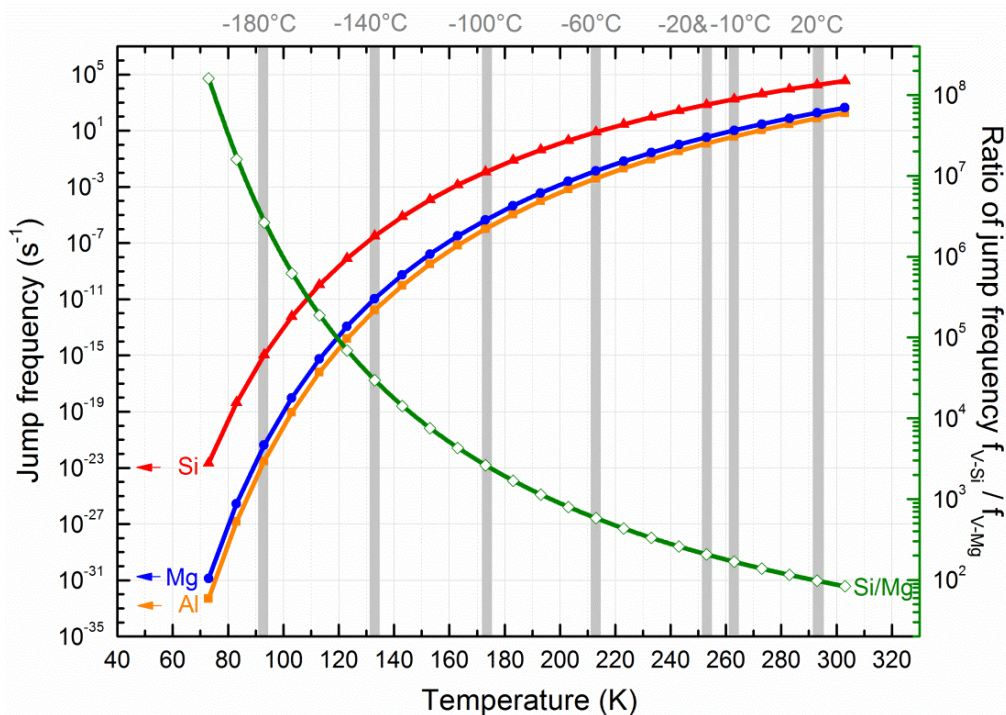


Figure 4.2.7. Jump frequency of a vacancy associated with an Al, Mg or Si atom at different temperatures, indicated by orange, blue and red curves, respectively. The ratio between f_{V-Si} and f_{V-Mg} is illustrated by the green curve.

Based on the calculations, the dependence of the APLT evolution during NA Si on the kind of solute as well as on solute concentration as shown in Fig. 4.2.8 can thus be interpreted.

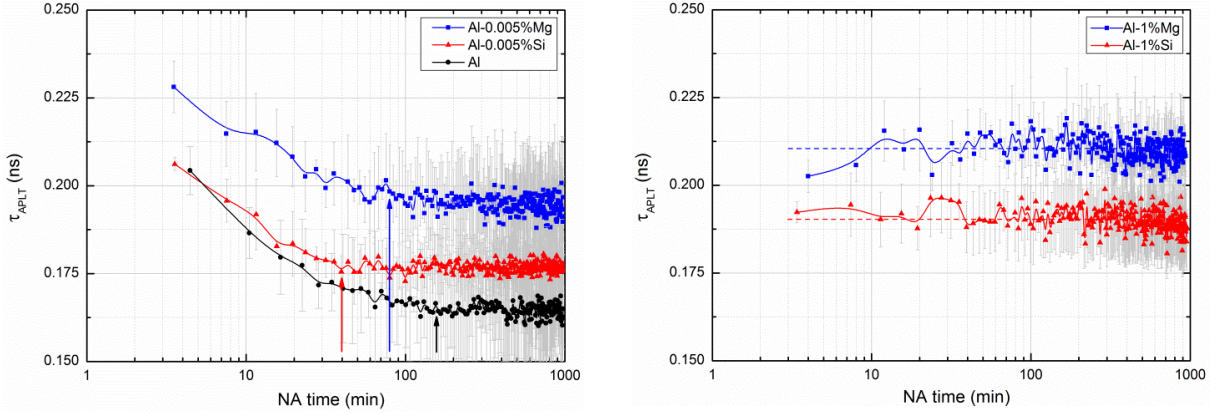


Figure 4.2.8. τ_{APLT} evolution in quenched (L) Al-0.005%Mg, Al-0.005%Si, Al and (R) Al-1%Mg, Al-1%Si alloys. Upwards arrows in the left figure indicate the saturation time of τ_{APLT} .

As shown above, the jump frequency of a vacancy in Al-Si alloys is much faster than in pure Al. The shorter time required to reach a stable APLT in Al-0.005%Si shown in Fig. 4.2.8 (L) can be qualitatively explained by the above proposition. Direct correlation between such transition times and the jump frequency is not straightforward, since the calculation of jump frequency applied depends not only on the activation energies E_d in Eq. (4.2.3), which differ between various sources, but also on the binding energies between vacancies and solute atoms in Eq. (4.2.4). For the most critical case of Mg, [Fuj77, San06] obtained 1.19 eV and 1.20 eV for the activation energy E_d . Particularly, various values of E_b have been reported ranging from strong attractive binding to a weak repulsive one [Wol07]. This could markedly influence the determination of the jump frequency which is based on these kinetic parameters. But in general, the mobility of a vacancy attached to a Mg atom is low at RT [Dlu86]. This was also verified in this work by measuring APLT in quenched Al-0.5%Mg and Al-1%Mg alloys stored at RT for two months, from which very slow changes were observed.

For alloy with low solute content, the PLTs of the vacancy-type defect ($\tau_v(\text{Al-0.005\%Mg}) \approx \tau_v(\text{Al}) < \tau_v(\text{Al-0.005\%Si})$) and their corresponding intensities ($I_v(\text{Al-0.005\%Mg}) > I_v(\text{Al}) \approx I_v(\text{Al-0.005\%Si})$) after long NA is difficult to understand, as τ_v might involve contributions of vacancy clusters with and without attached solutes. It is known that the PLT in a mono-vacancy increases or decreases slightly with the number of attached Mg or Si atoms [Cor81, Mel06]. However, it is too speculative to try to determine the exact number of solutes decorating the vacancy based on the present data only. Further experiments should be carried out to verify this point. One possibility could be that Si can act as an “inhomogeneous nucleation site” for vacancy

clusters. The high jump frequency of a vacancy attached to Si might result in fewer but larger vacancy clusters containing at least 6 vacancies in Al-0.005% Si alloy. But in Al-0.005%Mg alloy, smaller but densely distributed clusters (~ 2 vacancies) are formed, see Fig. 4.2.4.

With increasing solute content, the time for a vacancy to find the nearest solute will become shorter until to an extent that the fraction of solutes exceeds the fraction of vacancies in the alloy. This could result in a similar behaviour for both alloys that the decrease of the APLT becomes less pronounced for increasing amounts of solute, as seen in Fig. 4.2.8 (R), but the mechanism could be different. In Al-Si, when a vacancy is attached to Si, the vacancy can still move with a high jump frequency to other vacancies to form small vacancy clusters (with or without Si) [Kra85]. In Al-Mg, the jump frequency of a vacancy is slowed down by attaching to Mg, or in other words, vacancies will be retained by Mg atoms [Som02]. V-Mg complexes higher in number density will be formed instead (e.g. initially $\sim 80\%$ annihilation in vacancy-type defects in Al-0.5%Mg alloy). As a result, $\tau_v(\text{Al-0.5\%Si}) = 0.275$ ns and $\tau_v(\text{Al-0.5\%Mg}) = 0.260$ ns were obtained after quenching which are close to the PLT in vacancy clusters (~ 3 vacancies) and mono-vacancies, respectively [Dlu86, Mel06]. What we could learn from the results so far is that both Si and Mg attract vacancies, but Si will move together with a vacancy while Mg “traps” a vacancy and slows down its movement. This indicates that Si diffusion is the dominating mechanism in the initial stage of solute clustering in Al-Mg-Si alloys. The discussion above can be summarized by Fig. 4.2.9:

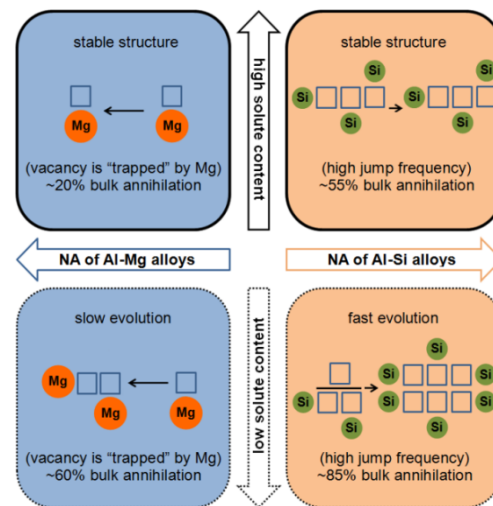


Figure 4.2.9. Illustration of the NA characteristics of Al-Mg and Al-Si alloys. Vacancy-solute configuration during the first 3000 min of NA is schematically shown. High and low solute content means 0.5% and 0.005%.

4.2.1.3 Evolution of τ_i & I_i during IA

The evolution of the PLT components upon isochronal annealing after ~2 months of NA was also shown in Fig. 4.2.2, Fig. 4.2.3 and Fig. 4.2.5. It was found that:

- Al-Mg alloys
 - Below 100 °C, no obvious change for all annihilation parameters is observed. V-Mg remains as a stable complex, which implies a strong binding energy between the two. This agrees with electrical resistivity measurements by [Pan63] and theoretical calculations by [Hir07, Lan13] (e.g. the binding energies of V-Mg and V-Si equal 0.026 eV and 0.033 eV by the latter, see Table 4.2.1).
 - Above 100 °C, the APLT and the defect concentration start to drop. A higher Mg content leads to a higher onset temperature for the decrease. Further annealing up to 250 °C leads to either the elimination of vacancy clusters smaller than the critical size, or the formation of few large vacancy clusters, as shown by the increase of τ_v , see Fig. 4.2.2. Both possibilities result in a decrease of I_v to <5%.
 - Above 250 °C, τ_v decreases to ~0.260 ns again and I_v re-increases. This might correlate to trapping of positrons by mono-vacancies, which are newly created or released from vacancy clusters at elevated temperatures.
- Al-Si alloys
 - In Al-0.5%Si alloy, the behaviour during isochronal annealing is consistent with previous work by [Dlu86, Kra85]. It was suggested that the continuous decrease of τ_v until 250 °C from 0.275 to 0.250 ns results from the formation and growth of incoherent Si nuclei by consuming vacancy clusters. The decrease of I_v to ~80 °C and the increase thereafter can be attributed to disappearance of the vacancy clusters and vacancies released from vacancy clusters, respectively. Some of these vacancies might be trapped in the incoherent Si nuclei, otherwise, they could be used for transporting further Si atoms to the nuclei [Dlu86].
 - Above 250 °C, τ_v increases slightly due to the transformation of small 3D clusters to plate-like Si precipitates. Beyond 275 °C, I_v decreases again for Al-0.5%Si alloy caused by coarsening [Dlu86, Kra85].
 - For Al-0.05%Si and Al-0.005%Si alloys, a similar annealing behavior to Al-0.005%Mg alloy is observed.

4.2.2 Doppler Broadening Annihilation Radiation

DBAR makes use of the positron sensitivity to the momentum distribution of the annihilation electrons. Thus, dissimilarities in electronic configurations, as given below:

- $[1s^2, 2s^2, 2p^6, 3s^2]$ **Mg**
- $[1s^2, 2s^2, 2p^6, 3s^2, 3p^1]$ **Al**
- $[1s^2, 2s^2, 2p^6, 3s^2, 3p^2]$ **Si**
- $[1s^2, 2s^2, 2p^6, 3s^2, 3p^6, 4s^1, 3d^{10}]$ **Cu**
- $[1s^2, 2s^2, 2p^6, 3s^2, 3p^6, 4s^2, 3d^{10}, 4p^2]$ **Ge**

have a notable impact on the specific elemental DBAR curves. Applying the HMA method and normalizing the spectra of well annealed pure Mg, Si, Cu and Ge by spectrum of Al yields so-called reference ratio curves [Aso96, Klo10, Liu11], see Fig. 4.2.10. Thus the unique shapes of these characteristic ratio curves reveal the electron momentum distribution of the corresponding material as probed by the positron wave function at the annihilation site.

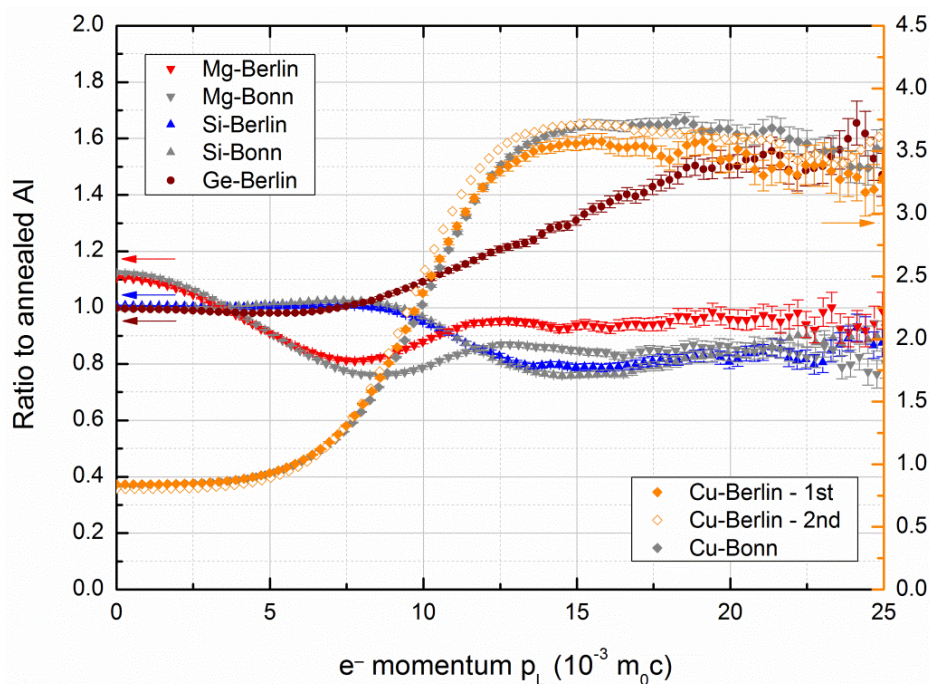


Figure 4.2.10. Reference ratio curves of various pure elements. Curves in gray color were measured previously by [Klo10], using the same materials. All sample curves can be reproduced except for Mg, which was probably affected by the easily formed oxidation layer.

With reference to Al, differences in electron momentum distribution between these elements are directly visible, for instance:

- Mg

Despite of the identical configuration of core-electrons [Ne], the less compact lattice structure of Mg compared to Al and Si results in an enhanced free-electron annihilation with positrons confined to the interstitial regions [Som02]. The ratio of Mg to Al starts at ~ 1.1 , continuously decreases and reaches its minimum at the position where the ratio of Si is maximal. Such a feature could be used for the interpretation of DBAR results of Al-Mg-Si alloys. In the high-momentum region, it becomes more and more critical to differentiate Mg from Si and Al due to many reasons: (1) Mg deviates from Si and Al only slightly; (2) statistics are poor in this region; (3) the signal-to-noise ratio is low ($< 1/1000$ for $p_L > 10 \times 10^{-3} m_0c$ [Klo10]) for the applied single Ge detector, which could be improved by at least two orders of magnitude by CDBS method employing two Ge detectors [Ala95, Aso96].

- Si

In the low-momentum region, the ratio curve of Si is approximately a constant at ~ 1 and shows an almost identical momentum distribution of the valence electrons in Si and Al. At $p_L \approx 8 \times 10^{-3} m_0c$, a peak can be observed (more clearly in alloys F and H as presented in Section 4.4.2), followed by a decrease of ratio to ~ 0.8 in the high-momentum region.

- Cu

Due to a larger atomic radius but smaller lattice constant of Cu than Al, and the lower probability of positron annihilation with free electrons compared to Al, a low ratio of Cu to Al in the low-momentum region is observed [Som02]. For high-momentum region at $p_L > 15 \times 10^{-3} m_0c$, the ratio is quite high (~ 3.5) compared to other elements (which are all below 1.6). This is mainly caused by the 3d-orbital electrons of Cu, i.e. for Al [Ne] $3s^2 3p^1$ while for Cu [Ar] $3d^{10} 4s^1$. Therefore such a fingerprint indicates the presence of Cu at the annihilation site.

Based on these features, the reference curves from pure Mg and Si as shown in Fig. 4.2.10 will be used to identify the local chemistry of the positron annihilation sites in Al-Mg, Al-Si and Al-Mg-Si alloys. However, Mg or Si samples containing mono-vacancies were not available for this work, because Mg is highly reactive with water and air especially at elevated temperatures, and oxidation during SHT and quenching led to a disturbing layer which seriously affects DBAR measurement. The formation energy of vacancies in Si was

measured to be approximately 3.85 to 4.0 eV [Bra08], about 7 times higher than in Al. This implies that the thermal creation of a number of vacancies in pure Si is not straightforward. Thus, these two cases will be excluded. Instead, V-Mg and V-Si complexes in as-quenched Al-Mg and Al-Si alloys will be used as an approximation.

After the reference curves for V-Al, Mg and Si have been made, the next step deals with ratio plots of V-Mg and V-Si in an Al matrix. Al-1%Mg has a comparable solute content compared to the investigated ternary Al-Mg-Si alloys, and it was shown in previous PALS measurements that the vacancy-type component of this alloy should be in the form of a V-Mg complex. While instead of the ratio plot of V-Si, the as-quenched Al-1%Si alloy is used as a substitute, because although on the one hand the existence of a 3V-Si complex was suspected for this alloy, on the other its solute content suggests a similar vacancy concentration (using Eq. (4.2.2)) and distribution as in the ternaries after quenching. In addition, dilute Al-Si alloys containing less Si might also be improper representatives since small vacancy clusters could be formed during the preparation (cooling and evacuation) lasting up to 5 min. Thus, by measuring an as-quenched Al-1%Mg or Al-1%Si alloys by DBAR, the ratio plots corresponding to V-Mg and V-Si can be approximated, see Fig. 4.2.11:

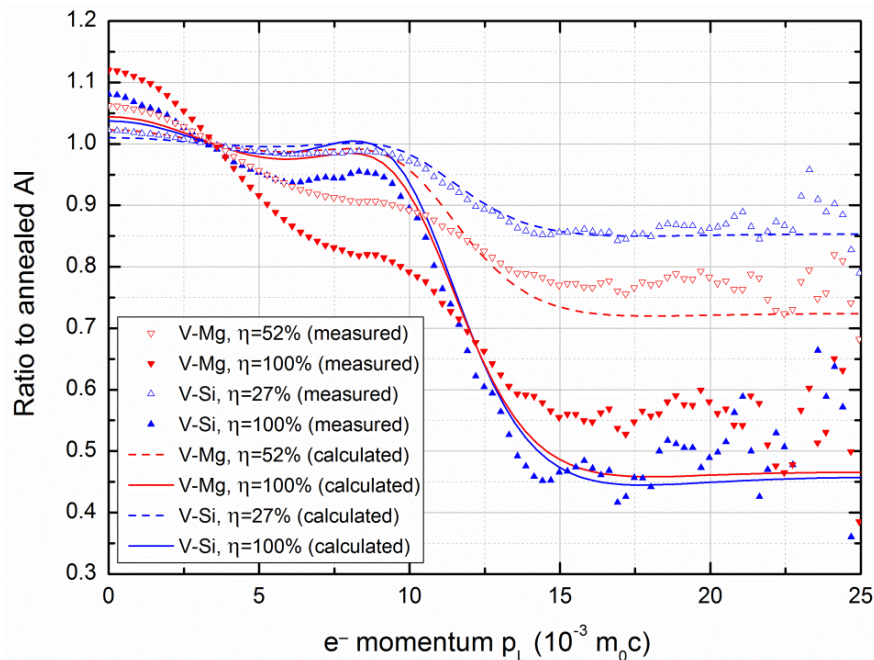


Figure 4.2.11. Ratio plots of as-quenched Al-1%Mg and Al-1%Si alloys. Calculated plots carried out by [Kor10] are also given for comparison. All ratio plots are corrected according to their corresponding annihilation fractions using Eq. (4.1.12). Errors are not given in order to show all plots in a clear manner, same for the DBAR figures in Section 4.4.2.

The annihilation fractions for Al-1%Mg and Al-1%Si were calculated from the decomposed PALS annihilation parameters using STM (η equals 52% for Al-1%Mg and 27% for Al-1%Si), based on which the ratio plots of both alloys were corrected using Eq. (4.1.12) for 100% trapping by defects. Except for the changes in amplitude, V-Mg differs from V-Si in a similar manner as the ratio plots of pure Mg and Si from each other. Owing to the practically identical core electron configurations of Mg, Al and Si, replacing one Al atom adjacent to a vacancy with Mg or Si will not result in a conspicuous ratio difference in the momentum region $p_L > 15 \times 10^{-3} m_0c$. Nevertheless for $p_L < 15 \times 10^{-3} m_0c$, except for the slightly higher peak at $p_L = 8 \times 10^{-3} m_0c$ of Al-1%Si alloy which might correlate to Si atoms attached to small vacancy clusters (~ 3 vacancies), more similarities can be seen between the ratio curves of V-Al and V-Si, see Fig. 4.1.4. This comparability was also found by a theoretical calculation employing the atomic superposition method [Mel06]. Only V-Mg reveals a different distribution due to the lack of the outermost electrons from the 3p orbital.

As for the case of a mono-vacancy in pure Al as shown in Fig. 4.1.4, DOPPLER calculations with different annihilation fractions were conducted for the vacancy-solute complex in binary Al-Mg and Al-Si systems. On the one hand, the calculated V-Si ratio curve agrees quite well with experimental value in the high-momentum region, but on the other hand certain deviations can be seen for the region $p_L < 15 \times 10^{-3} m_0c$. The agreement between the calculated V-Mg ratio curve to experiments in the high-momentum region is not satisfactory, but for momentum region $p_L < 15 \times 10^{-3} m_0c$ the deviation is even worse. For this inconsistency, one has to consider the quality of the Doppler calculation for the bulk materials, where Si is the element that matches best, Al is not that excellent and Mg is the worst (not shown in the ratio plots of reference curves). Therefore, the imperfect calculation is mainly a result of problems originating from Al, which is the reference in all ratio curves and limits the accuracy of all the calculations.

Moreover, it should be noted that any decoration of vacancies by alloying element such as Si or Mg atoms could yields a “real” peak between $p_L = 7 \times 10^{-3} - 10 \times 10^{-3} m_0c$, but could be disturbed by the confinement of positrons, since this structure is partially superposed on the disturbing confinement peak which roughly located at the same position, as already mentioned in Section 4.1.2. Thus, makes the interpretation of the DBAR ratio curve difficult.

4.3 From Binary Al-Mg and Al-Si to Ternary Al-Mg-Si Alloys

The interactions between vacancies and solute atoms in quenched Al-Mg and Al-Si binary alloys during NA were studied. Based on the present results, most of the microstructural changes are related to the formation of vacancy clusters of certain sizes, while solute clustering process could not be experimentally observed or deduced. However, it is known that in industrial Al-Mg-Si alloys, solute clusters are formed during NA, which has a key influence on the final mechanical properties of these alloys after “paint baking”. Therefore, it is essential to study Al-Mg and Al-Si alloys containing small amounts of the third alloying elements of Si or Mg to clarify the interactions between Mg, Si and vacancies. Results from PALS, DSC and resistivity experiments on “ternary” Al-0.5%Mg-0.05%Si and Al-0.05%Mg-0.5%Si alloys will be presented and compared to the binaries in this section.

4.3.1 Positron Annihilation Lifetime Spectroscopy

4.3.1.1 Adding 0.05% Si (Mg) to Al-0.5%Mg (Si) Alloy

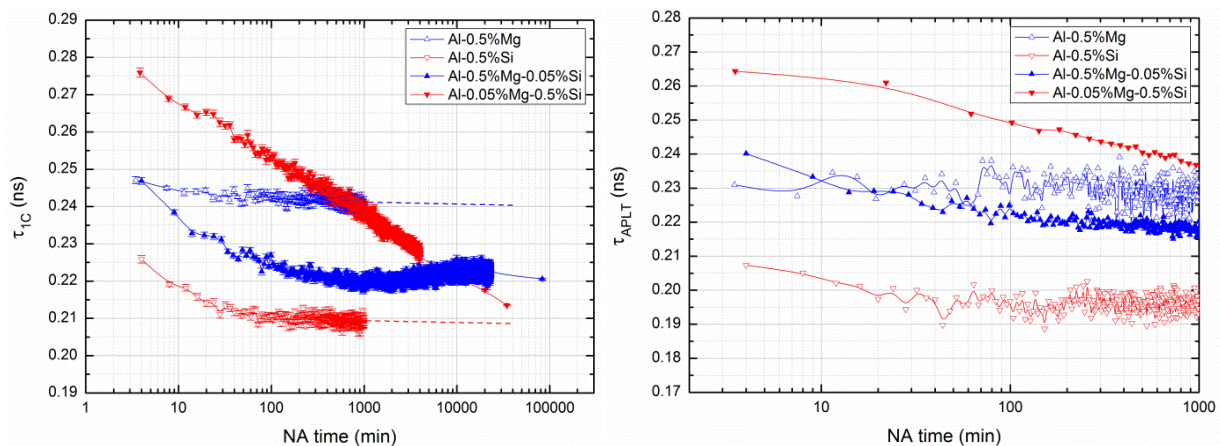


Figure 4.3.1. (L) Evolution of 1-component PLT τ_{1C} during NA, dashed line: extrapolation of data; (R) APLT evolution during NA, as calculated by 2-component analysis.

- 1-component analysis of Al-0.5%Mg and Al-0.5%Mg -0.05%Si alloys

In the Al-0.5%Mg alloy, τ_{1C} evolves slowly during NA. Although the initial PLT in an Al-0.5%Mg-0.05%Si alloy is similar to the one in Al-0.5%Mg alloy, the changes during NA are markedly different after addition of 0.05% Si. Distinct stages II, III and IV (PLT decrease, increase and re-decrease) were observed as the previously investigated alloys F and H [Ban11] (see Section 4.4). The transition times between stage II to III (~1000 min) and stage III to IV (~10000 min) are much longer than the ones of alloys F and H.

- 1-component analysis of Al-0.5%Si and Al-0.05%Mg-0.5%Si alloys

τ_{1C} decreases during the first 100 min of NA in Al-0.5%Si alloy. By adding 0.05% Mg, the NA kinetics of Al-0.5%Si alloy is completely changed. The initial PLT of 0.276 ns in Al-0.05%Mg-0.5%Si alloy is much higher than the PLT of 0.226 ns in Al-0.5%Si alloy. More importantly a monotonic decrease of PLT (almost linear on the logarithmic scale) for more than $\sim 5 \times 10^4$ min was observed after adding 0.05% Mg to Al-0.5%Si. This agrees with the observation from [Ban11], where a single crystalline Al-0.08%Mg-0.4%Si alloy was measured. But the cause of such a PLT evolution, particularly during PALS stage II, can hardly be figured out using 1-component analysis only.

It was found that fitting the PLT spectra of the two “ternary” alloys with low Mg or Si content with only one PLT component is not satisfactory since the fit variance is large. It might be an indication of additional positron trapping sites related to solute clusters (τ_s) or bulk (τ_f) besides vacancy-type defects (τ_v). To verify this point, a further analysis employing two PLT components was carried out for PALS stage II.

- 2-component analysis of Al-0.5%Mg and Al-0.5%Mg-0.05%Si alloys

Decomposed PLT components in binary Al-0.5%Mg alloy shows a very slow formation of small vacancy clusters, as shown in Fig. 4.3.2 (L) and in Section 4.2. The main positron traps ($\sim 80\%$) are V-Mg complexes which are small in size but high in number density, see Section 4.2.1.2. The bulk contribution is small ($\sim 20\%$), and the related PLT is always below the one in bulk Al (0.165 ns), as the so called “reduced bulk lifetime”.

But decomposition of the PLT spectra of Al-0.5%Mg-0.05%Si alloy is difficult. This is due to: (1) τ_{f+s} (as the weighted sum of τ_f and τ_s , see Section 4.4.1.4 for details) and τ_v are close to each other; (2) limited time resolution of the spectrometer; (3) low statistics in the FDA mode. In order to minimize uncertainties from fitting, the vacancy-related PLT τ_v was fixed to 0.255 ns (initial PLT τ_v in Al-0.005%Mg alloy) as the PLT of V-Mg complex. Such complexes are formed with a much higher probability than V-Si due to the much higher Mg content in this alloy. As shown in Fig. 4.3.2 (L), the PLT τ_{f+s} increases from 0.120 to 0.195 ns (between the reduced bulk lifetime in Al and the PLT in mono-vacancy in Al), while I_{f+s} starts from $\sim 10\%$ and approaches 60% after 1000 min of NA.

- 2-component analysis of Al-0.5%Si and Al-0.05%Mg-0.5%Si alloys

For Al-0.05%Mg-0.5%Si alloy, constraint-free fitting was possible and data files were summed up for each 40 min in order to improve the statistics, as shown in Fig. 4.3.2 (R). The initial PLT of vacancy-type defects equals ~ 0.280 ns (small vacancy clusters) and decreases slightly during NA, whereas τ_{f+s} increases from 0.105 to 0.190 ns after 1000 min of NA.

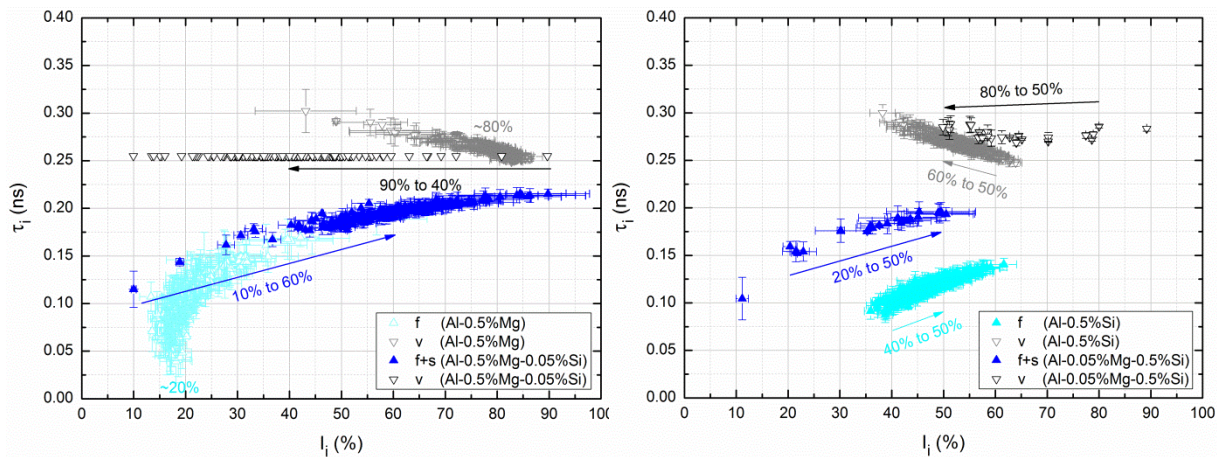


Figure 4.3.2. 1000 min evolution of decomposed PLT components of (L) Al-0.5%Mg and Al-0.5%Mg-0.05%Si (with fixed τ_v) and (R) Al-0.5%Si and Al-0.05%Mg-0.5%Si (annihilation parameters are all free) alloys. The trend of the intensity evolutions are indicated by arrows and percentages rather than giving the wide distribution of I_i caused by data scattering. The letter “f” stands for free positron annihilation in bulk Al, “v” relates to vacancy-type positron traps. Due to limited time resolution of the spectrometer, annihilations in bulk and vacancy-free solute clusters will be treated as one component, as indicated by “f+s”. Data for binary Al-0.5%Mg and Al-0.5%Si alloys are the same as in Fig. 4.2.4, but not averaged.

During the NA of Al-0.5%Mg and Al-0.5%Si alloys after quenching, the formation of small vacancy clusters leads to a decrease in concentration of vacancy-type defects. Thus, the increasing positron annihilations in the bulk cause a slight decrease of τ_{APLT} , as shown by the decomposed PLT components of these alloys, see Section 4.2.1.2.

However, the increase in τ_{f+s} and I_{f+s} during stage II in Al-0.5%Mg-0.05%Si alloy probably indicates the formation of coherent Mg-Si co-clusters (enriched in Mg), totally different from the ageing characteristics observed in binary Al-Mg or Al-Si alloys. Regarding the smaller re-increase of τ_{1C} during stage III (dominated by Mg [Ban11, Lay12]) compared to alloys F and H, one has to consider the repulsive Mg-Mg and Si-Si but attractive Mg-Si bindings [Hir07]. For an alloy containing 10 times more Mg than Si, the Mg aggregation to Mg-Si clusters (with or without a vacancy) in stage III cannot benefit from the excessive Mg content,

since if most Si atoms are consumed after forming solute clusters during stage II and are then decorated by several Mg atoms at their NN positions, further growth of those previously formed Mg-Si co-clusters due to Mg aggregation will become increasingly difficult due to the energetic repulsive Mg-Mg binding energy. The ageing kinetics of Al-0.5%Mg-0.05%Si alloy is considerably slower compared to the one of alloys F and H, which is probably caused by the very low Si content of this alloy, since Si is expected to accelerate the ageing kinetics.

In Al-0.05%Mg-0.5%Si alloy, 0.05% of Mg addition is a small amount, however it is still much higher than the vacancy concentration. Thus, Mg-Si co-clusters with a shorter PLT than in vacancy-type defects could still be formed and compete with them in trapping positrons, as indicated by its corresponding intensity I_{F+S} which increases from ~20% to ~50%, see dark blue arrow in Fig. 4.3.2 (R). Further growth of such clusters is unlikely since most Mg atoms have been decorated by Si atoms during stage II. As a result, no Mg-dominated stage III can be observed. Combining this suspicion with plausible vacancy cluster formation as well as certain bulk contribution as in Al-0.5%Si alloy, the continuous decrease of τ_{1C} in Al-0.05%Mg-0.5%Si alloy during NA can be explained.

4.3.1.2 Adding 0.1% or 0.5% Si (Mg) to Al-0.5%Mg (Si) Alloy

With further increasing content of the third alloying elements, the NA characteristics of various Al-Mg-Si alloys were measured and analyzed (1-component), as shown in Fig. 4.3.3:

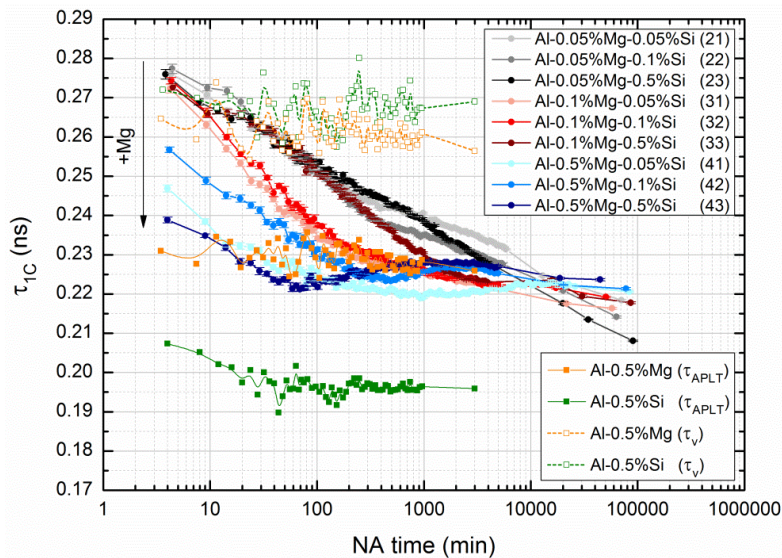


Figure 4.3.3. Overview of τ_{1C} evolution during NA of various Al-Mg-Si alloys (sphere symbols). The APLT and τ_v of binary Al-0.5%Mg and Al-0.5%Si alloys are also shown (square symbols). The initial PLT drops (black arrow) with increasing Mg content, this agrees with [Ban11].

Fig. 4.3.3 offers an overview of the different NA kinetics of various Al-Mg-Si alloys, in order to analyze the ageing characteristic of these alloys more clearly, the results from Fig. 4.3.3 are classified into two groups according to the solute concentrations as follows:

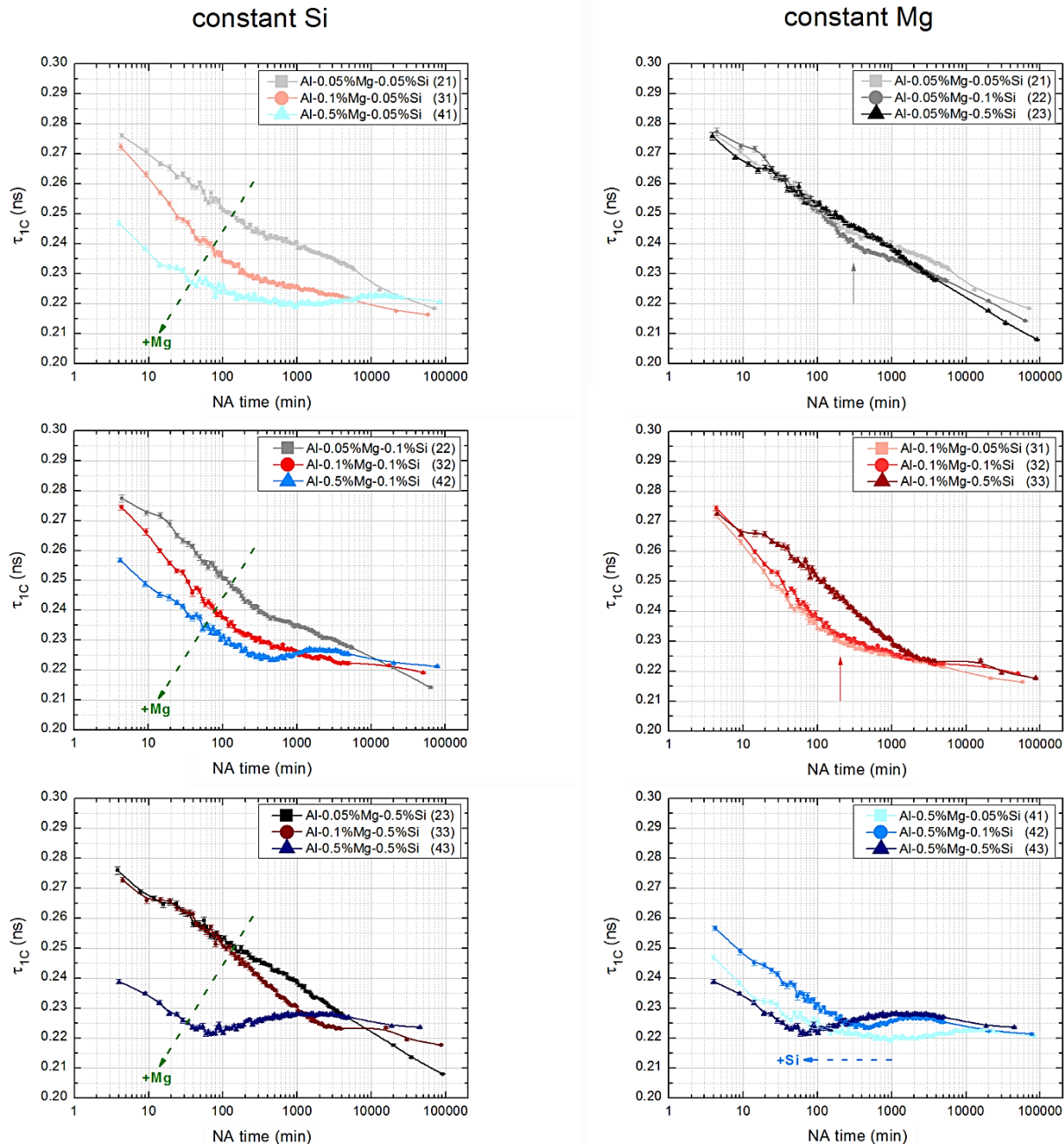


Figure 4.3.4. τ_{1C} evolution of Al-Mg-Si alloys during NA. Group with constant Si content is shown on the left hand side and with equal Mg content on the right hand side. Each measurement occurs twice, on the left and right sides. Numbers in the parentheses denote the alloy designations as listed in Table 3.1.1. The gray and red arrows (solid line) are used to roughly indicate the transition times between the suspected stages in alloys 21, 22 and 31, 32.

- Alloys containing 0.05% Mg: PLT decreases almost linearly throughout NA. Particularly alloy 23 containing 0.5% Si content shows very similar PLT evolution as the one previously observed in a single crystalline Al-0.08%Mg-0.4%Si alloy [Ban11]. In contrast, alloys with lower Si content such as alloys 21 and 22, the slope of the linear decrease of PLT was interrupted at ~ 300 min of NA. Whether this is correlated to the increase of Mg/Si ratio compared to alloy 23 or not could not be verified so far.
- Alloys containing 0.1% Mg: PLT decreases for a certain NA time, followed by a stage of lower slope, after which a slightly decrease of PLT was found on the logarithmic time-scale. Again alloy 33 with the highest Si content shows a slightly different ageing kinetics as compared to alloys 31 and 32 during the first ~ 3000 min of NA. However, similar PLT evolutions were observed in these alloys in the last stage, which might be related to stage IV [Ban11]. Moreover, transitions found in alloys 21 and 22 at ~ 300 min were also visible for alloys 31 and 32 at ~ 200 min, see gray and red arrows in Fig. 4.3.4, probably due to their similar solute contents.
- Alloys containing 0.5% Mg: on the premise that at least 0.4% ($> 0.1\%$) Mg atoms are available for solute clustering, 3 distinct stages (II, III and IV) exhibiting similar tendencies as in alloys F and H finally become visible [Ban11], see Section 4.4. It is shown that both Si (alloys 41, 42, 43) and Mg (alloys 23, 33, 43) can accelerate the initial ageing kinetics, and both solutes are required for the formation of solute clusters during stages II and III, agrees with [Cha11]. As an example, the acceleration of ageing kinetics and the increase of amplitude of stage III by increasing Si content are shown in Fig. 4.3.5:

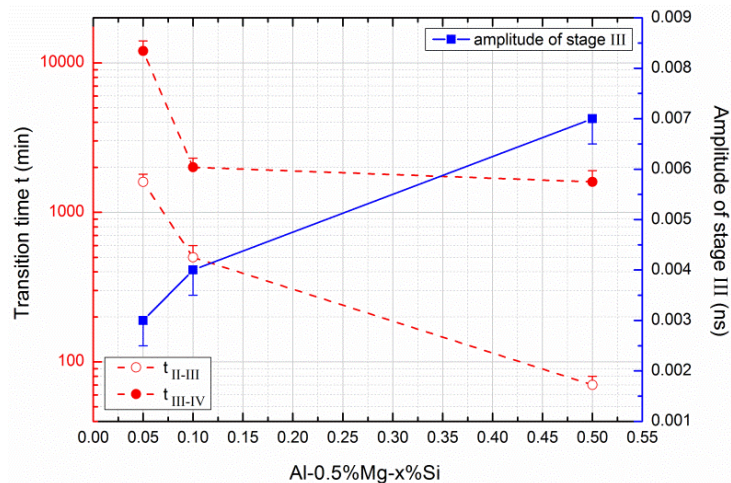


Figure 4.3.5. Dependence of transition times between stage II to III and III to IV (left y axis) and the increase of PLT during stage III (right y axis) on Si content.

4.3.2 Differential Scanning Calorimetry

4.3.2.1 Adding 0.05% Si (Mg) to Al-0.5%Mg (Si) Alloy

The remarkable interactions between Mg, Si and vacancy could also be verified by DSC:

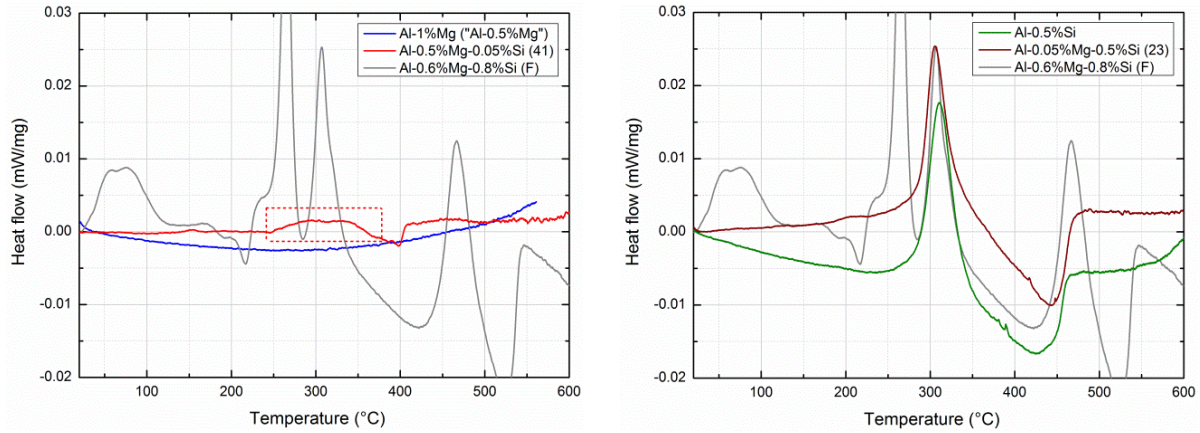


Figure 4.3.6. Heat flow curves (10 K/min) of (L) Al-0.5%Mg-0.05%Si and (R) Al-0.05%Mg-0.5%Si alloys. Other results on Al-1%Mg (this alloy was used as a substitute of Al-0.5%Mg alloy), Al-0.5%Si and Al-0.6%Mg-0.8%Si (F) alloys are also shown for comparison.

There is no solute cluster signal in both figures either because DSC is insensitive or because there are no clusters. However, adding 0.05% Si to Al-0.5%Mg leads to formation of β'' , β' (overlapping peaks marked by the red square) and β peaks as in alloy F in Fig. 4.3.6 (L). In contrast, 0.05% Mg addition to Al-0.5%Si alloy barely causes visible changes in the DSC signal, in which only the peak of Si precipitation is observed (the upwards shift of the DSC curve might be due to base line subtraction rather than a physical effect), see Fig. 4.3.6 (R).

4.3.2.2 Adding 0.1% or 0.5% Si (Mg) to Al-0.5%Mg (Si) Alloy

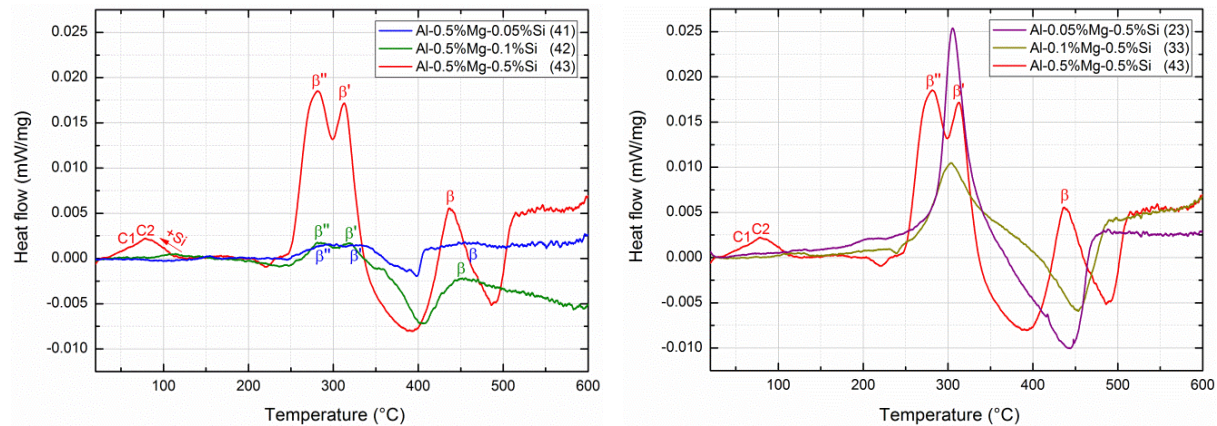


Figure 4.3.7. Heat flow curves (10 K/min) of ternary Al-Mg-Si alloys with constant (L) Mg and (R) Si contents, but different amounts of the third alloying elements. The curves of alloy 41 and 23 are the same as in Fig. 4.3.6.

With increasing Si content, clustering peaks C1 and C2 gradually appeared in alloys 42 (weak signal) and 43. At elevated temperatures (> 250 °C), precipitation peaks such as β'' , β' and β are all visible, see Fig. 4.3.7 (L). Clustering peaks can hardly be observed in alloy 33, obviously due to its too low Mg content. Actually to observe C1 and C2 in alloy H is also difficult, see Section 4.4.3. For alloy 33 which has only 0.1% Mg, the clustering signals are even weaker. Above 250 °C, the signal related to precipitation of Si is weaker in alloy 33 than 23 (whether this is correlated to the solute cluster formation cannot be verified so far), and β'' , β' peaks can still not be observed in this alloy, see Fig. 4.3.7 (R).

4.3.3 Electrical Resistivity

The ageing kinetics of Al-Mg-Si alloys was also investigated by resistivity experiments, see Fig. 4.3.8:

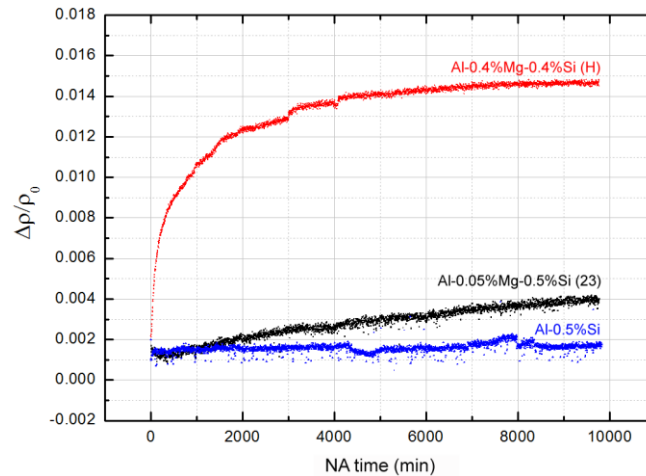


Figure 4.3.8. Resistivity evolution of Al-0.5%Si, Al-0.05%Mg-0.5%Si and Al-0.4%Mg-0.4%Si alloys during NA. Measurements were carried out by J. Kühn and M. Wüstenhagen.

For Mg-free binary Al-0.5%Si alloy which has a sufficient Si content, a constant resistivity was observed. In contrast, for alloy 23 (no PALS stage III or IV is observed, see Section 4.3.1) containing 0.05% Mg in addition to 0.5%Si, the increase in resistivity is slower as compared to alloy H. The fastest ageing kinetic is found in alloy H, which contains 0.4% Mg. The anomalous increase of resistivity is due to solute clustering [Sey09]. It is suspected that the fast increase of $\Delta\rho/\rho_0$ at the beginning of NA is associated with PALS stage II (Si-dominated) and the subsequent slow increase could be correlated to stage III (Mg-dominated), see red curve in Fig. 4.3.8. By comparing all three results, the notable effect of Mg during the formation and growth of solute clusters in Al-Mg-Si alloys can thus be confirmed.

4.4 Ternary Al-Mg-Si Alloys

It is known that age-hardenable Al-Mg-Si alloys can be strengthened through the formation of solute clusters during NA at RT and precipitates upon AA. The clusters formed during NA can positively or negatively influence subsequent AA which is of great practical relevance and therefore motivates us to study NA in more detail.

Atom probe tomography, although useful for analyzing small objects such as solute clusters, is currently too slow to resolve clustering kinetics and also a reliable detection of clusters is challenging. Integral techniques such as DSC, electrical resistivity and hardness have demonstrated that clustering in Al-Mg-Si alloys is a complex multi-stage process [Ban10]. In particular, by using positron annihilation lifetime spectroscopy, it could be shown that the evolution of PLT τ_{IC} in Al-Mg-Si alloys involves at least 4 stages, i.e. a stage I of nearly constant PLT, a stage II of decrease, a stage III of increase and, finally, another decrease in stage IV [Ban11].

In order to further clarify the underlying microscopic processes behind these stages, Al-Mg-Si alloys F and H from various states of NA were characterised at temperatures ranging from -180 to 20 °C by PALS method, utilizing its unique sensitivity to electron density differences in various atomic defects. Besides 1-component analysis of the PLT spectra, 2-component (fixed τ_v) and 3-component analysis (free fitting) were also carried out. The results are shown in Section 4.4.1.1 to Section 4.4.1.7.

In order to verify the PALS results obtained from multi-component analysis, two types of 3-state trapping models were employed. The validation of the sophisticated temperature and time dependence of the decomposed lifetime components are given in Section 4.4.1.8 to Section 4.4.1.9.

In addition, the chemical environment of the annihilation site was further identified by DBAR and CDBS method, as shown in Section 4.4.2.1 to Section 4.4.2.4.

Finally, the different stages observed from the positron perspective will be compared to the observations from DSC, electrical resistivity and hardness measurements, see Section 4.4.3 to Section 4.4.7.

4.4.1 Positron Annihilation Lifetime Spectroscopy

4.4.1.1 τ_{1C} Evolution in Al-Mg-Si Alloys at Room Temperature (FDA)

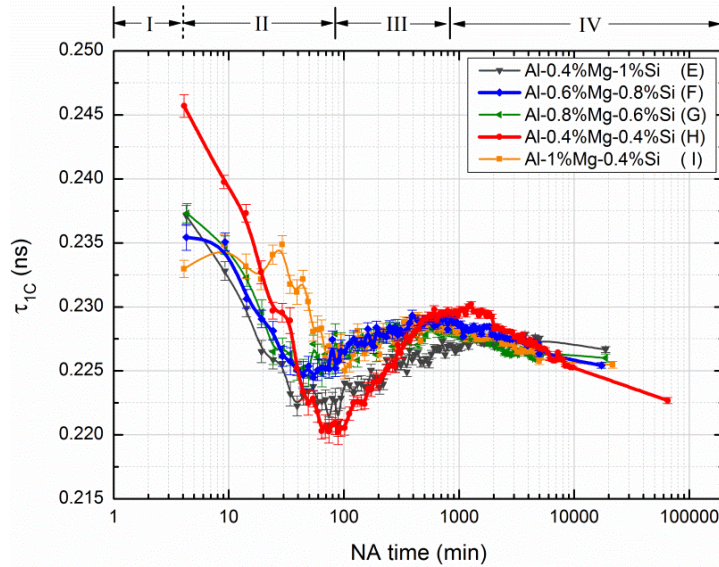


Figure 4.4.1. τ_{1C} evolution of alloys E, F, G, H and I (IWQ). During NA four observed stages are marked I to IV. The transition time between stages I to II (dashed line above the figure) depends on solute concentration and can be as high as 30 min.

The observations shown in Fig. 4.4.1 agree with [Ban11]: (1) constant (or slightly increasing) stage I: can be easily observed for alloys with high Mg content, e.g. alloys F and I. The initial PLTs are dominated by the Mg concentration, i.e. high Mg content results in lower initial PLT. This stage will be discussed in Section 4.4.1.2 and Section 4.4.1.6; (2) decrease in stage II: formation of Si-Mg co-clusters with a low PLT, therefore, τ_{1C} continuously drops. Si could be a dominating factor due to its high jump frequency; (3) re-increase in stage III: Si will be gradually consumed during clustering, thus the slow Mg aggregation into previously formed clusters could increase its PLT by a certain degree; (4) final decrease in stage IV: might be related to coarsening of clusters or ordering phenomena inside the clusters [Ban11].

The main emphasis was placed on investigating the observed stages I to III of alloys F and H in which solute clusters are formed that are suspected to be related to the negative and positive effects on subsequent AA. However, only limited information can be obtained due to fast NA kinetics of the Al-Mg-Si alloys and insufficient statistics when measuring in the FDA mode. Thus, the samples should be prepared and measured at low enough temperatures to improve the statistics to a level sufficient for multi-component analysis.

4.4.1.2 τ_{1C} Evolution in Alloys F and H at Low Temperatures (FDA)

Quenching the samples on a cold Cu block can largely suppress the disturbing ageing effects prior to the measurement, see Section 3.1.2.1. Ageing curves of alloys F and H depend strongly on the applied ageing temperature, see Fig. 4.4.2:

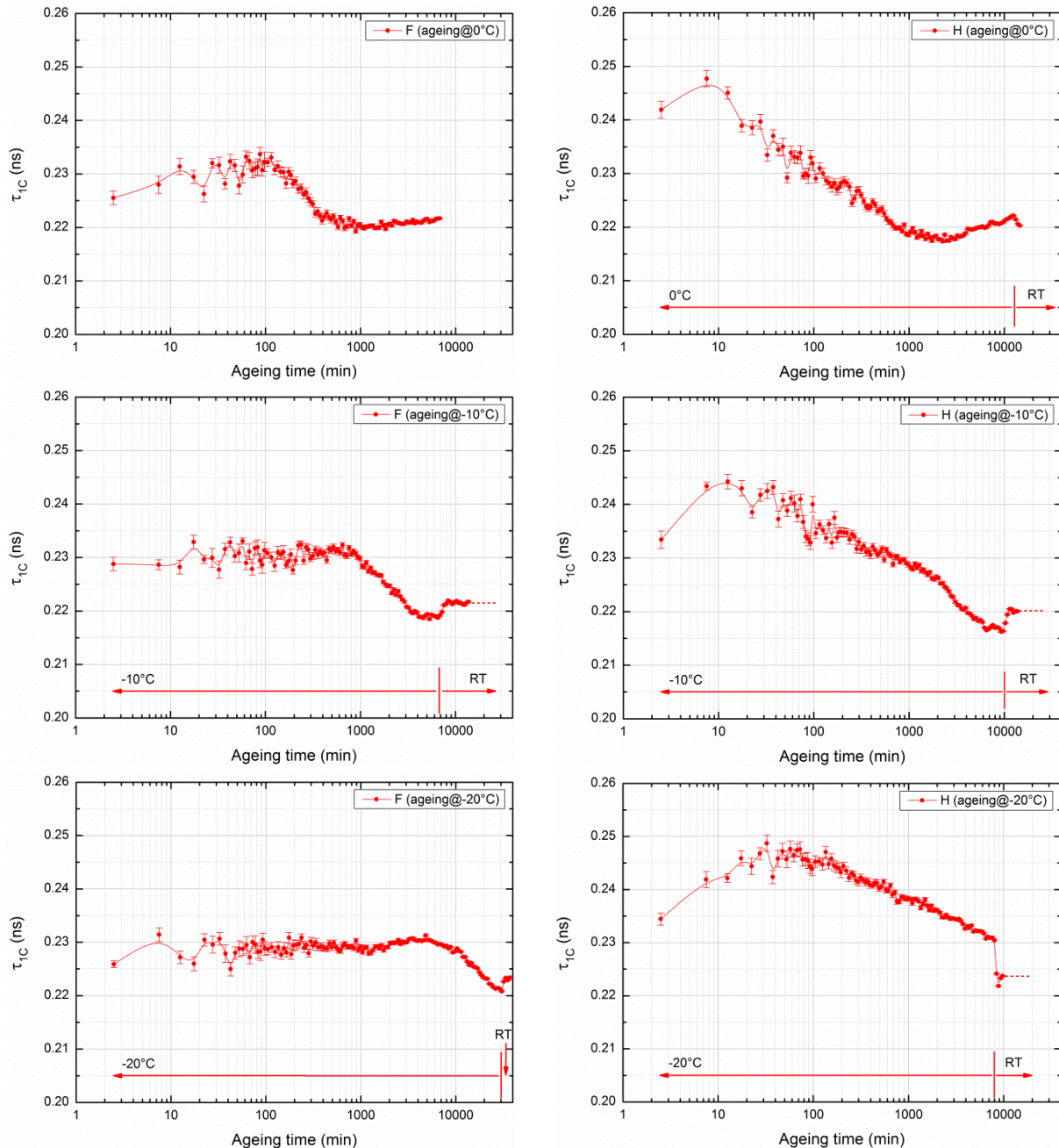


Figure 4.4.2. τ_{1C} evolution of (L) alloy F and (R) alloy H at LTs. The samples were quenched on a cold Cu block and kept at a temperature $T < 100$ °C throughout handling and transfer to the spectrometer. There, the temperature was increased to the specified level before the measurements. After a certain ageing time, the ageing temperature was further increased to RT to accelerate the kinetics for some of the samples. Dashed lines are extrapolations of the PLT evolution to long NA times.

As the ageing kinetics of an Al-Mg-Si alloy is thermally activated, slower ageing curves are observed when temperature is lowered, as shown by Fig. 4.4.2. Besides the similar tendencies shown by these measurements, the characteristics of the alloy aged at low temperature varies from the one observed at RT to some extent:

- Stage I: initial PLTs for alloy H are always higher than for alloy F at the same temperature, which might be the indication of a relatively higher contribution of vacancy-type defects to τ_{IC} . 2-component analysis is required to verify this point, see Section 4.4.1.6. Benefitting from an improved quenching rate and low measurement temperatures, stage I previously observed for alloy F only [Ban11] was also found for alloy H, with a much shorter duration, and τ_{IC} actually increases during this stage rather than having a constant value. So far we are lacking in the knowledge to interpret this stage physically, but the 2-component analysis in Section 4.4.1.6 will offer a plausible explanation.
- Stage II: it is believed that solute cluster formation during stage II is dominated by Si [Ban11]. At LTs such as at -20 °C, the jump frequency of a vacancy attached to Si is greatly reduced from $\sim 18200 \text{ s}^{-1}$ at 20 °C to 700 s^{-1} , as shown by the retarded τ_{IC} evolution in Fig. 4.4.2. Whether the solute clusters formed during and after this stage are different to the corresponding ones formed at RT cannot be verified so far.
- Stages III and IV: at LTs, the amplitude of the PLT re-increase during stage III is smaller than the one at RT, and the decrease in stage IV can hardly be seen even if the samples are heated up to RT afterwards, see alloy F aged at -10 °C as an example. This tendency may be related to the atomic jump frequencies of the vacancies attached to Si or Mg atoms during cooling. The degree of retardation for a vacancy attached to Mg is different to that of Si, e.g. f_{V-Mg} will be reduced by a factor of ~ 55 when temperature decreases from 20 to -20 °C, much more than for Si (~ 25), see Fig. 4.2.7. If this calculation is applicable to the real system, the solute clusters formed during stage I, II at LTs could be different to the ones formed at RT concerning size, number density and composition, which might affect the subsequent ageing in a direct or indirect manner.

Combining the results from LT PALS experiments and the one from a previous study [Ban11], the activation energies could be further determined making use of the temperature-dependent transition times between different PALS stages.

- Activation energy analysis

During the ageing of an Al-Mg-Si alloy, the physical properties such as APLT, resistivity, hardness etc. vary as a function of temperature T and time t , indicating certain reactions. Applying the Johnson-Mehl-Avrami (JMA) equation [Avr39], the degree of transformation D for heterogeneous nucleation is defined as [Mit92]:

$$D = 1 - \exp(-\beta^n), \quad (4.4.1)$$

where β is the state variable, the JMA exponent n indicates the reaction order (for heterogeneous reaction $n=1, 2$ and 3 for one, two and three dimensional nucleation growth, respectively), for isothermal annealing:

$$\beta = k(T)t, \quad (4.4.2)$$

where $k(T)$ is the temperature-dependent reaction rate and can be described by the classical Arrhenius equation:

$$k(T) = k_0 \exp\left(-\frac{E_a}{RT}\right), \quad (4.4.3)$$

where k_0 , E_a and R represent the pre-factor, activation energy of a certain reaction and the gas constant accordingly. Combining all the equations above and taking twice the natural logarithm of the first equation yields:

$$\ln(t^{-1}) = \left[\ln k_0 - \frac{1}{n} \ln[\ln(1-D)^{-1}] \right] - \frac{E_a}{RT}. \quad (4.4.4)$$

At different temperatures, the degree of transformation D should be constant at a certain stage of ageing (e.g. transition times at τ_{1C} minimum and maximum). Thus, the plot of $\ln(t^{-1})$ versus $(RT)^{-1}$ yields a line with a slope which represents the activation energy E_a . Other parameters such as k_0 , n , and D have not be known necessarily since they only contribute to the constant term. Based on the transition time $t_{II \rightarrow III}$ and $t_{III \rightarrow IV}$ at various temperatures (10 to 37 °C), the activation energies for stage II to III (τ_{1C} minimum) and stage III to IV (τ_{1C} maximum) were determined for alloys F and H by [Ban11]:

$$E_{a(F) II \rightarrow III} = 74 \pm 5 \text{ kJ/mol}, \quad E_{a(H) II \rightarrow III} = 87 \pm 5 \text{ kJ/mol}.$$

$$E_{a(F) III \rightarrow IV} = 94 \pm 7 \text{ kJ/mol}, \quad E_{a(H) III \rightarrow IV} = 96 \pm 4 \text{ kJ/mol}.$$

Applying the same methodology, ageing of alloys F and H isothermally at LTs (-30 to 0 °C) enables a more precise determination of the activation energies for stage I to II and II to III. The applied transition times are roughly marked with the gray spheres shown in Fig. 4.4.3. Extremely long ageing times are required for stage III to IV at LTs in both alloys. Therefore these will be excluded in the discussion.

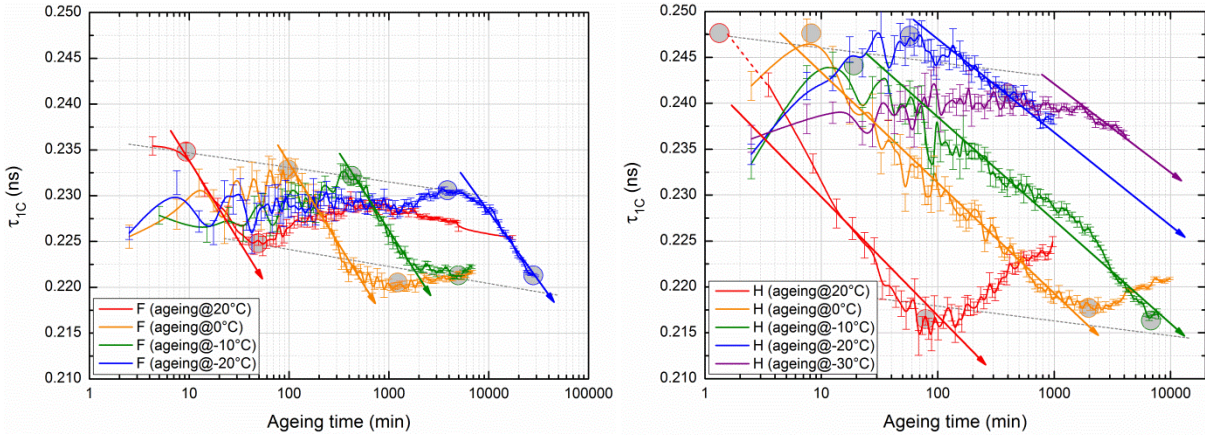


Figure 4.4.3. τ_{IC} evolution of (L) alloy F and (R) alloy H at different ageing temperatures ranging from -30 to 20 °C (CuQ + IWQ). Arrows are given to guide the eye.

Combining these values with the previous ones from [Ban11], Fig. 4.4.4 can be plotted, as shown below:

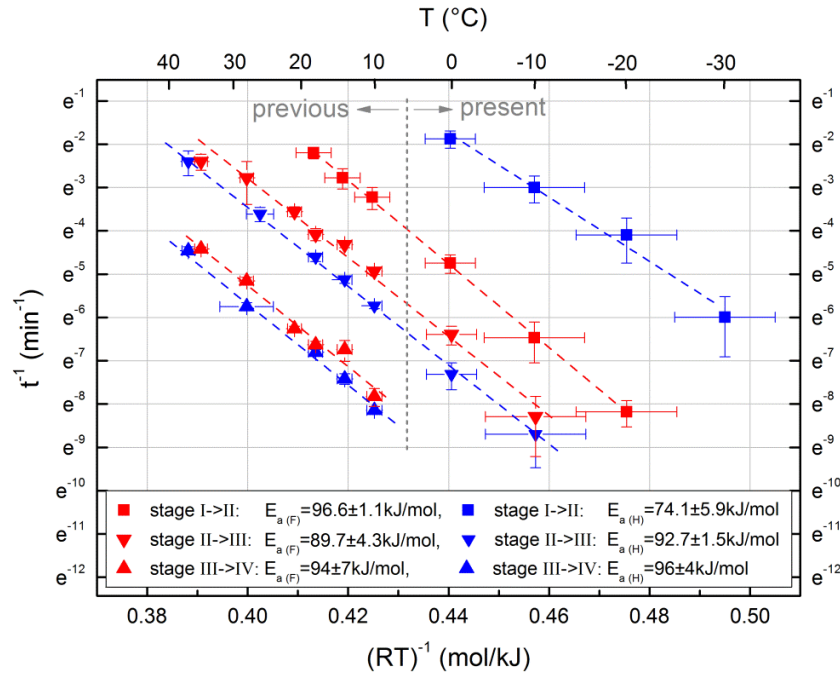


Figure 4.4.4. Activation energy analysis for alloys F and H. Straight lines are linear fits of the transition times between stage I to II, II to III and III to IV (the latter two are accordingly related to the τ_{IC} minimum and maximum) at different ageing temperatures (-30 to 37 °C).

Activation energies determined from isothermal ageing experiments on alloys F and H (-10 to 37 °C) are slightly higher than the previous results (10 to 37 °C):

$$E_{a' (F) \text{ II} \rightarrow \text{III}} = 89.7 \pm 4.3 \text{ kJ/mol}, \quad E_{a' (H) \text{ II} \rightarrow \text{III}} = 92.7 \pm 1.5 \text{ kJ/mol}.$$

The tendency found before that $E_{a (F) \text{ II} \rightarrow \text{III}} < E_{a (H) \text{ II} \rightarrow \text{III}}$ and $E_{a (F, H) \text{ II} \rightarrow \text{III}} < E_{a (F, H) \text{ III} \rightarrow \text{IV}}$ still holds in this study. The present results are higher than the highest literature values determined by DSC which cover a wide range from 33 [Dut91] to 79 kJ/mol [Doa00, Lia12]. It was speculated that the interaction between vacancies, solute atoms as well as between vacancies and solutes could be responsible for the discrepancies [Ban11]. In addition, inaccuracies concerning the experiments and the determination of the data points should also be noted (especially the ageing kinetics is retarded at LTs, which would lead to large errors in the transition time determination).

Even higher activation energies were found recently in another PALS experiment on an Al-0.46%Mg-1.05%Si-0.14%Fe alloy (wt.%) by [Lay12], which might be more than just a coincidence. A phenomenological model was developed there for stages II and III, in order to describe the diffusion of vacancies to sinks and the growth of solute clusters which decreases and increases the APLT accordingly. Effective activation energies of 111 and 156 kJ/mol were obtained for the decay of the vacancy-related kinetic coefficient and solute clustering coefficient, respectively. It was suggested that these high values could be correlated to the binding between vacancies and solute atoms. Moreover, PAS methods are very sensitive to vacancy-type defects, e.g. the change of APLT in alloy H is much larger than in alloy F, although the total solute content is much smaller in alloy H than in alloy F. This is probably caused by the higher vacancy defect contributions. However, the clustering peak of alloy H is much smaller than of alloy F as observed by DSC, again this might be correlated to the sensitivity of DSC to solute clustering. Thus, the higher E_a deduced from 1-component PALS analysis certainly represents a weighted mean of individual activation energies, especially the one related to vacancies, while for other techniques such as DSC or resistivity, more information on solute clustering will be recorded and used for E_a determination.

Finally, $E_{a (F) \text{ I} \rightarrow \text{II}}$ and $E_{a (H) \text{ I} \rightarrow \text{II}}$ equal 96.6 ± 1.1 and 74.1 ± 5.9 kJ/mol, respectively. The exact physical processes related to these energies are still unknown.

4.4.1.3 Temperature and Time Dependence of τ_{1C} in Alloy H (NDA + FDA)

The course of the 1-component PLT of alloy H during NA is known from previous studies and shows distinct stages, see Fig. 4.4.5, namely an “initial” stage II, where the PLT decreases from 0.245 to 0.215 ns within ~ 80 min, followed by stage III, a slow increase to 0.222 ns until ~ 900 min, and finally stage IV, where the PLT decrease slowly again. The existence of a very short (less than ~ 2 min at RT) and slight increase in stage I can be best observed at LTs as shown in Fig. 4.4.2 or in alloy with a higher Mg and Si content such as alloys F and I [Ban11]. The main focus of this and the following sections was put on the ageing kinetics of alloy H during stage II, namely, from 5 to 80 min after quenching.

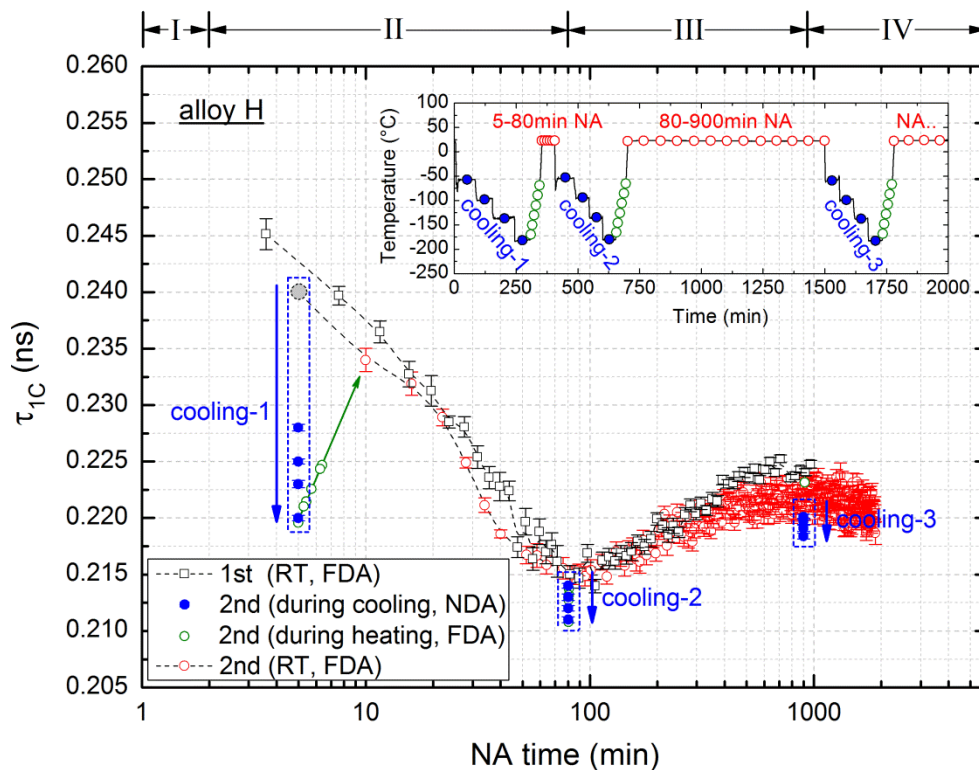


Figure 4.4.5. Temperature and time dependence of τ_{1C} in alloy H during NA. 1st run: τ_{1C} evolution during NA of alloy H measured at RT (black open symbols, IWQ). 2nd run: the temperature dependence of τ_{1C} in selected NA states of alloy H (IWQ). PLT measured at low temperatures during cooling (blue solid symbols), at intermediate temperatures during heating (green open symbols) and PLT in between at RT (red open symbols). Grey point is estimate of PLT for the sample aged for 5 min at RT of the 2nd run. The insert explains the temperature profile according to which samples were sequentially measured at -60 , -100 , -140 and -180 °C in the NDA mode during the 2nd run. After the measurements at this sequence, the LN_2 supply was turned off and samples were slowly warmed up to -60 °C, followed by a rapid active heating to RT to further age the samples, in between data were collected in the FDA mode.

A different temperature dependence of τ_{1C} in various states of ageing was observed in Fig. 4.4.5. For the sample NA for 5 min, τ_{1C} is markedly reduced from ~ 0.240 ns at 20°C to 0.220 ns at -180°C during cooling sequence 1. After 80 and 900 min of NA (cooling sequences 2 and 3), this dependence largely (but not completely) disappeared. This tendency agrees with [Klo10], in which a similar feature was also found for alloy F where, however, the temperature dependence of τ_{1C} shortly after IWQ is less pronounced than for alloy H.

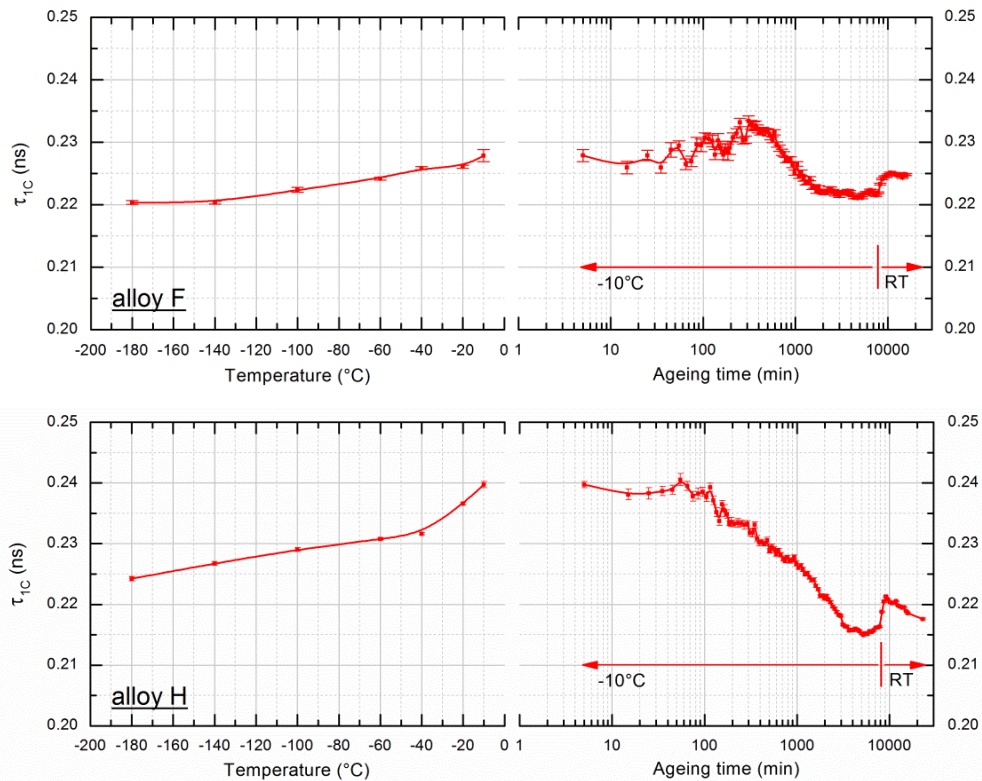


Figure 4.4.6. Temperature dependence of τ_{1C} in the AQ state (little ageing effect after CuQ) of alloys F and H. Afterwards, both alloys were further aged at -10°C and RT for some time.

The first data point in Fig. 4.4.5 is 5 min after IWQ, during which some solute clusters could already have formed. In order to avoid such a disturbing ageing effect before measurement and to access the real as-quenched state of the sample, alloys F and H were quenched on a cold Cu block and handled at temperatures lower than -100°C until the measurement started. The experiments in Fig. 4.4.5 were partly repeated and the results are shown in Fig. 4.4.6. A similar τ_{1C} dependence on temperature to the one shown in Fig. 4.4.5 was observed for alloy H, whereas the measurement of alloy F reveals the same feature as reported by [Klo10]. The increase of τ_{1C} for both alloys above -40°C is caused the combined effects of ageing during warming up and the inaccuracy from using 1-component analysis, see section 4.4.1.3.

In Fig. 4.4.5, the positron lifetime data collected during warming up roughly shows the same temperature dependence of τ_{1C} as during cooling, see Fig. 4.4.7 (L). Particularly for alloy H aged at RT for 5 min which certainly contains deep positron traps related to vacancies, the pronounced decrease of τ_{1C} during cooling sequence 1 strongly indicates the existence of an additional kind of positron traps, which are shallow and have been observed by a few experimental studies such as [Pag84, Saa89, Sme80]. As an example, the similar temperature dependence of τ_{1C} in alloy H (5 min of NA) and the τ_{APLT} in Si which contains deep traps neutral vacancies and shallow traps (st) is shown in Fig. 4.4.7 (R):

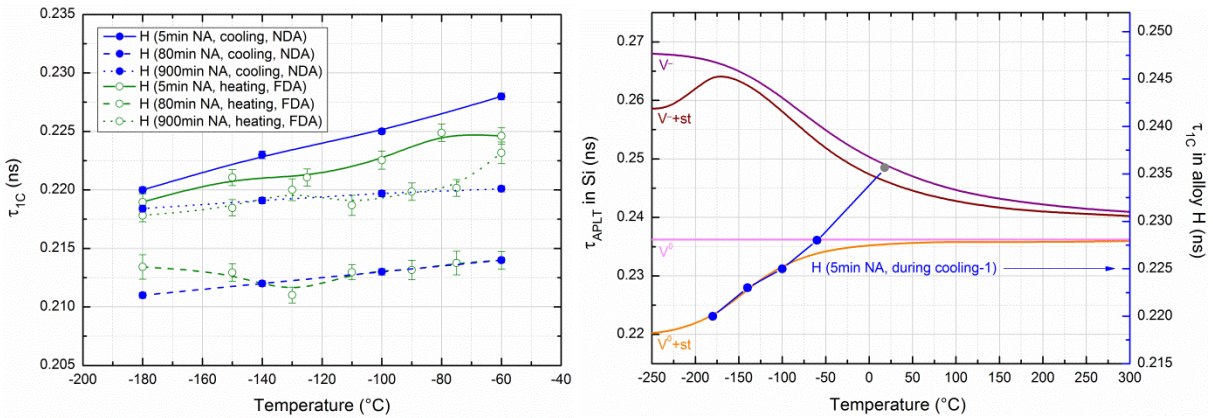


Figure 4.4.7. (L) Temperature dependence of τ_{1C} during cooling (blue solid symbols) and warming up (green open symbols) for various ageing states (5, 80 and 900 min of NA) of alloy H after IWQ; (R) Calculated temperature dependence of τ_{APLT} in Si, which contains deep positron traps (vacancies in different charge states, V^0 and V^-) and shallow positron traps (st) [Kra03], such a dependence is compared to the one of alloy H aged for 5 min at RT (gray and blue solid symbols). The same data (same symbols) as shown in Fig. 4.4.5 are used for both figures.

The comparison in Fig. 4.4.7 (R) indicates that the temperature dependence of τ_{1C} in alloy H after 5 min of NA points at the existence of “shallow traps”, which compete with the “deep traps” (> 1 eV of potential depth [Haa09, Klo10]) related to quenched-in vacancies. Grain boundaries certainly contain vacancy-like defects and act as deep traps [Dup93]; similarly, undisturbed dislocation lines which are treated as shallow traps [Sme80] also contain open volume defects such as bound vacancies by its tensile field. Thus, a positron which is pre-trapped by dislocations (as a precursor state) diffuses quickly along the line and will be trapped by such vacancies finally [Has91]. Moreover, grain boundaries and dislocation lines do not change during NA, and can be practically ruled out as a candidate for shallow traps.

Therefore such shallow traps could be small solute clusters in which positrons have lifetimes well above the value of bulk Al. At RT, the weak binding energies between positrons and shallow traps (typically 0.03 to 0.04 eV [Pag84, Saa89]) are insufficient to trap positrons since their thermal energies (~ 0.04 eV) are of the same order and thus they easily de-trap and barely contribute to annihilation. But when temperature and positron energies decrease, more and more positrons will be localized in the shallow traps (which become relatively deeper) due to the decrease of de-trapping. Under such circumstances, the increasing fraction of positron annihilating in the shallow traps faster than in vacancy-related defects notably affects the observed PLT τ_{1C} , which can be approximated as the weighted sum of each of the individual PLT components:

$$\tau_{1C} \approx \tau_{APLT} = \tau_f \cdot I_f + \tau_s \cdot I_s + \tau_v \cdot I_v, \quad (4.4.5)$$

where τ_{APLT} is the average positron lifetime, τ_f , τ_s and τ_v are the decomposed PLTs of free positrons, solute clusters and vacancy-related defects, I_f , I_s , and I_v denote the corresponding intensities. τ_f is the reduced PLT in bulk since it is shorter than the PLT in defect-free Al.

During subsequent NA, solute clusters increase in number of atoms and therefore size, thus, positrons will be trapped preferentially by these clusters due to the higher positron affinity to solutes. Eventually, they cannot be further regarded as “shallow traps” since positrons get trapped by these clusters even at RT as a result of the increase in their binding energies with positrons. Under such circumstances, a much weaker temperature dependence of τ_{1C} is expected, as compared to the one after 5 min of NA. Combining all relevant PLT components of alloy H and applying Eq. (4.4.5), the different types of temperature dependence of τ_{1C} of alloy H in Fig. 4.4.5 can thus be explained.

The temperature dependence of τ_{1C} after 5 min of NA in alloy F is much weaker than in alloy H, see Fig. 4.4.6, pointing at “semi-shallow traps” of larger solute clusters, which might be rapidly formed during or shortly after quenching [Ema03] due to higher solute content. In this case, the positron binding energies of these clusters are considerably higher as in alloy H. Therefore, it is no more essential to cool down the sample to suppress positron de-trapping from the corresponding traps as in alloy H. Thus, the weaker temperature dependence of the initial PLT in alloy F might be explained. In order to verify this explanation, the PLT spectra should be decomposed to determine the parameters in Eq. (4.4.5).

The theoretical APLT in Si is determined by two contributions V_0 and st . The resulting APLT levels off for $T > 0$ °C, others than for alloy H, see the gray symbol in Fig. 4.4.7 (R). For this discrepancy, one has to keep in mind that if positrons annihilate freely and / or in shallow traps in addition to vacancy-type defects, multi-component fitting of the PLT spectra is essentially required. For example, if only 1-component analysis is applied, the fraction of the free positron component can be approximated by an artificial broadening of the time resolution function, thus, an inaccurate τ_{1C} can be obtained. However, the APLT is a calculated annihilation parameter based on individual PLT components and, therefore, is more influenced by the shorter-lived positron contributions. For a more reasonable analysis of the results above a multi-component analysis should be performed, see Section 4.4.1.4.

4.4.1.4 Temperature and Time Dependence of τ_{f+s} & I_{f+s} in Alloy H (NDA)

In general, it is hard to analyze spectra with more than two decay components due to the high number of free annihilation parameters involved. In order to minimize the statistical uncertainties from fitting, a restricted 2-component (1.5-component) analysis was applied due to the limited time resolution (~ 0.220 ns) of the employed spectrometer [Saa89]. The longer vacancy-related PLT component τ_v was fixed to 0.245 ns (details are given in Section 4.4.1.5), and the shorter one τ_{f+s} then represents the superposition of other decay components related to positron annihilations in bulk and solute clusters, as shown in Fig. 4.4.8:

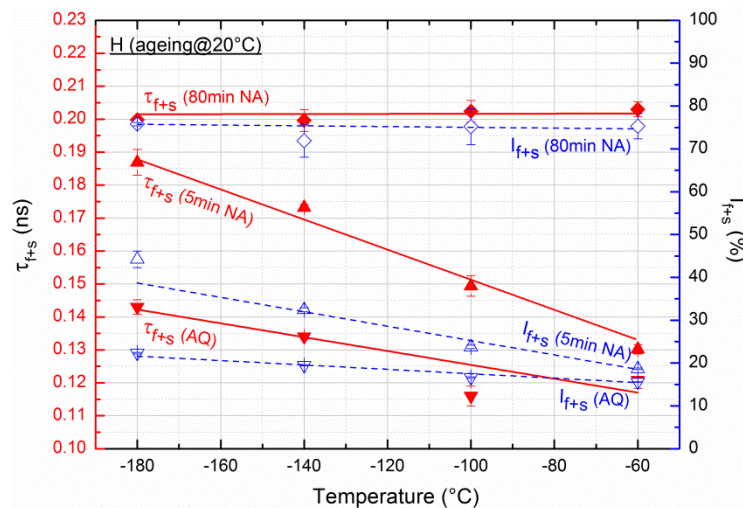


Figure 4.4.8. Dependence of τ_{f+s} (red) and I_{f+s} (blue) on measurement temperature and NA time in alloy H. The 2-component analysis is based on the same data as shown in Fig. 4.4.5 and Fig. 4.4.6. Straight lines are linear fits. The rationale for the additional experiment “AQ” was to include an experiment for the “real” as-quenched state where NA after quenching could be largely suppressed using CuQ, see Fig. 3.1.4 (R), and always keeping the sample at LT after.

It is shown in Fig. 4.4.6 that for the AQ state of alloy H, τ_{1C} decreases from 0.231 ns at -60 °C to 0.224 ns at -180 °C, slightly smaller than the one after 5 min of NA (0.228 to 0.220 ns, see Fig. 4.4.5). In contrast, the decomposed PLT component related to bulk and solute clusters τ_{f+s} increases along with the intensity I_{f+s} during cooling, similar to the observation by [Pag84]. Such increases are even more pronounced after ageing alloy H for 5 min, but disappear after 80 min of NA. Moreover, the value of τ_{f+s} and I_{f+s} increases during cooling as NA proceeds and levels off at ~ 0.200 ns and $\sim 75\%$ accordingly, see Fig. 4.4.8.

Immediately after solutionizing and quenching (“AQ” in Fig. 4.4.8), single solute atoms or clusters containing just few solute atoms and possibly Al atoms inside could be potential shallow traps, which can compete with the dominating vacancy-type defects in trapping positrons at LTs. The size of solute clusters might be still small at this stage so that even if the positrons are localized by these clusters during cooling, the corresponding PLT would still be close to the one of the Al reduced bulk. This can be observed from the relatively small increase of τ_{f+s} and low I_{f+s} in Fig. 4.4.8. However, after 5 min of NA, more and larger clusters will have formed so that a fraction of positrons can already be trapped at the boundary of these clusters at RT [Dlu87]. At LTs, the localization of positron wave function inside such clusters is even stronger. As a result, the PLT approaches the bulk value of the solute element [Bha92, Bha96, Kur04]. For the investigated alloy H, the PLT in Mg and Si are both higher than in Al. Thus, a higher τ_{f+s} and I_{f+s} is expected if more and more positrons are eventually localized by solute clusters at LTs, as shown in Fig. 4.4.8. After 80 min of NA, the size of solute clusters might be sufficiently large to trap positrons even at RT. In this case, the probability of positron annihilation inside the clusters is very high [Dlu87]. Therefore, no or a very weak temperature dependence of τ_{f+s} and I_{f+s} is observed.

Back to the question raised at the end of Section 4.4.1.3: the APLTs of alloy H (5 min of NA) at temperatures ranging from -180 to -60 °C were calculated based on the decomposed PLT components in Fig. 4.4.8. For τ_{APLT} at RT, however, the decomposition of PLT spectra collected at RT in the FDA mode cannot be carried out due to the very limited statistics, insufficient time resolution, and the fast ageing kinetics for the alloy at RT. Nevertheless, if the samples are aged at a lower temperature, e.g. 0 °C instead of RT, where the ageing kinetics is retarded, a decomposition of the PLT spectra is possible due to improved statistics.

Therefore, as a compromise, the PLT spectra of alloy H aged at 0 °C is decomposed (fixed τ_v , 1.5-component analysis, see Section 4.4.1.6) in order to complete the temperature dependence of the APLT in alloy H aged for 5 min at RT. The results are shown in Fig. 4.4.9:

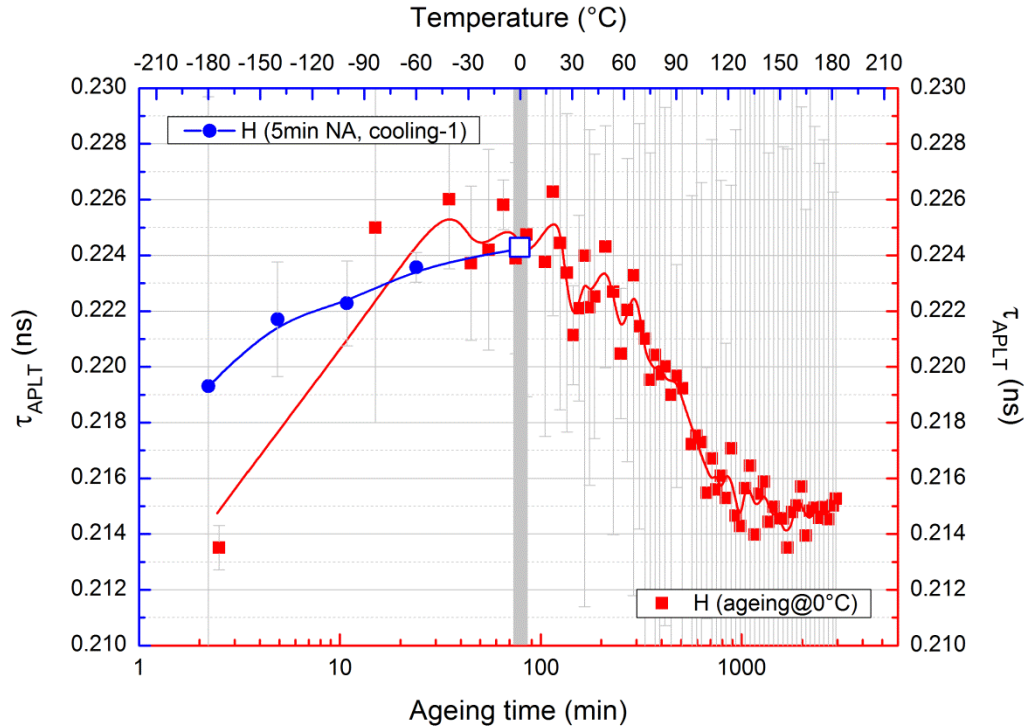


Figure 4.4.9. Dependence of APLT on temperature (-180 to 0 °C) in alloy H aged for 5 min at RT (IWQ). Data represented by blue solid symbols are based on experiments described in Fig. 4.4.5 (cooling-1), while the red solid symbols are the evolution of calculated APLTs of alloy H aged at 0 °C (CuQ), and the blue open symbol is estimated as the APLT of alloy H aged at 0 °C for ~80 min.

The samples of alloy H represented by blue solid symbols in Fig. 4.4.9 were aged at RT for 5 min after IWQ, while the measurement represented by the red solid symbols was started with little pre-ageing. Therefore, the ageing time at which the samples achieve an equivalent ageing state to the one aged at RT for 5 min has to be determined for the isothermal experiment at 0 °C. According to the transition times at different temperatures of alloy H as shown in Fig. 4.4.3 (R), this time was roughly estimated to be ~80 min. Combining the APLT represented by the blue open symbol (0.224 ns) after this ageing time to the blue solid symbols, the temperature dependence of the APLT of alloy H aged for 5 min at RT after quenching finally exhibits the same tendency as the one in Si which contains vacancies and shallow traps, as shown in Fig. 4.4.7 (R). Therefore, APLT in alloy H increases with increasing temperature, and levels off gradually at temperatures above 0 °C.

4.4.1.5 Time Dependence of τ_i & I_i in Alloy H (NDA, Prague)

The spectrometer time resolution plays a crucial role for decomposing a PLT spectrum into individual components. In order to validate the different interacting annihilation mechanisms such as bulk annihilation, solute clusters and vacancies, alloy H naturally aged for 5, 30, 70 and 140 min after IWQ was measured at $-150\text{ }^\circ\text{C}$ at the Charles University in Prague, where the very high time resolution (0.145 ns) of a digital spectrometer [Bec00, Bec05] allows to accurately separate PLT components which might lie very close to each other.

Three distinct PLT components can be resolved during stage II without fixing any of the fitting parameters in Eq. (4.4.5). The up to three PLTs τ_i found are shown in Fig. 4.4.10 as a function of their corresponding intensities I_i , as represented by the open symbols. In addition, the result shown in Fig. 4.4.8 is also plotted in Fig. 4.4.10 as solid symbols, so that a comparison can be made between both results obtained from HZB and Uni. Prague:

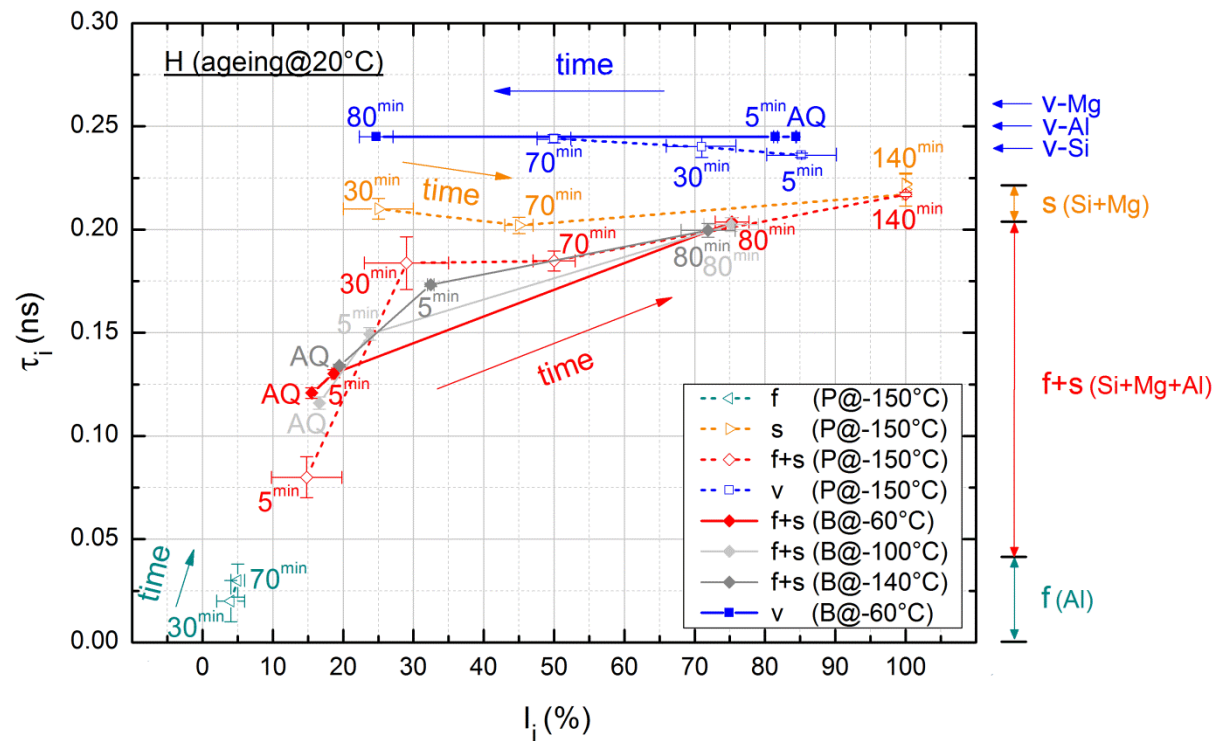


Figure 4.4.10. Evolution of decomposed PLT components in alloy H during stage II (III). PLTs τ_i as a function of intensities I_i are given. Measurements labelled with “P” and open symbols were performed at the Uni. Prague at $-150\text{ }^\circ\text{C}$, while data labelled with “B” and solid symbols show experiments conducted at HZB at LTs (-140 , -100 and $-60\text{ }^\circ\text{C}$) using the same alloy (data from Fig. 4.4.8). On the right, the PLTs in some vacancy-related defects as well as the range of (reduced) PLTs in solute clusters and bulk Al are shown. Unlike in Fig. 4.4.5, each point from Uni. Prague’s result corresponds to a newly quenched sample.

The vacancy-related long PLT component τ_v (blue open square) varies from 0.236 to 0.245 ns, slightly shorter than the PLT in a mono-vacancy in Al, and can be attributed to positrons trapped by V-Si complexes since Si is expected to decrease the lifetime of a positron trapped in a Al-vacancy, while Mg acts in the opposite direction [Cor81, Mel06]. In addition, the probability of V-Si formation is much higher than for V-Mg. The Si and Mg content is more or less equal in alloy H, but due to the stronger interaction between vacancy and Si [Hir07, Lan13], V-Si complexes are formed more efficiently than V-Mg. Certainly, the long PLT component could also be related to positron trapping in solute clusters other than those characterized by PLT τ_s . For example, cluster atoms that do not occupy substitutional sites one-to-one but leave some open volume could give rise to a PLT τ_v as well. During NA, I_v is significantly lowered from 85% to 50%, indicating a decreasing contribution of the associated defects to total PLT. Elimination of vacancies at sinks and vacancies trapped inside certain solute clusters could be responsible for this decrease in intensity, but such a decrease would be accompanied by an increase of a bulk component which we do not observe.

More likely, the decrease of I_v is caused by the formation and growth of coherent clusters enriched in Si and/or Mg (may also contain some Al atoms [Mur01]) in which the positrons have a lifetime τ_s ranging from 0.200 to 0.210 ns (orange open triangles). The positrons are localized by solute clusters owing to their preferential affinities to alloying elements, and according to [Kra03], the wave function of a positron will spread over the cluster. Thus, the annihilation parameters are determined by the corresponding bulk parameters of the clustering material. This PLT is much shorter than τ_v and implies that these clusters are vacancy-free. Therefore, identifying them with the shallow traps already detected is near at hand. By neglecting the interactions between solutes, the total vacancy concentration during solutionizing in an Al-Mg-Si alloy can be estimated employing the Lomer's equation [Lom58, Oht68]:

$$c_v = \exp\left(\frac{S_f}{k_B}\right) \exp\left(-\frac{E_f}{k_B T}\right) \left[1 - 12(c_{Mg} + c_{Si}) + 12 \left[c_{Mg} \exp\left(\frac{E_{V-Mg}}{k_B T}\right) + c_{Si} \exp\left(\frac{E_{V-Si}}{k_B T}\right) \right] \right], \quad (4.4.6)$$

where $c_{Mg(Si)}$ is the concentration of Mg (Si) and $E_{V-Mg(Si)}$ is the V-Mg (Si) binding energy. Other parameters are the same as in Eq. (4.1.1). The results are shown in Fig. 4.4.11.

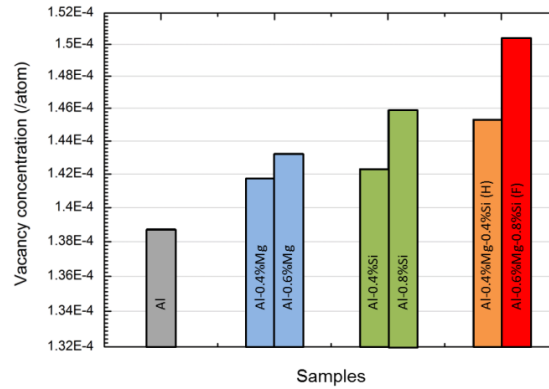


Figure 4.4.11. Calculated vacancy concentration for Al, Al-0.4%Mg, Al-0.6%Mg, Al-0.4%Si, Al-0.8%Si and Al-0.4%Mg-0.4%Si (alloy H), Al-0.6%Mg-0.8%Si (alloy F) alloys at 540 °C.

The vacancy concentration c_v increases with increasing solute content, due to the interactions between vacancies and solutes. Depending on the E_b values used for the calculation, c_v could be different. Furthermore, the actual c_v can be smaller than the calculated one due to losses during and after quenching, although the elimination of vacancy at sinks should be partly inhibited by the strong vacancy-solute interactions. If only $\sim 10\%$ (i.e. $\sim 8 \times 10^{-4}$ /atom) of solutes are consumed for cluster formation in alloy H and each cluster consists of 6 solute atoms, see Section 4.4.1.9, a concentration of $\sim 1.3 \times 10^{-4}$ /atom for solute clusters can be estimated. According to the values derived from theoretical trapping models, see Section 4.4.1.8 and Section 4.4.1.9, the vacancy-type defect concentration equals $\sim 0.8 \times 10^{-4}$ and $\sim 0.6 \times 10^{-4}$ /atom at the beginning and the end of stage II, respectively. In this case, even if 0.2×10^{-4} /atom vacancies are completely trapped inside the solute clusters, there will be still > 6.5 times more vacancy-free clusters than those clusters containing a mono-vacancy. Moreover, even if there were more vacancy-solute complexes than solute clusters, positron trapping by clusters would still dominate due to their much higher trapping rate [Som00], see Section 4.4.1.9. This agrees with the observed difference between I_s and I_v after 80 min of NA, see Fig. 4.4.10. Upon NA, these clusters gradually trap more and more positrons than the vacancy-containing defects provided that a critical cluster radius is exceeded, which can be estimated from the positron affinities of Mg (-6.18 eV), Si (-6.95 eV) and Al (-4.41 eV) [Nie95]. For example, the critical radius of Si precipitates can be determined as: $r_{Si} = 5.8 \text{ \AA} / (\Delta A [\text{eV}])^{1/2} = 3.8 \text{ \AA}$ [Pus89], where ΔA is the difference in positron affinities between Si and Al. Si has an atomic radius of 1.46 Å and the nearest neighbor distance in a fcc (face-centered cubic) Al lattice is 2.86 Å, indicating that already few Si atoms in a cluster are able

to localize positrons. For Mg, the situation is similar. Moreover, it is found that almost all the positrons are trapped by solute clusters after 140 min of NA, see Fig. 4.4.10.

The shortest PLT component (green open triangles) contributes only weakly. It originates from free annihilation in the Al bulk. This component can be distinguished in samples aged for 30 and 70 min, but not for 5 min. In order to facilitate discussion, we combine the contribution of free positrons τ_f and the solute cluster component τ_s to τ_{f+s} :

$$\tau_{f+s} = \tau_f \cdot \frac{I_f}{I_f+I_s} + \tau_s \cdot \frac{I_s}{I_f+I_s} , \quad (4.4.7)$$

$$I_{f+s} = I_f + I_s . \quad (4.4.8)$$

Based on these equations, the weighted sum of the free positron and the solute cluster contributions is given in Fig. 4.4.10 (red open diamonds), showing that both τ_{f+s} and I_{f+s} increase continuously during NA. This feature was also found from the experiments carried out at HZB using the same alloy. Instead of decomposing the PLT spectra into 3 components, only a 1.5-component analysis was applied to the spectra measured at -140, -100 and -60 °C due to the limited time resolution of the employed spectrometer. Results are given in Fig. 4.4.10 as solid symbols. The two data sets for the two spectrometers show the same trend, but differ in two details: (1) for short NA times, e.g. 5 min, τ_{f+s} (B) deviates from τ_{f+s} (P). This might be caused by inaccuracies created by fixing τ_v (1.5-component analysis), or more likely, due to the limited time resolution of the applied spectrometer at HZB (the free annihilation component cannot be accurately resolved from the solute cluster component); (2) the ageing kinetics of the alloy measured at the Uni. Prague appears slower, e.g. after 70 min of NA, the intensity I_{f+s} (P) is just ~50%, which is 25% lower than I_{f+s} (B). This could be due to a higher quenching rate and associated higher density of quenched-in vacancies in the experiments done at HZB, see Section 3.1.2.1, giving rise to a more efficient solute clustering [Des60, Mac96, Mar80].

So far, the early clustering kinetics of alloy H have been observed only for few NA states in the NDA mode which does not provide all the details that might be involved. However, it might be also interesting to investigate the ageing characteristics in the FDA mode, and observe the clustering process almost continuously, see Section 4.4.1.6.

4.4.1.6 Time Dependence of τ_i & I_i in Alloys F and H (FDA)

In Section 4.4.1.2, the evolution of the 1-component PLT in alloys F and H aged isothermally at various LTs has been discussed. Employing the decomposition procedure introduced in Section 4.4.1.4, the clustering behavior of both alloys during LT ageing is further studied. Due to the low count rate of the spectrometer at the Uni. Prague, it is impossible to collect and analyze data during in-situ ageing. Thus, the spectrometer at HZB is used.

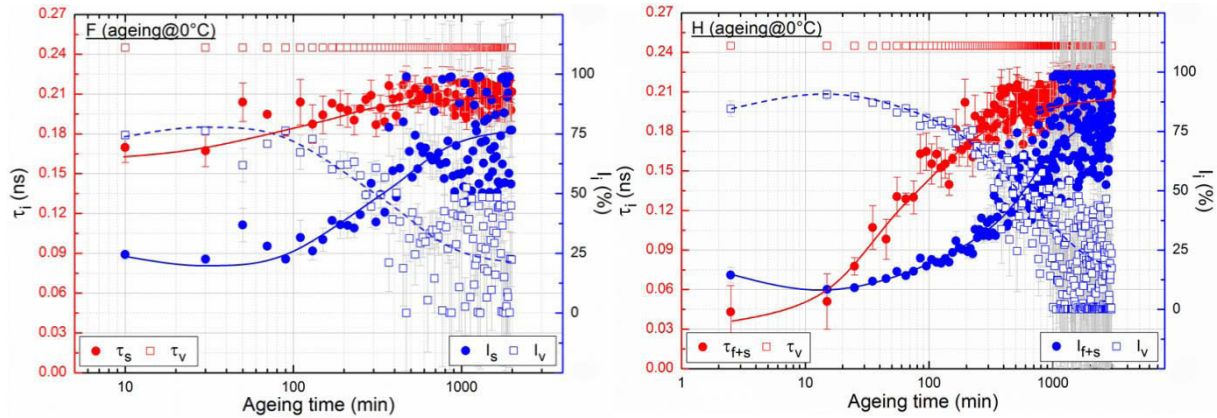


Figure 4.4.12. Evolution of (L) τ_s , τ_v in alloy F and (R) τ_{f+s} , τ_v in alloy H and the corresponding intensities I_s , I_v as well as I_{f+s} , I_v during isothermal ageing at 0 °C (CuQ). Decompositions of PLT were done assuming $\tau_v = 0.245$ ns. Blue and red lines are given to guide the eye.

As shown in Fig. 4.4.12, two competing PLT components can be separated for alloys F and H, accordingly related to vacancy-solute complexes on the one hand and solute clusters and bulk on the other. For the vacancy component with an assumed constant PLT, a general decrease in intensity was observed for both alloys (actually for alloys F and H, I_v slightly increases for the first 30 and 15 min of ageing, respectively). For the shorter PLT components, both PLTs and intensities generally increase during ageing at 0 °C and approach the equilibrium level at the end of stage II, see Fig. 4.4.12, indicating the formation and growth of solute clusters. This feature coincides with the one shown in Fig. 4.4.10.

Besides the similarities, differences concerning LT ageing kinetics between alloys F and H are also clearly visible, e.g. the initial PLT τ_s and intensity I_s of alloy F equals 0.170 ns and 25%, respectively, higher than τ_{f+s} (0.045 ns) and I_{f+s} (15%) in alloy H. In alloy F, τ_s is on the one hand higher than the bulk PLT in bulk Al, but on the other hand smaller than the bulk value of Mg and Si, which implies that some very small clusters could be already formed during or shortly after quenching [Edw98, Lay12, Mur99]. This observation supports the idea

that solute clusters are formed much more efficiently in alloy F than in alloy H (this idea has also been used to explain the weaker temperature dependence of τ_{1C} of alloy F aged for 5 min at RT, see Section 4.4.1.3). As a result, all positrons are trapped either by solute clusters or by vacancy-type defects, and no free annihilation is observed. Further development of these solute clusters in number density and size might be related to the “negative effect” after the subsequent AA of certain Al-Mg-Si alloys in a direct or indirect manner, further experiments should be carried out to verify this point.

In addition, the decomposed PLT components τ_s , I_s or τ_{f+s} , I_{f+s} of alloys F or H, respectively, aged at -30, -20 and -10 °C are compared with the ones at 0 °C in Fig. 4.4.13:

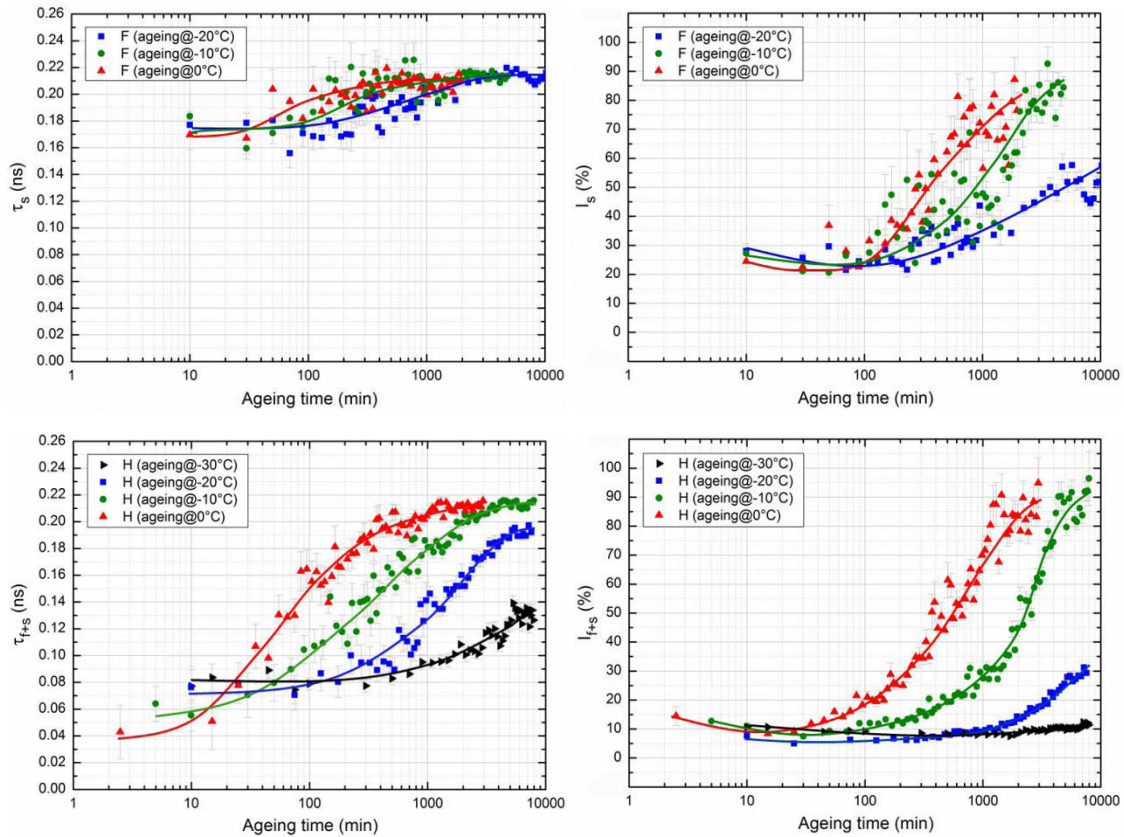


Figure 4.4.13. Decomposed PLT components of (L) τ_s in alloy F and τ_{f+s} in alloy H and (R) the corresponding intensities I_s and I_{f+s} as a function of ageing time. Samples were measured at various LTs directly after CuQ. Solid lines serve as eye guide only.

The evolution of PLT and intensity during isothermal ageing exhibits a clear temperature dependence, indicating that clustering process is thermally activated. For the measurements at $T \leq -20$ °C of both alloys, only a part of the evolution was recorded due to the very slow ageing kinetics at such temperatures (ageing is efficiently prohibited at $T \leq -40$ °C [Røy06]).

Back to the question about stage I raised in Section 4.4.1.2: although we are still lack of knowledge so far to explain it physically, it can be interpreted mathematically in Fig. 4.4.14:

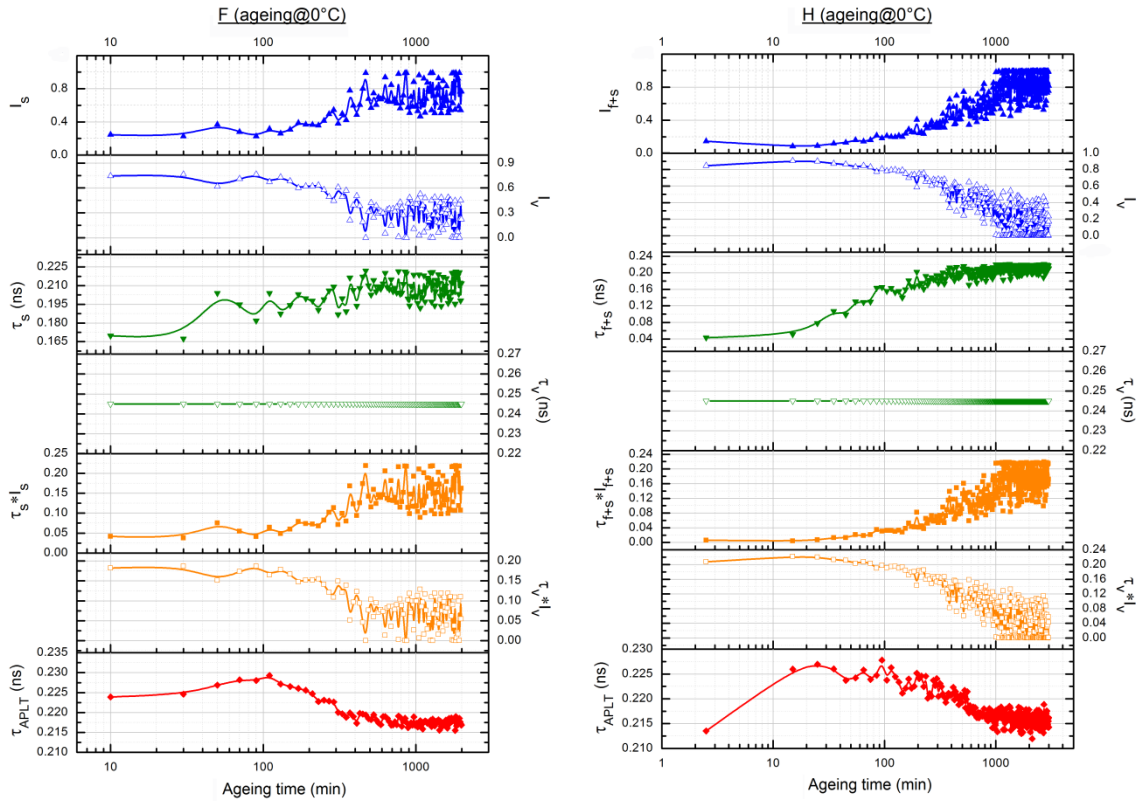


Figure 4.4.14. Evolution of various annihilation parameters of (L) alloy F and (R) alloy H aged at 0 °C (CuQ). The same data as shown in Fig. 4.4.12 are used.

The change of τ_{APLT} depends on the relative change of each individual parameter in equation $\tau_{APLT} = \tau_{(f+s)} \cdot I_{(f+s)} + \tau_v \cdot I_v$. As shown in Fig.4.4.14, $\tau_{(f+s)} \cdot I_{(f+s)}$ (orange solid symbols) generally increases due to enhanced positron annihilation in solute clusters during ageing, while $\tau_v \cdot I_v$ (orange open symbols) first increases for some minutes and then continuously decreases due to the decreasing contribution from vacancy-solute complexes. The cause of the initial increase of $\tau_v \cdot I_v$ is unknown, but it could be connected to an increase in concentration and/or in trapping rates of vacancy-type defects. Thus, the transition (red solid symbols) after a certain ageing time can be explained by the superposition of both contributions. For alloy H, after the slight increase of $\tau_v \cdot I_v$ for ~ 25 min (slightly longer than the one in Fig. 4.4.2), τ_{APLT} starts to decrease since it is then dominated by the decrease of $\tau_v \cdot I_v$ (slow cluster formation). For alloy F, besides the similar increase in $\tau_v \cdot I_v$ as in alloy H, the decrease of $\tau_v \cdot I_v$ is compensated by the rapid increase of $\tau_s \cdot I_s$ due to the fast formation of solute clusters, and a considerably longer stage I up to ~ 100 min is observed (agrees with the one in Fig. 4.4.2).

4.4.1.7 τ_{1C} Evolution in Artificially Aged Alloys F and H during NA (FDA)

A positron has a lifetime of 0.165, 0.225 and 0.218 ns in Al, Mg and Si, respectively. Therefore, a PLT of ~ 0.210 ns in solute clusters containing certain amounts of these atoms appears plausible, see Section 4.4.1.5. However, Mg (hcp, hexagonal close-packed) and Si (diamond) have lattice structures different from Al (fcc). Whether their PLTs in the bulk can be directly used for the Si-Mg co-clusters in Al is questionable. Unfortunately, no theoretical calculation concerning this issue is available so far. However, by ageing freshly quenched samples at 180 °C for certain times, the PLT in so formed structures such as Si-Mg clusters, GP (Guinier-Preston) zones and β'' precipitates can be experimentally studied.

- AA at 180 °C (< 5 min) + NA

After AA of alloys F and H at 180 °C for few minutes, the decreasing τ_{1C} during NA in stage II is replaced by a constant or increasing PLT in both alloys. For the subsequent stages, a similar PLT evolution as for alloys without prior AA is observed. The effects of 0.5 and 2 min of AA on PLT evolution during NA are quite alike for both alloys, see Fig. 4.4.15:

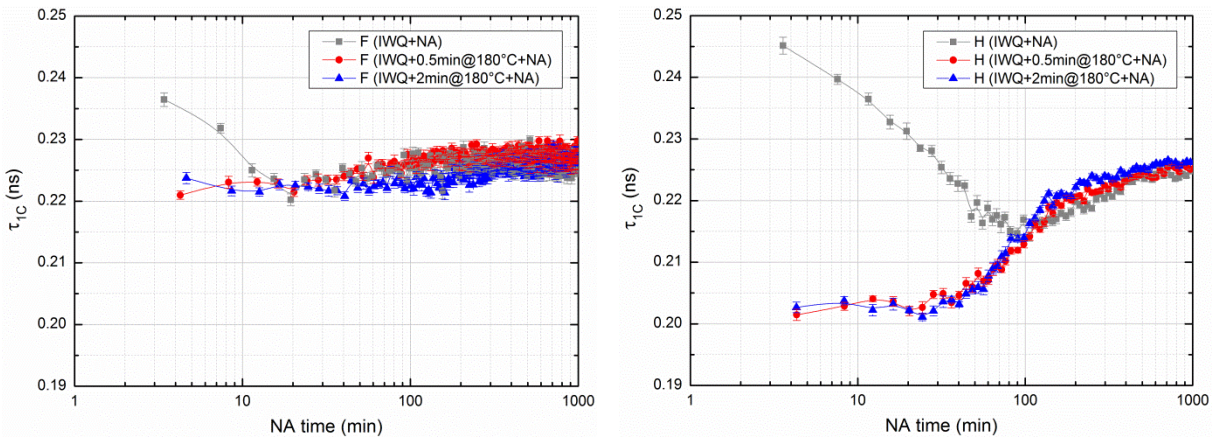


Figure 4.4.15. Evolution of τ_{1C} in artificially aged (L) alloy F and (R) alloy H during subsequent NA. Samples were either aged at 180 °C for 0.5 or 2 min. PLT evolution of alloys without prior AA are given as gray curves. For temperature profiles see Section 3.4.

Most likely, artificial ageing of both alloys has markedly promoted the rapid formation of coherent Si-Mg co-clusters or even GP zones with a PLT around 0.210 ns, although the times for AA were very short [Som00]. As the concentration of these structures is much higher than that of vacancy-related defects (as has been proposed in Section 4.4.1.5), they act as the main localization sites of positrons. As a result, a lower PLT ranging from 0.200 to 0.210 ns during stage II is observed in alloy H than without AA (in gray color), see Fig. 4.4.15 (R). In

alloy F, this decrease in initial PLT is analogous to the one of alloy H but its amplitude is much smaller (0.236 to 0.222 ns in alloy F and 0.245 to 0.203 ns in alloy H), see Fig. 4.4.15 (L). Two plausible reasons account for this difference: (1) the total concentration of defects in alloy H might be considerably lower than the one in alloy F due to its much lower solute content. In this case, bulk annihilation also contributes and brings down the PLT, see PLT component τ_f in Fig. 4.4.10; (2) the Mg/Si ratio of solute clusters formed in alloy F is higher than in alloy H, see Section 4.4.2.1, and PLT in Mg is higher than in Si. The further development of PLT during NA can be related to the secondary precipitation process due to the super saturation of solutes [Buh04], which is quite similar to stage III of NA.

- AA at 180 °C (≥ 5 min) + NA

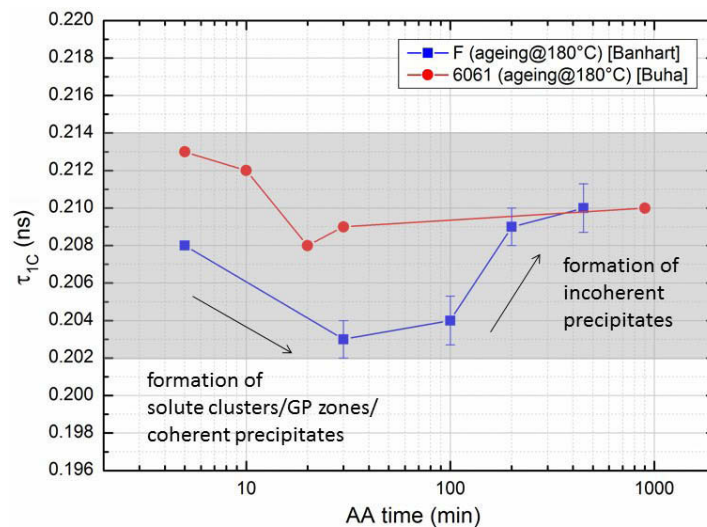


Figure 4.4.16. Evolution of τ_{1C} in artificially aged alloys F and 6061 during NA. Prior to NA, quenched samples were aged at 180 °C for various times (>5 min). It can be seen that all PLTs of the structures (solute clusters, GP zones, precipitates) formed during AA range from 0.202 to 0.214 ns, as indicated by the gray area. Measurements were carried out by J. Banhart and J. Buha, the shorter PLT by J. Banhart was due to source correction.

J. Banhart performed PALS experiments on alloy F which were artificially aged for times longer than 5 min after quenching, and a constant PLT around 0.210 ns was observed with prolonged AA times. This result coincides with [Buh04], who reported a similar PLT using almost identically heat treated 6061 alloys, see Fig. 4.4.16. Thus, ~ 0.210 ns could be the characteristic PLT in Si-Mg clusters, GP zones and β'' precipitates in Al, which are formed under the corresponding ageing conditions. Even so, it is essential and important to verify this point in the future work.

4.4.1.8 Modelling of the Temperature Dependence of τ_i & I_i in Alloy H (NDA)

The simple trapping model has been employed to describe the positron annihilation behavior in the bulk or in vacancy-related defects in pure Al, binary Al-Mg and Al-Si alloys. However, the existence of an additional positron trap has been verified by PALS experiments on ternary Al-Mg-Si alloys. This trap is shallow during the initial stage of ageing and might also change its characteristics during ageing. Therefore, an extended trapping model including two types of defects (shallow traps solute clusters and deep traps vacancy-type defects) should be applied in order to reasonably characterize the temperature and time dependence of these traps, as presented in the following.

Positrons can annihilate freely in the bulk or be trapped by various types of defects and annihilate afterwards. In the extended model, analogous to the STM, those positrons which are trapped by solute clusters with a trapping rate of κ_s , can de-trap from the shallow solute clusters at elevated temperatures with a de-trapping rate of δ_s , otherwise they annihilate in such defects with an annihilation rate of λ_s . Positrons trapped by a vacancy-related defects at a rate of κ_v remain there and eventually annihilate at a rate of λ_v , see Fig. 4.4.17 [Kra03]:

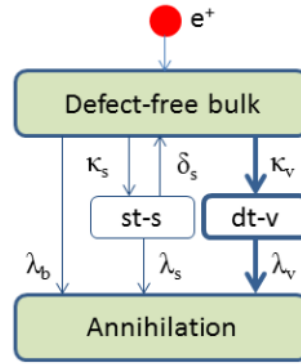


Figure 4.4.17. Schematic illustration of the extended trapping model. “st-s” stands for shallow trap-solute clusters, “dt-v” for deep trap-vacancy-type defects.

Neglecting any interaction between different defects, the trapping of positrons can be described by the following rate equations:

$$\begin{bmatrix} \dot{n}_b(t) \\ \dot{n}_s(t) \\ \dot{n}_v(t) \end{bmatrix} = \begin{bmatrix} -(\lambda_b + \kappa_s + \kappa_v) & \delta & 0 \\ \kappa_s & -(\lambda_s + \delta) & 0 \\ \kappa_v & 0 & -\lambda_v \end{bmatrix} \begin{bmatrix} n_b(t) \\ n_s(t) \\ n_v(t) \end{bmatrix}. \quad (4.4.9)$$

Using initial conditions given in Section 4.1.1.2, the solutions below can be obtained [Kra03]:

$$\tau_f = \frac{2}{\lambda_b + \kappa_s + \kappa_v + \lambda_s + \delta_s + \sqrt{(\lambda_b + \kappa_s + \kappa_v - \lambda_s - \delta_s)^2 + 4\kappa_s\delta_s}} = \frac{2}{\Xi + \Psi}, \quad (4.4.10)$$

$$\tau_s = \frac{2}{\lambda_b + \kappa_s + \kappa_v + \lambda_s + \delta_s - \sqrt{(\lambda_b + \kappa_s + \kappa_v - \lambda_s - \delta_s)^2 + 4\kappa_s\delta_s}} = \frac{2}{\Xi - \Psi}, \quad (4.4.11)$$

$$\tau_v = \frac{1}{\lambda_v}, \quad (4.4.12)$$

$$I_f = 1 - I_s - I_v, \quad (4.4.13)$$

$$I_s = \frac{\delta_s + \lambda_s - \frac{1}{\tau_s}}{\sqrt{(\lambda_b + \kappa_s + \kappa_v - \lambda_s - \delta_s)^2 + 4\kappa_s\delta_s}} \times \left(1 + \frac{\kappa_s}{\delta_s + \lambda_s - \frac{1}{\tau_s}} + \frac{\kappa_v}{\lambda_v - \frac{1}{\tau_s}} \right)$$

$$= \frac{\delta_s + \lambda_s - \frac{1}{2}(\Xi - \Psi)}{\Psi} \times \left(1 + \frac{\kappa_s}{\delta_s + \lambda_s - \frac{1}{2}(\Xi - \Psi)} + \frac{\kappa_v}{\lambda_v - \frac{1}{2}(\Xi - \Psi)} \right), \quad (4.4.14)$$

$$I_v = \frac{\kappa_v(\delta_s + \lambda_s - \lambda_v)}{\left(\lambda_v - \frac{1}{\tau_f}\right)\left(\lambda_v - \frac{1}{\tau_s}\right)} = \frac{\kappa_v(\delta_s + \lambda_s - \lambda_v)}{\left(\lambda_v - \frac{1}{2}(\Xi + \Psi)\right)\left(\lambda_v - \frac{1}{2}(\Xi - \Psi)\right)}, \quad (4.4.15)$$

with

$$\Xi = \lambda_b + \kappa_s + \kappa_v + \lambda_s + \delta_s, \quad (4.4.16)$$

$$\Psi = \sqrt{(\lambda_b + \kappa_s + \kappa_v - \lambda_s - \delta_s)^2 + 4\kappa_s\delta_s}. \quad (4.4.17)$$

Based on this model, the temperature dependence of PLT decompositions in alloy H (after 5 min of NA) was calculated. In the corresponding experiment a pronounced decrease in τ_{1C} during cooling was observed caused by the action of shallow traps, see Fig. 4.4.5. However, a large number of parameters are involved in the model as shown above, which makes it difficult to obtain meaningful fits. Thus, in order to simplify modelling as much as possible, some parameters were fixed to certain values, namely, λ_b , λ_s and λ_v were fixed to 1/0.160, 1/0.210 and 1/0.245 ns⁻¹ based on experimental results, see Fig. 4.4.10. Other quantities such as the trapping rates κ_s , κ_v and the de-trapping rate δ_s were first narrowed to a certain range and then determined by fitting. The detailed analysis will be presented in the following.

The trapping rate κ_s from a shallow defect such as three-dimensional precipitates can be related to the corresponding de-trapping rate δ_s thermodynamically as [Man81]:

$$\frac{\delta_s}{\kappa_s} = \frac{1}{V\rho_p} \left[\frac{\pi}{2} \operatorname{erf} \left(\sqrt{\frac{E_b}{k_B T}} \right) - \sqrt{\frac{E_b}{k_B T}} \exp \left(-\frac{E_b}{k_B T} \right) \right] \exp \left(-\frac{E_b}{k_B T} \right), \quad (4.4.18)$$

where V and ρ_p are the volume and number density of the precipitate, E_b is the binding energy between positron and precipitate. According to kinetic Monte Carlo (KMC) calculations, clusters containing ~ 5 atoms have number densities of $\sim 10^{24}$ to 10^{25} m^{-3} after ~ 3 to 5 min of NA [Lia12]. Assuming that all 5 solute atoms occupy the nearest neighbor position of the unit cell, a rough estimation of $1/(V\rho_p)$ ranging from ~ 300 to 3000 can be made (lattice constant of Al is 4.05 Å). For example, a value of 1000 for $1/(V\rho_p)$ will lead to a very high δ_s/κ_s ratio for E_b ranges from 0.01 to 0.09 eV (typical values for shallow traps), i.e. more de-trapping than trapping even at temperatures below $-120 \text{ }^\circ\text{C}$, see Fig. 4.4.18:

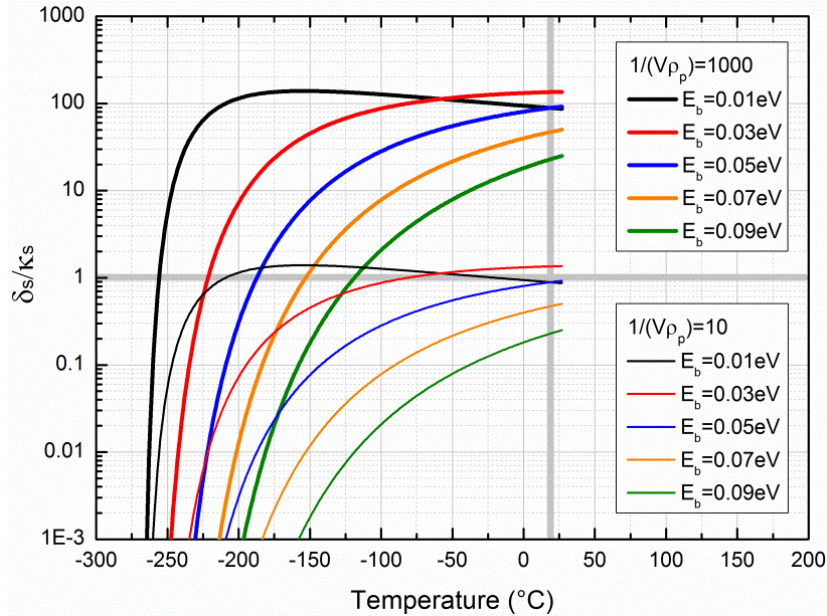


Figure 4.4.18. The ratio of δ_s/κ_s as a function of temperature. The calculations were carried out using two different sets of values for $1/(V\rho_p)$ and E_b based on Eq. (4.4.18).

This is obviously inconsistent to the experimental observations since shallow traps might already increasingly trap positrons at temperatures below $20 \text{ }^\circ\text{C}$. In order to reproduce such a feature, a minimum binding energy of 0.05 eV is required with $1/(V\rho_p) \approx 10$, which is only possible if the precipitates are large and have a high number density. For alloy H aged at RT for only 5 min, clusters with a high number density might be realistic but not a large size. Therefore, Eq. (4.4.18) cannot be used for modelling.

Another thermodynamic approach was also suggested by [Man81] and is sometimes used to describe the properties between trapping and de-trapping for small shallow traps [Saa89]:

$$\frac{\delta_s}{\kappa_s} = \frac{1}{\rho_s} \left(\frac{m^*}{2\pi\hbar^2} \right)^{3/2} (k_B T)^{3/2} \exp\left(-\frac{E_b}{k_B T}\right), \quad (4.4.19)$$

where ρ_s is the number density of small shallow traps, m^* is the effective positron mass [Maj66] ($0.511 \text{ MeV}/c^2$ as an approximation), \hbar is the normalized Planck constant. Using this equation, Fig. 4.4.19 can be derived:

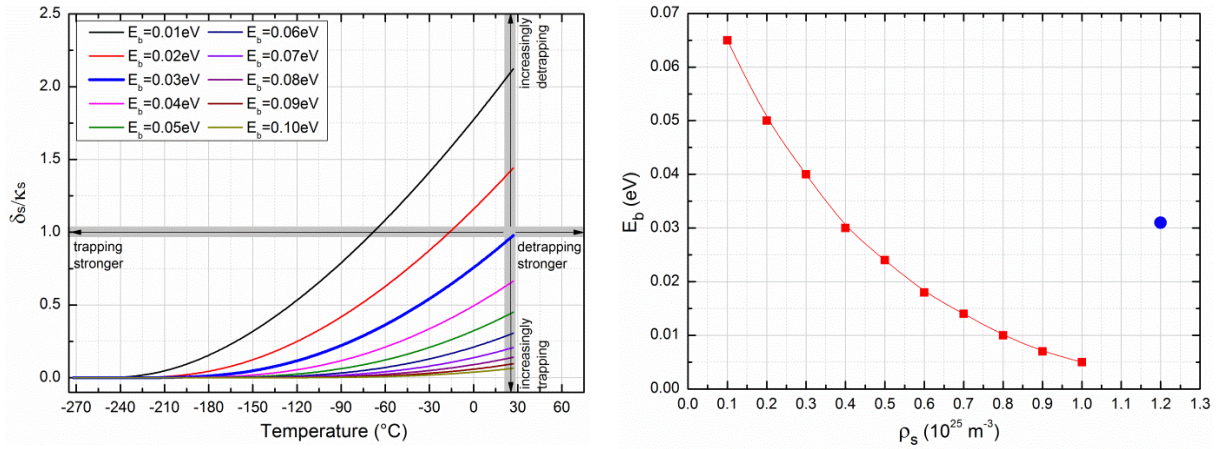


Figure 4.4.19. (L) The ratio of δ_s/κ_s as a function of temperature, $\rho_s = 0.4 \times 10^{25} \text{ m}^{-3}$; (R) Binding energy as a function of shallow traps number density. Blue dot is the result of fit.

The ratio of δ_s/κ_s was calculated with various ρ_s (0.1×10^{25} to $1 \times 10^{25} \text{ m}^{-3}$) and E_b (0.01 to 0.1 eV). Fig. 4.4.19 (L) gives an example calculated with a constant $\rho_s = 0.4 \times 10^{25} \text{ m}^{-3}$ but different E_b values. The blue curve which exhibits the desired behavior of the ratio δ_s/κ_s (< 1 for $T < 20 \text{ }^\circ\text{C}$, since the average thermal energy of a positron is about 0.04 eV at RT [Haa09], which is comparable with E_b) suggests a typical binding energy E_b of ~ 0.03 eV. All binding energies were calculated for different ρ_s similarly, as shown in Fig. 4.4.19 (R). This will be later used for the discussion. Both of ρ_s and E_b will be determined through fitting.

In addition, whether the trapping rate of shallow traps is temperature-dependent or not is still questionable. In this work, we applied a temperature-dependent κ_s as suggested by [Sme80]:

$$\kappa_s = \kappa_0 \cdot \exp(-\gamma T), \quad (4.4.20)$$

where κ_0 and γ are constants for a given positron binding energy and have to be determined by fitting. So far, all quantities required for fitting have been discussed. The fitting based on Eqs. (4.4.10 to 4.4.15) and Eqs. (4.4.19 to 4.4.20) to the experimental data was performed.

Full fitting was practically not applicable due to high number of fitting parameters. Thus, fitting was carried out intuitively (λ_b , λ_s and λ_v were fixed, all other parameters vary in the ranges which have been determined above). The results are shown in Fig. 4.4.20:

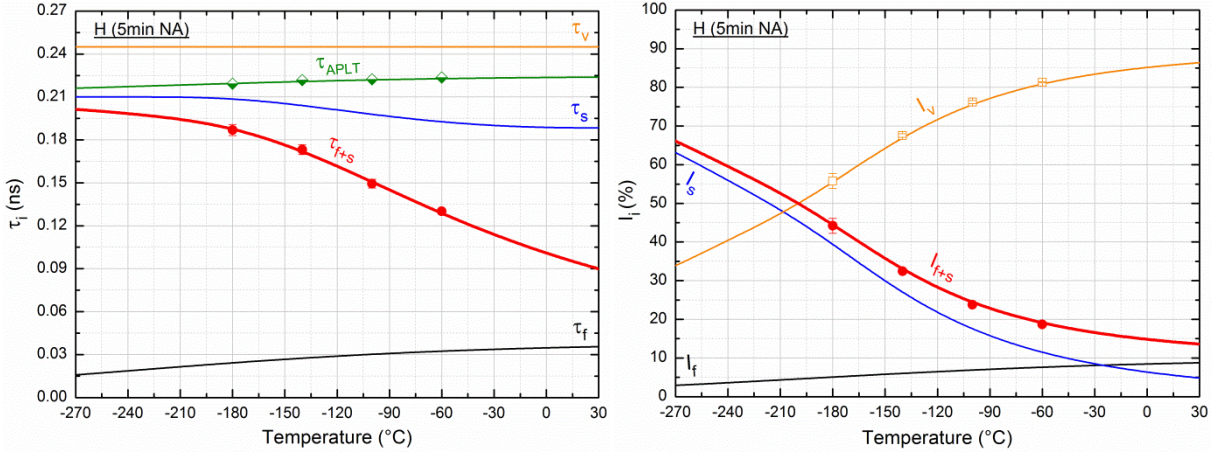


Figure 4.4.20. Temperature dependence of decomposed (L) τ_i and (R) I_i in alloy H after 5 min of NA. Experimental data (the same data as used in Fig. 4.4.8 to Fig. 4.4.10) and modelling results are accordingly represented by symbols and curves, respectively.

It can be seen that the experimental results obtained by 2-component analysis (with fixed τ_v) are consistent with the ones based on the extended trapping model. When temperature decreases from 20 to -273 °C, the following changes are observed:

- Reduced bulk (black curve): τ_f decreases from 0.040 to 0.015 ns while I_f also decreases from 9% to 3%, showing that such a contribution is suppressed during cooling.
- Solute clusters (blue curve): τ_s increases gradually from 0.190 to 0.210 ns probably due to the enhanced localization of positron wave function in the solute clusters when temperature drops. The marked increase of I_s from 5% to 63% also suggests increasing trapping of positrons by solute clusters. Both changes are caused by the decreasing δ_s/κ_s ratio towards LTs, where positron diffusion length decreases due to its reduced thermal energy and shallow traps become increasingly dominate. The superposition of bulk and solute cluster components exhibits the same feature as the experimentally determined τ_{f+s} and I_{f+s} . At RT, I_{f+s} contributes only 14%, which could be the reason for the difficulties encountered in decomposing the PLT spectra. Therefore, 1-component analyses were frequently carried out in previous studies [Ban11, Lay12].
- Vacancy-type defects (orange curve): although τ_v was fixed to 0.245 ns, I_s decreases markedly from 86% to 34% due to increasing trapping of positrons by clusters at LTs.

After fitting, the number density and binding energy of the shallow traps were determined as $1.2 \times 10^{25} \text{ m}^{-3}$ and 0.031 eV, respectively, see blue symbol in Fig. 4.4.19 (R). This combination deviates from the red symbols, i.e. $\rho_s = 1.2 \times 10^{25} \text{ m}^{-3}$ leads to an E_b value below 0.01 eV, while $E_b = 0.031 \text{ eV}$ corresponds to a ρ_s of $0.4 \times 10^{25} \text{ m}^{-3}$, see Fig. 4.4.19 (R). The number density and binding energy determined from fitting might represent a sum over solute clusters which differ slightly in their sizes (number of solutes), e.g. a mixture of clusters of size A with a ρ_s of $0.3 \times 10^{25} \text{ m}^{-3}$ ($E_b = 0.04 \text{ eV}$), of size B with a ρ_s of $0.4 \times 10^{25} \text{ m}^{-3}$ ($E_b = 0.03 \text{ eV}$) and size C a ρ_s of $0.5 \times 10^{25} \text{ m}^{-3}$ ($E_b = 0.02 \text{ eV}$). An appropriate combination of such clusters with a total ρ_s of $1.2 \times 10^{25} \text{ m}^{-3}$ and a mean E_b of 0.031 eV appears plausible. Although the exact reason for these values is unknown, such a ρ_s is realistic [Lia12, Mar13, Mor06, Rom11], and the E_b of 0.031 eV is also reasonable for shallow traps (close to the thermal energy of positrons at RT, $\sim 0.04 \text{ eV}$). Similar experiments analyzed differently (using Eq. (4.4.18) and STM) by [Klo10] proposed an E_b of $\sim 0.02 \text{ eV}$ using the same alloy.

No temperature dependence of the specific trapping coefficient μ is expected for charge neutral mono-vacancies in both semiconductors and metals [Dry95], as has been verified experimentally [Hau95, Klu91, Man87, Pet83, Wol92]. Combining this feature and applying Eq. (4.1.8) leads to the result that the trapping rate κ_v depends on the concentration of charge neutral mono-vacancies (as the ones in alloy H after 5 min of NA) rather than on temperature. Such dependencies are shown in Fig. 4.4.21 based on previous studies [Kra03, Pus90, Pus94]:

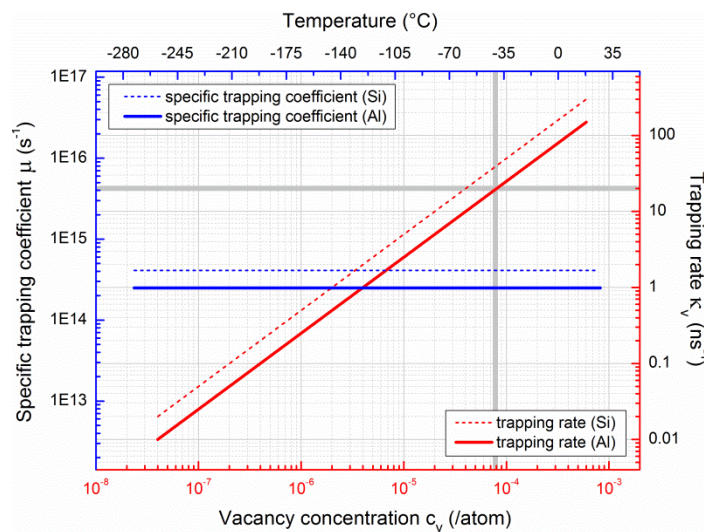


Figure 4.4.21. Temperature dependence of specific trapping coefficient μ in Si and Al (blue lines). Trapping rates κ_v (red lines) has been calculated using Eq. (4.1.8) as a function of vacancy concentration c_v .

Under such circumstances, the trapping rate κ_v was assumed temperature-independent for the fitting over the entire temperature range and its value was determined to $\sim 20 \text{ ns}^{-1}$. Using this value, the concentration of vacancy-solute complexes in alloy H after 5 min of NA could be further determined. As indicated by the gray cross in Fig. 4.4.21, $\kappa_v \approx 20 \text{ ns}^{-1}$ signifies a concentration of vacancy-type defects of $\sim 0.8 \times 10^{-4}$ /atom. This value is on the one hand lower than the calculated 1.46×10^{-4} /atom for alloy H, see Fig. 4.4.11 due to vacancy loss after quenching, but on the other hand, it is much higher than the one for pure Al ($\sim 0.2 \times 10^{-4}$ /atom, see Fig. 4.1.3), binary Al-Mg and Al-Si alloys (0.1×10^{-4} /atom to 0.3×10^{-4} /atom, see Fig. 4.2.5), pointing at strong interactions between Si, Mg atoms and vacancies.

The result obtained at the Uni. Prague as shown in Fig. 4.4.10 was validated by J. Cizek using 2 and 3-state trapping model (without fixing any parameter). Based on the decomposed annihilation parameters, the trapping rate into vacancy-type defects was calculated, yielding $\kappa_v = 7 \pm 9 \text{ ns}^{-1}$ after 5 min of NA, which is smaller than the result above of $\sim 20 \text{ ns}^{-1}$. Beside the experimental uncertainties and inaccuracies, the slightly higher κ_v in this study might have benefited from an improved quenching rate at HZB (more quenched-in vacancies).

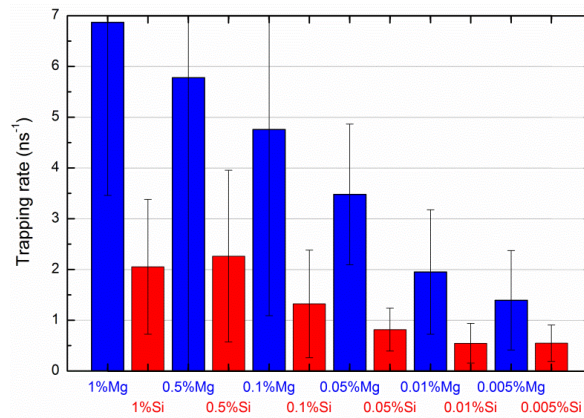


Figure 4.4.22. Trapping rate of binary alloys after 3000 min of NA, based on data shown in Fig. 4.2.2 and Fig. 4.2.3. A constant μ of $2.5 \times 10^{14} \text{ s}^{-1}$ was assumed, see Section 4.1.1.

Moreover, the trapping rate κ_v of vacancy-related defects in as-quenched Al-1%Mg alloy should be similar to the corresponding one as shown in Fig. 4.4.22 ($\sim 7 \text{ ns}^{-1}$) which is obtained after 3000 min of NA (actually it should be always the highest trapping rate among all investigated binaries during NA). Thus, κ_v (20 ns^{-1}) for alloy H after 5 min of NA is also higher than the values for binaries ($< 7 \text{ ns}^{-1}$) due to the higher concentration of vacancies.

The rest of fitting parameters κ_0 and γ in Eq. (4.4.20) equal 38 ns^{-1} and 0.01 K^{-1} , respectively.

4.4.1.9 Modelling of the Time Dependence of τ_{f+s} & I_{f+s} in Alloy H (FDA)

During NA, the shallow traps discussed in the previous sections become increasingly deeper. Therefore, another kind of extended trapping model dealing with two deep positron traps should be applied to model the time dependence of τ_{f+s} and I_{f+s} in alloy H during stages I and II. In order to simplify the complicated temperature dependence of the shallow component and to reduce the number of parameters which have to be determined by fitting, the trapping rate κ_s is replaced by κ'_s which is $\kappa_s - \delta_s$. This replacement is compensated by setting $\delta_s = 0$ in Eqs. (4.4.10 to 4.4.15). By using κ'_s , shallow traps can be virtually treated as “deep” traps. The solutions below are derived from Eqs. (4.4.10 to 4.4.15) with $\delta_s = 0$ [Kra03]:

$$\tau_f = \frac{1}{\lambda_b + \kappa'_s + \kappa_v} , \quad (4.4.21)$$

$$\tau_s = \frac{1}{\lambda_s} , \quad (4.4.22)$$

$$\tau_v = \frac{1}{\lambda_v} , \quad (4.4.23)$$

$$I_f = 1 - I_s - I_v , \quad (4.4.24)$$

$$I_s = \frac{\kappa'_s}{\lambda_b + \kappa'_s + \kappa_v - \lambda_s} , \quad (4.4.25)$$

$$I_v = \frac{\kappa_v}{\lambda_b + \kappa'_s + \kappa_v - \lambda_v} . \quad (4.4.26)$$

Before fitting, the time dependence of trapping rates for solute clusters and vacancy-type defects should be further specified by applying the models proposed by [Som00]:

- Solute cluster component

$$\kappa'_{s(t)} = \kappa'_{s(0)} + (\kappa'_{s(\infty)} - \kappa'_{s(0)})[1 - \exp(-t/t_s)] , \quad (4.4.27)$$

where $\kappa'_{s(0)}$ is the trapping rates of solute clusters at the beginning of stage I, and $\kappa'_{s(\infty)}$ can be roughly regarded as the trapping rate at the end of stage II. t_s is its characteristic time constant. Since the solute clusters gradually evolve during NA, it can be assumed that $\kappa'_{s(0)}$ equals zero and increases due to the formation and growth of solute clusters.

- Vacancy-related component

$$\kappa_{v(t)} = \kappa_{v(0)} \cdot \exp(-t/t_v), \quad (4.4.28)$$

where $\kappa_{v(0)}$ is the trapping rate of vacancy-type defects after quenching and should be close to $\sim 20 \text{ ns}^{-1}$ as determined in the last section. t_v is also a characteristic time constant. Since the diffusion-controlled annihilation process of quenched-in vacancies is thermally activated, therefore, t_v can be defined by the following Arrhenius type equation:

$$t_v = A \cdot \exp\left(\frac{E_a}{k_B T}\right), \quad (4.4.29)$$

where A is a pre-exponential factor, E_a an activation energy, k_B the Boltzmann constant and T the temperature.

To verify these models, the decomposed experimental PLT τ_{f+s} and its intensity I_{f+s} of alloy H aged at 0°C (during stage I and II) were fitted using Eqs. (4.4.21 to 4.4.28). Altogether, 4 parameters are determined by fitting, i.e. the trapping rates $\kappa'_{s(\infty)}$ and $\kappa_{v(0)}$ as well as the characteristic time constants t_s and t_v . Fitting of I_{f+s} was performed first due to its relatively simple form. If such obtained data set can also satisfactorily describe the time dependence of PLT τ_{f+s} , the fitting is then achieved. Otherwise, this procedure is repeated by adjusting the relevant parameters. The fitted results are shown in Fig. 4.4.23:

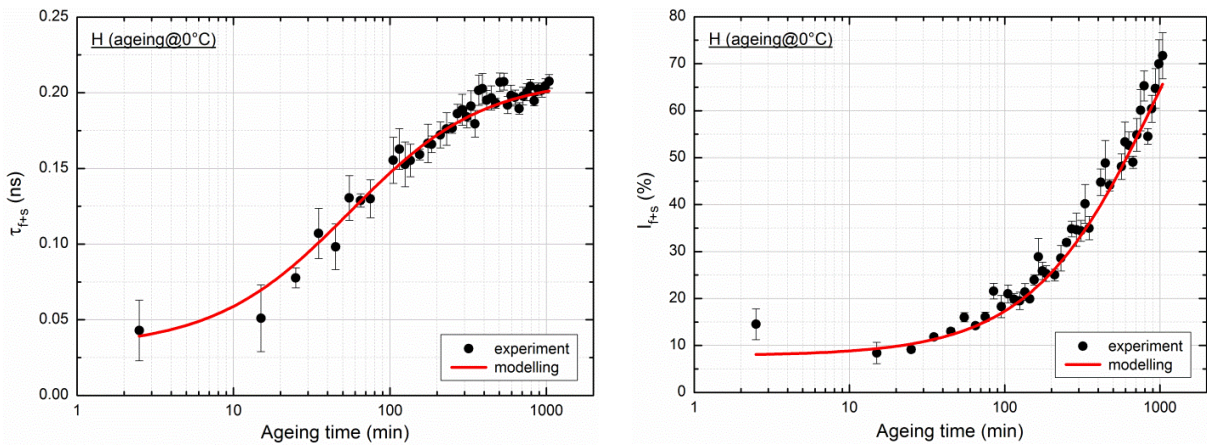


Figure 4.4.23. Modelling of the (L) PLT component τ_{f+s} and (R) its intensity I_{f+s} of alloy H during PALS stages I and II. Experimental data is the same as in Fig. 4.4.12 (R).

It can be seen from Fig. 4.4.23 that the trapping model introduced at the beginning of this section represents the experimental values very well except for the few initial data points. This could be caused by additional mechanisms which were not considered in the model or

by the simplified temperature dependence of shallow traps (replacement of $\kappa_s\text{-}\delta_s$ by κ'_s). Parameters determined through fitting are given in Table 4.4.1:

Table 4.4.1. Parameters determined from modelling of the time dependence of τ_{f+s} and I_{f+s} .

$\kappa'_{s(\infty)}$ (ns^{-1})	$\kappa_{v(0)}$ (ns^{-1})	t_s (min)	t_v (min)	adj. R-Square
130 ± 16	26 ± 3	3806	2010 ± 540	0.965

The constant trapping rate for vacancy-type defects for the as-quenched state $\kappa_{v(0)}$ equals $26 \pm 3 \text{ ns}^{-1}$, slightly higher than 20 ns^{-1} obtained from the other trapping model, see Section 4.4.1.8 for the sample naturally aged for 5 min. Due to the further improvement in quenching (CuQ) as well as due to the possible loss of vacancies to sinks during 5 min of NA, such a value is physically reasonable. Moreover, a vacancy concentration of $\sim 0.6 \times 10^{-4}$ /atom after 1000 min of ageing at 0°C is calculated using Eq. (4.4.28) and values in Table 4.4.1.

On the other hand, the trapping rate $\kappa'_{s(\infty)}$ for solute clusters at the end of stage II equals $130 \pm 16 \text{ ns}^{-1}$, ~ 5 times larger than that of vacancy-type defects. Due to our lack of knowledge about the specific trapping coefficient of solute clusters during ageing, a plausible value of 10^{15} s^{-1} for μ will be used [Dom05, Lip09]. Applying both values in Eq. (4.1.8), a solute cluster concentration of $\sim 1.3 \times 10^{-4}$ /atom can be estimated. This value is lower than the limit of saturated positron trapping and agrees with the experimental observations shown in Fig. 4.4.10 (very little bulk annihilation). According to atom probe studies [Tor11, Wan11] and kinetic Monte Carlo simulations [Lia12], about 10% of the solute atoms will go into clusters. Thus, dividing the total number of solute atoms 8×10^{-4} /atom (alloy H) by the concentration of clusters (1.3×10^{-4} /atom) leads to the result that each cluster contains ~ 6 solute atoms on average at the end of PALS stage II. Since identification of solute clusters strongly depends on the detection efficiency of an atom probe for Mg and Si atoms as well as the algorithm used (e.g. the maximum separation method), the real number of solutes per cluster could be larger than 6. The calculations are obviously not rigorous, but agree with the few available atom probe investigations qualitatively. For example, clusters containing 4 to 8 atoms were identified after 66 min [Cao13] and 1 week [Wan11] of NA; Most solute clusters were found to have 3 to 10 atoms on average by [Mar13]; After long ageing time (up to 4 weeks), [Rom11, Ser08] reported 25 to 30 solutes in solute clusters. Thus, the solute number per cluster estimated from PALS appears realistic.

PALS stages I and II are the most complicated stages among the entire evolution. The ageing mechanisms based on PALS experiments and theoretical modelling can be schematically described by the following figure:

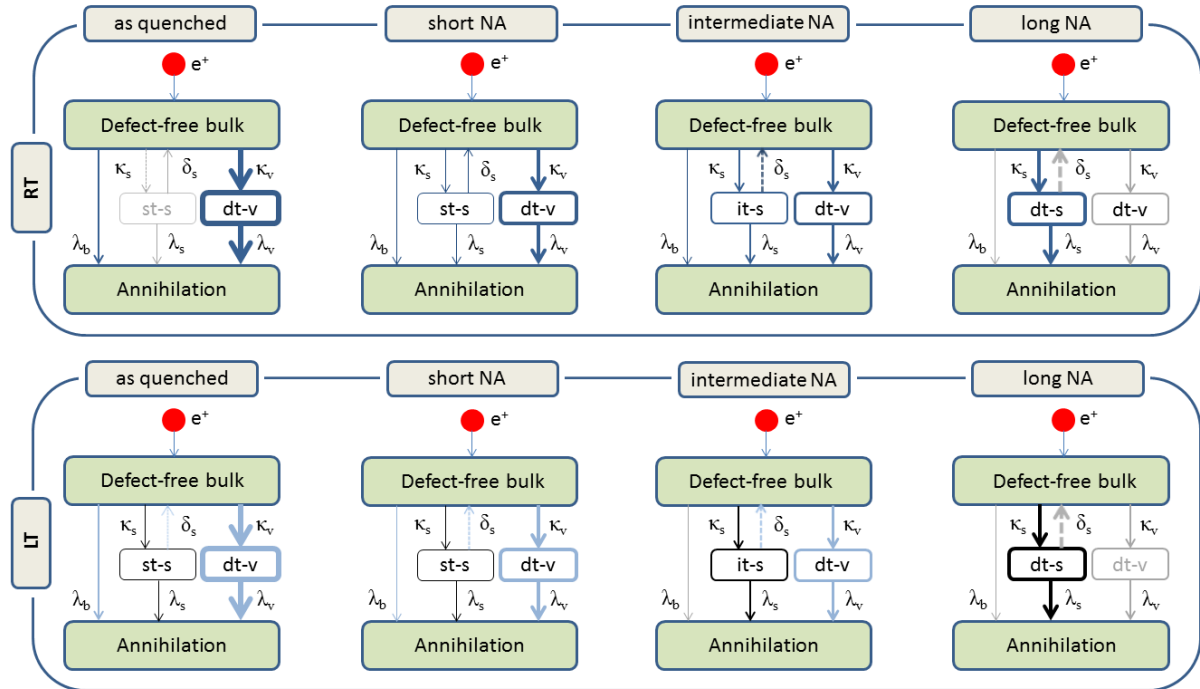


Figure 4.4.24. Temperature and time dependence of positron traps. κ and δ for trapping and de-trapping rate, respectively, λ for annihilation rate. “b” for free annihilation in bulk, “s” for solute clusters, “v” for vacancy-type defects, “st-s” for shallow trap-solute clusters, “it-s” for intermediate trap-solute clusters, “dt-s” for deep trap-solute clusters and “dt-v” for deep trap-vacancy-type defects. Thickness of the arrow indicates the contribution of the corresponding positron trap. Solid arrows mean dominant trapping or de-trapping rates while dashed arrows express the opposite. Gray boxes and lines refer to negligible positron traps, and darker or lighter arrow color denotes that the corresponding contribution increases or decreases from room temperature (RT) to low temperature (LT).

4.4.2 Doppler Broadening Annihilation Radiation

Naturally aged alloys F and H were measured by the DBAR method at $-60\text{ }^{\circ}\text{C}$. Various NA times were selected according to the characteristic times determined by PALS experiments:

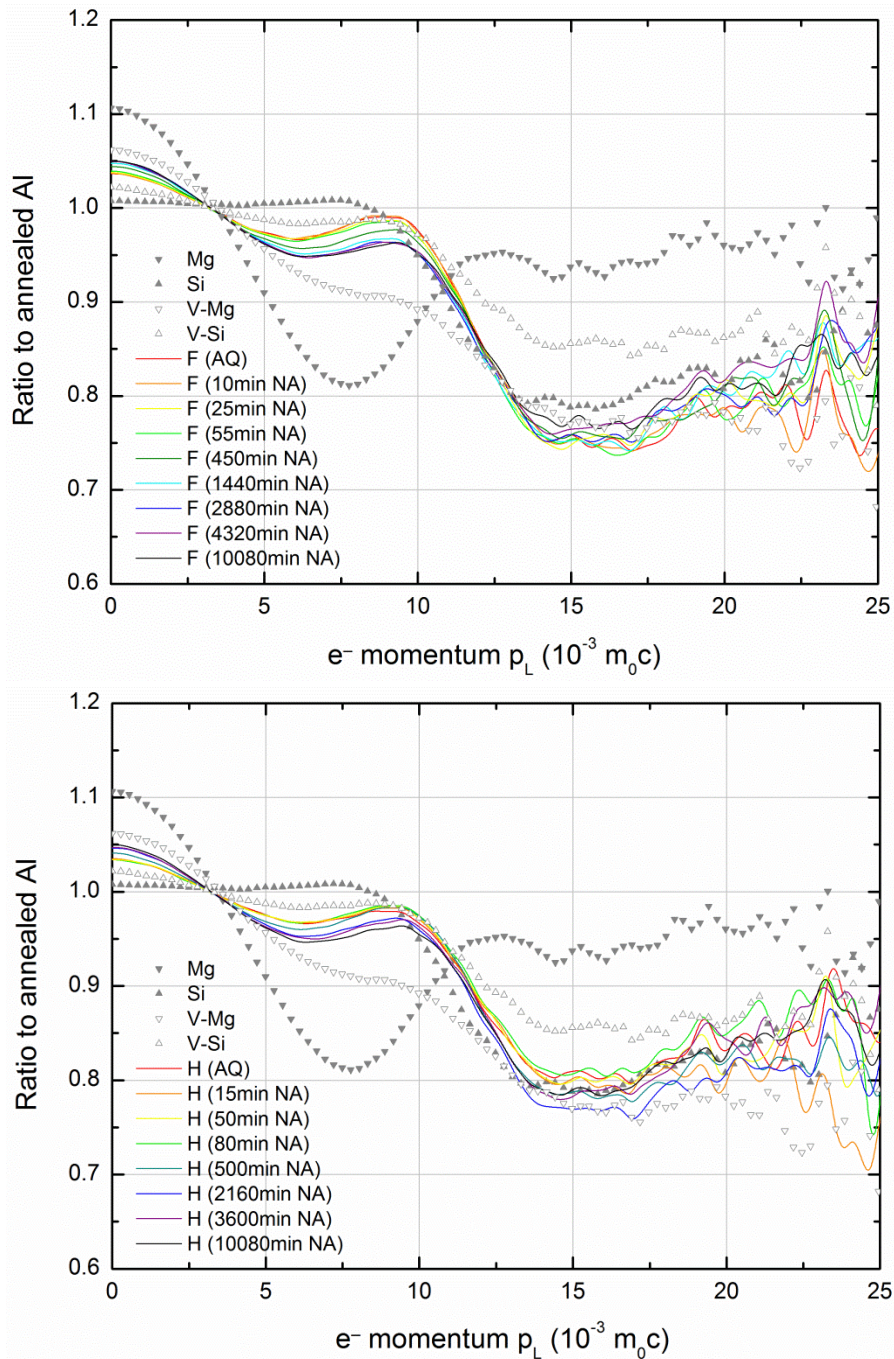


Figure 4.4.25. Ratio plots of alloys F and H aged at RT for various NA times. Curves for pure Mg (annealed at $450\text{ }^{\circ}\text{C}$ for 3 h and furnace cooled), Si (annealed at $900\text{ }^{\circ}\text{C}$ for 2 h and furnace cooled), V-Mg and V-Si (determined from quenched Al-1%Mg and Al-1%Si alloys, see Fig. 4.2.11) are also shown for comparison. Error bars are not given in order to show the overlapping curves in a clear manner.

The ratio profiles of alloys F and H are quite similar. With increasing momentum, the ratio decreases to a local minimum at $p_L \approx 7 \times 10^{-3} m_0c$, followed by an increase up to $p_L \approx 9 \times 10^{-3} m_0c$ and a further decrease. Ageing both alloys at RT leads to systematic changes of the ratio plot, e.g. increasing and decreasing ratio for low and intermediate-momentum region. These observations agree with previous work on alloy F [Ban12] and will be discussed as follows.

4.4.2.1 Low-momentum Region of Alloys F and H during NA (HMA)

Due to the positron sensitivity to low-momentum valence electrons, especially when vacancy-type defects are present, a reliable and quantitative analysis can be made with sufficient statistics by evaluating the S parameter. A direct comparison between S or W parameters determined by different energy window setting is difficult, but this problem can be solved by normalizing both parameters to the corresponding bulk values of S_{Al} and W_{Al} of annealed Al obtained using the same window settings (see Section 3.3.2.5). The evolution of S/S_{Al} and W/W_{Al} (will be called S and W parameters for simplicity) is shown in Fig. 4.4.26:

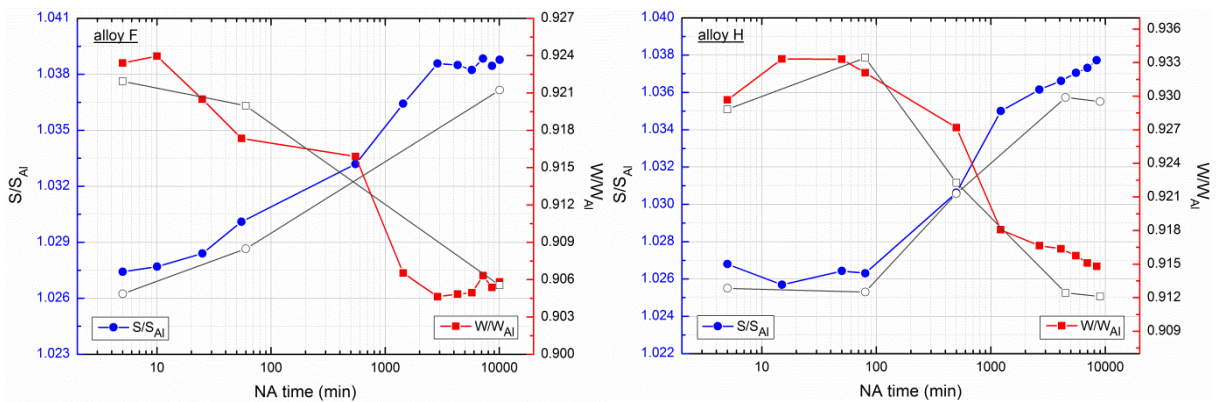


Figure 4.4.26. Normalized S (blue spheres) and W (red squares) parameters during NA of (L) alloy F and (R) alloy H after IWQ. Samples were measured at -60 °C. Gray curves are repetitions of the corresponding experiments, and the mean values from both will be used.

For alloy F, the S parameter increases continuously and levels off after ~ 2800 min of NA, while for alloy H, a nearly constant S is observed during the first 100 min, after which a tendency similar to alloy F is found (levels off after ~ 4400 min). The S parameter evolves only slowly after the first week of NA for both alloys. The time dependence of this parameter corresponds to the PALS stages shown in the previous section (i.e. the transition times where the slope of S or W curve changes coincide with that between PALS stages). Due to the statistical and methodological uncertainties, W parameter will not be discussed.

Due to the fact that positrons annihilate in various types of defects such as solute clusters and vacancy-type defects beside bulk metal during NA, these values, as listed in Table 4.4.2, are essentially required for the interpretation of S parameters [Dlu87, Dlu98]:

Table 4.4.2. S parameters for different traps ($i = b, v$ or p , “b” for bulk, “v” for vacancy, “p” for incoherent precipitate). The values in parentheses are derived from this study.

material	Al		Mg		Si			
trap	b	v	b	v	b	v*	2v	p
S_i/S_{Al}	1 (1)	1.04 (1.03)	1.10 (1.09)	1.13 (1.10)	0.98 (1)	(~1.025)*	1.033 – 1.067 (1.06)	1.02

The S value for a vacancy in bulk Si (as indicated by an asterisk in Table 4.4.2) is not available from the literature. Thus it must be determined independently. On the other hand, it is also important to verify the other existing values. S parameters of pure Mg and Si to Al were validated by DBAR measurements on annealed reference Mg, Si and Al samples.

However, to determine the S_v in bulk Mg and Si is challenging due to sample preparation, but it can be estimated as follows, based on the PALS measurements on the quenched binary Al-Mg and Al-Si alloys. Generally, the measured value of the S parameter is a linear combination of each of the individual S parameters $S_{d,i}$ and S_b which relate to significant trapping and annihilation of positrons by defects and bulk [Kra03]:

$$S = \sum_{i=1}^k \eta_i \cdot S_{d,i} + [1 - \sum_{i=1}^k \eta_i] \cdot S_b, \quad (4.4.30)$$

where “d” and “i” denotes defect and its type, “b” for bulk, η_i obeys the normalization condition. More specifically, this equation can be simplified for the case of binary alloys as:

$$S = \eta \cdot S_{V-Mg(Si)} + (1 - \eta) \cdot S_{Al}. \quad (4.4.31)$$

$S_{V-Mg(Si)}$ and S_{Al} relate to vacancy-solute complexes in Al and bulk Al. For Al-1%Mg and Al-1%Si alloys, the weighting factor η equals 52% and 27% (Section 4.2.2), and S equals 1.053 and 1.016, respectively. Thus, $S_{V-Mg(Si)}$ can be estimated by Eq. (4.4.31):

$$S_{V-Mg}/S_{Al} = 1.10$$

This value is lower than the literature value of 1.13, see Table 4.4.2, but still physically reasonable because it represents the S parameter for V-Mg in an Al matrix (fcc) rather than in a Mg matrix (hcp) as given in the literature. Therefore, the momentum distribution of valence electrons surrounding the vacancy should be different for these two cases.

$$S_{2V-Si}/S_{Al} = 1.06$$

Since PALS suggests di-vacancy-Si complexes as the main vacancy-type defects in the as-quenched Al-1%Si alloy [Liu12], this value should be related to 2V-Si in Al instead of V-Si. In many studies di-vacancy-type defects were induced in Si through implantation or irradiation, and the measured S parameters range from 1.033 to 1.067 after normalization [Ava96, Gol95, Mäk90, Nie93], partly in agreement with the present result. Moreover, the S value for V-Si was suggested by [Hau95] to be in the range of 1.02 to 1.03. Therefore, the average value of 1.025 is approximated and will be used in this study.

Based on these values, the evolution of the S parameters during NA for alloys F and H will be analyzed in two parts, according to the typical transition times observed from PLT evolution of the corresponding alloys, i.e. stages I + II and stages III + IV.

- Stages I + II

It should be mentioned that without assumptions the determination of all weighting factors from the only known experimental S value can hardly be carried out, because various kinds of positron annihilation sites are involved in this stage for both alloys, as already discussed in Section 4.4.1. Thus, the discussions made below are based on certain assumptions.

- Alloy F: PALS experiments show that at RT during stage II positrons increasingly annihilate in rapidly formed Si and Mg enriched co-clusters rather than in vacancy-solute complexes, which has been attributed to the high solute content of this alloy. Shortly after quenching, positron annihilation is dominated by vacancy-solute complexes, but cooling the sample to -60 °C where DBAR experiments were performed leads to certain changes in annihilation parameters. Although no LT PALS experiments on alloy F (after short NA) were performed, data from other experiments show that cooling the sample from 0 to -20 °C leads to an intensity increase of the solute cluster annihilation component from ~30% to ~45% for the equivalent ageing state, see Fig. 4.4.13. Thus, it is likely that at -60 °C the majority of positrons will be trapped by small solute clusters. If we assume complete positron trapping by vacancy-free solute clusters and neglect the contribution from their Al surroundings (< 7% for alloy H), the initial S parameter of 1.027 in Fig. 4.4.26 (L) can be approximated by the following equation [Dlu86]:

$$S = (1 - \omega) \cdot S_{Si} + \omega \cdot S_{Mg} , \quad (4.4.32)$$

where ω is the fractional weight of positron annihilation of the corresponding site. Employing the values given in Table 4.4.2, a Mg/Si ratio $\omega/(1-\omega)$ of 0.64 is calculated for the initial clusters which therefore are rich in Si. Taking the high mobility and concentration of Si in alloy F (twice as much Si as Mg) into account, such a chemical composition seems reasonable.

Nevertheless, if the contribution from vacancy-solute complexes cannot be neglected, vacancies associated with Si atoms should be dominating, since the experimentally determined S parameter (1.027) is closer to S_{V-Si} (1.025) than to S_{V-Mg} (1.13).

- Alloy H: due to the slower clustering process compared to alloy F, LT PALS measurements and modelling of alloy H show dominate positron trapping in vacancy-solute complexes shortly after quenching, see Fig. 4.4.13 and Fig. 4.4.20, i.e. the total amount of trapping in solute clusters and in the bulk after 5 min NA is less than 18% at $-60\text{ }^{\circ}\text{C}$, see Fig. 4.4.10. This will be neglected in order to simplify the estimate. The ratio between V-Si and V-Mg complexes can be calculated employing a similar method as Eq. (4.4.32):

$$S = (1 - \omega) \cdot S_{V-Si} + \omega \cdot S_{V-Mg} , \quad (4.4.33)$$

where the initial S value equals 1.026 in Fig. 4.4.26 (R), and the ratio between the number of V-Si and V-Mg will be ~ 100 , indicating that most positrons are trapped by V-Si complexes. This would be possible if the jump frequency of Si in Al is higher than that of Mg in Al and the binding energy of V-Si is stronger than that of V-Mg.

The discussions above are very speculative due to difficulties in accessing the very early kinetics of ternary Al-Mg-Si alloys. A more precise determination of the annihilation parameters for each individual PLT components should be carried out in future work, applying both of the positron lifetime and Doppler broadening techniques.

However, after a certain ageing time, the chemical composition of solute clusters can be determined in a more reliable way using Eq. (4.4.32). The contribution of vacancy-type defects will be neglected, since after stage II most positrons will be trapped by solute clusters for both alloys F and H, see Fig. 4.4.10 (e.g. results from the Uni. Prague shows that after 140 min of NA, only one PLT component τ_s of solute clusters can be observed) and 4.4.12. The results are shown as follows.

- Stages III + IV

After PALS stage II, saturated positron trapping by solute clusters (where positrons “see” these clusters as a mixed “bulk” consisting Si and Mg atoms) can be safely assumed for both alloys F and H ($I_s > 80\%$), based on the multi-component PALS analysis, see Fig. 4.4.10 and 4.4.12. Applying the same method as above, the Mg/Si ratio in these clusters can be estimated, and the results are shown in Fig. 4.4.27:

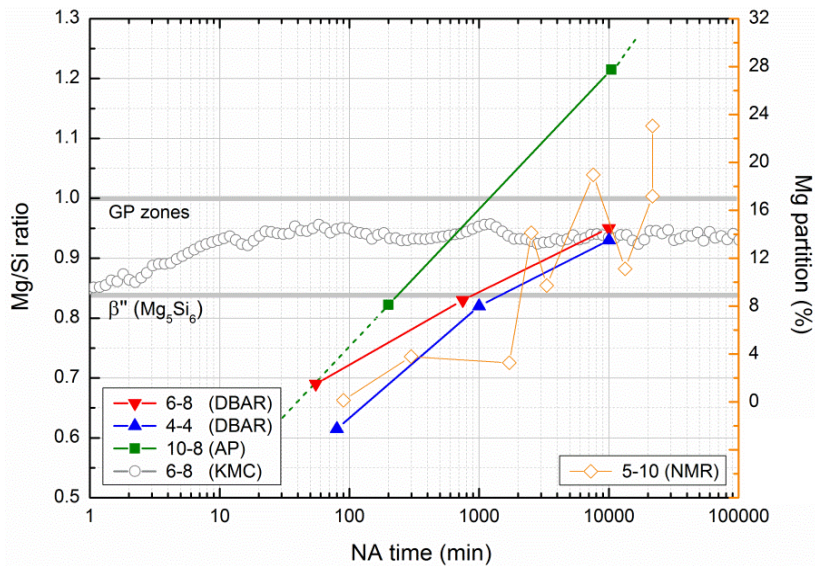


Figure 4.4.27. Mg/Si ratio of alloys F and H during NA derived from DBAR measurements. Some ratios determined from atom probe (AP) [Ser08], kinetic Monte Carlo (KMC) simulation [Lia12], and nuclear magnetic resonance (NMR, right y-axis) experiments [Lay12] on some other alloys are also given. The gray lines indicate the Mg/Si ratio in GP zones and β'' precipitates.

By the end of stage II, Si excess solute clusters are identified in alloys F and H according to the calculated Mg/Si ratio of 0.69 and 0.62, respectively. During further ageing, the ratios increase to 0.83 and 0.82 for alloys F (labelled as “6-8”) and H (“4-4”) at the end of stage III (~750 and ~1000 min for alloys F and H), indicating that the contribution from Mg to cluster formation is enhanced. A much more balanced composition between Si and Mg was achieved after ~10000 min of NA, where Mg/Si ratio approaches 0.95 and 0.93 for alloys F and H, see Fig. 4.4.27. The dominating contribution from Si for stage I, II and Mg for the subsequent stages was also proposed by [Cha12], based on DSC thermal analysis of the same alloys. However, it should be mentioned that the slightly higher positron affinity to Si (-6.95 eV) than to Mg (-6.18 eV) [Pus94] could lead to a stronger localization of positrons by Si. Thus, the “real” Mg/Si ratio could be higher than the values found here [Dlu86]. As shown in Fig.

4.4.27, different Mg/Si ratios have been reported, e.g. an Al-1.05%Mg-0.78%Si alloy (“10-8”, at.%) was aged at RT for ~ 200 min and was investigated using atom probe [Ser08]. It was found that the solute clusters are much richer in Si atoms than expected from the alloy composition. Further ageing results in an increase of this ratio, in the same manner as this work. However, the Mg-rich cluster that they found after 1000 min of NA have a Mg/Si ratio well above 1, see green dashed line in Fig. 4.4.27. The ageing behavior of an Al-0.46%Mg-1.05%Si-0.14%Fe (“5-10”, wt.%) alloy at RT was measured by [Lay12] employing solid-state NMR. A significant Mg partitioning from the solid solution into clusters after ~ 90 min of NA was found, corresponding to typical transition time between PALS stages II and III. In addition, kinetic Monte Carlo calculations on alloy F shows a similar behavior of the Mg/Si ratio as in this work [Lia12], especially for prolonged NA times (inaccuracies in time scale should be considered, e.g. vacancy loss is neglected in the simulation which would otherwise retards the kinetics). For the initial stage, Mg/Si ratio obtained from PALS is lower than the calculated one, which is either due to higher positron affinity to Si or to calculation errors.

4.4.2.2 Intermediate-momentum Region of Alloys F and H during NA (HMA)

Mg and Si can be easily distinguished by their characteristic ratio profiles around $p_L = 8 \times 10^{-3} m_0c$, where the ratio of Mg reaches its minimum while Si goes through a maximum, see Fig. 4.4.25. A simple approach with lower but sufficient accuracy will be used to derive some qualitative information on ageing kinetics of alloys F and H based on such signatures, i.e. by plotting the ratios of an alloy at $p_L = 8 \times 10^{-3}$ and $9 \times 10^{-3} m_0c$ as a function of NA time, see Fig. 4.4.28:

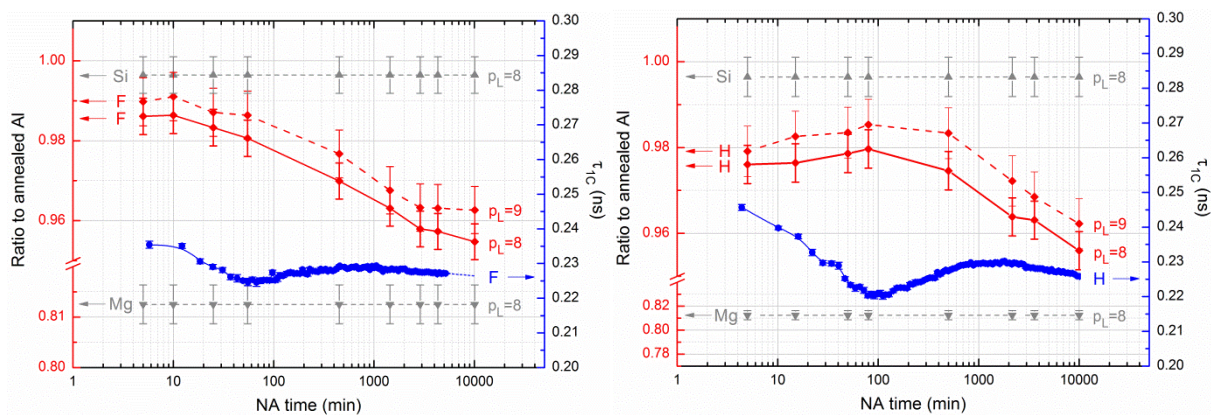


Figure 4.4.28. Doppler annihilation ratios at $p_L = 8 \times 10^{-3}$ (red solid line) and $9 \times 10^{-3} m_0c$ (red dashed line) of (L) alloy F and (R) alloy H during NA. The values for pure Mg and Si at the specified momenta (gray symbols) and PALS results for alloys F and H (blue curves) are also given.

- Alloy F: during the first 10 minutes of NA (stage I), a small enhancement in peak height towards Si was observed. Such a feature is not yet fully understood, see Section 4.4.1.6. During subsequent ageing up to ~ 10000 min, a continuous reduction in ratio (towards Mg) is observed. Thus, previous results pointing at an increasing Mg/Si ratio during NA are confirmed at this point. Nevertheless, the entire ratio curve is closer to Si in a general sense, indicating the dominance of Si at the annihilation site. The present results agree with [Ban12] who measured alloy F at -90 °C. However, a typical transition at ~ 60 min as seen in PALS is not observed in Fig. 4.4.28. This tendency was found for both selected momenta ($p_L = 8 \times 10^{-3}$ and 9×10^{-3} m_0c).
- Alloy H: in the as-quenched state, the ratio of alloy H exhibits more similarities to the V-Si complex rather than to V-Mg. Due to the variety of different positron annihilation sites such as bulk, solute clusters and vacancy-solute complexes which all compete in the initial stage of NA, a qualitative statement can hardly be made. With proceeding NA, the ratio increases up to 80 min towards Si and then drops continuously. This transition time matches the one between PALS stages II and III. Similar to alloy F, the overall distribution of the ratios in alloy H also reveals strong Si signals.

As mentioned in Section 4.1.2 and Section 4.2.2, one should be cautious when evaluating peak structures in the intermediate-momentum region, since the real information from the alloys could be markedly affected by the confinement peaks of positrons in the same region.

4.4.2.3 High-momentum Region of Alloys F and H during NA (HMA)

As discussed above, the annihilation site can be identified by combining ab-initio calculations and HMA. However, no calculations were available concerning solute clustering in Al-Mg-Si alloys so far. Besides, due to the insufficient signal to noise ratio, the statistical rareness of annihilation events related to high-momentum electrons, the absence of high-momentum structures together with the inaccuracies during mathematical evaluation in this momentum region, no systematical tendency was observed, and except the observation that the ratio curves of both alloys show always similar distributions to Si during NA, no other quantitative or qualitative statements can be made in a reliable way. Hence, CDBS measurements were performed at the Charles University in Prague, and the results are shown in the following.

4.4.2.4 Ratio Curve Analysis of Alloy H during NA (CDBS, Prague)

The chemical surroundings of the annihilation sites were probed by measuring the high-momentum distribution of the core electrons by CDBS at the Uni. Prague, benefiting from the improved signal to noise ratio and energy resolution.

Two Ortec coaxial HPGe detectors and the $27\text{-}\mu\text{Ci } ^{22}\text{Na}$ sources were used. The spectrometer has a coincidence count rate of $\sim 600 \text{ s}^{-1}$ and an energy resolution of $\sim 1.0 \text{ keV}$ at the annihilation peak (0.511 MeV). Alloy H (aged for 5 and 70 min) were measured at a constant temperature of $-150 \text{ }^\circ\text{C}$ and the results are shown together with pure Mg, Si references in Fig. 4.4.29:

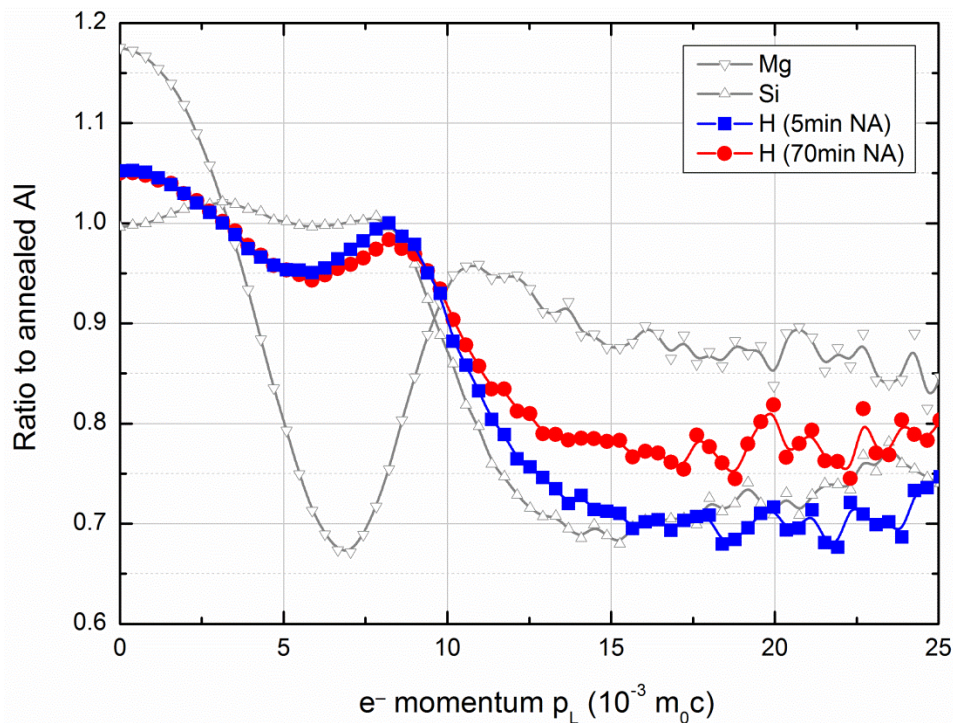


Figure 4.4.29. CDBS ratio plots of alloy H aged for 5 (blue solid squares) and 70 min (red solid spheres) at RT. The ratio curves for annealed reference samples of pure Si (6N) and pure Mg (4N) are also plotted (gray open triangles).

Compared to the single peak at $p_L \approx 8 \times 10^{-3} m_0c$ evaluated by HMA method as shown in Fig. 4.4.25, the Si ratio curve exhibits two characteristic peaks located at $p_L \approx 3 \times 10^{-3}$ and $8 \times 10^{-3} m_0c$ in Fig. 4.4.29. This is probably due to the higher energy resolution of the spectrometer at Uni. Prague. The ratio curve for pure Mg is characterized by a pronounced minimum at $p_L \approx 7 \times 10^{-3} m_0c$ followed by a local maximum located at $p_L \approx 11 \times 10^{-3} m_0c$, and agrees with the one in Fig. 4.4.25.

One can see that the ratio curves for alloy H measured after 5 min of NA exhibit a peak at $p_L \approx 8 \times 10^{-3} m_0c$, which is a signature for positrons annihilated by electrons at Si sites or in vacancies in Al. Actually, the high-momentum part ($p_L > 15 \times 10^{-3} m_0c$) of the ratio curve is almost identical with that for pure Si. This testifies that defects in quenched alloys are surrounded mainly by Si atoms. Hence, positrons are trapped mostly by V-Si complexes shortly after quenching (here ~ 5 min).

Inspection of Fig. 4.4.29 further shows that the peak at $p_L \approx 8 \times 10^{-3} m_0c$ is lower in the alloy aged for 70 min at RT. This indicates a decrease in the contribution of positrons annihilated by electrons at Si sites or vacancy in Al. Thus, the relative contribution to annihilation of V-Si complexes decreases in accordance with a decrease in the intensity of the component with the PLT $\tau_v \approx 0.245$ ns observed by PALS. This is accompanied by an enhancement in the high-momentum range suggesting a rising contribution of positrons annihilated by electrons at Mg sites. This is plausible since the appearance of coherent clusters characterized by the PLT $\tau_s \approx 0.210$ ns has been detected by PALS already and these clusters certainly contain Si and Mg atoms. As after 70 to 80 min of NA between 50% and 75% of the annihilation take place in such clusters (see Fig. 4.4.10) there must be a considerable amount of Mg in these vacancy-free clusters. This finding differs from the HMA results above and the measurement in a previous work [Ban12], where the signal remained dominated by Si sites even after long NA of alloy F. This discrepancy could be due to the different alloy used (alloy F instead of alloy H), the higher measurement temperature (-90 °C instead of -150 °C) and / or the different experimental method applied there (HMA instead of CDBS).

Based on the PALS and DBAR (CDBS) observations, the formation and growth of solute clusters during NA in Al-Mg-Si alloys can be schematically illustrated, see Fig. 4.4.30.

During ageing the Al-Mg-Si alloys F and H at RT, several distinct stages were successfully probed by applying positron annihilation techniques. The main aim of the next section focuses on the ageing behavior of these alloys, investigated by other applicable integral methods such as differential scanning calorimetry, electrical resistivity and hardness measurements as well as kinetic Monte Carlo simulations (carried out by C.S.T Chang, J. Kühn, Y. Yan and Z.Q. Liang). Similar features were found in these experiments which coincide with PAS observations, as shown in Section 4.4.3.

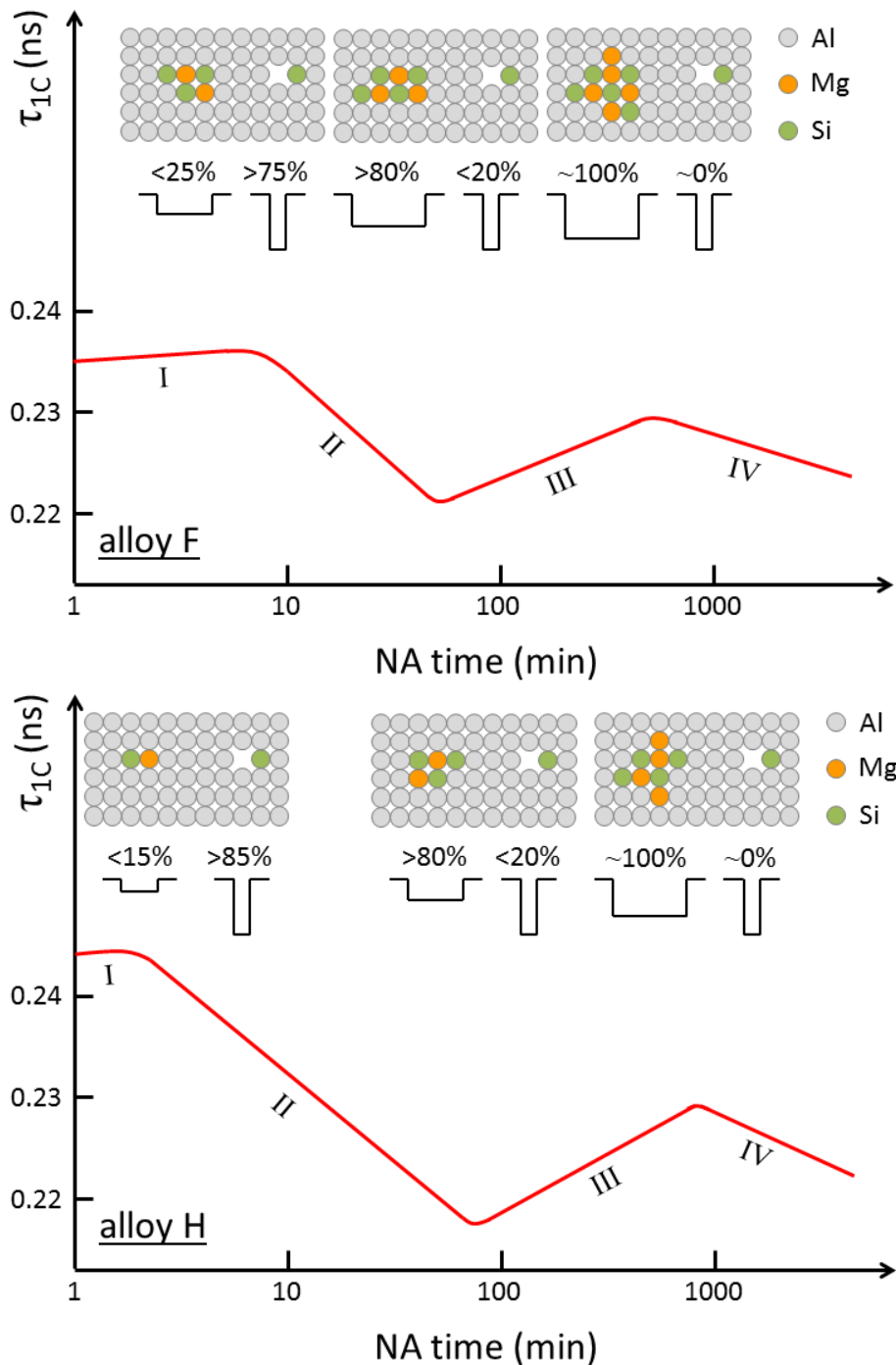


Figure 4.4.30. Schematic illustration of the clustering kinetics in alloys F (top) and H (bottom) during NA. For both figures, two objects (solute clusters and vacancy-solute complexes, bulk annihilation is neglected to simplify the sketch) compete with each other in trapping positrons. The trapping potential of solute clusters becomes broader and deeper with ageing time, thus increasingly trap positrons, as indicated by the corresponding fraction of trapped positrons, see Fig. 4.4.12.

4.4.3 Comparison with Differential Scanning Calorimetry Measurements

The heat transfer related to certain kinds of phase transformations such as clustering was investigated by means of isochronal DSC experiments. With a heating rate of 10 K/min, at least two overlapping clustering peaks were observed in the heat flow curves [Cha12], namely, peak C1 at ~ 55 °C and C2 at ~ 85 °C, as verified by several other studies [Dut91, Gup99]. In addition, a weak cluster peak C0 at $\sim RT$ can also be observed in some cases by [Cha11, Cha12].

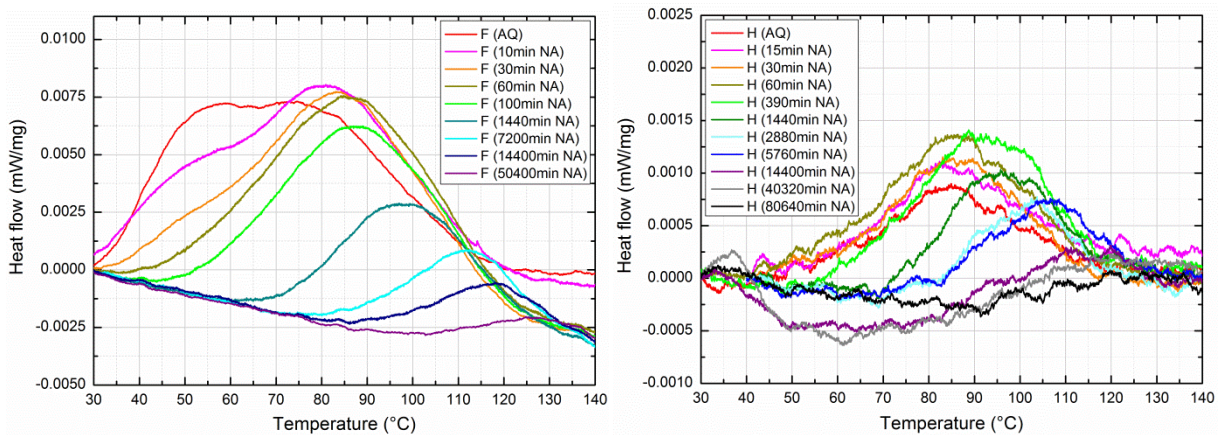


Figure 4.4.31. Heat flow curves of (L) alloy F and (R) alloy H during isochronal DSC runs at a heating rate of 10 K/min (only the clustering peaks are shown). Measurements were carried out by C.S.T. Chang and Y. Yan.

The clustering peaks for alloy F are clearly visible in the temperature range 30 to 140 °C, due to the high total solute concentration and the similar Mg and Si content (for alloys with equal total solute content, the heat effect is largest if Mg/Si ratio approaches 1 [Cha12]). C1 can be easily identified for the as-quenched state but gradually disappears during the first 60 min of NA, implying that C1 could be related to the initial PALS stages I and II. A notable reduction in peak area of C2 is observed after ageing the alloy for at least 60 min (stage III), which also coincides with the PALS results. To analyze the clustering peaks in alloy H is more difficult. C1 can barely be seen, since the low concentration of solutes results in a low total heat effect. Even so, a similar evolution of C2 as for alloy F is observed.

Furthermore, the dependence of the clustering peaks on the Mg/Si ratio was investigated [Cha12]. It was proposed that both Si and Mg are required for clustering, but C1 is more related to Si while C2 is Mg dominated (low activation energy C2 for high Mg content). These observations agree with positron results.

If non-interacting parallel reactions are incorporated in a complex process, the total degree of transformation (clustering) D_{total} can be described by the sum of the individual reactions D_{C1} and D_{C2} according to [Vya92]:

$$D_{total} = x \cdot D_{C1} + (1 - x) \cdot D_{C2}, \quad (4.4.34)$$

where D_{C1} and D_{C2} represent the simulated individual degree of cluster formation corresponding to C1 and C2 ($D_{C1(C2)} = A(T)_{C1(C2)}/A_{total}$, $A(T)_{C1(C2)}$ is the area under the curve up to the temperature T for C1 or C2, A_{total} is the total peak area of C1 and C2 [Cha12]). The contribution factor x equals 0.34, as derived from previous DSC measurements [Lia12]. Moreover, Eq. (4.4.34) was modified after the best fitting of the resistivity data to DSC results by [Küh13]:

$$D'_{total} = x \cdot D_{C1} + (1 - x) \cdot \sqrt[3]{D_{C2}}. \quad (4.4.35)$$

For alloy F, the simulated change of D_{C1} , D_{C2} as a function of NA time and the total degree of transformation D_{total} , D'_{total} calculated by Eqs. (4.4.34 to 4.4.35) are plotted in Fig. 4.4.32. A transition time at ~60 min could also be observed (blue dashed curves and orange solid curve) as the one between stages II and III found by PALS experiments:

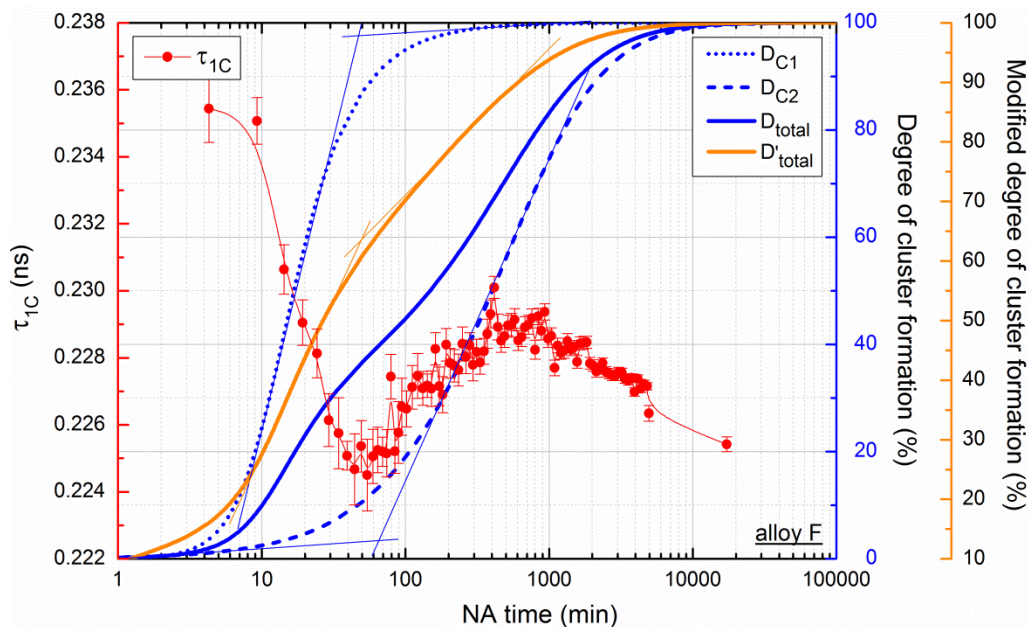


Figure 4.4.32. Kinetic modelling of the degree of cluster formation in alloy F aged at RT. Dashed curves stand for individual cluster formations of C1 and C2. The solid curves are the summation of both based on different algorithms. DSC data is provided by C.S.T. Chang and Z.Q. Liang.

4.4.4 Comparison with Electrical Resistivity Measurements

Various scattering effects such as at vacancies and impurities are known to notably affect the electrical resistivity of a metallic material. There are several studies that find an increment of resistivity during isothermal ageing of an alloy and ascribe it to the formation of solute clusters [Sey09]. At least three distinct stages were identified from experiments carried out by [Küh13], as shown in Fig. 4.4.33:

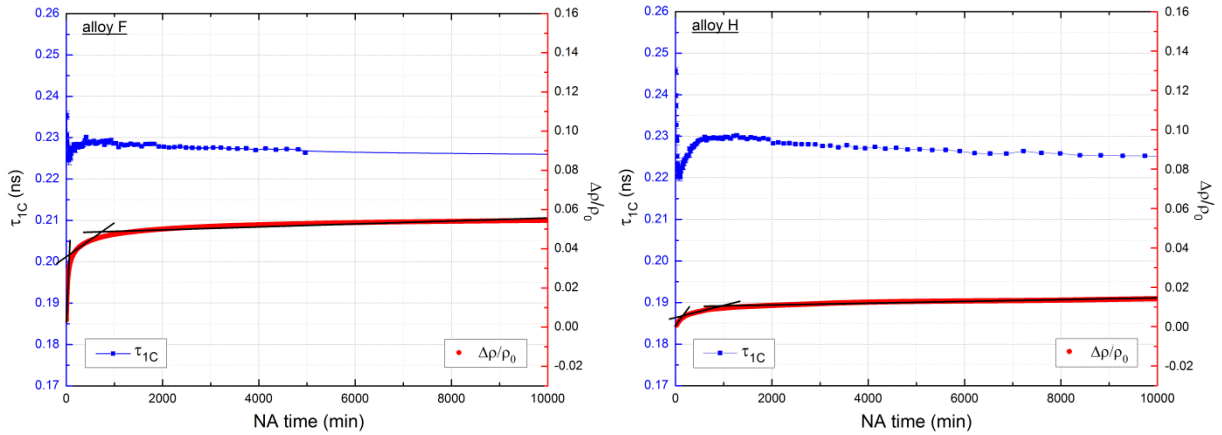


Figure 4.4.33. Electrical resistivity evolution of (L) alloy F and (R) alloy H during RT ageing after IWQ. Linear time scale is used to show the fast increase of resistivity in the initial stage of NA. Lines in black are plotted to guide the eye. PALS results of both alloys are also given.

Errors from measuring the geometrical size of the sample wire (e.g. cross section, length) can be eliminated by normalizing the increase in resistivity by using the following equation:

$$\frac{\Delta\rho}{\rho_0} = \frac{\rho_t - \rho_0}{\rho_0} = \frac{U_t - U_0}{U_0}, \quad (4.4.36)$$

where ρ_t and ρ_0 are the resistivity of the sample at times t and 0 , and the normalized change in resistivity depend only on the corresponding voltage U . The resistivity data from both alloys were evaluated by this equation, individual stages were observed in the evolution of $\Delta\rho/\rho_0$, i.e. a rapid increase of $\Delta\rho/\rho_0$ during PALS stage I to II (or DSC C1). This increase was markedly slowed down when NA proceeds, and after PALS stage III (DSC C2), only slight change in resistivity was observed. This tendency can be clearly seen from Fig. 4.4.33.

In addition, resistivity evolution at 0°C obtained by [Küh13] were also compared to parameters of positron lifetime decompositions at the same temperature, in order to obtain additional information concerning ageing kinetics, see Fig. 4.4.34.

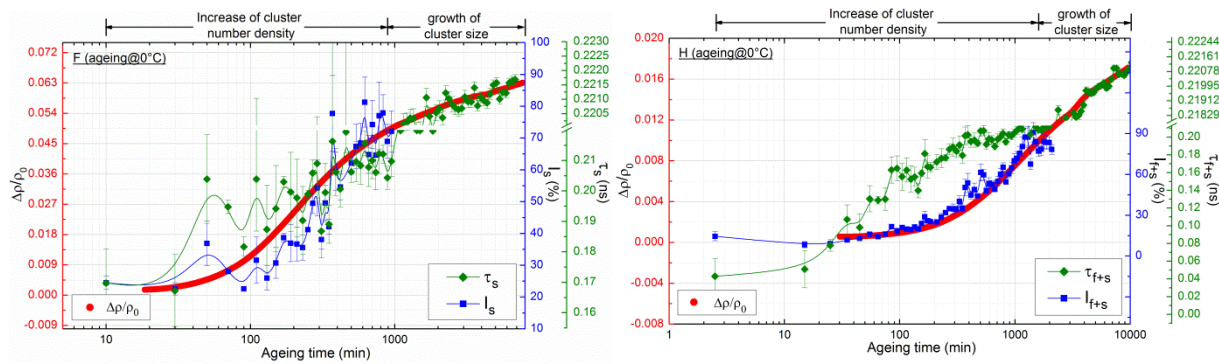


Figure 4.4.34. Comparison between PLT decomposition parameters and normalized resistivity changes during ageing of (L) alloy F and (R) alloy H at 0 °C. Y-axes were scaled to a specific range in order to reveal the similarities between resistivity and PALS parameters.

As shown in Fig. 4.4.34, the relative change in resistivity always matches the cluster intensity evolution better than the corresponding PLT for stages I and II (up to ~1000 min for alloy F and ~2000 min for alloy H). The same was observed by ageing both alloys at LTs (-20 and -10 °C, see appendix A.2). The resistivity was also calculated by [Cha13] using Eq. (4.4.37):

$$\rho = \rho_i + (\rho_f - \rho_i) \cdot \left[x \cdot \left(1 - \left[\frac{(k_1 \cdot t)^{n_1}}{i_1} + 1 \right]^{-i_1} \right) + (1 - x) \cdot \sqrt[3]{1 - \left[\frac{(k_2 \cdot t)^{n_2}}{i_2} + 1 \right]^{-i_2}} \right], \quad (4.4.37)$$

where ρ is the modelled resistivity, ρ_i and ρ_f are the initial and final resistivity, x equals 0.34 as above, k_1 and k_2 are the pre-exponential factors for the 1st and 2nd cluster reaction, n_1 and n_2 are similar to Avrami exponents, i_1 and i_2 are impingement factors [Sta01]. As shown in Fig. 4.4.35, this model agrees with experimental results quite well. Thus, from DSC parameters and some other discussion, it was suggested that stages I and II relate to the number density evolution of the solute clusters while stage III corresponds to their growth.

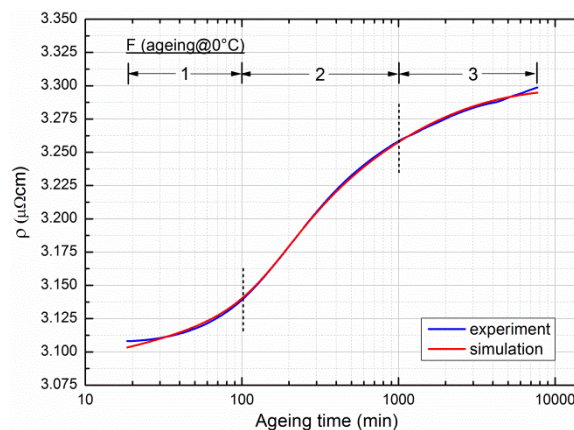


Figure 4.4.35. Experimental and simulated resistivity evolution of alloy F aged at 0 °C. “1”, “2” and “3” indicate the stages where fast, intermediate and slow increase of resistivity was observed. Data is provided by C.S.T. Chang and J. Kühn.

4.4.5 Comparison with Hardness Measurements

The formation of solute clusters hinders the movements of dislocations, thus hardening the material. For alloy F, the evolution of Vickers-hardness reveals two to three stages. Taking alloy F in Fig. 4.4.36 (a) as an example, a rapid increase of ~ 18 HV is observed during the first NA stage, while subsequent ageing results in a much slower hardening response, i.e. a comparable increase in hardness was achieved by ageing the alloy for ~ 4000 min. This tendency can be more clearly demonstrated using a linear time scale, see Fig. 4.4.36 (c). On the other hand, alloy H also exhibits faster hardening during the initial stage in a similar manner to alloy F, but the increment is much less, namely, only ~ 4 HV, see Fig. 4.4.36 (d). Transition times between fast and slow hardening stages for both alloys roughly match the PALS transition from stages II to III, at ~ 60 and ~ 80 min for alloys F and H, respectively.

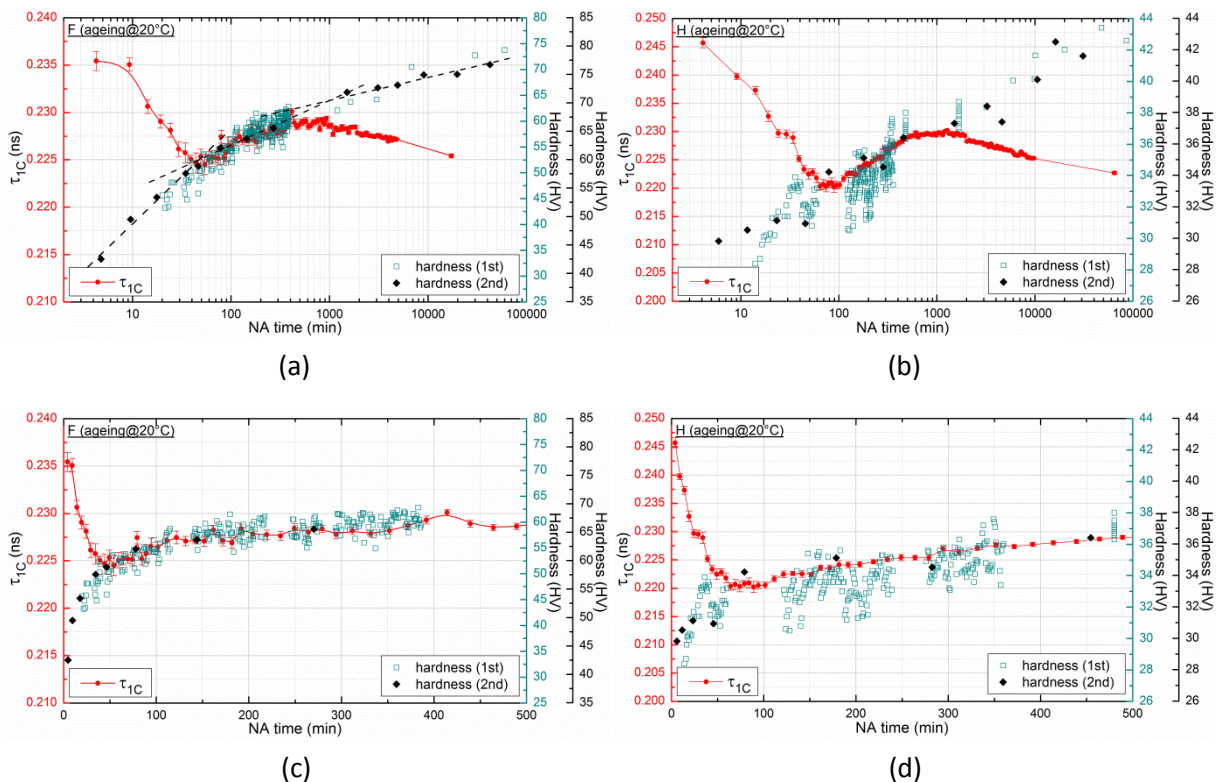


Figure 4.4.36. Hardness evolution in alloys F and H during NA. (a) and (b) are displayed against NA time on a logarithmic scale, while (c) and (d) are illustrated on a linear scale. Hardness data are given from two independent series of measurements (1st and 2nd) on different samples. Each black solid diamond represents the average of 10 hardness measurements, while every green open square corresponds to an individual measurement. PALS results of both alloys are also given. Y-axes were scaled to a specific range in order to reveal the similarities between hardness and PALS parameters. Hardness measurements were carried out by C.S.T. Chang and Y. Yan.

4.4.6 Comparison with Kinetic Monte Carlo Simulations

The simulation was performed using a box consisting of $25 \times 25 \times 25$ unit cells with all sites occupied by Al, Mg and Si atoms according to the alloy composition. A single vacancy was randomly generated and is preserved in the simulation box throughout simulation [Lia12]. After converting the Monte Carlo steps into real time, the natural ageing behavior of various quantities can be determined such as number density and size of solute clusters, which will be compared to PALS results on alloy F aged at 0°C , see Fig. 4.4.37:

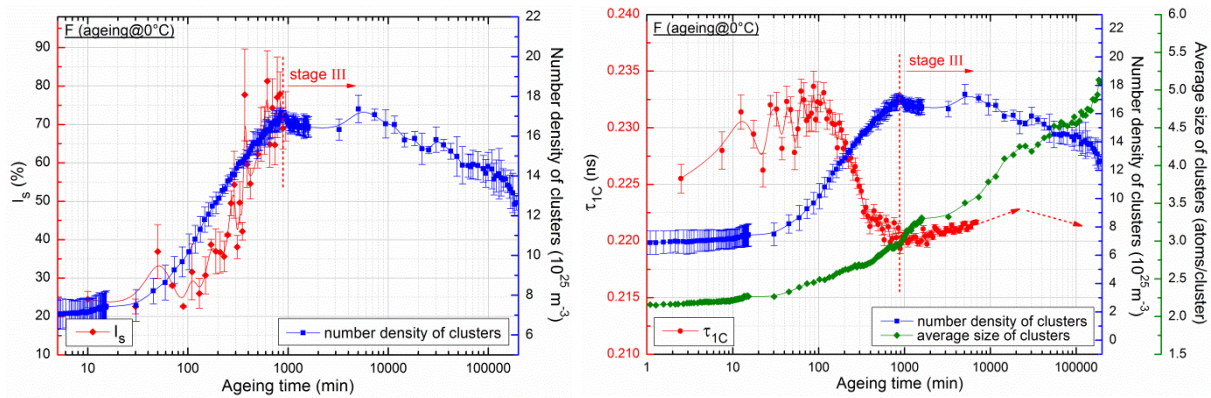


Figure 4.4.37. Kinetic Monte Carlo simulation of the number density and size of solute clusters, compared to the (L) solute cluster intensity I_s and (R) PLT τ_{1C} in alloy F aged at 0°C . Y-axes were scaled to a specific range in order to reveal the similarities between simulation and PALS parameters. Simulations were carried out by Z.Q. Liang.

The simulated quantities evolve in a manner similar to the annihilation parameters related to solute clusters, in particular, there is a matching between number density (KMC) and cluster intensity (PALS), see Fig. 4.4.37 (L). The same similarity was also found between the change in resistivity and solute cluster intensity in Fig. 4.4.34.

The decrease of number density after ~ 900 min is probably due to cluster growth by consuming small clusters or single solutes. If the average size of a certain cluster increases, its PLT should also become higher, especially when Mg atoms dominantly contribute to this stage. Apparently, this agrees with PALS observations for stage III, see Fig. 4.4.37 (R).

However, as mentioned by [Lia12], the simulated results depend strongly on the input parameters such as formation energy of vacancies, the binding energies between a vacancy and Mg or Si. Therefore, all the limitations and assumptions should be carefully considered when comparing the results from KMC to experimental data.

4.4.7 Overview of the Stages Observed with Different Experimental Methods

As shown in previous sections, distinct stages were observed during NA of Al-Mg-Si alloys using positron lifetime spectroscopy, DSC, hardness and resistivity. The changes of the corresponding properties correlate with the evolution of solute clusters and occur at similar ageing times, as summarized in Fig. 4.4.38 [Ban10]:

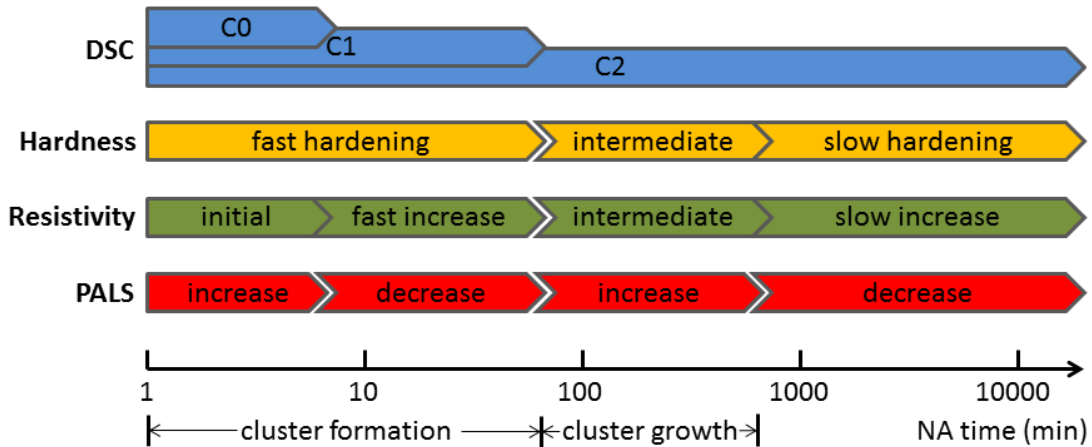


Figure 4.4.38. Schematic illustration of the various stages observed with different experimental methods during NA. The overlapping bars for DSC observations represent parallel reactions. White arrows between stages mean that these stages can be clearly distinguished, while the gray arrows are used to indicate less clear transitions.

4.5 Cu/Ge-containing Al-Mg-Si Alloys

Al-Mg-Si alloys can be strengthened through precipitation hardening following the sequence: SSSS (super-saturated solid solution) \rightarrow solute clusters \rightarrow GP zones (pre- β'') \rightarrow β'' (Mg_5Si_6) \rightarrow β' , U1, U2, B' \rightarrow β (Mg_2Si). The increase in strength due to formation of β'' precipitates will be compromised if an alloy was stored at RT for a certain time, as has been introduced in Chapter 1. Cu addition to many industrial 6000 alloys can partly reduce the negative strength response [Mia00, Mur01, Vau03] through producing finer microstructures. In this study, the effect of Cu addition on the kinetics of Al-Mg-Si alloys was studied by PALS during NA and DSC during constant heating.

After replacing Si by Ge which also belongs to group IV of the periodic table, Al-Mg-Ge alloys show a similar precipitation behavior as Al-Mg-Si, eventually developing the equilibrium phase Mg_2Ge [Mat10], although Ge has a larger atomic radius than Si. Study of such alloys could provide more insight into the complex precipitation behavior of Al-Mg-Si, but except few investigations focused on the precipitate structure [Bjø11, Bjø12], little attention has been paid to these alloys in the past. Particularly, clustering during NA has not yet been investigated. Therefore, in order to elucidate some of the differences between Al-Mg-Si and Al-Mg-Ge alloys, a series of Al-Mg-Ge, Al-Mg-Si and Al-Mg-Ge-Si alloys, some of them containing Cu were investigated.

4.5.1 Positron Annihilation Lifetime Spectroscopy

4.5.1.1 Cu-containing Al-Mg-Si Alloys

Fig. 4.5.1 shows the evolution of τ_{1C} in Cu-containing Al-Mg-Si alloys during NA. It is similar to the one from a previous investigation [Ban11]. The initial PLT (> 0.230 ns) and length of stage I (< 20 min) depend on the Mg and Si content: With higher Mg content and lower Si content, the initial value decreases as reported by [Ban11], while the duration of stage I increases. For alloy A2 (A2Cu), stage I is very short and barely visible due to its low Mg content. A plausible origin of stage I has been discussed in Section 4.4.1.6. During stage II, the PLT drops to its minimum (0.221 to 0.223 ns). Coherent clusters (~ 0.210 ns) enriched in Si and Mg, some possibly containing Cu, gradually form and compete with vacancy-related defects (~ 0.245 ns) in trapping positrons. The combination of both and the change of cluster composition will lead to the observed PLT evolution [Lay12, Liu14].

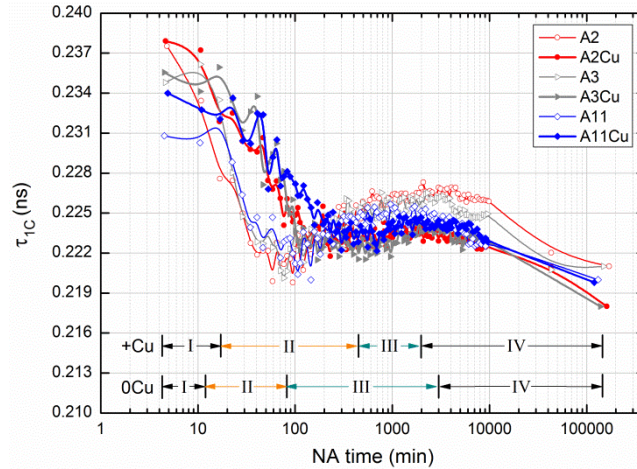


Figure 4.5.1. The PLT τ_{1C} as a function of NA time of various Al-Mg-Si and Al-Mg-Si-Cu alloys. The NA kinetics of such alloys was measured in-situ in the FDA mode.

After this, the PLT re-increases to a maximum within stage III. This stage occurs only if more than about 0.1% of Mg is present (Section 4.4.3) and is thought to be associated with the in-diffusion of Mg into the previously formed Si rich Si-Mg clusters in which the positrons annihilate [Ban11, Lay12]. Finally, the PLT re-decreases through stage IV to a value less than 0.221 ns, possibly due to coarsening or ordering of clusters. The various curves in Fig. 4.5.1 can be grouped into alloys without and with Cu. Alloys without Cu show a fast initial PLT decrease with a minimum after about 1 h of NA and a much more pronounced increase can be observed after. In contrast, the times to reach a similar ageing state for Cu-containing alloys are ~ 8 times longer (orange arrows), indicating a retarded clustering kinetics due to Cu addition during stage II. However, stage III for alloys containing Cu is considerably shorter than in the Cu-free alloys (green arrows), signifying that Cu could also promote further development of these clusters after a certain NA time.

Solute clusters are formed via diffusion of solutes aided by vacancies. The rate of such a process depends on both the vacancy concentration [Des60, Mac96, Mar80] and the diffusivity of the solute atom in the matrix. Due to the high solute-to-vacancy ratio after quenching (~ 100), only a small fraction of solutes is associated with mono-vacancies (the remainder is immobile) and become mobile as complexes if the binding with vacancy is attractive. Otherwise, the vacancies will go to sinks after some random work in the matrix. During diffusion of the complex, small vacancy or solute clusters can be formed rapidly, but the migration of these clusters becomes progressively sluggish, as they grow in size. Further

formation of new clusters or the growth of existing ones eventually requires the liberation of vacancies from inside the clusters. However the rate at which vacancies can escape and re-enter the matrix to transport more solutes depends on the binding energies between the vacancy and the cluster. Vacancies may be repeatedly trapped by and liberated from a cluster and an equilibrium between trapping and de-trapping of vacancies by clusters is finally reached, e.g. if every cluster contains ~ 10 solute atoms on average, each vacancy would have to deliver at least 100 solutes in order to form ~ 10 clusters [Mar13] (the exact number of solutes to be transported by a vacancy depends on the fraction of solute atoms in clusters).

According to the vacancy-pump model proposed by [Gir65], a vacancy could de-trap from a cluster freely by assuming a much stronger binding between a vacancy and a single solute than to a solute cluster, which however appears counter-intuitive. Due to this weakness in argument, a model has been proposed for the growth of solute clusters based on the binding energy E_b between a vacancy and a solute atom assuming that the probability for a vacancy to escape from a cluster scales with $\exp(-ncE_b)$, with n the number of atoms in that cluster and c a constant [Zur09]. This directly implies that after a fast formation of clusters attributed to a high concentration of available vacancies, a slower growth rate of clusters is expected since a considerable amount of vacancies is increasingly being trapped by the growing clusters. Therefore, small clusters are formed in a given time if strong binding exists between vacancy and solute, since one vacancy can only bring few solutes to form clusters [Fed61].

In order to understand the phenomena caused by Cu addition, the binding energies listed in Fig. 4.5.2 between vacancies and solutes are discussed. Many efforts have been made in the past to determine binding energies between a vacancy and various kinds of solutes. A collection of experimental values is available by [Mon76]. In calculations, the binding of V-Si was found to be attractive in all the studies e.g. [Hir07, Lan13, Sta06], while V-Mg exhibits attractive binding for most cases, except the one reported by [Wol07] who specifies a weak repulsive binding. In spite of few exceptions such as [Hir07], the interaction between a vacancy and a Cu atom was found to be stronger or at least comparable to the ones of V-Si and V-Mg according to [Mon76]. Our interpretation of the effect of Cu will be based on attractive and comparable binding energies between the vacancy and Si, Mg, Cu atoms (V-Si: 0.05 eV, V-Mg: 0.04 eV, V-Cu: 0.09 eV, using numerical ab-initio method SIESTA [Sta06]).

We chose this set of values because it is the only one where all three binding energies have been determined on an equal footing with modern methods. For the binding energy V-Ge we adopt the result by [Wol07] that it is 60% stronger than the V-Si binding.

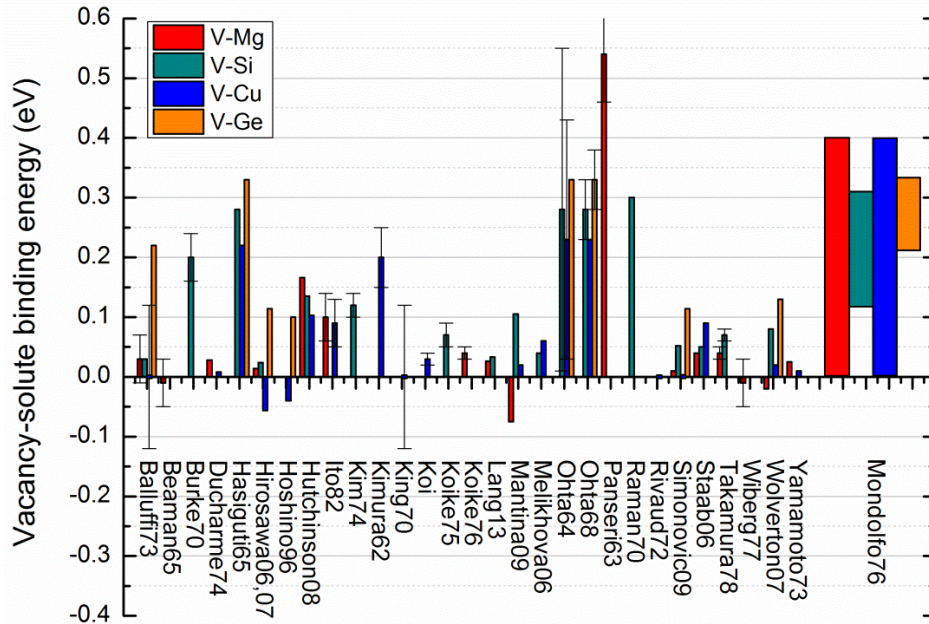


Figure 4.5.2. Vacancy-solute binding energies based on various sources. “+” energies means attractive bindings while “-” ones denote repulsive bindings. Broad columns on the right hand side represent the range of binding energies between a vacancy and a certain solute atom, based on the collection of [Mon76].

- Stage II

According to the binding energies calculated by [Sta06], vacancies will bind with Cu atoms instead of assisting Si-Mg cluster formation and therefore reduce the migration of Si and Mg, i.e. slow down the rate of cluster formation. This picture particularly applies to such systems where the added solutes do not interact with the main alloying elements on the one hand but have a large binding energy with vacancies on the other hand [Has64]. However, this simple mechanism would be small due to the relatively low concentration of Cu ($\sim 0.1\%$). The jump frequency f of a vacancy attached to Cu at $20\text{ }^{\circ}\text{C}$ was calculated using the same method [Man09] as introduced in Section 4.2, and the results are shown in Fig. 4.5.3 together with the ones for Si and Mg. The calculated jump frequency of Cu equals $\sim 230\text{ s}^{-1}$ and lies therefore very close to the one for Mg. Once a vacancy is attached to Si, the vacancy can move with a higher jump frequency to other vacancies or solutes [Liu12], whereas for Mg or Cu, the jump frequency of a vacancy is about two orders of magnitude smaller than for Si, i.e.

vacancies are retained by Mg [Som02] or Cu atoms in an Al-Mg-Si-Cu alloy. However, the vibrational frequency f' could also be affected by the atomic weight of solutes [Man12], and therefore, the jump frequency of a solute as calculated above could somehow alter. Even so, the migration rate of Cu is still slow compared to other type of solutes, as supported by a much lower mobility of Cu than Si and Mg in Al [Du03, Man12].

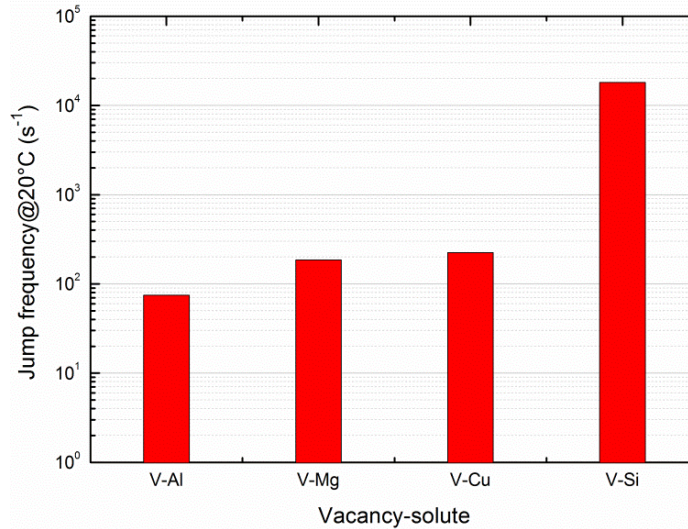


Figure 4.5.3. Jump frequency of a vacancy associated with various solute atoms.

According to atom probe data of 6111 alloy by [Mar13], clustering during NA up to 2 weeks is dominated by Si-Mg and Si-Mg-Cu clusters consisting of 2 to 10 atoms on average (since binding between small Si (Cu) and large Mg atoms might reduce the strain energy [Kim61]). Cu incorporation into atomic clusters was also observed by [Wen12]. Due to the attractive binding between V-Cu and Mg-Cu [Hir07] or even Si-Cu [Mar13], the migration of V-Si or V-Mg complexes necessary for the formation of binary Si-Mg clusters might be notably slowed down if a Cu atom is located in their vicinity [Pas66]. This is very likely since the distances among vacancies and solutes atoms or clusters are small in the initial stage of ageing. A diffusing bare vacancy or a V-Si or V-Mg complex could be temporarily trapped by the Cu atom. Furthermore, if each vacancy has to transport Si and Mg atoms to the cluster repeatedly, according to the vacancy-pump model, the influence of Cu on clustering would be larger than expected from its low concentration because every time a vacancy detaches from a cluster it can be temporarily trapped by a Cu atom with a certain probability. These probabilities will further increase when the matrix is depleted of Si and Mg atoms due to clustering. The total probability will be the sum of the individual probabilities. The formation

of ternary Si-Mg-Cu clusters could be even slower. This is because: (1) a vacancy delivers Cu atoms to a cluster only slowly, see Fig. 4.5.3; (2) de-trapping of a vacancy could be even more retarded due to the interaction between the vacancy and solute atoms in a cluster (Si, Mg and Cu). Under such circumstances, smaller Si-Mg and Si-Mg-Cu clusters are formed more slowly in the presence of Cu. This coincides with the observed slightly higher PLT at the end of stage II since it is cluster growth that reduces the PLT in stage II, see Fig. 4.5.1.

Retardation of clustering during NA has been observed by many authors and is consistent with the PALS observations of this study. For example, a reduced rate of NA caused by Cu addition to Al-Mg-Si alloys was indirectly found by TEM [Pas66]. Electrical resistivity measurements suggested a reduction of the migration rate of solute atoms by a factor of 10 due to Cu addition [Cha73]. Using the same Cu-containing Al-Mg-Si alloys as in this work, [Wen12] reported a slower increase of hardness during the first 2000 min of NA. The same effect was also reported by [Kim12], see Section 4.5.3. In analogy to our case it was shown that due to stronger interactions of vacancies with Sn than with Cu, Cu clustering or GP zone formation was suppressed in an Al-Cu-Sn alloy, because the number of vacancies enabling Cu diffusion is reduced [Kim61].

- Stage III

Beside the Si-Mg and Si-Mg-Cu clusters discussed above, considerable amounts of Mg-Cu and Si-Cu clusters containing 3 to 10 atoms on average were identified after 2 h of NA [Mar13]. Due to the Cu addition, the total number of clusters (Si-Mg, Si-Mg-Cu, Mg-Cu and Si-Cu) is 1.78 times higher than the number of Si-Mg clusters only. In another atom probe study [Mor06], adding Cu led to an increase in the total number of clusters by a factor of just ~ 1.26 after 1 week of NA. If smaller but more densely distributed clusters are formed in the Cu-containing alloys during stage II, then Mg atoms, which dominantly contribute to the further growth of clusters during stage III, would benefit from the shorter average distance to the clusters. The time t for a Mg atom to diffuse to a cluster scales with the average distance d squared, and this distance scales with the number density n to the power of $-1/3$. Thus $t \sim n^{-2/3}$. Taking the mean of the two experimental values 1.78 and 1.26 for the increase of n , 1.52, the migration time for a Mg atom to reach a cluster will be reduced to 0.76 the original value. This agrees qualitatively with observed shortening of stage III in Fig. 4.5.1 from

3000 to 2000 min. In this stage, retardation of clustering due to Cu could have become insignificant due to the “screening” of Cu by Si and Mg atoms in the cluster.

It was suggested that nucleation and growth of solute clusters is aided by Cu addition during NA. In the same work, it was also found that in the presence of Cu, the Mg/Si ratio in clusters became higher, which might be another indication of an attractive binding between Mg and Cu [Mor06]. [Li12] investigated the effect of minor Cu additions on the precipitation sequence of 6005 alloy by TEM and proposed that Cu could promote the formation of plate-like GP zones (corresponds to the “cluster (2)” formed by pre-ageing at 100 °C postulated by [Ser08]), which can transform into dense and fine needle-like β'' precipitates to improve the mechanical properties. Finally, our observations agree with the hardness [Kim12, Tor11, Wen12] and resistivity [Esm04] measurements that reflect the property of Cu to slow down early clustering but accelerate later stages, see Section 4.5.3.

4.5.1.2 Ge-containing Al-Mg-Si Alloys

Al-Mg-Ge alloys show qualitatively the same evolution of PLT τ_{1C} with NA time as Al-Mg-Si alloys, namely an initial decrease, followed by a re-increase, after which τ_{1C} drops to an equilibrium value, see Fig. 4.5.4:

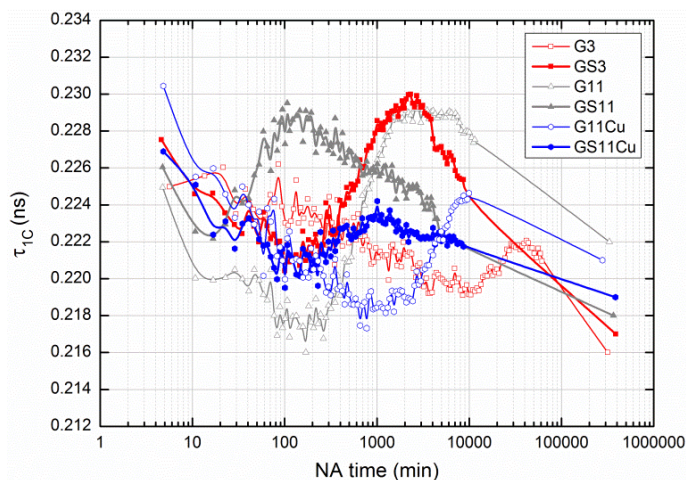


Figure 4.5.4. τ_{1C} evolution in Al-Mg-Ge, Al-Mg-Ge-Si and Al-Mg-Ge-Si-Cu alloys during NA.

Al-Mg-Ge and Al-Mg-Si alloys show largely the same evolution of PLT during stages II, III and IV, but stage I was not observed (except for alloy G3) and the initial PLT is no more related to the Mg content of the Ge-containing alloys, see Fig. 4.5.4. Therefore, the interplay between Ge and Mg on the one hand and Si and Mg on the other is qualitatively the same,

but the action of Ge and Si differ in that at a given Mg content, more Si accelerates the clustering process, whereas more Ge delays it. As shown in Fig. 4.5.5, the highest Ge content in alloy G3 leads to the longest transition times $t_{II \rightarrow III}$ and $t_{III \rightarrow IV}$ between stage II to III and III to IV, respectively, while for the alloy G11 with much less Ge, both transition times are markedly reduced. On the other hand, the ageing kinetics can be further accelerated as in alloy GS3 by substituting certain amounts of Ge by Si while keeping the Mg content nearly constant, thus suggesting a kind of compensation between the effects of Si and Ge. Finally, the fastest transition times were obtained in alloy GS11, which contains the highest amount of Mg and some Si, but the lowest Ge content, see Fig. 4.5.5. The effect of Cu in Al-Mg-Ge alloys for low Ge and Mg contents is partially the same as for Al-Mg-Si alloys during stage II (compare G11 and G11Cu), namely, Cu retards the decrease of PLT and leads to a less pronounced increase after the minimum. However, during the subsequent ageing, a further retardation of the NA kinetics due to Cu addition is observed.

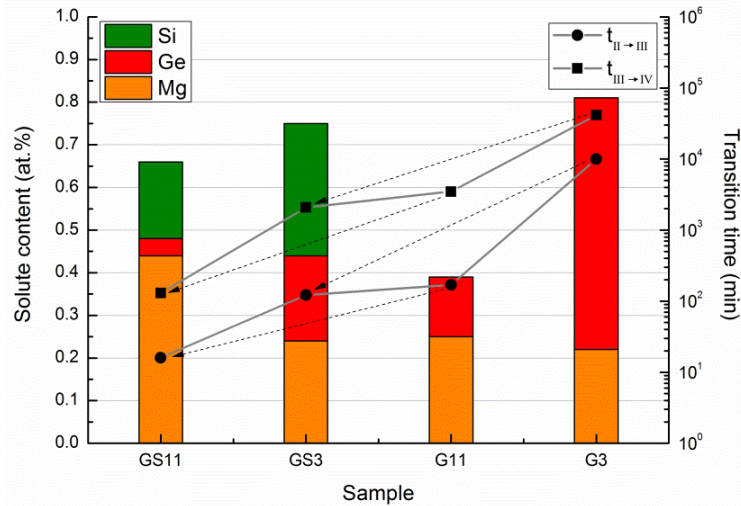


Figure 4.5.5. Dependence of transition times $t_{II \rightarrow III}$ for stage II to III (black solid spheres) and $t_{III \rightarrow IV}$ for stage III to IV (black solid squares) on sample compositions.

The diffusivity of a solute atom depends on various factors such as atomic size, excess valency and its solubility in Al [Man09]. Due to our lack of knowledge on Ge, the calculation of the corresponding jump frequency cannot be performed. However, if we assume a slow migration rate of V-Ge and associate this with the sluggish jump frequency of Mg, the extremely slow ageing kinetics of alloy G3 appears plausible. The rate of clustering in Al-Mg-Si alloys is much faster than in Al-Mg-Ge alloys, since Si atoms can rapidly diffuse towards Mg and form clusters even if the jump frequency of Mg is low. A correlation

between the vacancy-solute binding energy and solute size has been proposed, i.e. strong binding occurs as a rule between a vacancy and a large solute atom (with exceptions such as for Mg [Wol07]). Hence, a higher binding energy of V-Ge is expected than V-Si owing to the larger atomic radius of Ge ($r_{\text{Ge}} = 1.25 \text{ \AA}$, $r_{\text{Si}} = 1.10 \text{ \AA}$). [Has64] investigated Al-10%Zn-0.12%Ge and Al-10%Zn-0.1%Si (wt.%) alloys isothermally by means of electrical resistivity measurements. Retarded ageing kinetics were observed in the Ge-containing alloys at various temperatures ranging from 0 to 40 °C and a higher binding energy of V-Ge than V-Si was determined. Such a tendency confirms the binding energies for V-Ge and V-Si listed in Fig. 4.5.2. In such a case, the clustering processes in the alloys containing a certain amount of Ge should be retarded, due to the combined effects of the low mobility of V-Ge complexes as well as the reduced number of available vacancies for the transport of Mg and Si atoms, in a similar manner to Cu-containing alloys.

4.5.2 Differential Scanning Calorimetry

4.5.2.1 Cu-containing Al-Mg-Si Alloys

Previous DSC measurements on Al-Mg-Si alloys showed 2 to 3 overlapping peaks of designation (C0), C1 and C2 in the temperature range ~20 to 130 °C that are associated to clustering in different stages [Cha12]. These exothermic peaks and the ones related to pre- β'' , β'' , β' and β precipitates are clearly visible in Fig. 4.5.6:

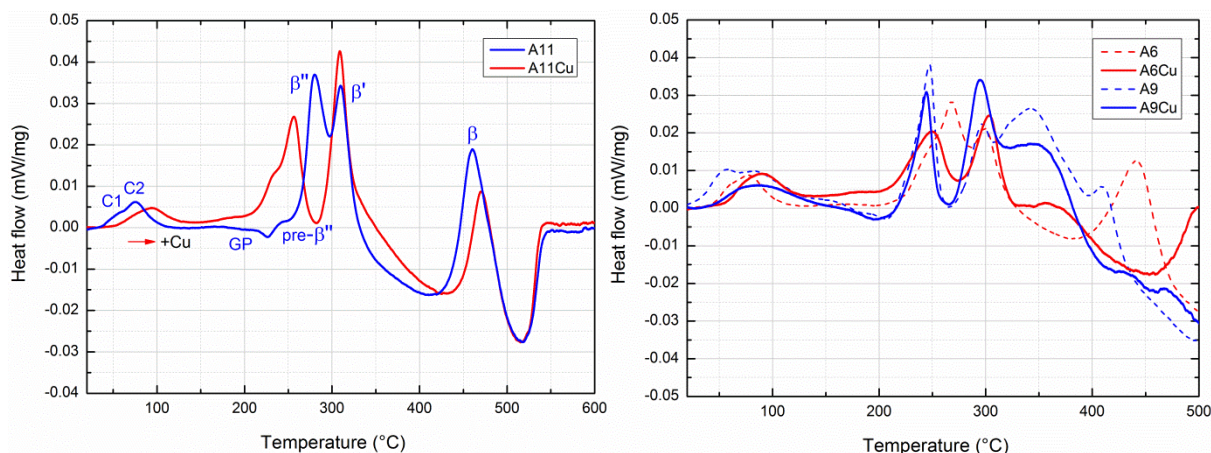


Figure 4.5.6. Heat flow curves of alloys (L) A11, A11Cu and (R) A6, A6Cu, A9, A9Cu at a heating rate of 10 K/min, measurements on the right hand side were carried out by [Cha13].

As shown in Fig. 4.5.6 (L), C1 formation is markedly suppressed due to ~0.1% Cu addition to alloy A11. The same tendency was also observed in alloys A6 and A6Cu in Fig. 4.5.6 (R),

and for the Si-rich alloys A9 and A9Cu, this effect is even more significant. Based on the discussion in Section 4.5.1.1, the reduced heat effect during clustering can be explained. However, the determination of peak area and position (after separating C1 and C2) is essentially required for a quantitative thermal analysis, making the evaluation of Cu effects during the formation of C2 difficult. Such analysis is beyond the aim of this work and will be excluded. For Cu-containing Al-Mg-Si alloys, the precipitation sequence changes to: SSSS \rightarrow solute clusters \rightarrow GP zones (pre- β'') \rightarrow β'' \rightarrow $\beta'+Q'$ \rightarrow Q. However, Q' and Q phases are mainly formed during over-ageing, whereas during conventional paint baking (under-ageing), formation of β'' precipitates is still the main contribution to hardening. Upon Cu addition, the peak area of the main strengthening phase β'' gets smaller and its position moves from 280 to 255 °C, whereas the β' peak becomes more pronounced. Alloys A2, A2Cu, A11 and A11Cu have also been investigated by TEM. A higher number density of β'' was generally observed for alloys containing Cu [Wen12], pointing at a promoted formation of the most important hardening phase β'' by adding Cu, by which the strength response of Al-Mg-Si alloy could be markedly improved.

4.5.2.2 Ge-containing Al-Mg-Si Alloys

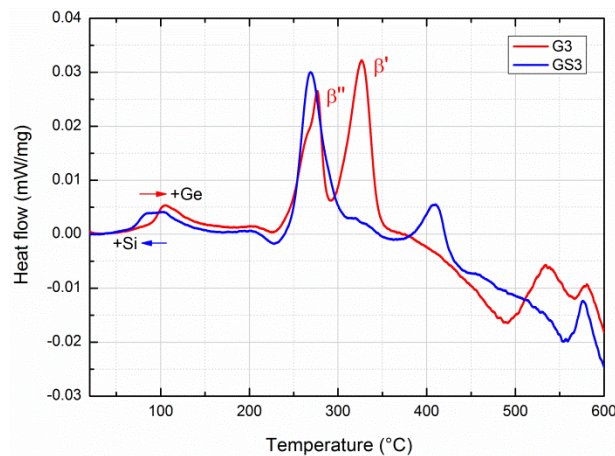


Figure 4.5.7. Heat flow curves of alloys G3 and GS3 at a heating rate of 10 K/min.

Similar to Cu, Ge as a replacement of Si eliminates the clustering peak C1 and shifts the C2 peak position to more than 100 °C. Besides, all other peaks presented in Fig. 4.5.7 follow the precipitation sequence described above. Precipitates similar to the β' phase in Al-Mg-Si alloys (represented by the very pronounced peak at 325 °C of the alloy G3) were also found by [Bjø12, Mat10] using STEM. On the other hand, the counterpart to β'' in the Al-Mg-Si

alloy system was not observed in an Al-Mg-Ge alloy aged 16 h at 200 °C [Bjø11], which is in contradiction with the distinct peaks located at 275 °C in the present work. The over-aging condition applied in [Bjø11] might be responsible for this inconsistency.

4.5.3 Hardness

4.5.3.1 Cu-containing Al-Mg-Si Alloys

The effect of Cu on hardness evolution of Al-Mg-Si alloys during NA were investigated by measuring alloys A11 and A11Cu as in this study [Wen12], Al-0.86%Mg-0.43%Si and Al-0.86%Mg-0.43%Si-0.13%Cu (at.%) alloys [Tor11], commercial 6022 Al-0.61%Mg-0.98%Si and 6111 Al-0.62%Mg-0.99%Si-0.73%Cu (wt.%) alloys [Kim12], results are shown in Fig. 4.5.8:

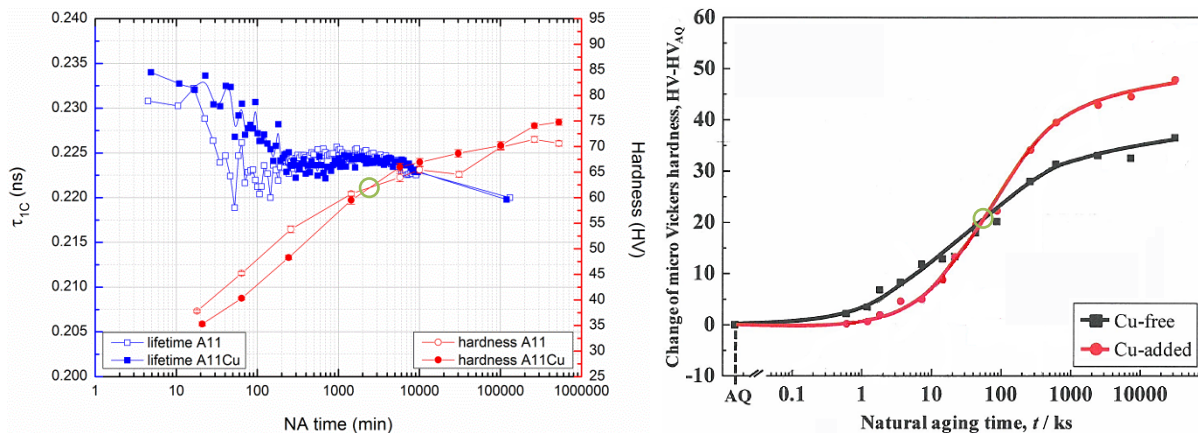


Figure 4.5.8. (L) Hardness evolution of alloys A11 and A11Cu during NA (red symbols) [Wen12], shown together with PALS results (blue symbols); (R) Change of hardness during NA of Cu-free alloy 6022 (black curve) and Cu-added alloy 6111 (red curve) [Kim12].

Briefly speaking, the hardness exhibits a quite similar tendency as the 1-component PLT, i.e. Cu retards the formation of solutes clusters during stage II, but promotes the growth of these clusters when NA proceeds. Roughly the same crossover time was observed, as indicated by the green circles in Fig. 4.5.8. However, it should also be noted that the hardness of A2Cu and Al-0.4%Mg-0.84%Si-0.13%Cu (at.%) alloys (both are Si rich) are always higher than the corresponding alloys without Cu addition during NA [Tor11, Wen12], which is different from the observations shown in Fig. 4.5.8 for Mg rich Al-Mg-Si-Cu and Al-Mg-Si alloys, particularly the one on the right hand side which also dealt with Si rich alloy. Whether the Cu effect on clustering correlates with the Mg/Si ratio of the alloys or not should be verified by further experiments.

4.5.3.2 Ge-containing Al-Mg-Si Alloys

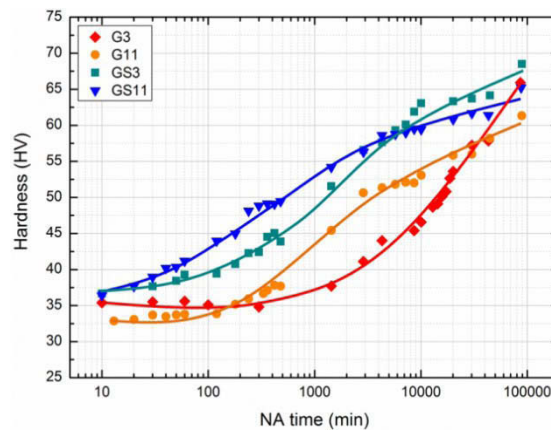


Figure 4.5.9. Hardness evolution of alloys G3, G11, GS3 and GS11 during NA. Each point represents the average of 10 hardness measurements.

The hardness evolution of Ge-containing alloys during NA is shown in Fig. 4.5.9, from which a very similar ageing kinetics as has been shown in Fig. 4.5.4 and Fig. 4.5.5 can be observed (alloy G3 is the slowest among all while alloy GS11 the fastest). Thus, the PALS observation of the retarded NA kinetics of Ge-containing Al-Mg-Si alloys due to Ge addition is verified.

Chapter 5

Conclusions

This work has presented an experimental and theoretical investigation on the clustering kinetics of pure Al, binary Al-Mg and Al-Si, ternary Al-Mg-Si as well as Cu/Ge-containing Al-Mg-Si alloys during natural ageing (NA) by using positron annihilation spectroscopy (PAS), differential scanning calorimetry (DSC) and hardness. The main findings are summarized in the following:

Pure Al

- Positron annihilation lifetime spectroscopy (PALS) results show that 77% of the positrons are trapped by mono-vacancies in pure Al after quenching, 23% annihilate freely in the bulk. The simple trapping model (STM) yields an initial vacancy (V) concentration of $\sim 0.2 \times 10^{-4}$ /atom, see Table 4.1.3. During the first 100 min of NA, small but stable vacancy clusters are gradually formed, pointing at attractive binding between vacancies. Comparison with existing calculations allows us to estimate the size of the vacancy clusters as 3, see Fig. 4.1.1 and Table 4.1.1.

Binary Al-Mg and Al-Si alloys

- V-Mg and 2V-Si complexes or mono-vacancies were found in as-quenched Al-Mg and Al-Si alloys with 0.005% solute content, respectively. After NA for 1000 min, a denser distribution of smaller complexes of solutes and 2 to 3 vacancies were found in Al-0.005%Mg alloy, whereas fewer but larger vacancy clusters consisting of at least ~ 6 vacancies are formed in Al-Si alloy for equal solute content, see Fig. 4.2.2 and Fig. 4.2.3. This indicates that Si enhances the jump frequency of vacancies while Mg can trap vacancies and slow down their jump frequency. How many solutes are associated to these vacancy clusters cannot be specified in present work.

- For as-quenched alloys with much higher solute contents, V-Mg complexes were observed in Al-1%Mg alloy, whereas in Al-1%Si alloy small vacancy clusters (~3 vacancies) were identified, probably associated with Si atoms. Compared to the very dilute alloys containing only 0.005% Mg or Si, there is little further evolution of these vacancy-solute complexes when NA proceeds, see Fig. 4.2.2 and Fig. 4.2.3.
- A vacancy concentration of 0.1×10^{-4} /atom to 0.3×10^{-4} /atom was estimated with the STM for all as-quenched binary Al-Mg and Al-Si alloys, see Fig. 4.2.5.
- Binding of V-Mg and V-Si was found to be attractive.
- Mg-Mg or Si-Si clustering could not be verified by PALS, DSC and electrical resistivity experiments, see Fig. 4.2.6 and Fig. 4.3.8.
- The ageing characteristics of binary Al-Mg and Al-Si alloys could be completely changed by adding even very small amount (0.005%) of the third alloying elements of Si or Mg, respectively. Clustering of Si-Mg atoms occurred instead of vacancy clustering, see Fig. 4.3.1 and Fig. 4.3.2.

Ternary Al-Mg-Si alloys

- PALS stage I (constant or slightly increasing positron lifetime, PLT)
 - The previous observation of this stage in alloy F (Al-0.6%Mg-0.8%Si) was confirmed. Moreover, a much shorter stage I was also found in alloy H (Al-0.4%Mg-0.4%Si) using low temperature (LT) PALS, see Fig. 4.4.2.
- PALS stage II (decreasing PLT)
 - Both Si and Mg are essential for clustering, higher solute content leads to faster ageing kinetics, see Fig. 4.3.5.
 - In alloy H, shallow positron traps are formed during the initial stage of NA as verified by temperature-dependent (-180 to 20 °C) 1-component PALS analysis. These are identified as vacancy-free coherent solute clusters. For alloy F, the temperature dependence is much weaker due to faster initial ageing than alloy H, see Fig. 4.4.6.
 - Two types of competing positron traps were further identified by multi-component PALS analysis at LT of alloys F and H shortly after quenching, one related to vacancy-solute complexes, the other to vacancy-free solute clusters. The first trap is deep, i.e. irreversibly traps positrons, the second shallow, from which positrons can escape, which creates the signature of a temperature-dependent PLT, see Fig. 4.4.10.

- The temperature-dependent PLT in alloy H shortly after quenching can be reasonably described using an extended trapping model (bulk, shallow and deep traps). A number density of $1.2 \times 10^{25} \text{ m}^{-3}$ and positron binding energy of 0.031 eV of the shallow positron traps was determined through fitting. In addition, the initial (5 min of NA) concentration of vacancies in alloy H was estimated to $\sim 0.8 \times 10^{-4}$ /atom, much higher than in pure Al and binary alloys, see Section 4.4.1.8.
- During stage II, the contribution from vacancy-solute complexes decreases, while the solute clusters increasingly trap positrons, thus reflecting their continuous growth and power to trap positrons, see Fig. 4.4.10. The formation and growth of solute clusters is much more efficient in alloy F than alloy H, due to higher concentration of solute atoms and quenched-in vacancies, see Fig. 4.4.12.
- The PLT evolution during stage II of alloy H was also fitted by another extended trapping model (bulk and two types of deep traps). By the end of stage II, the concentration of vacancies and solute clusters was estimated to $\sim 0.6 \times 10^{-4}$ /atom and $\sim 1.3 \times 10^{-4}$ /atom, respectively. Each cluster contains ~ 6 solutes, see Section 4.4.1.9.
- DBAR (CDBS) experiments demonstrate that shortly after quenching the vacancy-related defects are Si-rich for both alloys, probably due to the: (1) the binding for V-Si is stronger than for V-Mg; (2) much higher jump frequency of Si than that of Mg. During stage II, clusters form that include Mg beside Si, see Fig. 4.4.29.
- Activation energies for stage II to III were determined for alloys F and H to 89.7 and 92.7 kJ/mol, respectively, see Fig. 4.4.4.
- PALS stage III (re-increasing PLT)
 - At least 0.1% of Mg is required in order to observe this stage, see Fig. 4.3.4.
 - Almost all of the positrons are trapped by solute clusters, see Fig. 4.4.10. However, the weak contribution from vacancy-type defects still exists, see Fig. 4.4.5.
 - Both Mg and Si are involved during further development of the previously formed clusters, but this stage is dominated by Mg, see Fig. 4.3.4.
 - DBAR experiments showed that the Mg/Si ratios of the solute clusters in alloys F and H equal 0.69 and 0.62 by the end of stage II, and both ratios increase to 0.95 and 0.93 after ~ 10000 min of NA, respectively, suggesting an increasing content of Mg during the growth of solute clusters in stage III, see Fig. 4.4.27.

The PAS experiments yield a consistent picture of the phenomena during early clustering during NA. All results are supported by other methods such as DSC, resistivity and hardness.

Cu/Ge-containing Al-Mg-Si alloys

- The evolution of PLT τ_{1C} follows qualitatively the same pattern for all the Cu/Ge-containing Al-Mg-Si alloys studied, see Fig. 4.5.1 and Fig. 4.5.4.
- For alloys with equal Mg contents, Ge notably retards the ageing kinetics compared to Si, pointing at effects of atomic size or vacancy-solute binding energies. The alloy with the highest Mg and Si content shows the fastest NA kinetics, the alloy with the highest Ge content the slowest, see Fig. 4.5.4 and Fig. 4.5.5.
- Adding Cu to both Al-Mg-Si and Al-Mg-Ge alloys slows down the formation of clusters but it later promotes their subsequent growth in the former alloys. Possible reasons could be related to the interactions between vacancies and solutes or solute clusters, see Fig. 4.5.1 and Fig. 4.5.4.

A.2 Comparison between LT PALS and Resistivity Experiments

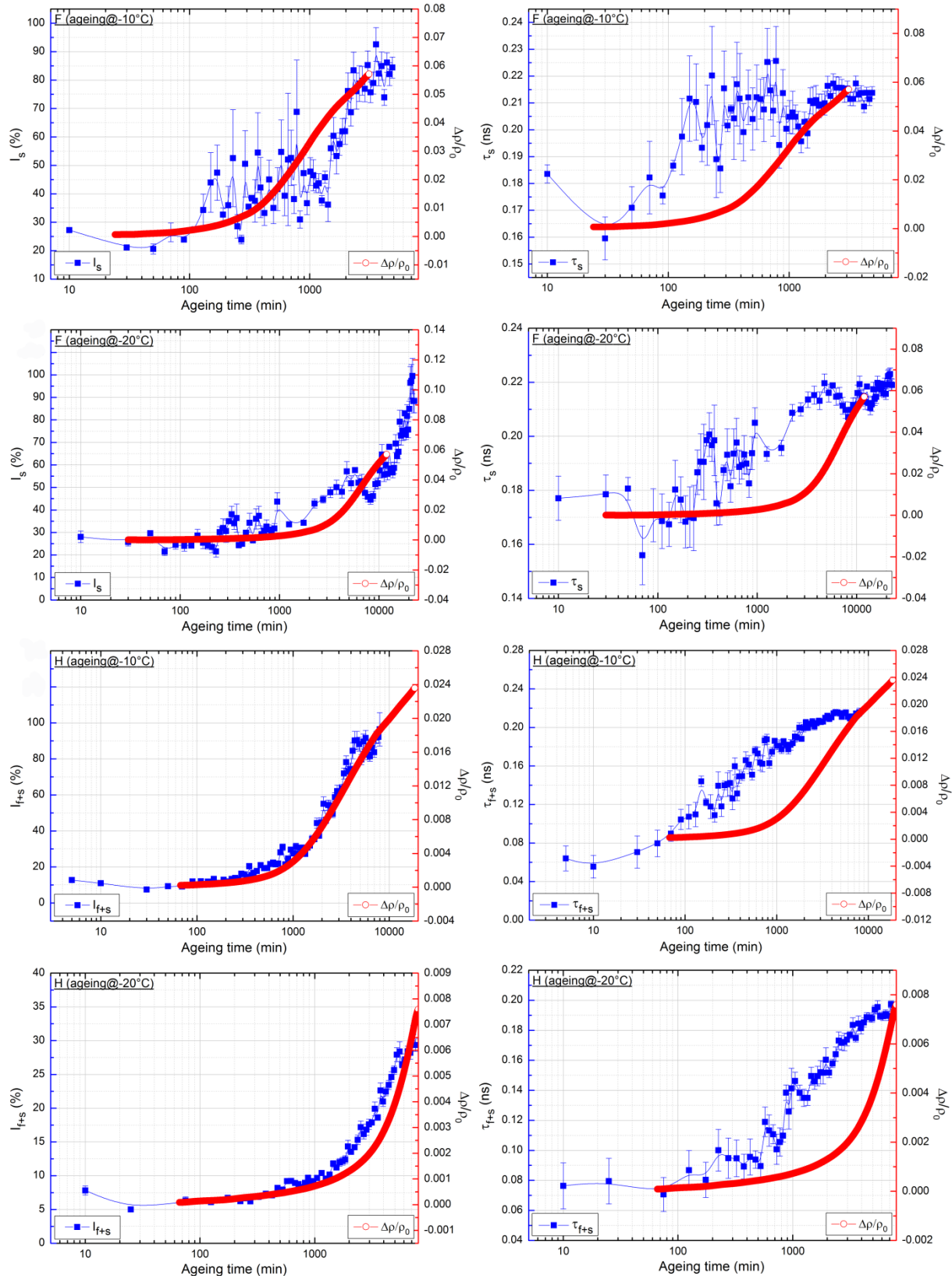


Figure A.2.1. PALS and resistivity experiments of alloys F and H during LT ageing.

A.3 Modified High Voltage Divider for XP2020Q PMT

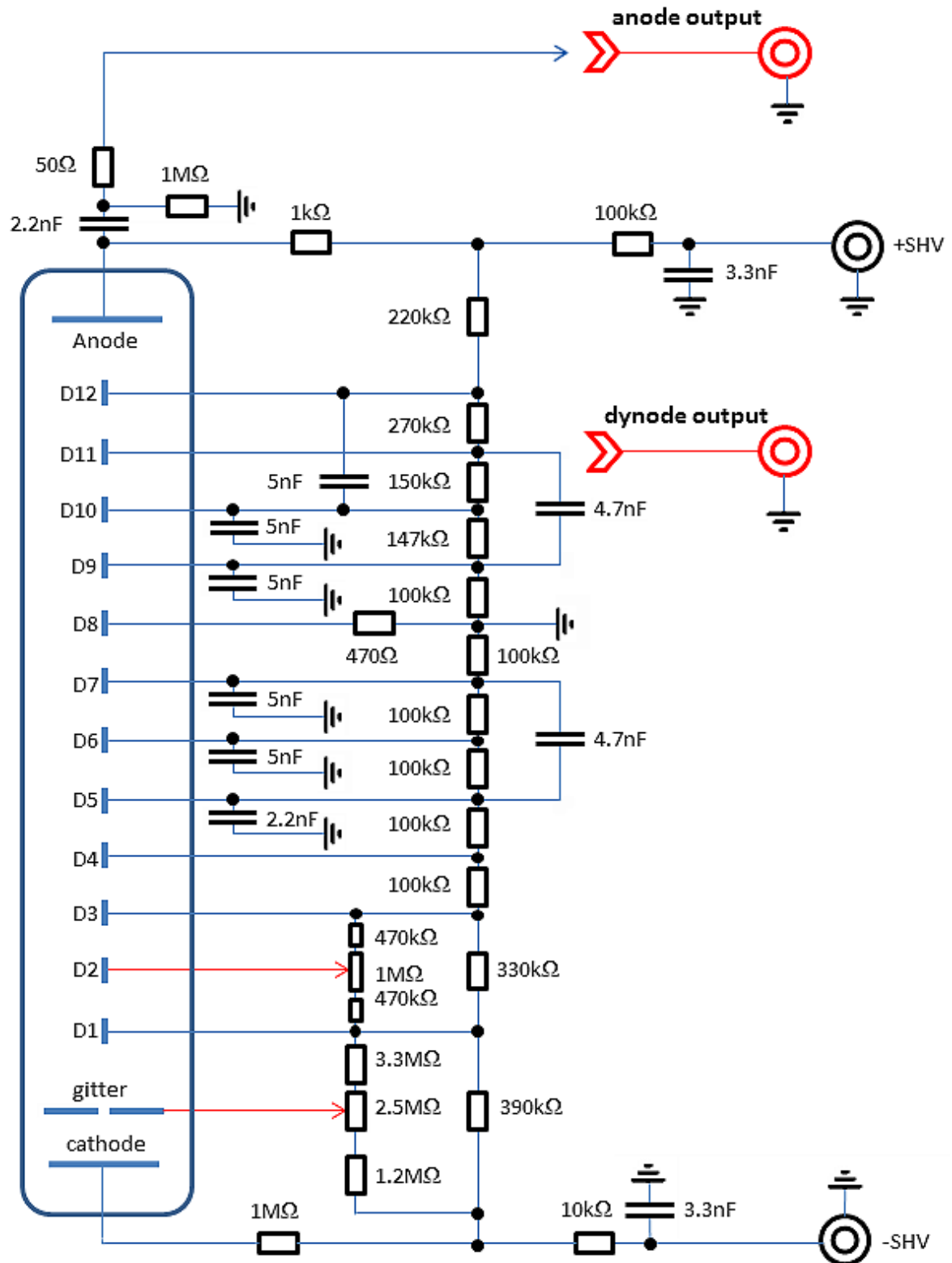


Figure A.3.1. The electric circuit of the modified high voltage divider for XP2020Q PMT.

A.4 Three-view Drawing of the Sample Environment

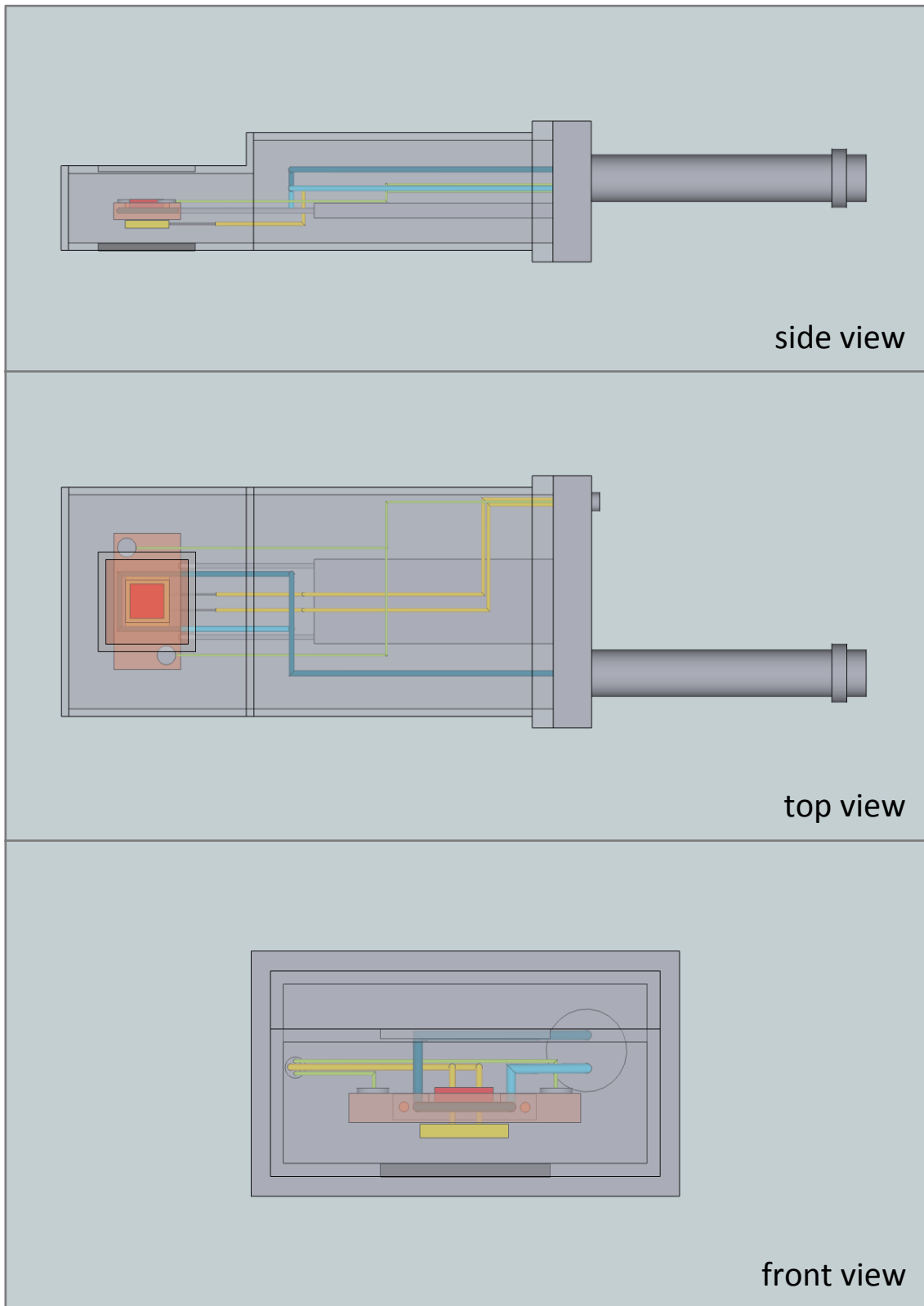


Figure A.4.1. Sample environment used for LT PALS and DBAR experiments.

A.5 Cooling Baths [CITxx]

Table A.5.1. The most common cooling baths and their respective temperature.

mixture		temperature
100 g water	+	100 g ice 0 °C
100 g water	+	29.9 g NH ₄ Cl -3 °C
100 g water	+	75.4 g NaNO ₃ -5 °C
100 g ice	+	28.2 g BaCl ₂ -7 °C
100 g water	+	35.1 g NaCl -10 °C
100 g water	+	244.8 g CaCl ₂ ·6H ₂ O -12 °C
100 g water	+	132.6 g NH ₄ SCN -16 °C
100 g ice	+	61.3 g (NH ₄) ₂ SO ₄ -19 °C
100 g ice	+	29.9 g NaCl -21 °C
100 g ice	+	81.8 g CaCl ₂ ·6H ₂ O -22 °C
100 g ice	+	63.9 g NaBr -28 °C
100 g ice	+	28.2 g MgCl ₂ -33 °C
100 g ice	+	92.3 g 66.1% H ₂ SO ₄ -37 °C
100 g ice	+	122.2 g CaCl ₂ ·6H ₂ O -40 °C
100 g ice	+	143.9 g CaCl ₂ ·6H ₂ O -55 °C
100 g ice	+	30.9 g KOH -63 °C
ethanol	+	dry ice -72 °C
CHCl ₃	+	dry ice -77 °C
acetone	+	dry ice -86 °C
ether	+	dry ice -100 °C

References

- [Ada88] J.B. Adams, S.M. Foiles, W.G. Wolfer, *Journal of Material Research*, 4 (1989) 102-112.
- [Ala95] M. Alatalo, H. Kaupinnen, K. Saarinen, M.J. Puska, J. Mäkinen, P. Hautajärvi, R.M. Nieminen, *Physical Review B*, 51 (1995) 4176-4185.
- [Ala96] M. Alatalo, B. Barbiellini, M. Hakala, H. Kauppinen, T. Korhonen, M.J. Puska, K. Saarinen, P. Hautajärvi, R.M. Nieminen, *Physical Review B*, 51 (1996) 2397-2409.
- [Aso96] P. Asoka-Kumar, M. Alatalo, V.J. Ghosh, A.C. Kruseman, B. Nielsen, K.G. Lynn, *Physical Review Letters*, 77 (1996) 2097-2100.
- [Ava96] V. Avalos, S. Dannefaer, *Physical Review B*, 54 (1996) 1724-1728.
- [Avr39] M. Avrami, *Journal of Chemical Physics*, 7 (1939) 1103-1112.
- [Bal73] R.W. Balluffi, P.S. Ho, *Diffusion*, American Society of Metals, Metals Park, Ohio, (1973) 83.
- [Ban10] J. Banhart, C.S.T. Chang, Z.Q. Liang, N. Wanderka, M.D.H. Lay, A.J. Hill, *Advanced Engineering Materials*, 12 (2010) 559-571.
- [Ban11] J. Banhart, M.D.H. Lay, C.S.T. Chang, A.J. Hill, *Physical Review B*, 83 (2011) 014101.
- [Ban12] J. Banhart, M. Liu, Y. Yong, Z. Liang, C.S.T. Chang, M. Elsayed, M.D.H. Lay, *Physica B*, 407 (2012) 2689-2696.
- [Bar95] B. Barbeellini, M.J. Puska, T. Torsti, R.M. Nieminen, *Physical Review B*, 51 (1995) 7341-7344.
- [Bar96] B. Barbeellini, M.J. Puska, T. Korhonen, A. Harju, T. Torsti, R.M. Nieminen, *Physical Review B*, 53 (1996) 16201-16213.
- [Bec00] F. Becvar, J. Cizek, L. Lestak, I. Novotny, I. Prochazka, F. Sebesta, *Nuclear Instruments and Methods in Physics Research A*, 443 (2000) 557-577.

- [Bec05] F. Becvar, J. Cizek, I. Prochazka, J. Janotova, Nuclear Instruments and Methods in Physics Research A, 539 (2005) 372-385.
- [Ber67] S. Berko, J.C. Erskine, Physical Review Letters, 19 (1967) 307-309.
- [Bha92] A. Bharathi, C.S. Sundar, Materials Science Forum, 105-110 (1992) 905-908.
- [Bha96] A. Bharathi, C.S. Sundar, Metals Materials and Processes, 8 (1996) 31-44.
- [Bjø11] R. Bjørge, P.N.H. Nakashima, C.D. Marioara, S.J. Andersen, B.C. Muddle, J. Etheridge, R. Holmestad, Acta Materialia 59 (2011) 6103.
- [Bjø12] R. Bjørge, C. Dwyer, M. Weyland, P.N.H. Nakashima, C.D. Marioara, S.J. Andersen, J. Etheridge, R. Holmestad, Acta Materialia, 60 (2012) 3239.
- [BNLxx] Brookhaven National Laboratory, National Nuclear Data Center, <http://www.nndc.bnl.gov/chart/>.
- [Bra77] W. Brandt, R. Paulin, Physical Review B, 15 (1977) 2511-2518.
- [Bra08] H. Bracht, A. Chroneos, Journal of Applied Physics, 104 (2008) 076108.
- [Buh04] J. Buha, P.R. Munroe, R.N. Lumley, A.G. Crosky, A.J. Hill, Proceedings of the 9th International Conference on Aluminium Alloys, (2004) 1028-1033.
- [Bur70] J. Burke, A.D. King, Philosophical Magazine, 21 (1970) 7.
- [Cal05] A. Calloni, A. Dupasquier, R. Ferragut, P. Folegati, M.M. Iglesia, Physical Review B, 72 (2005) 054112.
- [Cao12] L. Cao, P.A. Rometsch, H. Zhong, Y. Mulji, S.X. Gao, B.C. Muddle, Japan Institute of Light Metals, Tokyo, (2010) 395-400.
- [Cao13] L.F. Cao, P.A. Rometsch, M.J. Couper, Materials Science and Engineering A, 559 (2013) 257-261.
- [Car03] K.M. Carling, G. Wahnström, T.R. Mattsson, N. Sandberg, G. Grimvall, Physical Review B, 67 (2003) 054101.
- [Cha73] D.K. Chatterjee, K.M. Entwistle, Journal of the Institute of Metals, 101 (1973) 53-59.

- [Cha11] C.S.T. Chang, J. Banhart, *Metallurgical and Materials Transactions A*, 42 (2011) 1960-1964.
- [Cha12] C.S.T. Chang, Z.Q. Liang, E. Schmidt, J. Banhart, *International Journal of Materials Research*, 103 (2012) 955-961.
- [Cha13] C.S.T. Chang, personal communication.
- [CITxx] Chem_Is_Try, <http://www.applichem.com>, (2013).
- [Cor44] J.M. Cork, R.W. Pidd, *Physical Review*, 66 (1944) 227-230.
- [Cor81] C. Corbel, R.P. Gupta, *Journal of Physical Letters*, 42 (1981) 549.
- [Dan81] S. Dannefaer, *Applied Physics A*, 26 (1981) 255-259.
- [Den09] P. Dendooven, Presentation, University of Groningen, (2009) 21-22.
- [Des60] W. Desorbo, H.N. Treafis, D. Turnbull, *Acta Metallurgica*, 8 (1960) 277-295.
- [Djo95] N. Djourellov, M. Misheva, *Journal of Physics: Condensed Matter*, 8 (1996) 2081-2087.
- [Dlu80] G. Dlubek, W. Gerber, A. Vehanen, J. Yli-Kaupilla, *Kristall und Technik*, Bd 15, H 12 (1980) 1409-1413.
- [Dlu81] G. Dlubek, O. Brümmer, B. Möser, *Physica Status Solidi*, 63 (a) (1981) 115.
- [Dlu86] G. Dlubek, O. Brümmer, P. Hautojärvi, *Acta Metallurgica*, 34 (1986) 661-667.
- [Dlu86] G. Dlubek, R. Krause, O. Brümmer, *Journal of Material Science*, 21 (1986) 853-858.
- [Dlu87] G. Dlubek, *Material Science Forum*, 13-14 (1987) 11.
- [Dlu98] G. Dlubek, P. Lademann, H. Krause, S. Krause, R. Unger, *Scripta Materialia*, 39 (1998) 893-899.
- [Doa00] L.C. Doan, Y. Ohmori, K. Nakai, *Materials Transactions Japan*, 41 (2000) 300.
- [Dom05] P. Domonkos, M. Elprup, B.N. Singh, Riso National Laboratory, Roskilde, Denmark, unpublished, (2005).

- [Doy78]** M. Doyama, *Journal of Nuclear Materials*, 69-70 (1978) 350-361.
- [Dry95]** J. Dryzek, *Journal of Physics: Condensed Matter*, 7 (1995) 383-392.
- [Dry96]** J. Dryzek, J. Kansy, *Nuclear Instruments and Methods in Physics Research A*, 380 (1996) 576-581.
- [Du03]** Y. Du, Y.A. Chang, B. Huang, W. Gong, Z. Jin, H. Xu, Z. Yuan, Y. Liu, Y. He, F.Y. Xie, *Material Science and Engineering A*, 363 (2003) 140.
- [Duc74]** A.R. DuCharme, G.K. Straub, *Journal of Applied Physics*, 45 (1974) 946.
- [Dup93]** A. Dupasquier, R. Romero, A. Somoza, *Physical Review B*, 48 (1993) 9235.
- [Dup07]** A. Dupasquier, R. Ferragut, M.M. Iglesias, M. Massazza, G. Riontino, P. Mengucci, G. Barucca, C.E. Macchi, A. Somoza, *Philosophical Magazine*, 87 (2007) 3297-3233.
- [Dut91]** I. Dutta, S.M. Allen, *Journal of Materials Science Letters*, 10 (1991) 323-326.
- [Edw98]** G.A. Edwards, K. Stiller, G.L. Dunlop, M.J. Couper, *Acta Materialia*, 46 (1998) 3893-3904.
- [Eld71]** M. Eldrup, Dissertation, Technical University of Denmark, (1971).
- [Ema03]** D. Emadi, L.V. Whiting, M. Sahoo, J.H. Sokolowski, P. Burke, M. Hart, *The Minerals, Metals and Materials Society*, (2003) 983-989.
- [Erh91]** P. Erhart, P. Jung, H. Schultz, H. Ullmaier, *Atomic Defects in Metal*, Landolt-Börnstein, New Series, 25, Springer-Verlag, Berlin, (1991).
- [Esm04]** S. Esmaeili, D.J. Lloyd, *Scripta Materialia*, 50 (2004) 155-158.
- [Fed61]** T. Federighi, G. Thomas, *Philosophical Magazine*, 7 (1961) 127-131.
- [Fuj77]** S. Fujikawa, K. Hirano, *Materials Science and Engineering*, 27 (1977) 25-33.
- [Fur11]** T. Fura, Presentation, Hydro Aluminium Bonn, (2011).
- [Gav07]** V. Gavini, K. Bhattacharya, M. Ortiz, *Physical Review B*, 76 (2007) 180101.
- [Gir65]** L.A. Girifalco, H. Herman, *Acta Metallurgica*, 13 (1965) 583-590.

- [**Go195**] R.D. Goldberg, P.J. Schultz, P.J. Simpson, *Applied Surface Science*, 85 (1995) 287-291.
- [**Got98**] G. Gottstein. *Physikalische Grundlagen der Materialkunde*, Springer-Verlag, Berlin, (1998).
- [**Gow92**] T. Goworek, W. Gorniak, J. Wawryszczuk, *Nuclear Instruments & Methods in Physics Research A*, 321 (1992) 560-570.
- [**Gre00**] D. Green, *The Physics of Particle Detectors*, Cambridge University Press, Cambridge, (2000) 38.
- [**Gup80**] R.P. Gupta, *Physical Review B*, 22 (1980) 5900-5911.
- [**Gup99**] A.K. Gupta, D.J. Lloyd, *Metallurgical and Materials Transactions A*, 30 (1999) 879-890.
- [**Haa06**] M. Haaks, T.E.M. Staab, K. Maier, *Nuclear Instruments Methods A*, 569 (2006) 829.
- [**Haa07**] M. Haaks, R. Valentini, R. Vianden, *Physica Status Solidi*, 4 (2007) 4036-4039.
- [**Haa09**] M. Haaks, *Habilitationsschrift*, Rheinische Friedrich-Wilhelms Universität Bonn, (2009) 16.
- [**Has64**] F. Hashimoto, M. Ohta, *Journal of the Physical Society of Japan*, 19 (1964) 1331-1336.
- [**Has65**] R.R. Hasiguti, *Journal of the Physical Society of Japan*, 20 (1965) 625.
- [**Has91**] E. Hashimoto, T. Kino, *Journal of the Physical Society of Japan*, 60 (1991) 3167-3171.
- [**Has94**] E. Hashimoto, M. Iwami, Y. Ueda, *Journal of Physics: Condensed Matter*, 6 (1994) 1611-1616.
- [**Hau95**] P. Hautojärvi, C. Corbel, *Positron Spectroscopy of Solids*, (1995) 491.
- [**Hau95**] P. Hautojärvi, *Journal De Physique*, 5 (1995) C1-6.
- [**Hid77**] E. Hidvegi, E. Kovacs, *Materials Science and Engineering*, 27 (1977) 39-43.

- [Hir58] P.B. Hirsch, J. Silcox, *Philosophical Magazine*, 3 (1958) 897-908.
- [Hir78] K. Hirano, S. Fujikawa, *Journal of Nuclear Materials*, 69-70 (1978) 564-566.
- [Hir06] S. Hirosawa, F. Nakamura, T. Sato, T. Hoshino, *Journal of Japan Institute of Light Metals*, 56 (2006) 621-628.
- [Hir07] S. Hirosawa, F. Nakamura, T. Sato, *Materials Science Forum*, 283 (2007) 561-565.
- [Hos96] T. Hoshino, R. Zeller, P.H. Dederichs, *Physical Review B: Condensed Matter*, 53 (1996) 8971-8974.
- [Hut08] C.R. Hutchinson, B.M. Gable, N. Ciccossillo, P.T. Loo, T.J. Bastow, A.J. Hill, *Proceedings of the 11th International Conference on Aluminum Alloys*, (2008) 788-794.
- [Ito82] K. Ito, Y. Ohtsu, K. Shima, S. Tanigawa, *Proceedings of Yamada Conference V*, University of Tokyo Press, (1982) 453-456.
- [Jen89] K.O. Jensen, *Journal of Physics: Condensed Matter*, 1 (1989) 10595-10602.
- [Jus12] J. Justina, Master thesis, Texas A&M University, (2012) 6.
- [Kan85] I. Kanazawa, H. Murakami, T. Kurihara, Y. Sakurai, M. Doyama, *Journal of Physics*, 15 (1985) 11-18.
- [Kan96] J. Kansy, *Nuclear Instruments and Methods in Physics Research A*, 374 (1996) 235-244.
- [Kar69] A. Karpeles, *Journal of Radiochimica Acta*, 12 (1969) 212.
- [Kim61] H. Kimura, R.R. Hasiguti, *Acta Metallurgica*, 9 (1961) 1076-1078.
- [Kim62] H. Kimura, A. Kimura, R.R. Hasiguti, *Acta Metallurgica*, (1962) 607-619.
- [Kim74] S.M. Kim, W.J.L. Buyers, P. Martel, G.M. Hood, *Journal of Physics F: Metal Physics*, 4 (1974) 343-350.
- [Kim12] J.H. Kim, T. Sato, personal communication (2012).
- [Kin70] A.D. King, J. Burke, *Acta Metallurgica*, 18 (1970) 205.

- [Klo07] B. Klobes, Diplomarbeit, Rheinische Friedrich-Wilhelms-Universität Bonn, (2007).
- [Klo10] B. Klobes, Dissertation, Rheinische Friedrich-Wilhelms-Universität Bonn, (2010) 73.
- [Klo10] B. Klobes, B. Korff, O. Balarisi, P. Eich, M. Haaks, K. Maier, R. Sottong, Physical Review B, 82 (2010) 054113.
- [Klu91] J.E. Kluin, T. Hehenkamp, Physical Review B, 44 (1991) 11597.
- [Hoh64] P. Hohenberg, W. Kohn, Physical Review B, 136 (1964) 864.
- [Koh65] W. Kohn, L.J. Sham, Physical Review A, 140 (1965) 1133.
- [Koh10] I. Kohlbach, B. Korff, T.E.M. Staab, Physica Status Solidi (b), 247 (2010) 2168-2178.
- [Koi75] M. Koike, T. Taira, K. Furukawa, J. Takamura, Fall Meeting, The Physical Society of Japan, (1975) 10p-N-12.
- [Koi76] M. Koike, K. Furukawa, J. Takamura, Fall Meeting, The Physical Society of Japan, (1976) 6a-M-10.
- [Koi76] M. Koike, K. Furukawa, J. Takamura, H. Hira, N. Yamamoto, F. Nakamura, ibid. 457-460.
- [Kon10] A.B. Konik, Dissertation, University of Iowa, (2010) 26.
- [Kor07] B. Korff, Diplomarbeit, Rheinische Friedrich-Wilhelms-Universität Bonn, (2007) 58-59.
- [Kor10] B. Korff, Dissertation, Rheinische Friedrich-Wilhelms-Universität Bonn, (2010).
- [Kov75] I. Kovacs, J. Lendvai, T. Ungar, Materials Science and Engineering, 21 (1965) 169-175.
- [Kra85] R. Krause, G. Dlubek, O. Brümmer, S. Skladnikiewitz, H. Daut, Crystal Research and Technology, 20 (1985) 267-269.

- [Kra03]** R. Krause-Rehberg, *Positron Annihilation in Semiconductors*, Springer-Verlag, Berlin, (2003).
- [Kra09]** R. Krause-Rehberg, A. Krille, K.M. Kosev, Presentation, International Conference on New Material Design Technology, (2009).
- [Kri08]** A.M. Krille, Diplomarbeit, Martin-Luther-Universität Halle-Wittenberg, (2008) 5.
- [Kur04]** J. Kuriplach, F. Becvar, J. Cizek, I. Prochazka, *Materials Science Forum*, 445-446 (2004) 132-134.
- [Küh13]** J. Kühn, Master Thesis, Technische Universität Berlin, (2013) 94.
- [Lan13]** P. Lang, E.P. Karadeniz, W. Mayer, A. Falahati, E. Kozeschnik, *Proceedings of the 8th Pacific Rim International Congress on Advanced Materials and Processing*, TMS, (2013) 3181-3188.
- [Lav83]** M. Laval, M. Moszynski, R. Allemand, E. Cormoreche, P. Guinet, R. Odru, J. Vacher, *Nuclear Instruments and Methods in Physics Research*, 206 (1983) 169-176.
- [Lay12]** M.D.H. Lay, H.S. Zurob, C.R. Hutchinson, T.J. Bastow, A.J. Hill, *Metallurgical and Materials Transactions A* (2012).
- [Len76]** B. Lengeler, *Philosophical Magazine*, 34 (1976) 259-264.
- [Leo94]** W.R. Leo, *Techniques for Nuclear and Particle Physics Experiments*, Springer-Verlag, Berlin, (1994).
- [Li11]** H. Li, Y.D. Shao, K. Zhou, J.B. Pang, Z. Wang, *Nuclear Instruments and Methods in Physics Research A*, 625 (2011) 29-34.
- [Li12]** K. Li, M. Song, Y. Du, X. Fang, *Archives of Metallurgy and Materials*, 57 (2012) 457-467.
- [Lia12]** Z.Q. Liang, C.S.T. Chang, C. Abromeit, J. Banhart, J. Hirsch, *International Journal of Materials Research*, 103 (2012) 980-985.
- [Lia12]** Z.Q. Liang, Dissertation, Technischen Universität Berlin, (2012).

- [Lip09] J. Lipka, *Jordan Journal of Physics*, 2 (2009) 73-88.
- [Liu09] M. Liu, *Diplomarbeit, Rheinische Friedrich-Wilhelms-Universität Bonn*, (2009) 42.
- [Liu11] M. Liu, B. Klobes, K. Maier, *Scripta Materialia*, 64 (2011) 21-24.
- [Liu12] M. Liu, Y. Yan, Z.Q. Liang, C.S.T. Chang, J. Banhart, *Proceedings of the 13th International Conference on Aluminium Alloys*, (2012) 1131-1137.
- [Liu14] M. Liu, J. Cizek, C.S.T. Chang, J. Banhart, *Materials Science Forum*, 794-796 (2014) 33-38.
- [Lom58] W.M. Lomer, *Vacancies and Other Point Defects in Metals and Alloys*, The Institute of Metals London, (1958) 79.
- [Lun13] C.R. Luna, C. Macchi, A. Juan, A. Somoza, *Journal of Physics: Conference Series*, 443 (2013) 012019.
- [Mac80] I.K. MacKenzie, J. Fabian, *Journal of Nuovo Cimento B*, 58 (1980) 162-167.
- [Mac96] D.S. Mackenzie, *Proceedings of the 16th ASM Heat Treating Society Conference and Exposition*, (1996) 213-219.
- [Maj66] C.K. Majumdar, *Physical Review*, 149 (1966) 406-408.
- [Makxx] I. Makkonen, M. Hakala, M.J. Puska, unpublished.
- [Mäk90] J. Mäkinen, E. Punkka, A. Vehanen, P. Hautojärvi, J. Keinonen, M. Hautala, E. Rauhala, *Journal of Applied Physics*, 67 (1990) 990.
- [Man81] M. Manninen, R. Nieminen, *Applied Physics A*, 26 (1981) 93-100.
- [Man87] S. Mantl, W. Kesternich, W. Triftshäuser, *Journal of Nuclear Materials*, 69-70 (1987) 593.
- [Man09] M. Mantina, Y. Wang, L.Q. Chen, Z.K. Liu, C. Wolverton, *Acta Materialia*, 57 (2009) 4102-4108.
- [Man12] M. Mantina, Y. Wang, R. Arroyave, S.L. Shang, L.Q. Chen, Z.K. Liu, *Journal of Physics: Condensed Matter*, 24 (2012) 305402.

- [Mar80] J.W. Martin, *Micromechanisms in Particle-Hardened Alloys*, Cambridge University Press, Cambridge, (1980) 31.
- [Mar13] R.K.W. Marceau, A. de Vaucorbeil, G. Sha, S.P. Ringer, W.J. Poole, *Acta Materialia*, 61 (2013) 7285-7303.
- [Mat10] K. Matsuda, J. Nakamura, H. Nishita, T. Kawabata, Y. Uetani, T. Sato, S. Ikeno, *Material Science Forum*, 654-656 (2010) 930.
- [Mel92] C.L. Melcher, J.S. Schweitzer, *IEEE Transactions on Nuclear Science*, 39 (1992) 502-505.
- [Mel06] O. Melikhova, J. Kuriplach, J. Cizek, I. Prochazka, *Applied Surface Science*, 252 (2006) 3285-3289.
- [Mia00] W.F. Miao, D.E. Laughlin, *Metallurgical and Materials Transaction A*, 31(2000) 361.
- [Mit92] E.J. Mittemeijer, *Journal of Materials Science*, 27 (1992) 3977-3987.
- [Mon76] L.F. Mondolfo, *Aluminium Alloys, Structure and Properties*, Butterworth London, (1976) 24-28.
- [Mon94] M.A. Monge, J. del Rio, *Physics of Condensed Matter*, 6 (1994) 2643-2646.
- [Mor06] A.I. Morley, M.W. Zandbergen, A. Cerezo, G.D.W. Smith, *Material Science Forum*, 519-521 (2006) 543-548.
- [Mur99] M. Murayama, K. Hono, *Acta Materialia*, 47 (1999) 1537-1548.
- [Mur01] M. Murayama, K. Hono, W.F. Miao, D.E. Laughlin, *Metallurgical and Materials Transactions A*, 32 (2001) 239.
- [Nie79] R.M. Nieminen, J. Laakkonen, *Applied Physics*, 20 (1979) 181-184.
- [Nie93] B. Nielsen, O.W. Holland, T.C. Leung, K.G. Lynn, *Journal of Applied Physics*, 74 (1993) 1636.
- [Nie95] R.M. Nieminen, *Proceedings of the International School of Physics "Enrico Fermi"*, *Positron Spectroscopy of Solids*, IOS, (1995) 443-489.

- [Oha64] M. Ohta, F. Hashimoto, *Journal of the Physical Society of Japan*, 19 (1964) 130.
- [Oha64] M. Ohta, F. Hashimoto, *Journal of the Physical Society of Japan*, 19 (1964) 1331.
- [Oht68] M. Ohta, F. Hashimoto, T. Tanimoto, *Memoirs of the School of Engineering, Okayama University*, 3 (1968) 39-50.
- [Pag84] B. Pagh, H.E. Hansen, B. Nielsen, G. Trumpy, K. Petersen, *Applied Physics A*, 33 (1984) 255-263.
- [Pan58] C. Panseri, T. Federighi, *Istituto Sperimentale Metalli Leggeri*, (1958) 1238.
- [Pan63] C. Panseri, T. Federighi, *Acta Metallurgica*, 11 (1963) 575.
- [Pas66] D.W. Pashley, J.W. Rhodes, A. Sendorek, *Journal of the Institute of Metals London*, 94 (1966) 41-49.
- [Pet83] K. Petersen, *Positron Solid-State Physics*, North-Holland, Amsterdam, (1983) 298.
- [Pet98] A.K. Petters, *Diplomarbeit, Martin-Luther Universität Halle-Wittenberg*, (1998).
- [Pho07] Photonis, Test sheet of Philips XP2020 Photomultiplier, <http://my-enterprises.com/pdf/XP2020.pdf> , (2007).
- [Pow66] R.W. Powell, C.Y. Ho, P.E. Liley, *National Standard Reference Data Series 8, Purdue University*, (1966) 22.
- [Pus83] M.J. Puska, R.M. Nieminen, *Journal of Physics*, 13 (1983) 333-346.
- [Pus89] M.J. Puska, R.M. Nieminen, *Journal of Physics*, 1 (1989) 6091.
- [Pus90] M.J. Puska, C. Corbel, R.M. Nieminen, *Physical Review B*, 41 (1990) 9980-9993.
- [Pus94] M.J. Puska, R.M. Nieminen, *Reviews of Modern Physics*, 66 (1994) 841-897.
- [Raj87] H. Rajainmäki, *Applied. Physics A*, 42 (1987) 205-208.

- [**Ram70**] K.S. Raman, E.S.D. Das, K.I. Vasu, *Scripta Metallurgica*, 4 (1970) 291-294.
- [**Riv72**] G. Rivaud, J.P. Riviere, J. Grilhe, *Scripta Metallurgica*, 6 (1972) 65.
- [**Rom11**] P.A. Rometsch, L.F. Cao, X.Y. Xiong, B.C. Muddle, *Ultramicroscopy*, 111 (2011) 690-694.
- [**Røy06**] J. Røyset, T. Stene, J.A. Sæter, O. Reiso, *Materials Science Forum*, 519-521 (2006) 239-244.
- [**Ryt82**] K. Rytola, *Nuclear Instrument Methods*, 199 (1982) 491-496.
- [**Saa89**] K. Saarinen, P. Hautojärvi, A. Vehanen, R. Krause, G. Dlubek, *Physical Review B*, 39 (1989) 5287-5296.
- [**Sah13**] G.B. Saha, *Physics and Radiobiology of Nuclear Medicine*, Springer-Verlag, New York, (2013) 92.
- [**Sai96**] M. Saito, *Physical Review B*, 53 (1996) 7810-7814.
- [**San06**] N. Sandberg, R. Holmestad, *Physical Review B*, 73 (2006) 014108.
- [**Sau11**] O. Sausa, M. Iskrova, B. Slavikova, V. Majernik, J. Kristiak, *Materials Science Forum*, 666 (2011) 115-118.
- [**Sch86**] H.E. Schaefer, R. Gugelmeier, M. Schmolz, A. Seeger, *Proceedings of the 8th International Conference on Vacancies and Interstitials in Metals and Alloys*, (1986) 111.
- [**Sch87**] H.E. Schaefer, *Physica Status Solidi*, 102 (1987) 47-65.
- [**See73**] A. Seeger, *Journal of Physics F*, 3 (1973) 248.
- [**Seg84**] D. Segers, P. van Mourik, M.H. van Wijngaarden, B.M. Rao, *Physica Status Solidi A*, 81 (1984) 209.
- [**Ser08**] A. Serizawa, S. Hirose, T. Sato, *Metallurgical Materials Transactions A*, 39 (2008) 243-251.
- [**Sey09**] H. Seyedrezai, D. Grebennikov, P. Mascher, H.S. Zurob, *Materials Science and Engineering A*, 525 (2009) 186-191.

- [Shu76] M.A. Shulmann, S. Berko, Proceedings of the 4th International Conference on Positron Annihilation, (1976).
- [SIExx] SIESTA official website, Materials Science Institute of Barcelona, <http://departments.icmab.es/leem/siesta/>.
- [Sim09] D. Simonovic, M.H.F. Sluiter, Physical Review B, 79 (2009) 054304.
- [Sme80] L.C. Smedskjaer, M. Manninen, M.J. Fluss, Journal of Physics F: Metal Physics, 10 (1980) 2237.
- [Sol02] J.M. Soler, E. Artacho, J.D. Gale, A. Garcia, J. Junquera, P. Ordejon, D. Sanchez-Portal, Journal of Physics: Condensed Matter, 14 (2002) 2745-2779.
- [Som00] A. Somoza, A. Dupasquier, I.J. Polmear, P. Folegati, R. Ferragut, Physical Review B, 61 (2000)14454-14463.
- [Som02] A. Somoza, M.P. Petkov, K.G. Lynn, Physical Review B, 65 (2002) 094107.
- [Sta96] T.E.M. Staab, B. Somieski, R. Krause-Rehberg, Nuclear Instruments and Methods in Physics Research A, 381 (1996) 141-151.
- [Sta99] T.E.M. Staab, R. Krause-Rehberg, B. Kieback, Journal of Materials Science, 33 (1999) 3833.
- [Sta00] T.E.M. Staab, E. Zschech, R. Krause-Rehberg, Journal of Material Science, 35 (2000) 4667-4672.
- [Sta01] M.J. Starink, Journal of Materials Science, 36 (2001) 4433-4441.
- [Sta06] T.E.M. Staab, personal communication (2006).
- [Sto75] M.J. Stott, P. Kubica, Physical Review B, 11 (1975) 1.
- [Tak78] J. Takamura, M. Koike, K. Furukawa, Journal of Nuclear Materials, 69-70 (1978) 738-740.
- [Tho27] L.H. Thomas, Proceedings of Cambridge Philosophical Society, 23 (1927) 542-548.

- [Tor11] M. Torsaeter, S. Wenner, W. Lefebvre, R. Holmestad, Norges Teknisk-Naturvitenskapelige Universitet, (2011), unpublished.
- [Val05] R. Valentini, Diplomarbeit, Rheinische Friedrich-Wilhelms-Universität Bonn, (2005).
- [Van80] L. Dorikens-Vanpraet, D. Segers, M. Dorikens, *Applied Physics*, 23 (1980) 149-152.
- [Van81] L. Dorikens-Vanpraet, D. Segers, M. Dorikens, F. Van Brabander, *Applied Physics*, 24 (1981) 29-31.
- [Vau03] D. Vaumousse, Dissertation, University of Oxford, (2003).
- [Vin57] G.H. Vineyard, *Journal of Physics and Chemistry of Solids*, 3 (1957) 121.
- [Vri87] J. De Vries, F.E.T. Kelling, *Nuclear Instruments and Methods in Physics Research A*, 262 (1987) 385-393.
- [Vri87] J. De Vries, Dissertation, Delft University of Technology, (1987) 106.
- [Vya92] S.V. Vyazovkin, V.I. Goryachko, A.I. Lesnikovich, *Thermochimica Acta*, 197 (1992) 41-51.
- [Wan04] Y. Wang, S. Curtarolo, C. Jiang, R. Arroyave, T. Wang, G. Ceder, L.Q. Chen, Z.K. Liu, *Calphad*, 28 (2004) 79-90.
- [Wan11] N. Wanderka, N. Lazarev, C.S.T. Chang, J. Banhart, *Ultramicroscopy*, 111 (2011) 701-705.
- [Wei67] H. Weisberg, S. Berko, *Physical Review*, 154 (1967) 249-257.
- [Wei04] L. Wei, Z.M. Zhang, C.X. Ma, C.L. Zhou, B.Y. Wang, T.B. Chang, S.X. Ren, *Materials Science Forum*, 445-446 (2004) 516-518.
- [Wen12] S. Wenner, C.D. Marioara, S.J. Andersen, R. Holmestad, *International Journal of Materials Research*, 103 (2012) 948.
- [Wer49] C. Wert, C. Zener, *Physical Review*, 76 (1949) 1169-1175.
- [Wib77] J. Wiberg, O. Vingsbo, *Physical Review B*, (1977) 1511.

- [Wikxx] http://en.wikibooks.org/wiki/Radioactive_Waste_Management/Radiation_Interaction_Fundamentals.
- [Wol92] J. Wolff, J.E. Kluin, T. Hehenkamp, Materials Science Forum, 105-110 (1992) 1329.
- [Wol07] C. Wolverton, Acta Materialia, 55 (2007) 5867.
- [Yam73] R. Yamamoto, M. Doyama, Physics Letters A, 43 (1973) 247-248.
- [Zhu05] V.V. Zhuk, A.V. Stoykov, R. Scheuermann, Report, Laboratory of Neutron Physics, Joint Institute for Nuclear Research, Russia, (2005) 6.
- [Zol65] H. Zoller, A. Ried, Aluminium 41, (1965) 626.
- [Zur09] H.S. Zurob, H. Seyedrezai, Scripta Materialia, 61 (2009) 141-144.

Acknowledgements

First of all I want to express my gratitude to my supervisor, Prof. Dr. J. Banhart for giving me the chance to take part in his research project (*DFG, grant Ba 1170 / 22-1*). As a conscientious German scholar, he taught me how to think and work in a scientific way. I am deeply indebted to him for his expert and valuable guidance. Heartfelt thanks to Prof. Dr. R. Krause-Rehberg (*University of Halle*) and Prof. Dr. K. Maier (*University of Bonn*), without their persistent support and important suggestions, this work would not have been possible at all.

I would like to express my sincere thanks to Dr. C.S.T. Chang, who granted to my every request concerning scientific discussion and experimental works. Many thanks to PD Dr. M. Haaks (*University of Bonn*) and Dr. B. Klobes (*Forschungszentrum Jülich*) for answering my questions and correcting the manuscript.

I would also like to give my appreciation to Prof. Dr. J. Hirsch (*Hydro Aluminium Bonn*), Prof. Dr. R. Holmestad, Dr. S. Wenner (*NTNU, Norway*), Dr. C.D. Marioara (*SINTEF, Norway*) for providing the high quality sample materials and Dr. M. Elsayed, Dr. M. Jungmann (*University of Halle*), Mr. N. Räth, all colleagues of the HISKP cyclotron group (*University of Bonn*) for producing the required isotopes.

My special gratitude goes to Mr. W. Altmann, Mr. H.J. Wittmaack (*Dept. Technical User Support BER II, HZB*), Dr. T. Wilpert (*Dept. Large Scale Facilities, HZB*), Dr. D. Alber, Dr. G. Bukalis (*Dept. Operation Reactor BER II, HZB*), Mrs. J. Böhm (*Dept. Technical Services, HZB*), Mr. R. Kasper (*Dept. Manufacturing, HZB*), Dr. D. Wallacher (*Dept. Sample Environments, HZB*), Dr. N. Wanderka (*Inst. Applied Materials, HZB*), PD Dr. G. Schumacher (*Dept. Microstructure and Residual Stress Analysis, HZB*), Dr. F. Garcia-Moreno, Miss B. Pfretzschner (*TU Berlin*), Mrs. C. Leisner, Mrs. C. Förster, Mr. H. Stapel (*Inst. Applied Materials, HZB*), Mr. J. Bajorat (*Dept. Central Data Processing and Networks, HZB*), Dr. G. Buchert (*Dept. Radiation Service, HZB*) and Mr. J. Kampe (*Warenannahme, HZB*) for providing me the necessary equipment and technical support.

The assistance and cooperation of my dear colleagues Dr. B. Korff (*University of Bremen*), Dr. Z.Q. Liang, Mr. J. Kühn (*Novelis*), Mr. E. Schmidt (*University of Cambridge, United Kingdom*),

Dr. Y. Yan, Mr. M. Wüstenhagen, Dr. A. Manzoni, Dr. F. Vogel (*Inst. Applied Materials, HZB*) and Dr. J. Rana (*Dept. Microstructure and Residual Stress Analysis, HZB*) had contributed a lot to this work. Particularly, the positron annihilation experiments carried out by our collaborator Prof. Dr. J. Cizek (*Charles University in Prague, Czech Republic*) are essential for the validation of the present results, thanks very much for his time and efforts. Those people, who directly or indirectly, have lent their helping hands for this work, are gratefully acknowledged.

I am thankful to my dear friends Dr. Y. Lu, Dr. J.Y. Yuan, Dr. Y.P. Fu, Miss. F.F. Chu, Miss. M. Nie, Dr. X.Z. Lin, Mr. G.C. Yin, Dr. A.R. Jeong, Mr. A. Ott, Mr. K. Palczynski, Mr. N. Heptner and all “M4Z” comrades-in-arms for the wonderful times we spent together, they made my stay in Berlin and Bonn one I will always remember.

Particular thankfulness to my family S.W. Lu, C.Y. Lin and Y. Lu for their invaluable support. Finally I wish to express my deepest love to my grandpa Yimin Liu, Zhijun Wang, grandma Xuying Yang, Lanying Qiao and our forever Ama - Prof. Dr. Sabina Laetitia Kowalewski for their endless love...